UNIVERSIDADE FEDERAL DE SÃO CARLOS

CENTRO DE CIÊNCIAS EXATAS E TECNOLOGIA

PÓS-GRADUAÇÃO EM ENGENHARIA CIVIL

Gilvan Bezerra dos Santos Junior

DESIGN OF AN UHPC WITH LOCAL MATERIALS: PROCEDURES, PROPERTIES AND MODELLING PARAMETERS

Dosagem de UHPC com materiais locais: Procedimentos, propriedades, e parâmetros de modelagem

SÃO CARLOS - SP

2023

Gilvan Bezerra dos Santos Junior

DESIGN OF AN UHPC WITH LOCAL MATERIALS: PROCEDURES, PROPERTIES AND MODELLING PARAMETERS

A thesis submitted to the Graduate Program in Civil Engineering in partial fulfillment of the requirements for the degree of Doctor of Philosophy in Civil Engineering.

Concentration area: Structures and Geotechnics

Supervisor: Prof. Dr. Guilherme Aris Parsekian

Co-Supervisor: Prof. Dr. Marco Antônio Carnio

SÃO CARLOS - SP

2023

Gilvan Bezerra dos Santos Junior

DESIGN OF AN UHPC WITH LOCAL MATERIALS: PROCEDURES, PROPERTIES AND MODELLING PARAMETERS

A thesis submitted to the Graduate Program in Civil Engineering in partial fulfillment of the requirements for the degree of Doctor of Philosophy in Civil Engineering.

EXAMINING COMMITTEE

_____

Prof. Dr. Guilherme Aris Parsekian (UFSCar)

_____

Prof. Dr. Marco Antônio Carnio (PUC-Campinas)

_____

Prof. Dr. Leandro Mota Trautwein (UNICAMP)

_____

Profa. Dra. Lia Lorena Pimentel (PUC-Campinas)

_____

Profa. Dra. Gláucia Maria Dalfré (UFSCar)

_____

Profa. Dra. Ana Elisabete Paganelli Guimarães de Avila Jacintho (PUC-Campinas)

ACKNOWLEDGEMENTS

ABSTRACT

Santos Junior, Gilvan Bezerra dos. Design of UHPC with local materials: Procedures, properties, and modelling parameters. 212p. Ph.D. Thesis. Civil Engineering, Federal University of São Carlos, São Carlos, SP, Brazil, 2023.

Ultra-high performance concrete (UHPC) is a cementitious composite with high compressive and tensile strength and ductile behavior. Its mixture comprises Portland cement, silica fume (SF), a filler, fine sand, superplasticizer admixture, a low water-to-binder ratio, and a high steel microfiber volume. Although UHPC production is now disseminated worldwide, its manufacturing and property evaluation are complex. Hence, a correct selection of materials and equipment is necessary. This thesis focuses on developing and evaluating a UHPC mixture with local materials and available regular laboratory equipment. Initially, in selecting materials, each local raw material's mineralogical and chemical compositions and particle size were determined for an accurate choice. The mixing procedure was tested in a three-speed horizontal pan mixer with different stages to obtain a homogeneous and self-compacting mixture. The design method utilized was the Modified Andreasen and Andersen. After determining the initial composed mix curve, some adjustments refined the mix design to obtain the required properties. To validate the UHPC developed, the physical and mechanical properties were evaluated. The tests were performed according to the Brazilian Standards and the French NF P18-470. The compression test was carried out with low load rates to obtain the post-peak descending branch. The tensile curve was determined indirectly through an inverse analysis by 3-point and 4-point bending tests. In addition, the splitting test response was evaluated. Lastly, the mechanical tests were utilized to obtain the parameters needed to define the material in a finite element numerical analysis. This work confirms that producing UHPC with local materials and regular laboratory equipment is possible. Starting from the correct selection of materials and procedures, 130 MPa compressive and 6.5 MPa elastic tensile 28-day strengths were achieved with a practically self-compacting material and superior durability parameters of 1.02% air content and 3.0% water porosity. The step-by-step inverse analysis response was compared to simplified methods, and the French Standard Institute (AFNOR) and Japan Society of Civil Engineers (JSCE) standardized tensile curves presented a better fit. Furthermore, the Concrete Damage Plasticity (CDP) model parameters were obtained and calibrated according to compression and flexural responses.

Keywords: UHPC, particle packing, inverse analysis, CDP parameters

RESUMO

Santos Junior, Gilvan Bezerra dos. Dosagem de UHPC com materiais locais: Procedimentos, propriedades, e parâmetros de modelagem. 212p. Tese de doutorado em Engenharia Civil – Universidade Federal de São Carlos, São Carlos – SP, Brasil, 2023.

Concreto de ultra alto desempenho (UHPC) é um compósito cimentício definido por suas elevadas resistências à compressão e à tração, assim como um comportamento dúctil. Sua mistura é composta por cimento Portland, sílica ativa, filler, areia fina, aditivo superplastificante, baixa relação água-cimento, e elevado volume de microfibras metálicas. Apesar da produção do UHPC atualmente ser disseminada mundialmente, sua fabricação e análise de suas propriedades são processos complexos. Portanto, uma correta seleção dos materiais e equipamentos é necessária. Esta tese tem como objetivo desenvolver e avaliar um UHPC com materiais locais e equipamentos de laboratório normalmente disponíveis. Inicialmente, na etapa de seleção dos materiais, as composições mineralógicas e químicas dos insumos, assim como o tamanho de suas partículas, foram determinadas para uma escolha mais adequada. O procedimento de mistura foi testado em um misturador horizontal de três velocidades variando as etapas do processo para se obter um material homogêneo e autoadensável. O método de dosagem utilizado foi o Andreasen e Andersen Modificado. Após determinar as proporções dos materiais iniciais, alguns ajustes foram necessários para refinar o traço e obter as propriedades desejadas. Para validar o UHPC desenvolvido, suas propriedades físicas e mecânicas foram avaliadas. Os ensaios foram realizados de acordo com as normas brasileiras e a norma francesa NF P18-470. O ensaio de compressão foi conduzido com uma baixa taxa de carregamento com o intuito de se obter o trecho pós pico do diagrama tensão-deformação. A curva do comportamento à tração foi determinada indiretamente através de uma análise inversa dos ensaios de flexão de 3 e 4 pontos. Além disso, a resposta do ensaio de compressão diametral foi analisada. Por último, as respostas dos ensaios mecânicos foram utilizadas para obter os parâmetros necessários para a definição do material em uma análise numérica em elementos finitos. Este trabalho confirma que é possível produzir UHPC com materiais locais e equipamentos de laboratório comumente encontrados. Iniciando pela correta seleção dos materiais e procedimentos, obteve-se um material com 130MPa de resistência à compressão e limite elástico à tração de 6,5MPa, ambos aos 28 dias. O UHPC foi classificado como praticamente autoadensável e obteve-se notáveis parâmetros de durabilidade, como 1,02% de ar incorporado no estado fresco e 3% de porosidade. As curvas obtidas na análise inversa foram comparadas com respostas de métodos simplificados, sendo aquelas obtidas pelas normas da Associação Francesa de Normalização (AFNOR) e Sociedade Japonesa de Engenheiros Civis (JSCE) as que tiveram melhores correlações. Além disso, os parâmetros do modelo de plasticidade do dano do concreto (CDP) foram obtidos e calibrados com as curvas dos ensaios de compressão e de flexão.

Palavras chave: UHPC, empacotamento de partículas, análise inversa, parâmetros do CDP

LIST OF FIGURES

LIST OF TABLES

LIST OF ABBREVIATIONS

2%F	2% Of Fiber Content
3S	Three Stage Mixture
4S	Four Stage Mixture
a/d	Span-To-Depth
ABNT	Associação Brasileira de Normas Técnicas
ACI	American Concrete Institute
AFNOR	Association Française de Normalisation (*French Standard Institute*)
APEG	Allyl Ether-Based
ASTM	American Society for Testing and Materials
b/s	Binder-To-Sand
CA	Coarse Aggregate
CC	Conventional Concrete
CDP	Concrete Damage Plasticity
CH	Calcium Hydroxide
CMOD	Crack Mouth Opening Displacement
CP	Cimento Portland (*Portland Cement*)
CPM	Compressive Packing Model
CS	10x20cm Specimen
CSA	Calcium Sulfoaluminate
C-S-H	Calcium Silicate Hydrate
DSS	Dry Silica Sieved
DSWT	Dry Silica Without Treatment
DTT	Direct Tensile Test
EA	Early Age
FE	Finite Element
FM	Fineness Modulus
GGBFS	Ground Granulated Blast Furnace Slag
HPC	High-Performance Concrete
HSC	High-Strength Concrete
HUTM	Hydraulic Universal Testing Machine
IC	Internal Curing
ITZ	Interfacial Transition Zone
JSCE	Japan Society of Civil Engineers
LECA	Lightweight Expanded Clay

LP	Limestone Powder
LVDT	Linear Variable Differential Transformer
LWA	Lightweight Aggregates
LWS	Lightweight Sand
MOR	Modulus of Rupture
MPEG	Methacrylic Acid-Based
MS	Manufactured Sand
MS	5x10cm Specimen
N/D	Notch-To-Depth
NBR	Norma Brasileira (*Brazilian Standard*)
NF	Norme Française (*French Standard*)
nS	Nano-Silica
ODS	Oven-Dried Sand
PCE	Polycarboxylate Superplasticizers
PE	Polyethylene
PP	Polypropylene
PSD	Particle Size Distribution
PVA	Polyvinyl Acetate
RC	Reinforced Concrete
RH	Relative Humidity
RHA	Rice Husk Ash
RILEM	Réunion Internationale Des Laboratoires Et Experts Des Matériaux, Systèmes De Construction Et Ouvrages (*International Union Of Laboratories And Experts In Construction Materials, Systems And Structures*)
RPC	Reactive Powder Concrete
RPM	Revolutions per Minute
RSS	Residual Sum of Squares
SAM	Silica in Aqueous Medium
SAP	Superabsorbent Polymers
SCM	Supplementary Cementitious Materials
SEM	Scanning Electron Microscope
SF	Silica Fume
SFC	Superfine Cement
SP	Superplasticizers
SRA	Shrinkage Reducing Admixture

TG	Thermogravimetry
UHPC	Ultra High-Performance Concrete
VPV	Volume Of Permeable Voids
w/b	Water-To-Binder
w/c	Water-To-Cement
WF	Mixture Without Filler
wt.	Weight

LIST OF SYMBOLS

e	Eccentricity
h	Notional Size of Member
h	Height of the Section
p	Span
P_{mix}	Composed Mix
P_{tar}	Target Mix
D	Particle Size
E	Modulus of Elasticity
K	Failure Surface Adjustment
K	Fiber Orientation Factor
L	Length
R	Ideal Gas Constant
S	Loading/Unloading Slope
$T(t)$	Actual Temperature
d	Damage Variable
g	Energy Absorption Capacity
q	Distribution Modulus
t	Time (Age)
t'	Load Applying Age
t'_{adj}	Adjusted Age at Loading
u	Perimeter
f_{b0}/f_{c0}	Yield Stress in the Biaxial and Uniaxial States Ratio
$f'_{c,t}$	Compressive Strength at any Time
f'_c	Compressive Strength at 28 Days
$f_{cm,calc}$	Theoretical Compressive Strength
f_{cm}	Mean Value of the Compressive Strength at 28 Days
$f_{ct,3b,28}$	28-Days Tensile Strength (3-Point Bending)
$f_{ct,4b,28}$	28-Days Tensile Strength (4-Point Bending)
$f_{ct,el,3b,28}$	28-Days Elastic Tensile Strength (3-Point Bending)
$f_{ct,el,4b,28}$	28-Days Elastic Tensile Strength (4-Point Bending)
$f_{ct,el,sp,28}$	28-Days Elastic Tensile Strength (Splitting Test)
$f_{ct,el,sp,7}$	7-Days Elastic Tensile Strength (Splitting Test)
$f_{ct,el}$	Tensile Limit of Elasticity

$f_{ct,sp,28}$	28-Days Tensile Strength (Splitting Test)
$f_{ct,sp,7}$	7-Days Tensile Strength (Splitting Test)
$f_{ctf,1\%}$	Post-Cracking Strength Corresponding to a 0.01H Crack Width
f_{ctf}	Post-Cracking Strength
$f_{ctf}*$	Post-Cracking Stress Limit
$f_{t,u}$	Ultimate Tensile Strength
f_t	First Craking Tensile Strength
$g_{f,A}$	Dissipated Energy per Unit Volume
l_{ch}	Characteristic Length
t_e	Ambient Temperature Equivalent Age
w_{1k}	Crack Width after the First Crack
w_{2k}	Crack Width at Zero Tensile Stress
α	Compressive Strength Curve Reduction Factor
γ	SRA Effect Coefficient
γ	Normalized Compressive Strain
δ	Midspan Displacement
ε	Strain
η	Normalized Post-Crack Modulus
λ	Parameter of Fiber Pull-Out
μ	Constant Stress Level
σ	Stress
τ	Equivalent Bond Strength Between Fiber and Matrix
φ	Creep Coefficient
ψ	Dilation Angle
χ	Curvature
ω	Normalized Compressive Yield Strain
α_E	Correction Factor Depending on Used Aggregates
α_{trn}	Normalized Transition Strain
β_{tu}	Normalized Ultimate Tensile Strain
δ_{pc}	Average Residual Crack Openings
δ_u	Ultimate Crack Opening
ε_1	Associated Strain of 0.5mm Crack Width
ε_2	Associated Strain of 4.3mm Crack Width
ε_{as}	Autogenous Shrinkage
$\varepsilon_{as\infty}$	Ultimate Autogenous Shrinkage

ε_{cc}	First Cracking Strain
ε_{cr}	First Cracking Tensile Strain
ε_{cu}	Ultimate Compressive Strain
ε_{cy}	Compressive Yield Strain
ε_{el}	Associated Strain Limit of Elasticity
ε_{lim}	Limit Strain
ε_{pc}	Post-Cracking Strain
ε_{soft}	Associated Strain of Composite Tensile at Softening
$\varepsilon_{t,max}$	Maximum Tensile Strain
$\varepsilon_{t,u}$	Ultimate Tensile Strain
ε_{trn}	Tensile Transition Strain
ε_{tu}	Ultimate Tensile Strain
$\varepsilon_{u,1\%}$	Associated Strain of 0.01H Crack Width
$\varepsilon_{u,el}$	Elastic Limit Strain
$\varepsilon_{u,pic}$	Associated Strain of 0.3mm Crack Width
ε_u	Ultimate Strain
λ_{cu}	Normalized Ultimate Compressive Strain
σ_{cc}	First Cracking Stress
σ_{fpc}	Maximum Fiber Tensile Stress
σ_{pc}	Post-Cracking Stress
φ_{bc}	Basic Creep Coefficient
φ_{dc}	Drying Creep Coefficient
χ_f	Fiber Factor
$\emptyset$	Diameter

TABLE OF CONTENTS

1 INTRODUCTION

Ultra-high performance Concrete (UHPC) is a cementitious composite that presents high compressive and tensile strengths and ductile behavior, i.e., it can yield significant deformations even after matrix cracking. It is classified as a reactive powder concrete (RPC) and can achieve high mechanical performance and outstanding durability. The UHPC mix is comprised of Portland cement, SF, a filler, fine sand, and superplasticizer admixture; it has a low water-to-binder ratio and a high steel microfiber volume. The microfibers are added to change the HSC brittleness, increasing the post-cracking tensile behavior.

The UHPC components should be designed to comply with a particle size range that enables arrangement using the packing method. This is one of the design bases that allow for the improvement of material density, increased mechanical properties, and durability. In addition, the mixing procedure needs high mixing energy and defined stages to make the mixture homogeneous and self-compacting. Some researchers utilize unconventional procedures, such as pre-setting pressure and thermal curing, to reach very high compressive strength. One example is found in the study by Richard and Cheyrezy (1995), which reports an 810 MPa RPC.

Its notorious physical and mechanical properties are from the high packing density and high content of superplasticizers and steel fibers. The compression is characterized by a strength of at least 130 MPa and a non-brittle post-cracking response. The tensile behavior, disregarded for conventional concrete (CC), is defined with a limit of elasticity greater than 6 MPa and a ductile behavior, which improves flexure, shear, punching shear, and torsion performance. Furthermore, UHPC is a self-compacting material with superior durability parameters due to its improved microstructure decreasing permeability.

Due to the mechanical behavior improvement, it is possible to use UHPC in innovative circumstances. Numerical modeling is an instrument to simulate different scenarios based on the material's properties. These simulations can predict the structural behavior of varying geometries, loading conditions, and interaction with other elements. The CDP model is commonly used to simulate the concrete inelastic structural behavior considering the material damage.

Furthermore, the models must be calibrated with the experimental results to validate the numerical response.

Although UHPC production is now disseminated worldwide, this manufacture and properties evaluation is complex. A correct selection of the materials and equipment is necessary. This work presents a methodology to aid the materials selection and mix procedure, detailing how to assess each component and the methods to design and produce the best UHPC mixture. As an initial stage, the methodology assists the material triage before producing a trial batch and was validated with the experimental results. The physical and mechanical properties are evaluated to characterize the UHPC behavior. Lastly, a numerical model is developed to simulate the material produced and provide the parameters to replicate the UHPC behavior in other studies. The main objective is to provide a methodology to design, produce, and assess UHPC with local materials and available regular laboratory equipment, seeking the best properties.

1.1 OBJECTIVES

The research aims to develop a methodology to design, produce, and evaluate a UHPC mixture with local materials and available regular laboratory equipment, seeking better properties with them. More specifically, the objectives of this study are the following:

- Define a procedure for designing and producing UHPC with a selection of available local materials and available local laboratory equipment.
- Develop a UHPC mixture that must be self-compacting, have a compressive strength of more than 130 MPa, and exhibit ductile behavior.
- Obtain the complete physical and mechanical behavior, including damage curves, using the available local laboratory equipment.
- Provide the CDP parameters for modeling the UHPC developed.

1.2 SIGNIFICANCE OF RESEARCH

UHPC may no longer be considered a new material due to the utilization level in countries such as Canada, the United States, France, and South Korea. In the last decades, bridges, footbridges, and pre-cast elements were built with

UHPC in those cited places. Despite the quantity of research and national standards, e.g., for the standard French NF P 18-470 published on July 29, 2016, in Brazil, it is not usual to use UHPC in regular structures.

One of the main difficulties of UHPC production is the selection of suitable raw materials with specific properties and particle sizes and equipment to mix them. Even with a commercial pre-mix composed of cement, SF, sand, and filler, obtaining UHPC properties is not simple. Control of the mixture design of this material is the first step to it becoming known by structural engineers, and all its qualities may be appreciated.

Therefore, the research is motivated by the need for parameters to assist local UHPC production, ensuring that the material is self-compacting, ductile, and has remarkable compressive and tensile strength. In addition, a mechanical properties analysis is presented and behavior parameters are provided, allowing for the assessment of the material's structural behavior and to help future projects.

1.3 THESIS SCOPE AND ORGANIZATION

An initial literature review concerning the specific parameters of each raw material and mixture procedure to achieve the UHPC characteristics is presented. To investigate the best material selection and to assess if the available regular laboratory equipment is sufficient to produce UHPC, an experimental program is then presented. Next, the physical and mechanical properties were evaluated, including the flow rate, elastic modulus, compressive strength, tensile flexural strength, and damage parameters. From these tests, it was possible to assess parameters for modeling the material behavior in Finite Element Method software. The thesis consists of six chapters, which are briefly described here to elucidate the sequence of the work.

Chapter 1 presents an introduction contextualizing the research, the objectives to be achieved, the motivation, and an overall view of how the thesis is organized.

Chapter 2 presents a literature review concerning UHPC and its properties, comprising the procedures for mix design, mixture, placement, and

curing, including pre-setting pressure and thermal curing, and the material's mechanical behavior.

In Chapter 3, the methodology to characterize the raw materials, as well as the methods to develop and evaluate the UHPC, are detailed. The concrete characterization Brazilian standards and the French *NF P18-470 – Concrete – Ultra-high performance fibre-reinforced concrete – Specifications, performance, production, and conformity*, were mainly referenced.

Chapter 4 presents the mix design and mixture procedure validations. In addition, the evaluation of the physical and mechanical properties is detailed. From the initial batch, several adjustments are described with the aim of improving the material characteristics and the evolution of compressive strength until the goal of obtaining a UHPC material is fulfilled. To evaluate the mechanical behavior, the stress-strain curves and damage parameters for compression and tension are presented, in addition to failure modes and crack patterns.

In Chapter 5, a Finite Element model is developed to obtain the material parameters validated by the experimental results.

Lastly, Chapter 6 summarizes the conclusions.

2 ULTRA-HIGH PERFORMANCE CONCRETE COMPONENTS AND PROPERTIES

Developing an ideal structural material means improving compression and tension properties and extending durability. In particular, CC is an excellent compressive resistant material but needs to be reinforced in tension. The use of fibers started in the 1960s, focusing on improving concrete behavior beyond tensile strength, such as resistance to cracks, endurance to wear and shocks, and toughness (Ipek, Yilmaz, and Uysal, 2012). These properties can be achieved by eliminating concrete coarse aggregates to optimize the granular mixture, enabling the obtainment of a homogeneous and dense cementitious matrix that exhibits high mechanical performance (Richard and Cheyrezy, 1995). Furthermore, the search for minimal porosity is the premise of excellent UHPC performance in terms of strength and durability (Courtial *et al.*, 2013).

2.1 CONSTITUENT MATERIALS

This topic explains the importance of selecting each raw material for UHPC production. It summarizes literature studies based on micro- and macrostructure improvement.

2.1.1 Cement

Cement is the essential component of cementitious composites because it is responsible for binding the other constituent materials. The cement hydration products improve the material density and, therefore, the mechanical behavior. Selecting an ideal cement type may contribute to achieving better properties. The Brazilian cement specification is regulated by ABNT NBR 16697 (2018), which classifies each cement type available on the market. Although this classification would be more precisely related to "blended cement" than only "cement" as additions are allowed, in this text, only the last word will be used. The cement types are classified as Ordinary Portland Cement (CP I), Composite Portland Cement (CP II), Blast Furnace Portland Cement (CP III), Pozzolanic Portland Cement (CP IV), High Initial Strength Portland Cement (CP V), and White Portland Cement (CPB). Table 1 presents the composition of regular Brazilian cement. For UHPC, it is preferable to use cement with a low C_3A specific surface

and an adequate C_3A/SO_4^{2-} ratio and alkali content, which minimizes its water demand (Dils, Boel, and De Schutter, 2013; De Larrard and Sedran, 1994). This is because cement with a low C_3A content may decrease the hydration heat and the ettringite formation (Courtial *et al.*, 2013).

Table 1: Composition of a Brazilian cement

COMPOSITION \ TYPE			CP II-F-32[a]	CP II-F-40[b]	CP II-Z-32[c]	CP IV-32-RS[d]	CP V-ARI[e]
CHEMICAL	Al_2O_3	%	4.12	4.21	8.62	9.73	4.31
	SiO_2	%	18.24	17.79	21.49	29.46	18.48
	Fe_2O_3	%	2.83	2.75	3.19	3.97	2.91
	CaO	%	61.21	61.53	53.21	44.81	63.04
	MgO	%	2.81	3.10	1.95	2.84	2.90
	SO_3	%	2.60	3.05	2.63	2.18	2.82
	C_3A[f]	%	6.14	6.51	17.45	19.08	6.51
	Loss on ignition	%	6.70	6.05	7.20	4.64	3.66
	Free CaO	%	1.21	1.78	0.72	1.12	1.70
	Insoluble Residue	%	1.01	0.74	10.62	25.38	0.53
	Alkali content (Na_2O and K_2O)	%	0.72	0.70	0.76	1.11	0.69
PHYSICAL	Thermal expansion	mm	0.15	0.40	0.27	0.25	0.30
	Setting time (min)	Start	191	174	254	241	177
		End	257	234	310	303	236
	Normal consistency	%	25.9	29.7	28.6	30.30	29.9
	Blaine	cm²/g	3354	4504	3754	4325	4418
	Fineness #200	%	2.62	0.01	1.42	0.67	0.04
	Fineness #350	%	10.38	0.14	6.75	2.89	0.24
	Compression Strength (28-day)	MPa	40.7	51.4	42.6	45.50	53.20

a   composite cement with limestone filler (32MPa 28-day compressive strength).
b   composite cement with limestone filler (40MPa 28-day compressive strength).
c   composite cement with pozzolan (32MPa 28-day compressive strength).
d   pozzolanic cement sulfate resistant (32MPa 28-day compressive strength).
e   high initial strength cement.
f   determined by Bogue equation

Source: Itambé® (2021)

Dils, Boel, and De Schutter (2013) report the analysis of six Belgian cement types, assessing the influence of their mineralogical and chemical

parameters on material performance. As a result, workability is directly affected by the C_3A specific surface. Due to a higher specific surface, more superplasticizers are necessary to fully cover the cement particles. In addition, sulfate ions may compete with the superplasticizer for the resting anchor points on the C_3A. Therefore, the C_3A/SO_4^{2-} ratio is a parameter that impacts workability. A good indicator of the SO_4^{2-} concentration in the pore solution is the cement's alkali content (K_2O and Na_2O). Furthermore, the presence of alkalis influences the reactivity of C_3A. Thus, the desired cement composition combines a low C_3A specific surface, an acceptable SO_3 content, and a moderate alkali amount (K_2O and Na_2O). Table 2 presents the cement composition with the best workability and mechanical response.

Table 2: Best cement mineralogical and chemical composition to produce UHPC

SiO_2	%	20.90	**Blaine**	cm²/g	3975
Al_2O_3	%	3.64	d_{50}	µm	10.40
Fe_2O_3	%	5.19	C_3S	%	59.82
CaO	%	63.68	C_2S	%	14.88
MgO	%	0.77	$C_2S + C_3S$	%	74.70
SO_3	%	3.03	C_3A	%	0.87
Na_2O	%	0.17	C_4AF	%	15.80
K_2O	%	0.63	C_3A-specific surface	cm²/g C3A	34.78

Source: Dils, Boel, and De Schutter (2013)

Alkaysi *et al.* (2016) studied the durability of UHPC produced with ASTM C150 White Cement Type I, Portland Type V, and a blend of Portland Cement Type I with ground granulated blast furnace slag (GGBFS). Using Portland Cement Type V with sulfate-resisting properties results in better durability parameters, such as lower chloride penetration and air content (%). In addition, White Cement Type I allows a high compressive strength response (173.6 MPa). Despite this, Blended Portland Cement Type I and GGBFS allow a higher value (190.9 MPa).

Wang, Chen, and Wu (2019) assessed the UHPC with calcium sulfoaluminate (CSA) cement. Its utilization is suitable for rapid strength development and durability in aggressive environments. Besides the similar 28-

day tensile response, the UHPC with CSA exhibited significant early-age strain-hardening behavior. The strength increases quickly from four hours to one day, while it shows a slight variation at later ages, as presented in Figure 1. This occurs because the CSA cement hydrates rapidly at the early stage (Wang, Chen, and Wu, 2019). Furthermore, the mixture with CSA cement results in a rapidly denser concrete matrix and reduced porosity than the UHPC with Portland cement. The material without CSA at 28-day presents better strain-hardening behavior with a better distribution of microcracks.

Figure 1: Strain-stress curves of UHPC with (ES-UHPC) and without (N-UHPC) CSA at 1 day and 28 days
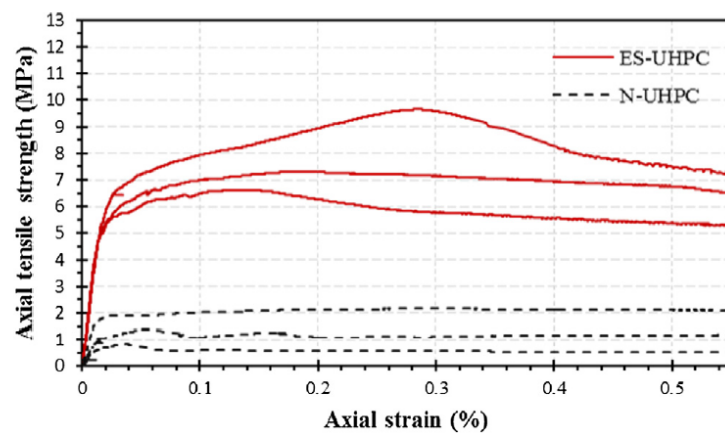
(a) 1 day
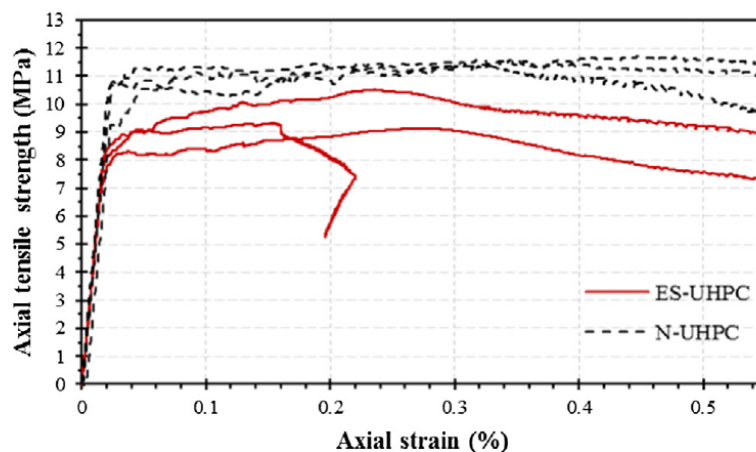
(b) 28 days

Source: Wang, Chen, and Wu (2019)

The correct selection of cement type provides adequate self-compaction workability with reduced air content in the concrete (Dils, Boel, and De Schutter, 2013). Moreover, the material's durability, as resistance to chloride and sulfate attacks increases with increasing compression strength.

2.1.2 Silica Fume (SF)

Amorphous silica contributes directly to reducing the porosity and improving the density of UHPC. One commonly used amorphous silica is SF, a by-product of industrial silicon production through the oxidization of gaseous SiO at temperatures above 2000°C; and it has particle sizes in the sub-micrometer range (Lee *et al.*, 2018; Oertel *et al.*, 2014). Incorporating SF to obtain a denser matrix is one of the most productive and economical methods because of its fine particles and high pozzolanic activity (Wu, Shi, and Khayat, 2016). Besides SF, micro-silica, nano-silica, and wet-chemically synthesized silica (Stoeber suspension monomodal particles) are utilizable and characterized according to their particle size and physical properties. Table 3 presents an example of an analytical composition of SF extracted from X-ray fluorescence (XRF) spectroscopy. Richard and Cheyrezy (1995) mention that the most harmful impurities in SF are carbon and alkalis, commenting that the former could decrease the efficiency of the superplasticizer, and the latter reduce the pozzolanic activity (Lin *et al.*, 2019; De Larrard and Sedran, 1994). The impurity of SF may not negatively influence the compressive strength (Oertel *et al.*, 2013).

Table 3: Chemical composition of SF

SiO_2	%	98,580
CaO	%	0,241
Al_2O_3	%	0,142
Fe_2O_3	%	0,031
SO_3	%	0,141
K_2O	%	0,533
Na_2O	%	0,093
MgO	%	0,162
Cl	%	0,011

Source: Oertel *et al.* (2013)

The SF function may be divided into the filler effect, seeding effect, and pozzolanic effect. The filler effect is the silica's ability to fill the voids among the cement particles and other constituent materials (Lee *et al.*, 2018). Spherical SF particles assist the filler effect, termed the "ball effect" (Figure 2) (Lin *et al.*, 2019), which is the principle of a better packing density. The nucleation of calcium silicate hydrate (C-S-H) phases occurs on the surface of filler materials; it accelerates the cement hydration, which is known as the seeding effect (Lee *et al.*, 2018). In addition, the silica's high specific surface area contributes to a better seeding effect.

Figure 2: Particle morphology of SF
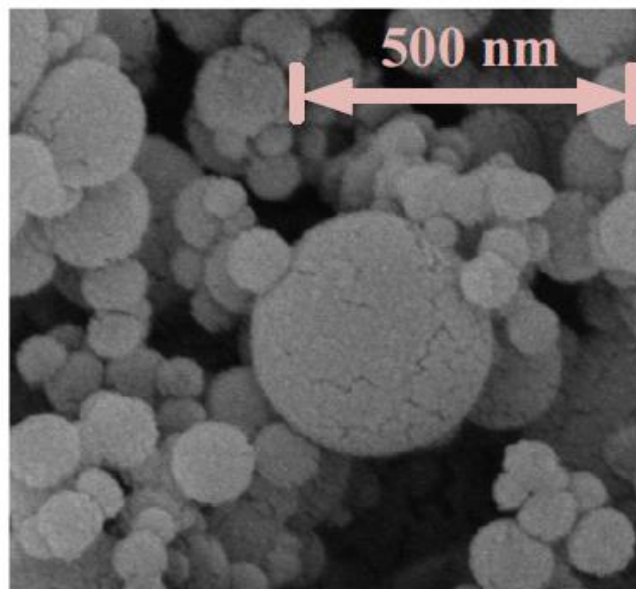
Source: Lin *et al.* (2019)

Based on its high pozzolanic activity, silica reacts with portlandite $(Ca(OH)_2, CH)$, improving the UHPC mechanical properties (Lee *et al.*, 2018). From the first contact of cement with water, ions Ca^{2+} and OH^- are rapidly released from the cement particles' surface. When SF is incorporated, the dissolution of SiO_4^{4-} ions can absorb Ca^{2+} and OH^- ions to form C-S-H (Wu, Shi, and Khayat, 2016). The filler effect accelerates the hydration of the clinker phases (especially C_3A and C_3S) at an early age, while the pozzolanic reaction starts later, enhanced with pH and temperature (Lee *et al.*, 2018).

The UHPC flowability improves significantly with the SF incorporation of up to 15%, as shown in Figure 3a. This result may be attributed to the filler effect

that enhances mixture lubrication due to some entrapped water released between the small particles agglomerated and the perfect sphericity of the silica particles (Wu, Shi, and Khayat, 2016; Richard and Cheyrezy, 1995). Furthermore, the addition beyond 15% decreases the flowability due to its high surface area, which demands a higher water amount.

SF content had a significant effect on mechanical properties. With 20% cement weight replacement, the compressive and flexural strengths increase by 28% and 29%, respectively. High SF amounts decrease the mechanical strengths and flowability due to increased plastic viscosity and yield stress, resulting in air entrapment (Wu, Shi, and Khayat, 2016). Furthermore, the strength improvement results from the pozzolanic effect. Figure 3b presents the result of a thermogravimetry analysis that can illustrate the efficiency of the SF on CH reaction to form C-S-H.

Considering the result of a denser material, the bond strength between the fiber and matrix increases with increasing silica content (Figure 3c). Wu, Shi, and Khayat (2016) report the optimum SF content as between 15% and 25%. Richard and Cheyrezy (1995) establish the value of 0.25 as typical for the SF/cement ratio.

Figure 3: Influence of SF content on UHPC microstructure: (a) flowability with mini-slump flow, (b) content of CH from TG analyses, and (c) fiber bonding strength from pullout tests

(a)

(b)

(c)
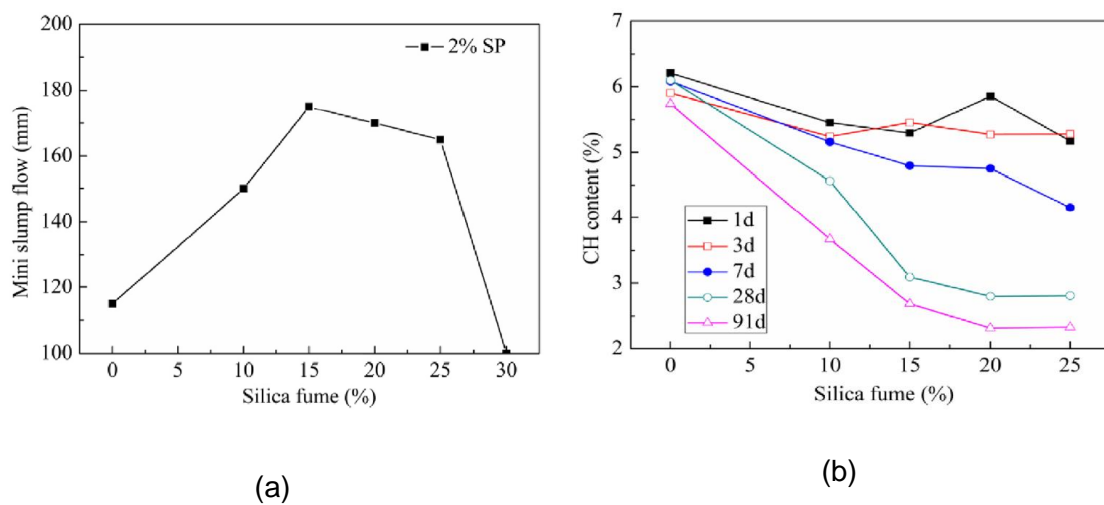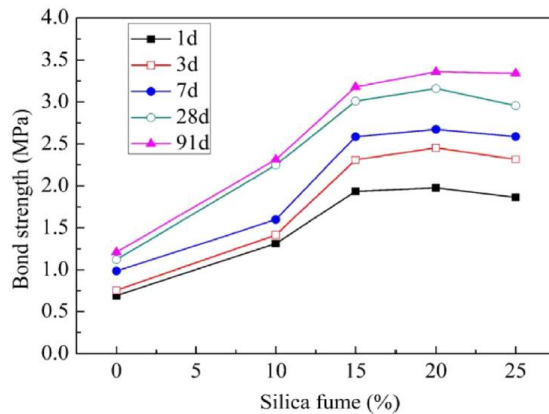
Source: Wu, Shi, and Khayat (2016)

Lee *et al.* (2018) analyzed the role of micro silica in the hydration and strength of UHPC. The authors confirm the low pozzolanic activity at early ages and the acceleration of the pozzolanic reaction with 72 h of curing at a high temperature of 90°C. The utilization of two different micro silica types exhibited the distinct roles of the filler and pozzolanic effect.

Ghafari *et al.* (2014) conducted an experimental study to evaluate the influence of nano-silica (nS) addition on the properties of UHPC. Their results indicate that nS consumed 10% more $Ca(OH)_2$ than SF paste, resulting from the pozzolanic activity. Concerning flowability, their findings showed a decrease in slump flow values when incorporating nS (wt.%) cement replacement into the mixture. The nS particles absorbed the lubrification water due to its high specific surface area, preventing the particles' free movement. Conversely, the addition of 3 wt.% nS resulted in a 24% increase in the 7-day compressive strength. At 28 days and 90 days, the difference was small because of the early age pozzolanic reactivity of nS in cement paste. In addition, when the nS addition is higher than 4 wt.%, the nanoparticles tend to agglomerate, reducing mechanical strength. The authors concluded that the matrix phase of UHPC containing nS is significantly denser and more homogeneous than just with SF. The addition of nS particles reduces capillary pores and refines the pore structure (Ghafari *et al.*, 2014). Furthermore, nano-silica could improve UHPC because of its advanced properties (e.g., higher purities, smaller primary particles, and higher specific surface areas) (Oertel *et al.*, 2014).

Oertel *et al.* (2013) utilized wet-chemically synthesized silica (Stoeber particles) with high chemical purity (SiO_2 of 99.97 wt.%). They investigated these particle characteristics on the calculated particle packing densities, microstructure, and compressive strength of UHPC. The authors report the beneficial effect of monomodal particles in filling voids, resulting in a high particle packing density that improves compressive strength. The Stoeber particles are dispersed among the primary particle sizes and the smallest agglomerates. Obtaining the ideal SF dispersion by a standard mortar mixing procedure might be difficult. Using ultrasound helps improve the dispersion of SF in water. The use of commercial silicas should increase concrete strength by providing particles that will be dispersed in their primary particle sizes (Oertel *et al.*, 2013).

2.1.3 Aggregates

One of the main bases of UHPC production is eliminating coarse aggregate and limiting the sand size to improve particle packing. The aggregate's function in CC is to form a skeleton of continuous granular elements in the cementitious paste. In addition, it is recommended to use an aggregate whose strength is higher than the desired concrete to improve its mechanical properties (De Larrard and Sedran, 1994). The aggregate size limitation to fine sand (600 μm maximum) has some objectives, such as the reduction of the size of microcracks between particles, increasing the mechanical properties of the paste and reducing porosity (Richard and Cheyrezy, 1995). To select the sand, the parameters defined are mineral composition, mean particle size, granular range, particle shape, and mixture ratio by weight (Richard and Cheyrezy, 1995).

Quartz is the most common sand mineral composition, composed of silica (silicon dioxide or SiO_2). According to Richard and Cheyrezy (1995), quartz sand has some advantages. It is a rigid material, allows an excellent paste/aggregate interface, and is readily available at a low cost. Other aggregate types are available, such as manufactured sand (MS). Yang *et al.* (2019) analyzed the properties of UHPC with partial aggregate replacement with manufactured sand composed of calcite (limestone with aragonite, $CaCO_3$). The fluidity is reduced continuously with an increased MS substitution percentage, which may be explained by the surface properties and PSD. However, adding MS could increase the compressive strength of UHPC up to 14.6%, attributing this

improvement to its rough surface, with better interlocking and fine powders, which could absorb free water and reduce the water-to-binder ratio. Furthermore, the fine powders presented in calcite MS may cause a significant increase in autogenous shrinkage.

Grading fine aggregate plays a significant, albeit indirect, role in obtaining a workable mix design with a low w/c ratio (Sobuz *et al.*, 2016). Figure 4 presents the compressive strength and sand fineness modulus (FM) relation. Sobuz *et al.* (2016) attribute the strength reduction with FM to the packing density rather than the water requirement for the cement's hydration. However, a slight increase may occur at an early age, a consequence of insufficient water for the rapid hydration of cement. The FM acts as a limit to strength rather than the w/c ratio.

Figure 4: Influence of FM on compressive strength
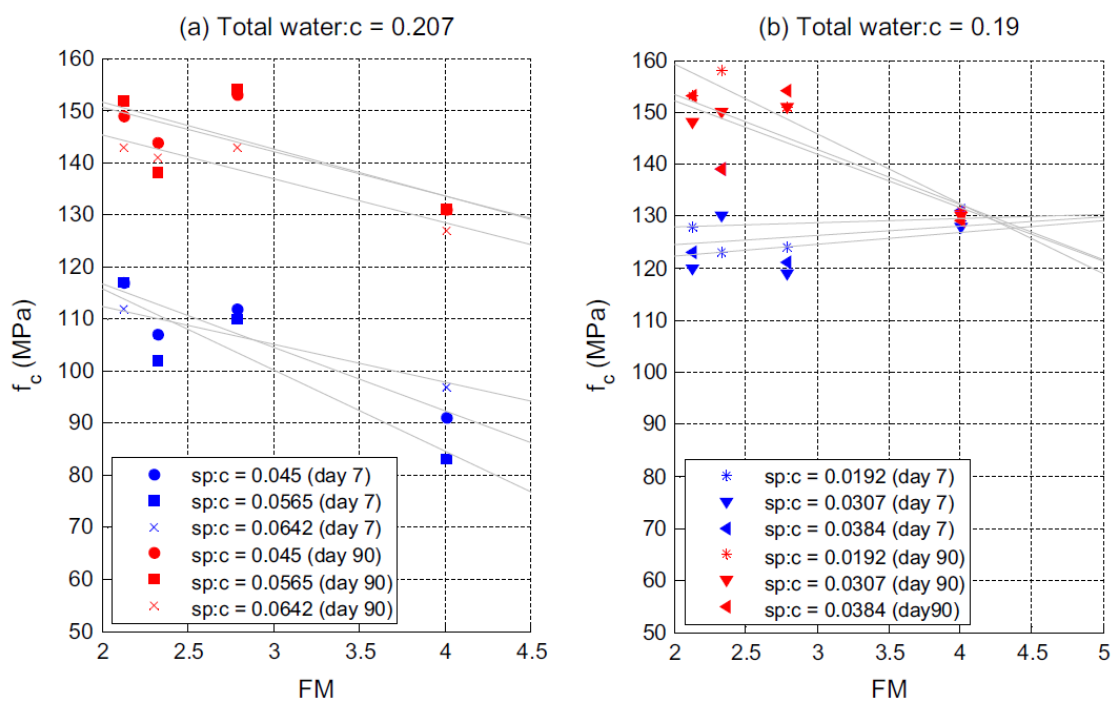
Source: Sobuz *et al.* (2016)

In addition to the increase in compressive strength, the aggregate shape may influence the microstructure development. Employing backscatter scanning electron microscopy, Yang *et al.* (2019) observed that during the cement hydration process, the rough surface and edges of MS were beneficial in obtaining a better connection in the paste and aggregate interfacial transition

zone (ITZ). Moreover, the multi-edges may also promote interlocking between MS particles, further improving the binding force in ITZ. De Larrard and Sedran (1994) suggest that they preferred rounded grains from a rheological point of view.

To evaluate the binder-to-sand (b/s) ratio on the UHPC properties, Xie *et al.* (2018) analyzed the flowability, strength, and shrinkage parameters. The authors inferred that the flow and passing ability increase with the b/s ratio. This behavior may be attributed to the increased paste volume covering the fine aggregates' surface, reducing friction between the sand particles in the fresh UHPC (Xie *et al.*, 2018). The compressive strength analysis indicates that there is an optimum b/s ratio value. In particular, the decrease in strength may result from the sand-to-sand mechanism of stress transfer when a reduction in fine aggregate content occurs. In addition, the weakness of the ITZs between the fine aggregate and binder is due to excessive unhydrated cementitious materials (Xie *et al.*, 2018). The authors observed an increase in the unit weight and a reduction in porosity that can be attributed to the b/s ratio increase. In the shrinkage investigation, autogenous and free total decrease with an increase in the b/s ratio. UHPC with a lower b/s ratio has a higher degree of exothermic reaction and generates more heat due to a higher degree of reaction, therefore, tends to have a more significant autogenous shrinkage at the early curing stage (Xie *et al.*, 2018). An optimal b/s ratio may be considered 1-1.1 for a typical UHPC mix to minimize the shrinkage effect without significantly compromising the compressive strength.

Sobuz *et al.* (2016) mentions the possibility of including the coarse aggregate (CA) in UHPC mixes. The main objective of its inclusion is the reduction of UHPC costs. Despite the decrease in compressive strength in the range of 0–7%, it requires consideration of a coarse aggregate/fine aggregate ratio because the presence of CA leads to an increase in micro-cracking due to shrinkage (Sobuz *et al.*, 2016). The flexural strength may be reduced due to the lower bond strength of the steel fibers. In particular, the coarse aggregate in the mixture may reduce the amount of fine powders, and consequently, a more flowable and shorter mixing time can be obtained (Yoo, Kim, and Kim, 2018). A homogeneous morphology of the paste structure and the compact ITZ structure

are the theoretical rationales for preparing UHPC without removing coarse aggregate (Wang *et al.*, 2012).

2.1.4 Filler

The packing density improvement induces choosing materials by particle size to fill the voids between bigger grains. Usually, one of the intended particle sizes is between cement and SF, which is necessary for granular mixture optimization. As a result, the filler utilization leads to compressive and flexural strengths increasing up to 25% due to the improved density (Courtial *et al.*, 2013). It may replace the unreacted cement since they have the same particle size. The nucleation effect that comes from the fine particles may also promote cement hydration (Yu, Spiesz, and Brouwers, 2014). In addition, crushed crystalline quartz powder is essential for the heat-treated UHPC due to its reaction to form hydration products (Richard and Cheyrezy, 1995).

Yu, Spiesz, and Brouwers (2014) analyzed the filler effect in cement replacement. Utilizing quartz powder to replace about 20% cement, flexural and compressive strength decrease is not apparent. However, the efficiency of steel fibers and cement may be enhanced despite a 10% strength decrease, using limestone powder (LP) to replace 30 wt.% cement. Wang *et al.* (2012) present an optimum content of LP to replace the cement in a mix with SF and GGBFS. Figure 5 exhibits the fluidity improvement with LP incorporation despite decreased compressive strength after 20 wt.% replacement. In addition, the LP may accelerate the hydration process of cement and SF (Wang *et al.*, 2012). With the same water and SP amount, fillers replacing cement can significantly improve the workability of concrete (Yu, Spiesz, and Brouwers, 2014).

Figure 5: Influence of the amount of LP on strength and fluidity of UHPC
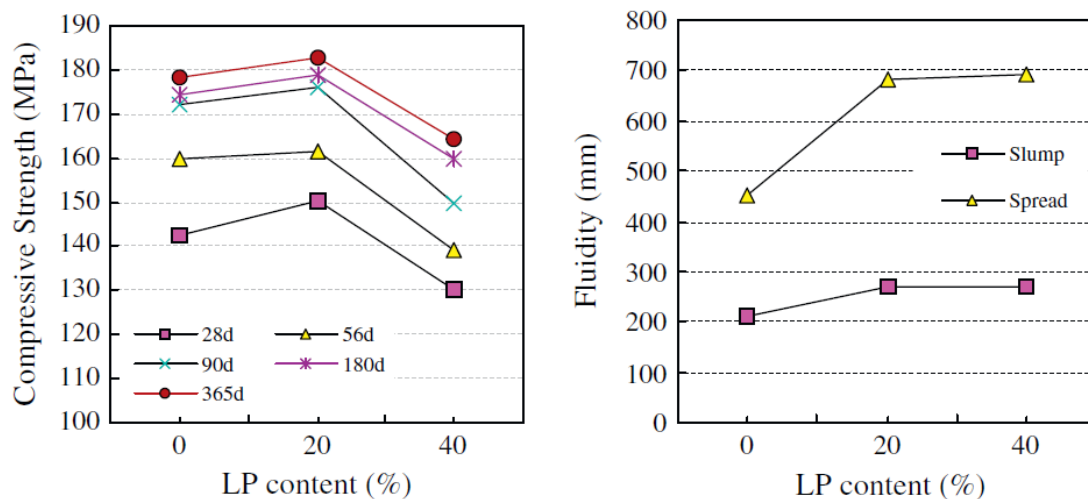
Source: Wang *et al.* (2012)

Superfine cement may improve the packing density due to its small particle size. With particles thinner than 6 µm, adding 20% of SFC reduces the voids ratio by 17%, develops better workability at a lower w/c ratio, and increases the 28-day cube compressive strength by 30% (Chen and Kwan, 2012). As the packing density increases, the amount of water needed to fill the voids decreases, increasing the excess water for forming water films. It coats the particles to lubricate the solid surfaces, giving the cement paste the desired flowability.

2.1.5 Fibers

The fibers have a fundamental role in the performance of UHPC. They allow ductile behavior, improve toughness, and work against the propagation of cracks propagation due to the stress transfer from the matrix to the fibers. Incorporating fibers may reduce shrinkage and cracks, providing ductility under tension and compression (Hannawi *et al.*, 2016). This improvement is due to the high elastic modulus of steel fibers, which can reduce crack width and delay cracking propagation during the shrinkage development process, including drying and autogenous shrinkage (Wu, Shi, and Khayat, 2019). Due to their short length, the fibers may function as aggregate in UHPC, increasing the elastic modulus and compressive strength (Ipek *et al.*, 2011). In contrast, their high volume combined with their dimensions makes the fibers the primary source of heterogeneity, inducing local stress concentration, facilitating the initiation of

microcracks in the matrix, and resulting in a reduction of tensile strength (Rossi, Daviau-Desnoyers, and Tailhan, 2016).

Richard and Cheyrezy (1995) suggest an economic optimum fibers ratio of 2% by volume or about 155 kg/m³. Mixtures with this fiber amount and a fiber aspect ratio (length/diameter) ranging from 65 to 100 show no significant fluidity change. Furthermore, Wille and Parra-Montesinos (2012) present the fiber factor χ_f defined as the product of the fiber-volume fraction and the fiber aspect ratio. The authors suggest an upper limit for χ_f of approximately two to avoid a decrease in UHPC workability. A higher amount or aspect ratio may exhibit the formation of fiber balls, also known as fiber clusters, leading to insufficient fiber dispersion (Yoo and Yoon, 2015; Wu, Shi, and Khayat, 2019). The fibers are classified based on their physical and chemical properties, including their nature, geometry, aspect ratio (L/∅), and mechanical properties (Hannawi *et al.*, 2016). In addition to fiber content, the fiber shape, fiber aspect ratio, and matrix strength can affect the performance of UHPC (Wu, Shi, and Khayat, 2019). The age evolution of the matrix and matrix/fiber interface invariably leads to improved bending behavior of the composite (Rossi, 2013).

Yu, Spiesz, and Brouwers (2014) attribute the negative effect of steel fibers on the workability to the fiber's elongated shape and its higher surface area, the higher stiffness, and the possible deformed type that improves the fiber/matrix anchorage, causing an increase in the cohesive forces between the fibers and the matrix. Wu *et al.* (2017) complement the impact on the flowability by the alteration in the fresh paste granular skeleton structure and the tendency of the steel fiber to be perpendicular to the flow. Figure 6 presents the relation between the steel fiber content and its workability for different air entrained in fresh UHPC. A hybrid fiber reinforcement with different lengths may improve workability because the short and long fibers restrict each other's rotation to avoid the perpendicular orientation to the flow direction (Wu *et al.*, 2017).

Figure 6: Variation of the relative slump flow of UHPC with different cement amounts as a function of steel fiber content
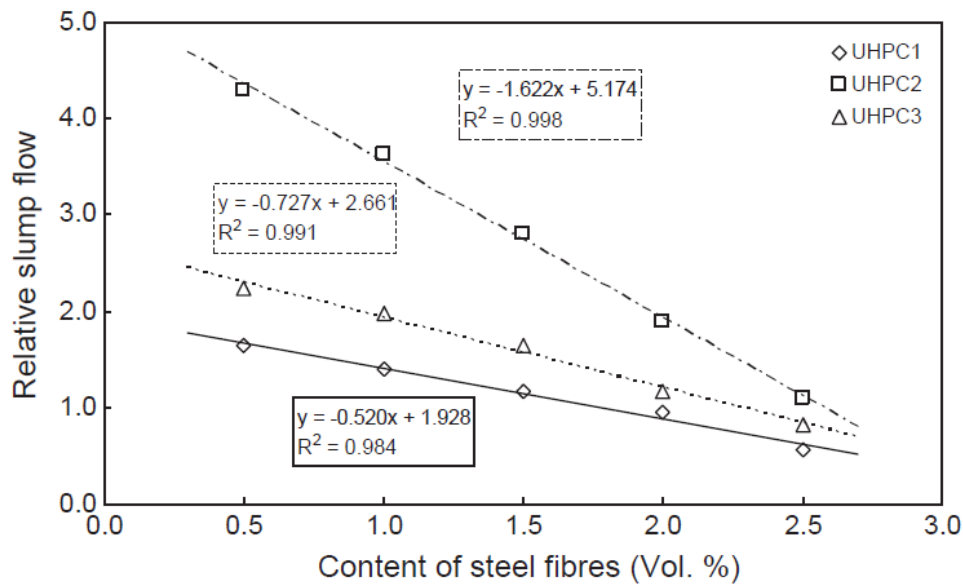
Source: Yu, Spiesz, and Brouwers (2014)

Hannawi *et al.* (2016) evaluated the microstructure and mechanical behavior of UHPC with six distinct types of fibers, which are distinguishable by their nature (steel, mineral, and synthetic), dimensions (macroscopic or microscopic), and mechanical properties (density, elastic modulus, and strength). The scanning electron microscope (SEM) observations of the microstructure show that steel and mineral fibers (wollastonite and basalt) have a more compact fiber/matrix ITZ than synthetic fiber (PVA and PP-PE). In addition, the use of synthetic fibers results in increased porosity due to the weak adhesion between the fiber and the matrix, as shown in Figure 7. The consequence of this porous interface is an interconnection between the pores, increasing permeability (Hannawi *et al.*, 2016). Regarding compressive strength and elastic modulus of the UHPC specimens, the fibers had little influence, except for steel fibers, which have high rigidity and can increase the compressive strength by up to 23%.

Kang *et al.* (2016) studied a hybrid blend of straight steel fiber and synthetic or mineral microfiber. The authors concluded that a combination of high-strength synthetic and steel fibers might be adopted to improve the tensile behavior of UHPC, despite the compressive strength being lower by 4.7%. In the study by Yu, Spiesz, and Brouwers (2015), fibers with different lengths improved UHPC mechanical properties, preventing crack propagation. Short fibers bridge

the microcracks while long fibers resist macrocracks efficiently, leading to multiple effects. Furthermore, the different geometry may restrict the rotation of each fiber during casting, especially in critical regions like borders, which improves flowability and occasionally aligns them.

Figure 7: SEM observation at the fiber/cement paste interface with steel and synthetic (PVA) fiber
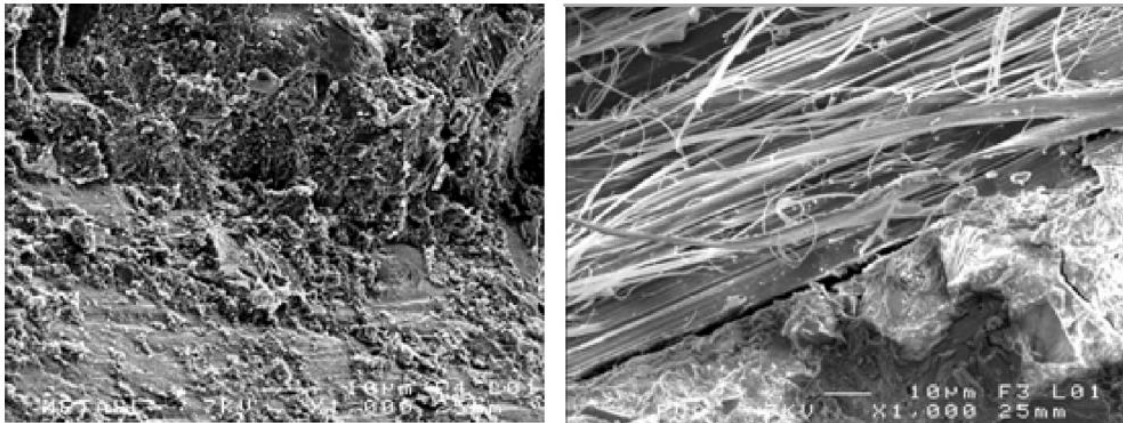
(a) Concrete with steel fiber   (b) Concrete with synthetic fiber (PVA)

Source: Hannawi *et al.* (2016)

Yoo and Yoon (2015) investigated the effects of the length and shape of steel fibers on UHPC's mechanical and structural properties. The specimens with steel fibers showed slightly higher compressive strength and elastic modulus than those without fibers. No noticeable difference was observed with different lengths and shapes of fibers, as shown in Figure 8a. However, both fiber shapes significantly improved flexural performance, attributed to the deflection-hardening behavior due to fiber bridging at the crack interface (Figure 8b). Furthermore, fiber length and volume fraction did not influence the first-cracking properties because this property is more closely related to matrix tensile cracking than fiber bridging capacity (Park *et al.*, 2017).

The increase in fiber length enhanced the flexural load-deflection curve because of the increase in effective bonding between the fiber and matrix (Yoo and Yoon, 2015). At the same time, it is recognizable that smaller fibers have better dispersion in concrete, leading to a more uniform material. This homogeneous distribution may lead to a higher packing density of the cement matrix (Hannawi *et al.*, 2016). Yoo and Yoon (2015) noted that beams, including

steel fibers, continuously increased crack quantity until near the peak load. This observation indicates that the UHPC may redistribute the tensile stresses before the fiber pullout. Moreover, specimens with twisted steel fibers produced more micro-cracks than smooth steel fibers. According to Park *et al.* (2017), at low fiber volume fractions (≤ 1.0%), long fibers present the best cracking response. In contrast, medium-length fibers present the best cracking response at high fiber volume fractions (> 1.5%).

Figure 8: Mechanical test results with smooth (S) and twisted (T) steel fibers and 13, 19.5, and 30 mm lengths: (a) average compressive stress-strain curve, (b) average flexural load-deflection curve
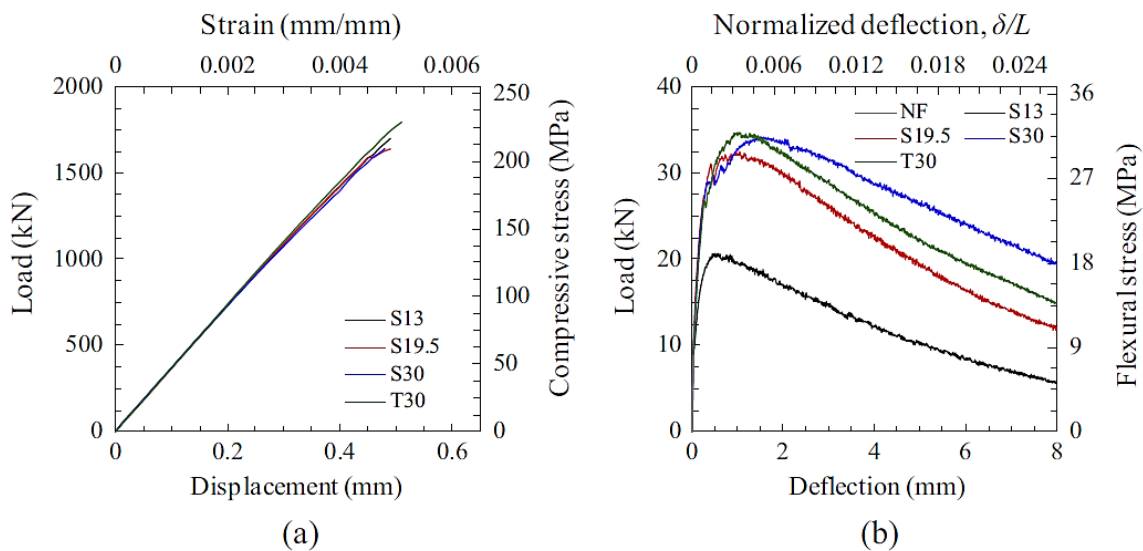
Source: Yoo and Yoon (2015)

In their study, Wu, Shi, and Khayat (2019) evaluated three shapes of steel fibers, including straight, corrugated, and hooked, at four fiber contents of 0%, 1%, 2%, and 3% by specimen volume. Each fiber has a diameter of 0.2 mm, a length of 13 mm (Figure 9), and a tensile strength of approximately 2800 MPa. The authors observed that the volume and shape of fibers influenced the compressive strength. The increase in compressive strength is due to an increase in density and rigidity in the presence of steel fibers and the enhancement of the restraining action of fibers to the propagation of microcracks before reaching the ultimate strength (Wu, Shi, and Khayat, 2019). The improved performance was with 3% of deformed shapes fibers (corrugated and hooked). However, to

produce the deformed steel fiber, an additional manufacturing process is required (to deform the fiber), increasing manufacturing time and cost (Park *et al.*, 2017).

Figure 9: Steel fiber shapes: (a) straight, (b) corrugated, and (c) hooked

(a)　　　　　　　　(b)　　　　　　　　(c)
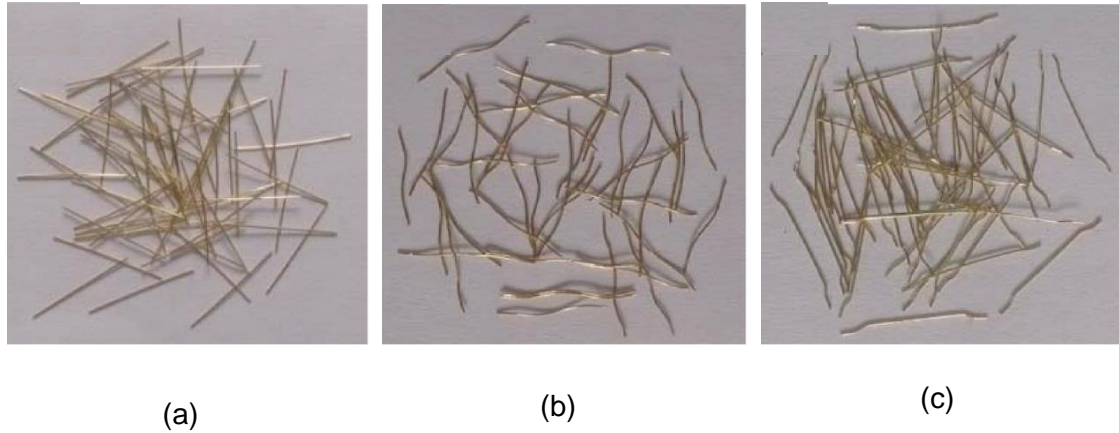
Source: Wu, Shi, and Khayat (2019)

Figure 10 illustrates the effect of steel fiber volume fraction and shape on the flexural performance of UHPC. As shown in Figure 10a, the fiber amount influences the flexural capacity of prisms due to the number of fibers available to arrest microcracks. More microcracks are formed between earlier cracks at higher fiber volume fractions, resulting in improved energy absorption capacity (Park *et al.*, 2017). In Figure 10b, the hooked steel fibers have a greater peak load, followed by the corrugated fibers, as expected, because deformed ends can restrain the initiation and propagation of cracking during load. In addition, deformed fibers can enhance flexural strength by improving the fiber-matrix bond strength associated with mechanical anchorage from the deformed section (Wu, Shi, and Khayat, 2019).

Figure 10: Flexural load-deflection curves of UHPC with (a) different straight fiber volumes at 28 d and (b) different fiber shapes at 28 d

(a)

(b)
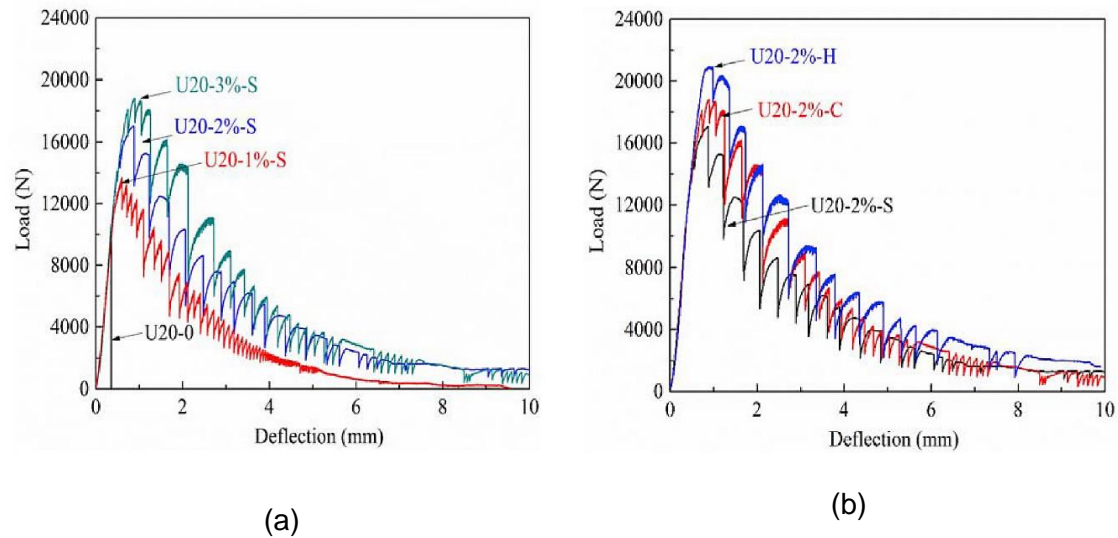
Source: Wu, Shi, and Khayat (2019)

The incorporation of steel fibers significantly reduced the UHPC shrinkage. To the flexural analysis, the volume and shape directly influence shrinkage development, reducing it up to 58% and 36%, with 3% hooked fiber volume, in autogenous and drying shrinkage, respectively. Steel fibers function as rigid inclusions in the matrix and hinder the initiation and propagation of microcracks due to bond strength with the surrounding matrix (Wu, Shi, and Khayat, 2019).

In Yoo, Kim, and Park (2019), the analysis of fiber spacing and loading rate on the pullout behaviors showed that the pulling-out process of a straight steel fiber does not influence the pullout resistance of the surrounding fibers. This response occurs because the frictional shear resistance does not affect the surrounding matrix and fibers. The pullout resistance of fibers in the cement matrix is enhanced when the loading rate increases in a damaged matrix (Yoo, Kim, and Park, 2019). In addition, the fiber pullout behavior is affected by the fiber present in the matrix, improving the pullout load by up to 30%, depending on the fiber content (Zhou and Qiao, 2019).

Some studies propose to reduce the UHPC cost by decreasing the fiber volume without hindering flexural performance. The cost of 1% fiber volume content in UHPC is higher than that of the same matrix volume (Yu, Spiesz, and Brouwers, 2015). Huang, Gao, and Khayat (2021) considered the significantly increased flexural properties with the flow-induced casting method and a higher

fiber length. The authors affirmed that combining these two parameters could reduce the fiber volume by up to 2%. Park *et al.* (2017) suggest that the volume fraction of steel fibers can be reduced by approximately 0.5% by replacing short fibers (13 mm) with medium (19.5 mm) or long (30 mm) fibers and, in addition, obtaining an improvement in the energy absorption capacity.

2.1.6 Admixtures

The UHPC workability and low water/binder (w/b) ratio is possible only with admixtures, mainly polycarboxylate superplasticizers (PCE). The PCE disperses the cementitious materials through electrostatic and steric repulsion between particles (Li and Kwan, 2015). Its use may reduce approximately 58% of the UHPC paste water demand, limiting the w/b ratio to reduce porosity (Li, Yu, and Brouwers, 2017). Besides the workability improvement, Li and Kwan (2015) report that superplasticizers (SP) disperse the solid particles, reducing the degree of agglomeration and increasing packing density. As the packing density increases, the minimum void ratio decreases. Their results show a saturation of PCE dosage and that any increase beyond this point does not bring further improvement in packing density. For particular types of SP and the cementitious materials used, they found 3.0%, by mass, as the saturation SP dosage. When examining the flowability of spread flow, a relationship between SP dosages shows an exponential trend (Li, Yu, and Brouwers, 2017). Moreover, the further addition of PCEs may not prolong the fluid-retaining ability.

Li, Yu, and Brouwers (2017) analyzed different PCE-type superplasticizers with different dispersing and retarding abilities. The results indicate the importance of carefully selecting the appropriate types and dosages of PCE for the UHPC design. Their findings exhibit the retardation effect of the usage of PCE, as illustrated in Figure 11. A higher PCE dosage delays the hydration process, which is presented as a normalized heat flow peak, even after the saturation point. It indicates that the adsorbed and the remaining water in the aqueous-phase PCEs contribute to retarding cement hydration, unlike the spread flow response. In addition, the same effect was observed in the setting time—that a higher amount of superplasticizers increases the final and initial set times. Furthermore, the retardation effect influences UHPC early-age shrinkage and strength, leading to slower development. The PCE dosage response differences

become smaller after 24 h and three days due to early-age shrinkage and strength.

Figure 11: Calorimetry test results of UHPC pastes

SP1 $y=8.79+10.6x+1.526x^2$
SP2 $y=8.12+7.07x-0.628x^2$
SP3 $y=8.22-0.09x+4.681x^2$
SP4 $y=7.91+10.8x+0.600x^2$
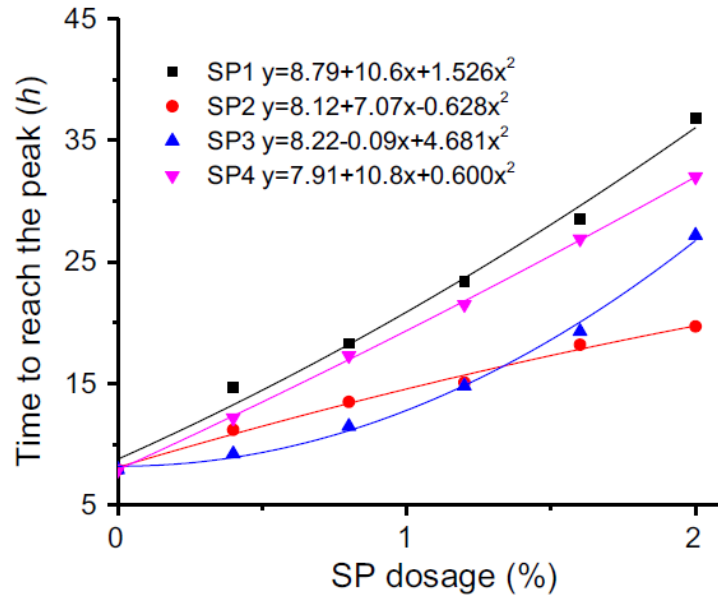
Source: Li, Yu, and Brouwers, 2017)

Despite the increase in the pozzolanic activity, SF addition reduces the flowability of concrete (Schröfl, Gruber, and Plank, 2012). Compared with cement particles, they have different surface chemical compositions and specific surface areas of 13000 cm²/g and 160000 cm²/g for cement and SF, respectively. Schröfl, Gruber, and Plank (2012) recommend utilizing more than one superplasticizer type to optimize the UHPC rheology improvement. This combination may reduce the admixture dosage, causing a smaller amount of air-entraining in the mix. The authors evaluated the performance of the methacrylic acid-based PCE (MPEG) and allyl ether-based PCE (APEG); as a result, it was revealed that MPEG strongly interacts with the surfaces of the hydrating cement, and APEG preferably adsorbs on SF particles. Both polymers do not perturb each other via competitive adsorption (Schröfl, Gruber, and Plank, 2012). Figure 12 presents a schematic representation of these PCEs blending. Although APEG-PCE has a better affinity for silica's surface, the MPEG-PEC exhibits a more balanced affinity for cement and silica particles, as illustrated in Figure 13. It is essential to investigate the PCE affinity when the UHPC mixture has supplementary cementitious materials (SCM) due to their different adsorption.

Figure 12: Schematic representation of simultaneous and preferential adsorption of a blend of methacrylic acid ester-based and allyl ether-based on cement and SF particles, respectively
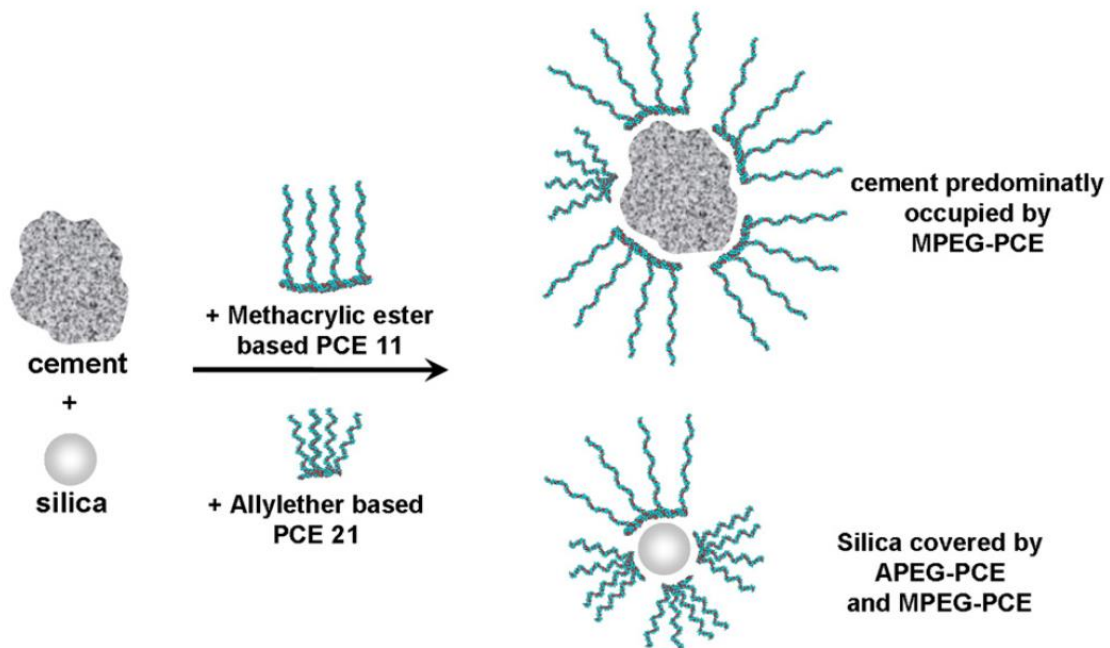
Source: Schröfl, Gruber, and Plank (2012)

Figure 13: Selective adsorption of MPEG-PCE and APEG-PCE on cement and SF in UHPC paste
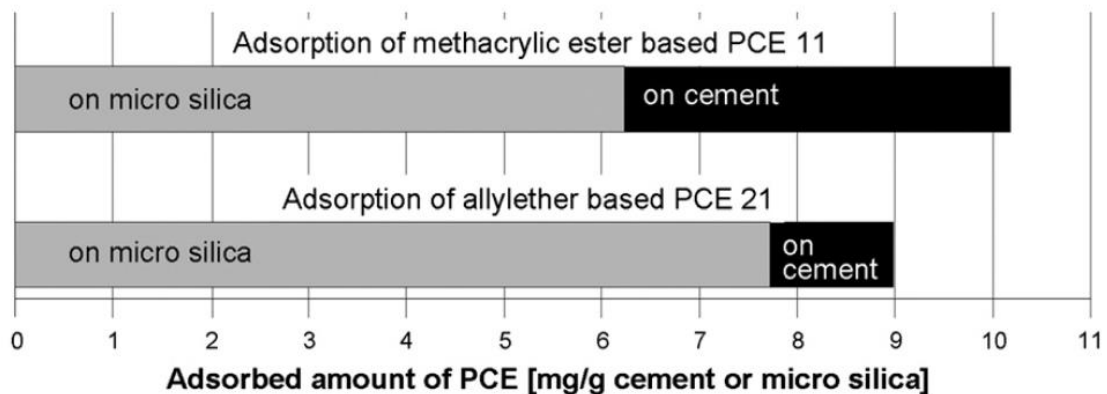
Source: Schröfl, Gruber, and Plank (2012)

Chemical admixture, as CSA-based expansive agent (EA), may reduce up to 10% of the UHPC shrinkage strains (Yoo *et al.*, 2019). According to Yoo *et al.* (2019), the UHPC is highly susceptible to early-age microcracking due to autogenous shrinkage and a smaller cross-sectional area than CC. This condition affects material durability and has an impact on mechanical properties. Despite

the higher measurement of autogenous shrinkage before 24 h, the mixture with more than 6% CSA EA reduces the final shrinkage strain. Furthermore, the tensile strength of UHPC with straight steel fibers increases with an increase in the CSA EA amount. On the other hand, strain and energy absorption capacities decrease because of the higher tensile stiffness, which causes lower strain values. In addition, the compressive strength increases with CSA EA use.

Yoo *et al.* (2013) evaluate the effect of shrinkage-reducing admixture (SRA) on resisting the high autogenous shrinkage of UHPC. The SRA incorporation eases the surface tension in the capillary pores of the concrete and subsequently reduces the drying and autogenous shrinkage of the concrete (Xie *et al.*, 2018). The presence of SRA decreases the number and width of the microcracks due to autogenous shrinkage. SRA reduces the compressive strength and strain at peak load, despite the mixture with 2%, relative to cement weight, presenting nearby results. Similarly, pullout strength decreases by including SRA in the matrix (Figure 14). The reduced shrinkage diminishes the radial confinement pressure, leading to the friction bond between the fiber and the matrix (Yoo *et al.*, 2013). Conversely, UHPC prepared with a higher SRA content exhibits better flowability and passing ability (Xie *et al.*, 2018). From SEM micrographs, Xie *et al.* (2018) observed that the increased SRA led to an increase in the amount of unhydrated binder and ettringite, indicating a lower degree of hydration and increased pore space.

Figure 14: Effect of SRA content (0%, 1%, and 2%) on pullout behavior of smooth steel fiber embedded in UHPC matrix with L_E = 9.5 mm
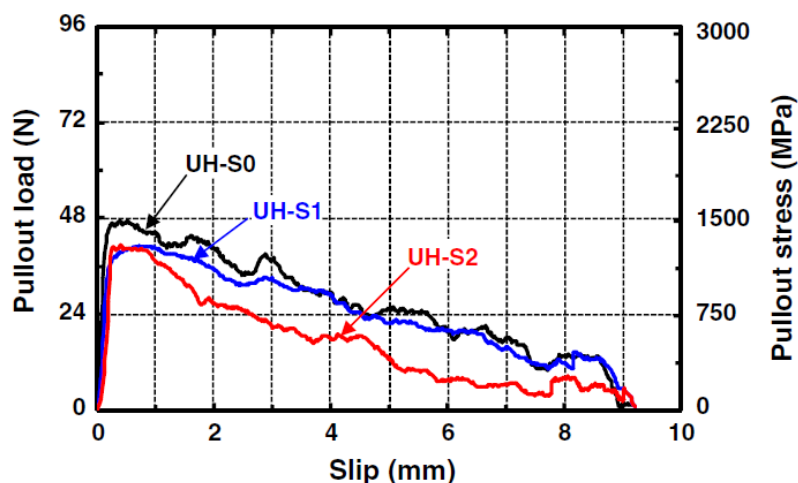
Source: Yoo *et al.* (2013)

Although the first crack is more affected by the matrix tensile strength than the fiber reinforcement effect, adding SRA reduces the first crack and ultimate tensile strengths and strains (Yoo *et al.*, 2013). The ITZ SEM images may explain this performance loss. The authors identified a more porous zone between the fiber and the matrix as the percentage of SRA increased, as can be observed in Figure 15.

Figure 15: SEM images according to SRA content: (a) 0%, (b) 1%, and (c) 2%

(a)

(b)

(c)
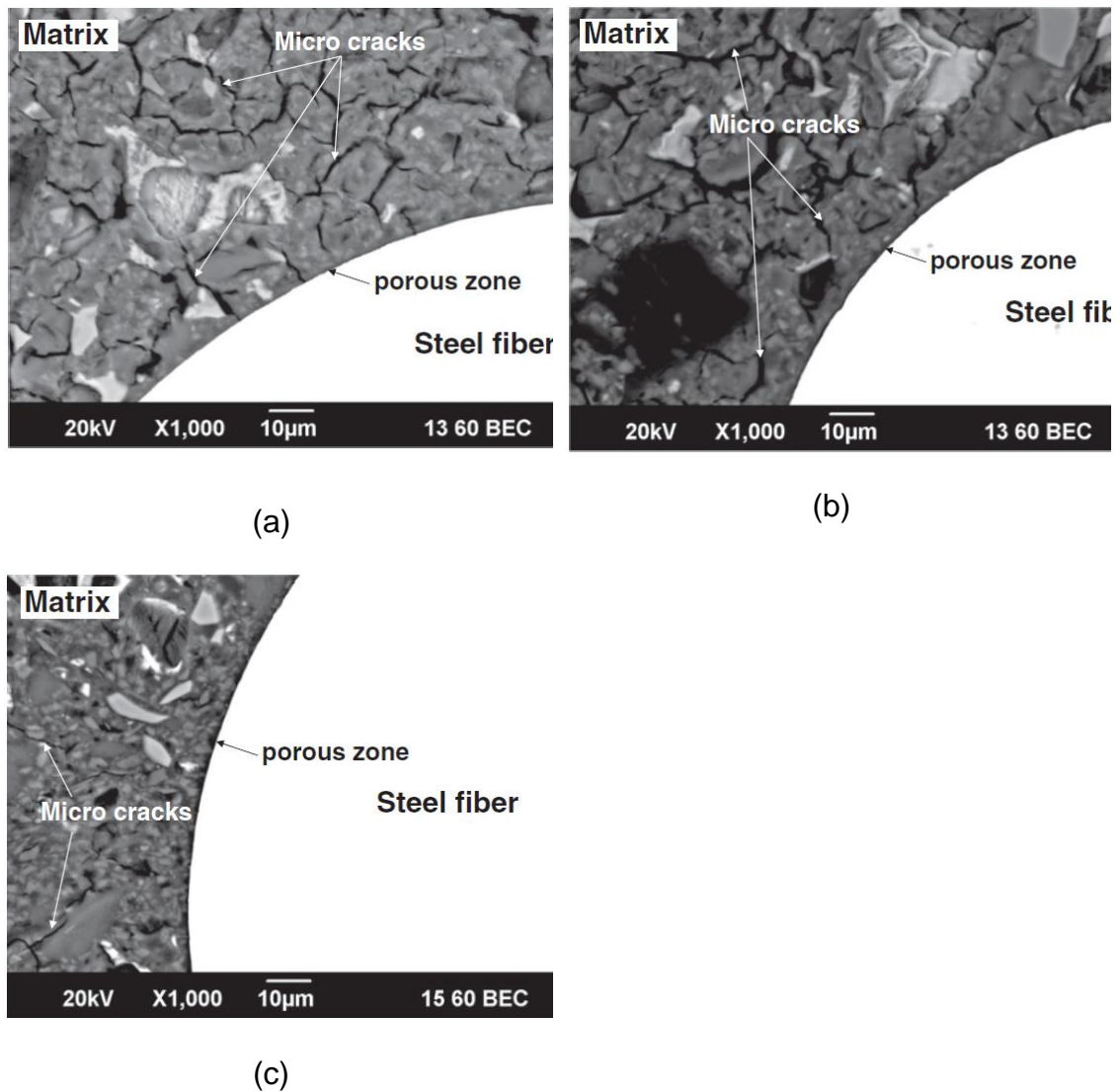
Source: Yoo *et al.* (2013)

2.2 MIX DESIGN

The UHPC mix design principle is to obtain the proportions of the raw materials to have a dense, fluid, and ductile composite and indirectly durable and strengthened. It is important to note that concrete requisites include fresh, hardening, and hardened composite specifications (De Larrard and Sedran, 2002). An optimal UHPC mixture meets these different requisites maximizing all its properties combined.

A better packing density of the granular ingredients is the key to a resistant and durable concrete. Researchers worked to decrease the cementitious materials' porosity to achieve these properties (Wille *et al.*, 2012). The continuous grading of the particles enables a better fitting between them; hence, a suitable selection of the materials is fundamental (Yu, Spiesz, and Brouwers, 2014). The optimum packing density includes the minimum matrix initial porosity and aggregates' size and strength selection (De Larrard and Sedran, 1994). Otherwise, the high complexity and geometry of the fibers and the effect of their inclusion hinder consideration in the packing methods (Yu, Spiesz, and Brouwers, 2014).

In theory, the UHPC mix design optimization requires the determination of a critical material viscosity to have a minimal content of voids and the minimization of the maximum paste thickness to obtain a dense packing matrix (De Larrard and Sedran, 1994). Wille *et al.* (2012) produced a UHPC mixture, optimizing the cementitious matrix to improve the compressive strength, packing density, and fluidity. The mixture development basis is the spread measure validated by the compressive strength and single pullout tests. According to the authors, to increase the packing density, the flowability of the paste must be increased, maintaining the amount of water constant (or the same flowability while reducing water content); therefore, the void filled with water reduces. As the result of the matrix optimization, Figure 16 illustrates the particles' ranges and how they fit the size distribution scale. In addition, matrix optimization allows the reduction of the superplasticizer amount. Improvement in particle packing through enhanced fine particle dispersion and a decrease in the smallest particle size led to an improved bond-slip hardening behavior (Wille *et al.*, 2012). Especially with regard to UHPC, the optimizations aim for both technical and economic purposes.

Figure 16: Median and range of PSD (10, 90%) for all particles used in the mix design (in mm)
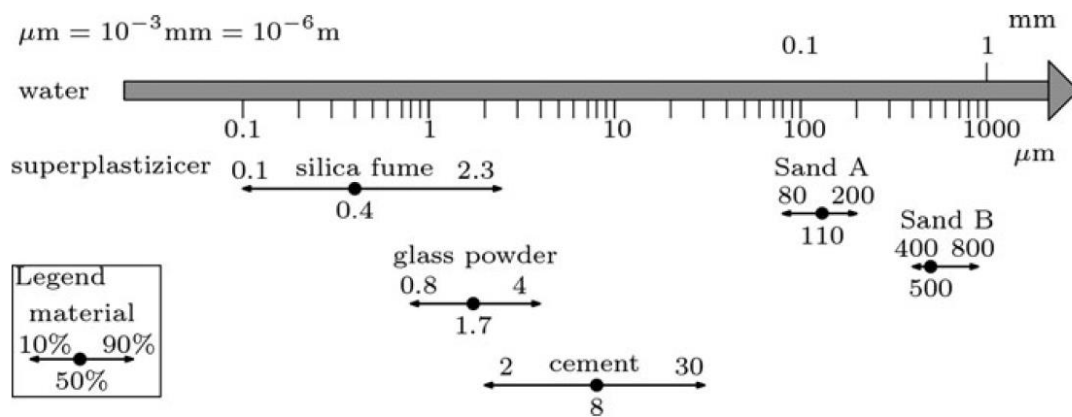
Source: Wille *et al.* (2012)

To optimize the granular mixture, Richard and Cheyrezy (1995) sought the minimum quantity of water to obtain the desired flowability. After that, the lower porosity is analyzed with the relative density parameter d_0/d_s, where d_0 is the density of the concrete at demolding, and d_s is the solid density of the granular mixture assumed to be compact. It is related to the w/b ratio, as shown in Figure 17. According to the materials utilized, the theoretical optimum water content is at the maximum relative density due to the minimum entrapped air.

Figure 17: Variation in relative density with water content
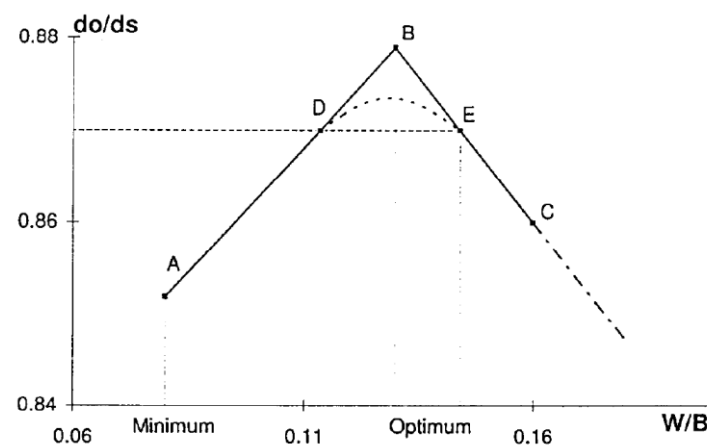
Source: Richard and Cheyrezy (1995

De Larrard and Sedran (1994) present the evolution of their packing method based on primary works, which predict the viscosity of multimodal suspensions of non-reactive particles. The authors developed the linear packing

density model for grain mixtures, then the solid suspension model, considering a random packing of particles like a high but finite viscosity suspension. The random packing leads to a lower packing density but is more accurate than a monodisperse arrangement. The compressive packing model (CPM) is the third generation of the author's packing models (De Larrard and Sedran, 2002). It is based on the packing density of monosized particle classes, the size distribution of the mix, and compaction energy. With the particle classes' packing density, the model calculates the packing density of the mix. In addition, the method considers that a particle fills the space around the coarser grain and has two interaction effects: the wall effect, exerted by coarse grains, and the loosening effect, exerted by the finer particles. Figure 18 presents the interaction effects.

Figure 18: Ternary packing of particles, where the intermediate class is dominant
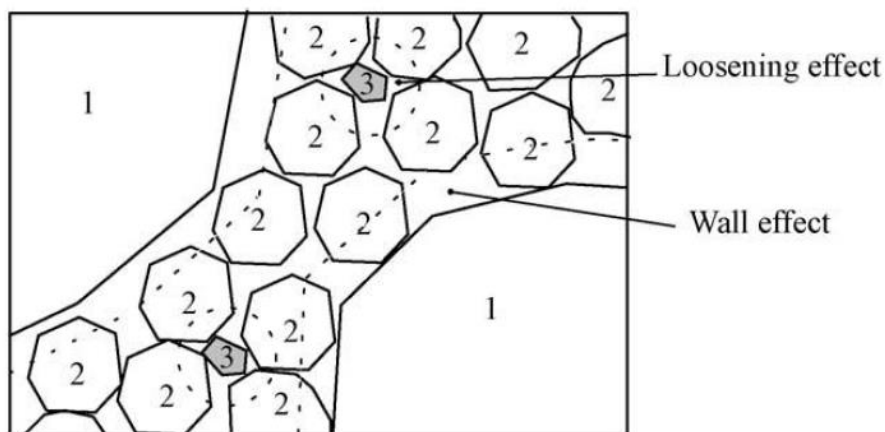
Source: De Larrard and Sedran (2002)

The Modified Andreasen and Andersen is the most successfully utilized particle packing method, which considers a minimal theoretical porosity by an optimal PSD of all the materials in the mix (Yu, Spiesz, and Brouwers, 2014). The method equation is as follows:

$$P(D) = \frac{D^q - D^q_{min}}{D^q_{max} - D^q_{min}}$$

(1)

where P(D) is a fraction of the total solids smaller than size D or the cumulative percentage of the PSD curve, D is the particle size (μm), D_{max} and D_{min} are the maximum and minimum particle size (μm), and q is the distribution modulus.

Equation 1 is a target function for optimizing the composition of the granular materials mixture. The distribution modulus q determines the proportion between the fine and coarse particles in the mixture. Yu, Spiesz, and Brouwers (2014) suggest the value of q fixed at 0.23, considering a high fines content.

The process of obtaining the proportions of each UHPC component may be manually estimated and evaluated compared with a target curve or with optimization methods. In the former, utilizing PSD of every constituent material, the proportions are chosen to seek each material particle size portion to compose the mix curve until the target is approximate. Yu, Spiesz, and Brouwers (2014) used an optimization algorithm based on the least squares method, as presented in Equation 2, expressed by the sum of the squares of the residuals (RSS).

$$RSS = \sum_{i=1}^{n} \left(P_{mix}\left(D_i^{i+1}\right) - P_{tar}\left(D_i^{i+1}\right) \right)^2 \tag{2}$$

where P_{mix} is the composed mix, and P_{tar} is the target grading calculated from Equation 1.

To evaluate the quality of the curve fit, Yu, Spiesz, and Brouwers (2015) calculated the coefficient of determination (R^2) as presented in Equation 3.

$$R^2 = 1 - \frac{\sum_{i=1}^{n} \left(P_{mix}\left(D_i^{i+1}\right) - P_{tar}\left(D_i^{i+1}\right) \right)^2}{\sum_{i=1}^{n} \left(P_{mix}\left(D_i^{i+1}\right) - \overline{P_{mix}} \right)^2} \tag{3}$$

where $\overline{P_{mix}} = \frac{1}{n}\sum_{i=1}^{n} P_{mix}\left(D_i^{i+1}\right)$, which represents the mean of the entire distribution.

Figure 19 presents the PSD curve of the composed mix of the UHPC raw materials and the target curve. Note that the composed mix is very close to the target curve.

Figure 19: PSD of the UHPC components, the target curve, and the resulting integral grading line of the mix
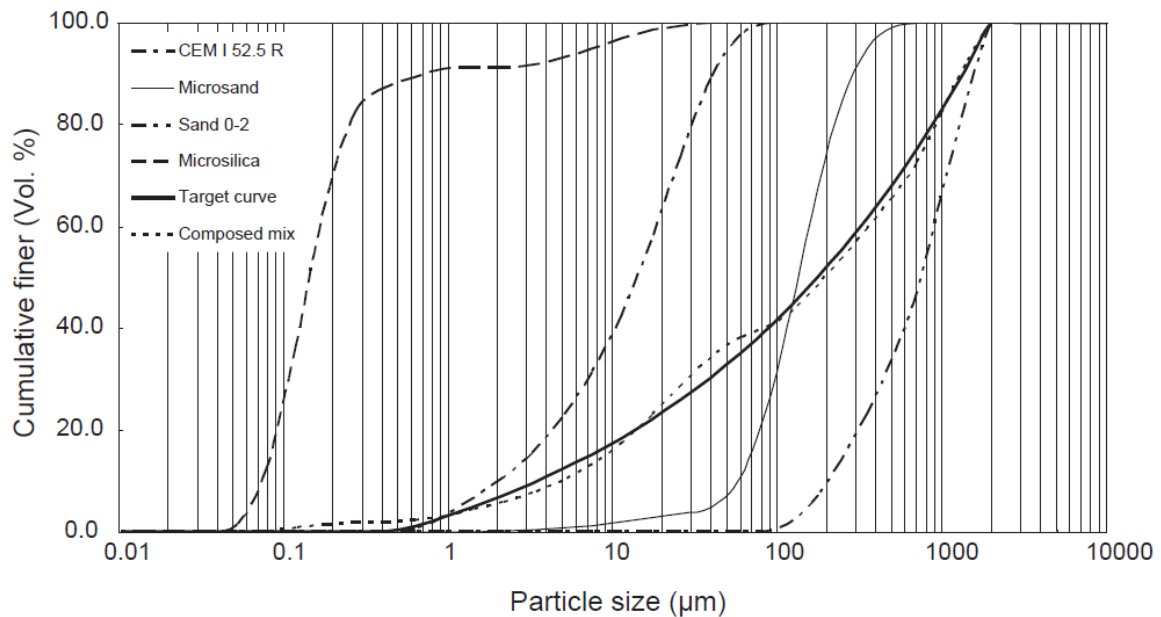
Source: Yu, Spiesz, and Brouwers (2014)

Based on the Modified Andreasen and Andersen particle packing model, it is possible to produce a UHPC with a low binder amount (Yu, Spiesz, and Brouwers, 2014). In Yu, Spiesz, and Brouwers (2015), the UHPC developed has about 620 kg/m³ of binder and 2% vol. of fibers. After producing a trial batch, some adjustments are required to refine the mix design to obtain the required properties (De Larrard and Sedran, 2002).

2.3 MIXING PROCEDURE

Although well-established for CC production, the mixing procedure directly influences the UHPC properties. It involves selecting the equipment type to define the mixture speed, duration, and method to obtain a better material dispersion with minimum pores. Mixing UHPC requires a high-intensity mixer due to its high

packing density and the presence of the fibers (Savino *et al.*, 2018). In addition, a Hobart® or mortar mixer was used in most research studies to produce UHPC (Hiremath and Yaragal, 2017). The mixing procedure efficiency may be evaluated visually by the material homogeneity and mechanical test results that asses the flowability and strength.

Most research utilizes a resemblant mixing procedure. It may be described as a three-stage method with the following sequence: First, mix all dry materials like cement, SF, fillers, and sand; then, add the water and the superplasticizer joined; and lastly, the fibers are carefully incorporated and dispersed in the mixture. The friction of the sand with the smaller particles in the first stage may break its agglomeration and improve packing. Chen and Kwan (2012) suggest the partition of the water addition to ensure thorough mixing. According to references, the total mixing time varies from six to forty minutes. The first stage is verified as a preponderance of a slow mixing speed of 60 RPM, then the rate rises to 120 RPM and is maintained or increased in the last stage. Conversely, De Larrard and Sedran (1994) utilized the following procedure: Mix the water, SF, and 33% of superplasticizer until the slurry looks homogenous; then incorporate the cement progressively with 50% of superplasticizer; combine the sand and mix for one minute at high speed; and lastly, add the residual 17% of superplasticizer and mix for one minute at high speed.

Schachinger, Schubert, and Mazanec (2004) evaluated different equipment and mixture procedures to achieve a minimum air void content. The following mixing procedure results from the authors' optimization investigations and the duration of each step varies according to the equipment.

Step 1. Homogenization of all dry materials (excluding steel fibers).

Step 2. Addition of water and half of the superplasticizer to wetting the material's surface and avoid SF agglomeration.

Step 3. A two-minute break to establish a sufficient contact duration between the cement and the water. It is necessary to improve the effectiveness of the remaining superplasticizer.

Step 4. Continuous addition of steel fibers.

Step 5. Addition and blend in the remaining superplasticizer by preference 5 minutes after the first contact between water and cement.

Additional remarks about the mixing speed are necessary to improve the efficiency. Step 2 needs to increase the mixing power because of the cohesive forces on wetting surfaces. After the pause in step 3, the agglomeration due to the start of cement hydration demands the highest power (Schachinger, Schubert, and Mazanec, 2004).

Hiremath and Yaragal (2017) studied the effect of the mixing method, speed, and duration on the UHPC fresh and hardened properties. The authors evaluated a mixing procedure with three and four stages. The former blends all dry materials in the first stage, unlike the latter, which mixes only the binder materials first. The UHPC produced with the four-stage method, showed a 13.5% higher flow value, attributed to the full superplasticizer potential and an early Ca^{2+} ion from cement particles released due to a high proportion of water at the initial stage. Furthermore, this method presented a 28-day compressive strength that is 22% higher. The lack of mixing stages may also be one reason for the voids' higher presence and unhydrated cement grains. Otherwise, the four-stage mixing method provides more portions of the C-S-H phase, improving the adhesion between hydration products and fine aggregate (Hiremath and Yaragal, 2017).

An optimal value of 100 RPM results in a higher flow value and compressive strength in the mixing speed analysis. Figure 20a presents the ascending and descending branches of the flow table test outcome. The lower speeds make water distribution difficult throughout the mix and do not break the particle agglomeration; also, high speeds allow moisture evaporation (Hiremath and Yaragal, 2017). The compressive strength testing results in the same trend, as illustrated in Figure 20b. Insufficient mixing speed slows down the hydration process due to the non-uniform distribution of moisture and decreases particle packing. Otherwise, excessive speeds allow bonded water to escape, leading to pore formation (Hiremath and Yaragal, 2017).

Figure 20: Effect of the mixing speed (a) on flowability and (b) on compressive strength

(a)

(b)
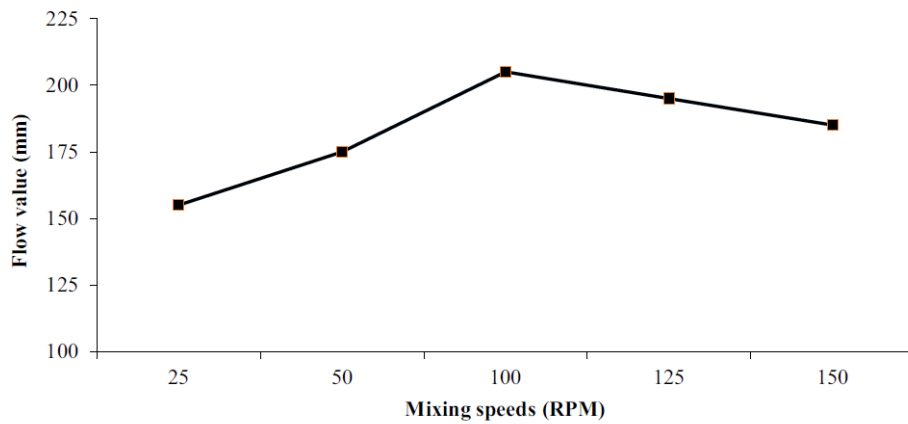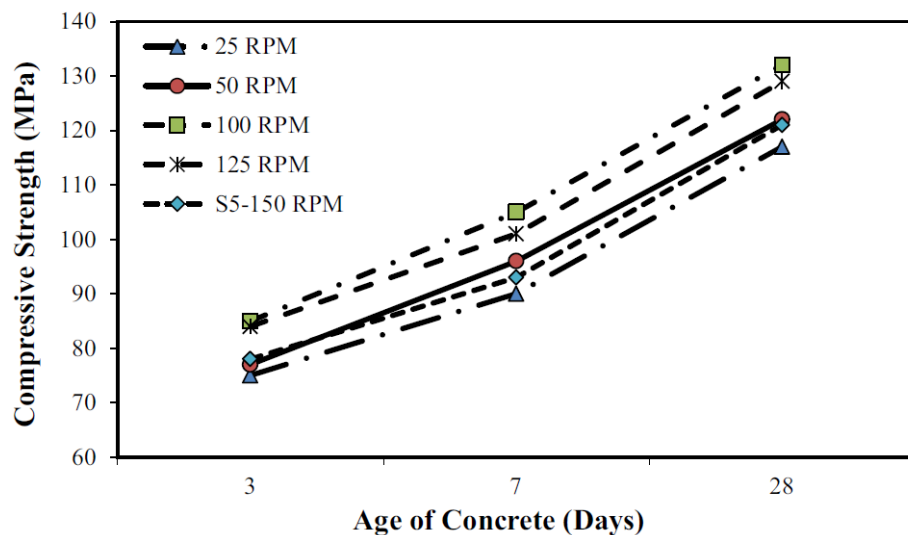
Source: Hiremath and Yaragal (2017)

The authors observed that at a mixing duration of 15 min, the flow value and compressive strength are maximum. The duration was evaluated in a four-stage mixture, varying the interval of each stage. As presented in Figure 21a, in mixing durations greater than 15 min, the material fluidity is reduced due to the evaporation of mixed water (Hiremath and Yaragal, 2017). As the mixing time is longer, the UHPC flowability is reduced, making the dispersion of air bubbles difficult, which originated from the superplasticizer chemical activity, and the fibers' inner movement. This side effect of SP in the form of additional pores is

not yet clearly determined, although it affects the air void structure (Nowak-Michta, 2020). The decline in the fresh properties directly affects the compressive strength, as shown in Figure 21b.

Figure 21: Effect of the mixing duration (a) on flowability and (b) on compressive strength

(a)

(b)
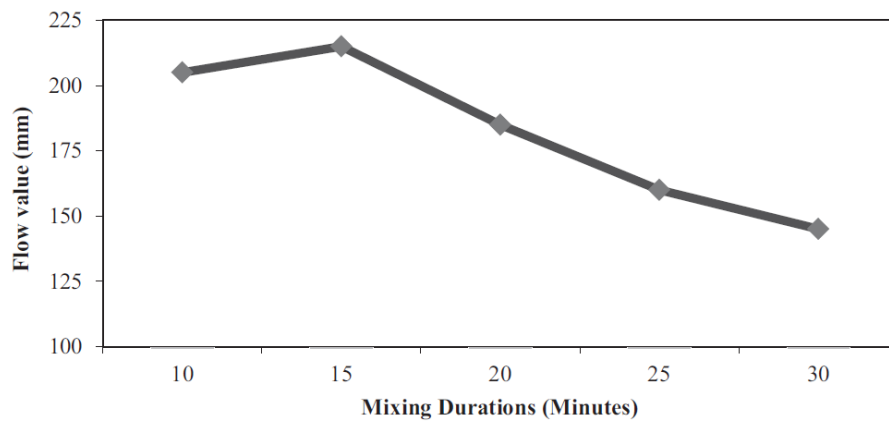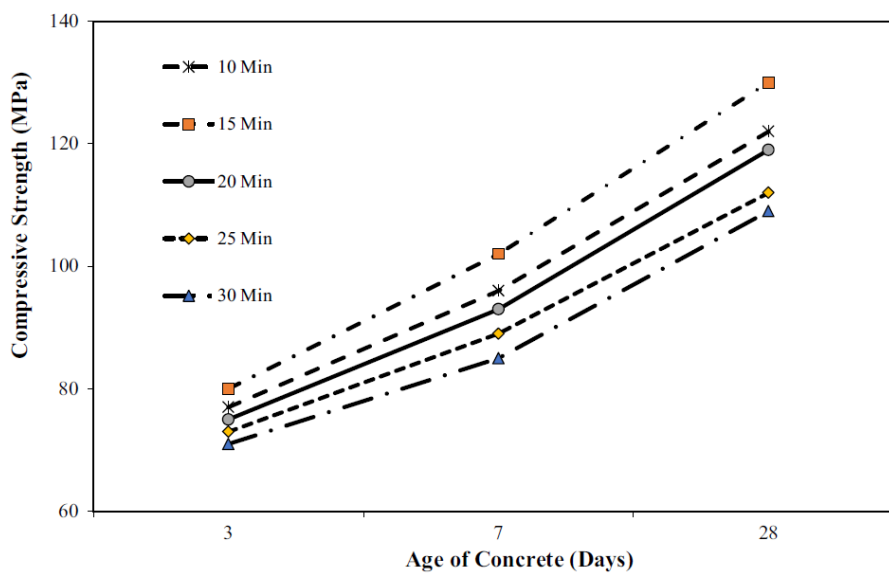
Source: Hiremath and Yaragal (2017)

2.4 PLACEMENT AND CONSOLIDATION

The placement method affects the mechanical characteristics of concrete. In UHPC, the placement flow direction may lead to fiber orientation despite the fibers being presupposed as randomly distributed. In addition, the absence of coarse aggregate and the high amount of superplasticizer promote the fiber movement inside the mixture. The fiber orientation distribution influences tensile strength and behavior. It is affected by fiber characteristics (diameter, length, volume fraction); friction between the fiber and the matrix; the concrete's rheological property; the specimen's geometry; and the placing method (Kang and Kim, 2012; Yoo, Kang, and Yoon, 2014).

Different mechanical properties occur in the same structural member at different sections according to the placement flow direction because of the fiber distribution, as seen in Figure 22. From image analysis of fiber orientation and dispersion in the study by Yoo, Kang, and Yoon (2014), due to the wall effect, the fibers near the mold tend to be more aligned in the flow direction than those apart from the mold (Figure 22a). Whether placed by the center, they observed that the fibers were more uniformly dispersed than placed by the corner, causing more fibers at the crack plane, which leads to the enhancement of the fiber bridging effect. In addition, Wille and Parra-Montesinos (2012) identified the critical cracks propagation following the perimeter of the funnel generated during the middle-casting method. Kang and Kim (2012) report a variation of the fiber orientation distribution in a shear flow. For example, a UHPC beam tends to show an arrangement of the fibers at the corners and becomes more parallel to the flow direction as the flow distance increases. Conversely, the arrangement is perpendicular to the flow direction in the radial flow as the flow distance increases.

The vertical placement of UHPC cylinders results in more random fiber orientation (Figure 22b, left); on the other hand, the fibers tend to be more aligned when placed longitudinally (Figure 22b, right) (Garas, Kurtis, and Kahn, 2012). At the pre-cracking and post-cracking tensile behaviors analyses, Kang and Kim (2011) demonstrate that direct tensile test specimens molded parallelly have 10% and 40% values higher for first cracking and maximum stress, respectively, than

the specimens molded transversely. This response attributes more uniformly dispersed and aligned fibers to the parallelly placing method.

There is a difference in fiber dispersion along the depth of structural members. The steel fibers exhibit a high degree of orientation in the upper half following the flow pattern. The formwork surface may modify the fiber direction near the flow. The orientation tends to be aligned with smooth glue-laminated plywood. Rough surfaces exhibit a greater fiber degree of randomness (Švec *et al.*, 2014).

Figure 22: Fibers dispersion (a) along the UHPC beam and (b) mid-height of cylinders samples
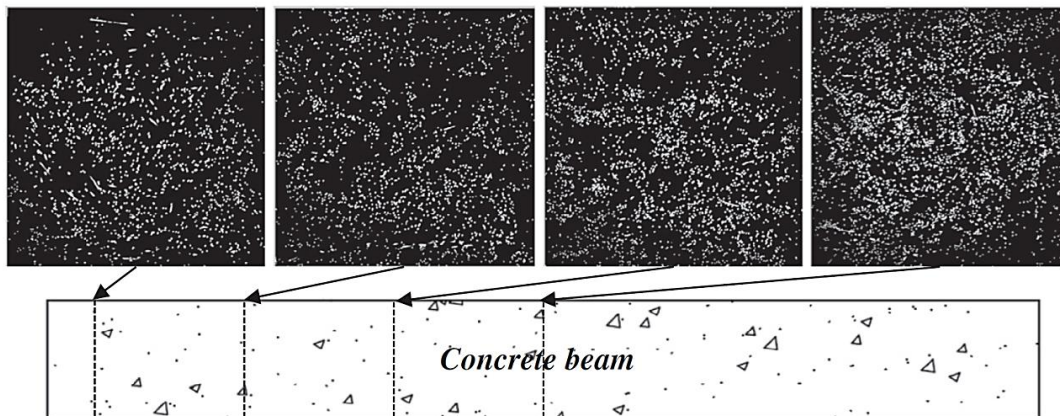
(a)
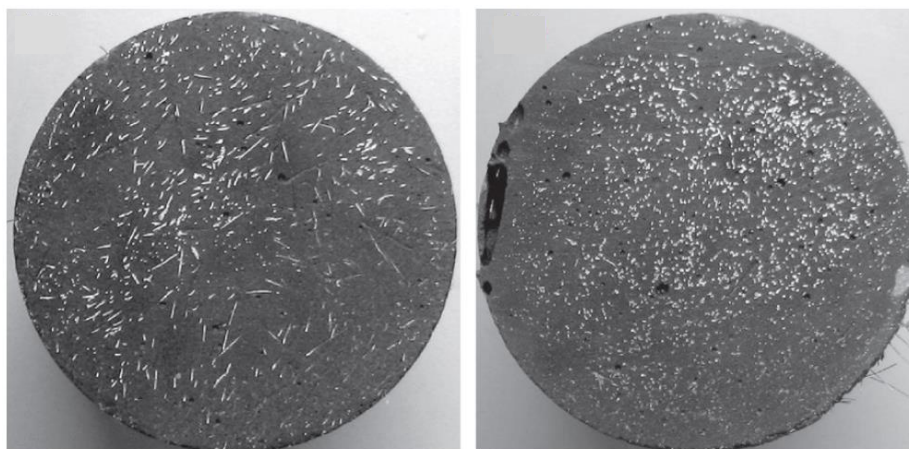
(b)

Source: Yoo, Kang, and Yoon (2014); Garas, Kurtis, and Kahn (2012)

Baril *et al.* (2016) analyzed the capacity and structural ductility reduction in thin slabs with a casting flow defect affecting the fiber distribution. Although the different fiber distributions did not significantly affect the strength of the first crack, the microcrack development changed according to the casting defect, mainly if it passed through the applied load point. The authors suggest a capacity reduction factor of about 3.8, higher than the orientation factor K, proposed by AFNOR (2016), which rarely exceeds the factor of 2.

When producing UHPC members, it is helpful to induce flow direction. In flexural behavior, prism specimens with concrete placed in the center show higher peak load and lower post-peak ductility in the softening region than specimens placed in the corner (Yoo, Kang, and Yoon, 2014). Huang, Gao, and Khayat (2021) improved the UHPC properties by inducing the fiber alignment with a novel cast method. In Figure 23 may be seen that samples with the induced flow and higher fiber volume present a better flexural behavior. In the post-cracking stage, it is evident that the fibers effectively bridged the cracks, increasing the load-carrying capacity, either to the same fiber amount or increasing the quantity.

Figure 23: Flexural load-deflection curves of samples prepared using two casting methods with different fiber volumes and 13 mm lengths
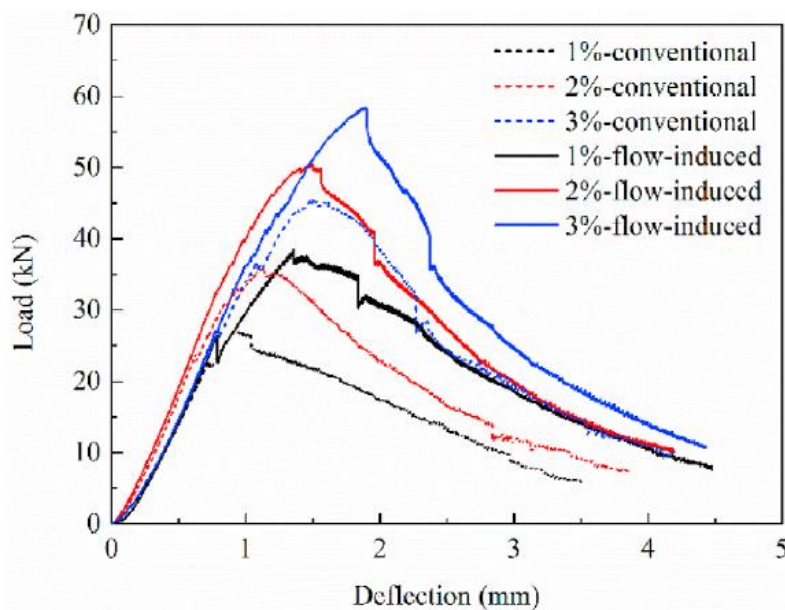
. Source: Huang, Gao, and Khayat (2021)

The placement method barely affects deflection and crack mouth opening displacement (CMOD) at peak load, likewise with the fracture energy G_F (Yoo, Kang, and Yoon, 2014). AFNOR (2016) determines that test samples shall be produced by the corner. Furthermore, a better prediction of fiber orientation distribution may accurately model tension behavior (Kwon *et al.*, 2012). It is necessary to treat UHPC as an anisotropic material for an effective enhancement of structural performance considering fibers that are intersecting and aligned in the fracture plane (Kang and Kim, 2012; Švec *et al.*, 2014). In addition, for superior performance, like high durability and strength, a reduced amount of voids is desired in the mixture.

The UHPC is designed to be a self-compacting material. The compaction process works to reduce the amount of the total amount of voids. Additional measures are necessary whether utilized because, due to the high dosage of superplasticizer, the extra vibration generates swelling overflow or bubbles (Ipek *et al.*, 2011). Figure 24 shows voids (bubbles) that migrate to the surface. In addition, besides the properties of the cement paste, the aggregate size affects the optimum vibration frequency. For instance, a mean grain diameter of < 1 mm requires a frequency of 200 Hz, which is not usual in concrete construction (Schachinger, Schubert, and Mazanec, 2004).

Figure 24: Surface voids in UHPC sample without pre-setting pressure
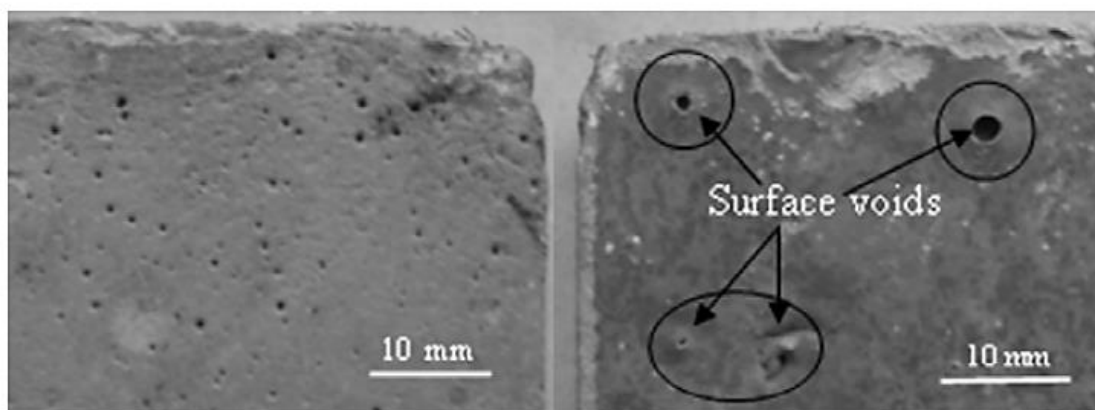
Source: Ipek *et al.* (2011)

2.5 SHRINKAGE AND CREEP

In UHPC, the shrinkage leads to cracks at early ages, and its evaluation may improve the material's durability and strength. Shrinkage of concrete occurs due to water loss caused by evaporation or chemical change resulting from the hydration of cement and carbonation (Tam, Tam, and Ng, 2012), the most common of which are autogenous shrinkage, drying shrinkage, and chemical shrinkage. Whereas autogenous shrinkage causes the reduction of volume associated with the internal consumption of water during cement hydration, drying occurs with the withdrawal of water from the hardened concrete stored in unsaturated air to the surroundings. The chemical shrinkage is like the autogenous; however, the reduction is from the hydrated cement paste's absolute volume (solid and liquid phases) (Tam, Tam, and Ng, 2012). In particular, the high content of the UHPC binder and the low water-to-cement ratio increase the levels of autogenous shrinkage compared to ordinary concrete (Xie *et al.*, 2018). A sizable portion of the total shrinkage is caused by autogenous shrinkage instead of drying shrinkage, although the increase in ambient temperature may reduce this difference (Figure 25) (Yo, Kim, and Kim, 2018; Yalçinkaya and Yazici, 2017).

Figure 25: Free shrinkage behaviors of UHPC under (a) ambient curing and (b) heat curing
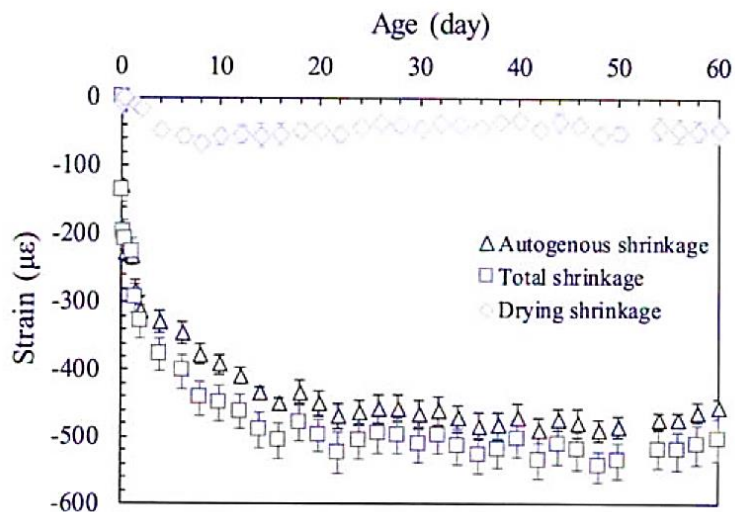
(a)
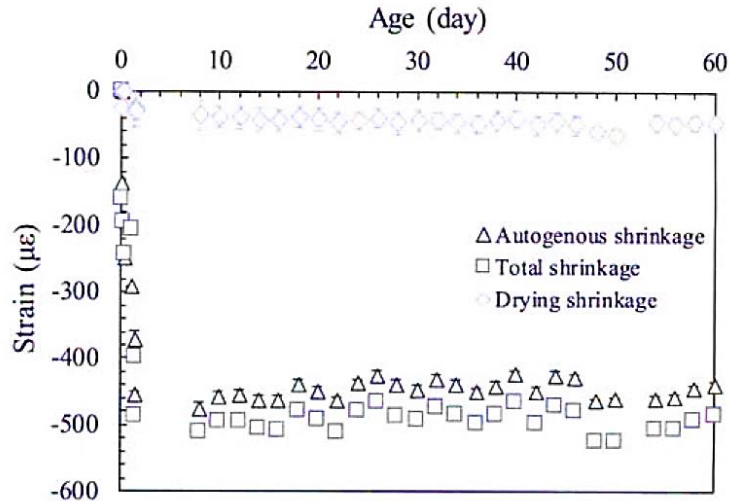
(b)

Source: Yo, Kim, and Kim (2018)

Yalçinkaya and Yazici (2017) studied the effects of ambient temperature (20°C, 30°C, and 40°C) and relative humidity (50%RH, 60%RH, and 70%RH) on early-age shrinkage. The temperature increase resulted in a higher autogenous and drying shrinkage due to rising cement hydration and water loss to the ambient. Conversely, the relative increase in humidity reduces the drying shrinkage, although slightly.

Yoo, Kim, and Kim (2018) studied the UHPC shrinkage behavior under ambient and heat-curing conditions. The authors present that the heat curing accelerated cement's hydration process, hence, the development of autogenous shrinkage at an early age. In addition, after three days of heat curing, there was no increase in total, autogenous, and drying shrinkage. Li *et al.* (2017) concluded that cement and secondary hydration finish at ten hours of heat curing, and the early-age shrinkage tends to stabilize. This result may be seen in Figure 25.

As a result of a study of prediction models for the autogenous shrinkage of UHPC, Yoo, Kim, and Kim (2018) propose, based on non-linear regression analyses, a model to simulate the behavior of both ambient- and steam-cured. The following equations (4–7) define the proposed model.

$$\varepsilon_{as}(t) = \gamma \varepsilon_{as\infty} \beta(t) \qquad\qquad (4)$$

$$\varepsilon_{as\infty} = -2300 \exp[-7.2(w/b)] \tag{5}$$

$$\beta(t) = 1 - \exp\left(-0.65\sqrt{t}\right) \tag{6}$$

$$t_e = \int_0^t exp\left[\frac{E_a(T)}{R}\left(\frac{1}{T_{ref}+273} - \frac{1}{T(t)+273}\right)\right]dt \tag{7}$$

where ε_{as} is the autogenous shrinkage, t is a time (age), γ is a coefficient to describe the effect of shrinkage-reducing admixture (SRA) (suggested as 0.85), $\beta(t)$ is the development function of autogenous shrinkage, $\varepsilon_{as\infty}$ is the ultimate autogenous shrinkage, w/b is the water-to-binder ratio, t_e is an equivalent age in the function of the ambient temperature, $E_a(T)$ is the activation energy (approximately 40000 J/mol or 45000 J/mol), R is the ideal gas constant (8.315 J/mol.K), T_{ref} is the reference temperature of 20°C, and $T(t)$ is the actual temperature.

Xie *et al.* (2018) evaluated three techniques to reduce shrinkage, including reducing the binder amount using an SRA and partially replacing mixing water with crushed ice. The binder-to-sand ratio, as mentioned previously, optimizes binder usage. An optimal b/s ratio may be considered 1-1.1 for a typical UHPC mix to minimize the shrinkage effect without significantly comprising the compressive strength (Xie *et al.*, 2018). In shrinkage-reducing admixture utilization, the authors presented that the SRA decreased the autogenous shrinkage significantly (approximately 69%), starting right after the initial casting. Furthermore, a higher SRA content develops a lower drying shrinkage. The crushed ice use exhibited a lower autogenous shrinkage decrease (approximately 19%) than SRA utilization. Its purpose is to attenuate the rate of hydration and, hence, reduce autogenous shrinkage as the internal temperature of UHPC decreases. The best mix for reducing the impact of shrinkage without significant compressive strength reduction in the long term will be to use a 1% SRA or a crushed ice dosage of 50% (Xie *et al.*, 2018). In addition, longitudinal steel reinforcement may function as an ultimate early-age shrinkage reducer. For instance, a 4.52% reinforced ratio reduces up to 60% by the restraint effect (Li *et al.*, 2017).

As well as shrinkage, the creep of UHPC presents reduced values in comparison to CCs. The creep phenomenon is an intrinsic time-varying characteristic of cementitious materials, continuously increasing deformation under long-term loading (Xu *et al.*, 2018). According to Xu *et al.* (2018), parameters such as low w/b ratio and the presence of steel fibers influence the UHPC creep response. Determining the creep development is difficult due to the complex interacting effects, for instance, ongoing hydration and aging, stress level, loading history, and their couplings (Switek-Rey, Denarié, and Brühwiler, 2016). In addition, the works studied identified the difficulty of separating the tensile creep from autogenous shrinkage.

The creep reduction due to the presence of steel fiber may reach up to 25% despite an overmixed minimizing of this ability. The higher fiber content decreases the flowability, resulting in a weak ITZ and causing more internal defects (Xu *et al.*, 2018). A denser material presents a lower creep development as well. This effect may occur by reducing the w/b ratio. When the w/b is higher, the hardened concrete has higher water evaporation, internal microporosity, and creep coefficient (Xu *et al.*, 2018). According to Switek-Rey, Denarié, and Brühwiler (2016), the UHPC's lower creep than CCs is due to the development of autogenous shrinkage that uses a significant part of the viscous potential of the material to react to the forces due to self-desiccation in the pore structure. Therefore, a lower w/b ratio causes higher autogenous shrinkage and lower creep. Figure 26 presents the effect of the steel fibers' content and the w/b ratio on the creep coefficient.

Figure 26: Creep coefficient of UHPC considering w/b 0.16 (C16SF) and 0.22 (C22SF), as well as 1% (C16SF1) and 2% (C16SF2) of steel fibers
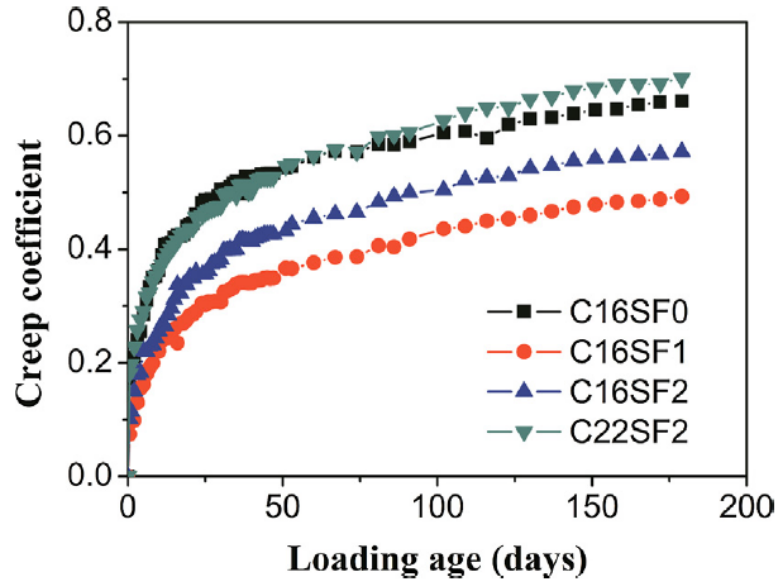
Source: Xu *et al.* (2018)

Garas, Kurtis, and Kahn (2012) studied the thermal treatment effect on tensile and compressive creep. As the shrinkage, the creep development decreases up to 172% to tensile creep and 163% to compressive creep. In addition, the authors' observations present the dependency of concrete maturity on creep response at the loading time. Therefore, the thermal treatment increased the material maturity, reducing the creep.

Xu *et al.* (2018) propose a method to determine the basic (φ_{bc}) and drying creep (φ_{dc}) coefficient and, consequently, the creep coefficient (φ), based on the fib Model Code 2010 (FIB, 2012). The following equations (8–21) define the proposed model. The theoretical compressive strength ($f_{cm,calc}$) was applied due to the influence of the elastic modulus on creep.

$$\varphi(t,t') = \varphi_{bc}(t,t') + \varphi_{dc}(t,t') \tag{8}$$

$$\varphi_{bc}(t,t') = \beta_{bc}(f_{cm,calc}) \cdot \beta_{bc}(t,t') \tag{9}$$

$$\varphi_{dc}(t,t') = \beta_{dc}(f_{cm,calc}) \cdot \beta_{dc}(RH) \cdot \beta_{dc}(t') \cdot \beta_{dc}(t,t') \tag{10}$$

$$\beta_{bc}(f_{cm,calc}) = \frac{1.8}{f_{cm,calc}^{0.7}} \tag{11}$$

$$f_{cm,cal} = 10 \cdot \left(\frac{E_{c,28}}{21.5\alpha_E}\right)^3 \tag{12}$$

$$E_{c,28} = 21.5\alpha_E \left(\frac{f_{cm}}{10}\right)^{1/3} \tag{13}$$

$$\beta_{bc}(t,t') = \ln\left[\left(\frac{30}{t'_{adj}} + 0.035\right)^2 (t-t') + 1\right] \tag{14}$$

$$\beta_{dc}(f_{cm,calc}) = \frac{412}{f_{cm,calc}^{1.4}} \tag{15}$$

$$\beta_{dc}(RH) = \frac{1 - RH/100}{(h/1000)^{1/3}} \tag{16}$$

$$\beta_{dc}(t') = \frac{1}{0.1 + (t'_{adj})^{0.2}} \tag{17}$$

$$\beta_{dc}(t,t') = \left[\frac{(t-t')}{\beta_h + (t-t')}\right]^{\gamma_{dc}} \tag{18}$$

$$\gamma_{dc} = \frac{1}{2.3 + \dfrac{3.5}{\sqrt{t'_{adj}}}} \tag{19}$$

$$\beta_h = 1.5 \cdot h + 250 \cdot \alpha_{f_{cm}} \leq 1500 \cdot \alpha_{f_{cm}} \tag{20}$$

$$\alpha_{f_{cm}} = \left(\frac{35}{f_{cm,calc}}\right)^{0.5} \tag{21}$$

where t is the concrete age since mixing; t' is the load applying age; $\beta_{bc}(f_{cm})$ represents the modified coefficient considering the strength effect on basic creep; $\beta_{bc}(t,t')$ represents the time process function of basic creep; $\beta_{dc}(f_{cm})$, $\beta_{dc}(RH)$, $\beta_{dc}(t')$ represents the correction factors on drying creep; $\beta_{dc}(t,t')$ represents the time process function of drying creep; f_{cm} is the mean value of the compressive strength at 28 days; α_E is a correction factor depending on used aggregates; t'_{adj} is the adjusted age at loading; RH is the relative humidity of the ambient environment in %; and h is the notional size of member in mm ($= 2A_c/u$, where A_c is the cross-section in mm² and u is the perimeter of the member in contact with the atmosphere in mm).

2.6 UNCONVENTIONAL PROCEDURES

This topic presents the procedures to achieve higher structural performance, which is not usual in CC production.

2.6.1 Pre-setting Pressure

Pre-setting pressure is a force applied in fresh concrete to remove pores, like water and air. This method may increase the adherence between the paste and the fibers, improving mechanical properties. The pressure applied during the setting phase, 6–12 h since the mixing procedure, may cause microcracks because of the aggregates expanding in the unloading phase. Nevertheless, the procedure minimizes the effect of autogenous shrinkage (Ipek *et al.*, 2011). As seen in Figure 27, the pre-setting pressure significantly increases the compressive strength compared with a sample control. In the study by Helmi *et al.* (2016), a pre-setting pressure of 8 MPa applied five hours after casting increased strength by 33%. In addition, samples pressurized at 25 MPa and 100 MPa resulted in a compression increase of 104% and 130%, respectively. The Young's modulus increase rate is lower than the compressive strength due to the increased adherence between fiber and concrete interface; hence, the increase in ductility (Ipek *et al.*, 2011).

Figure 27: Pre-setting pressure to the compressive strength and Young's modulus effect
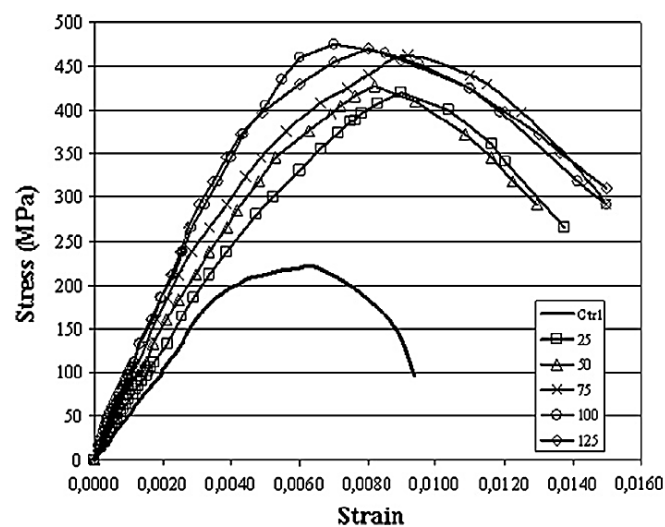
Source: Ipek *et al.* (2011)

In flexural tests, a pre-setting pressure of 5 MPa may increase the flexural strength by 34% and more than thrice in toughness (Figure 28). In addition, values of higher pressures do not have a significant result in comparison to the 5 MPa pressure (Ipek, Yilmaz, and Uysal, 2012).

Figure 28: The load-deflection graphics of pre-setting pressure and non-pre-setting pressure
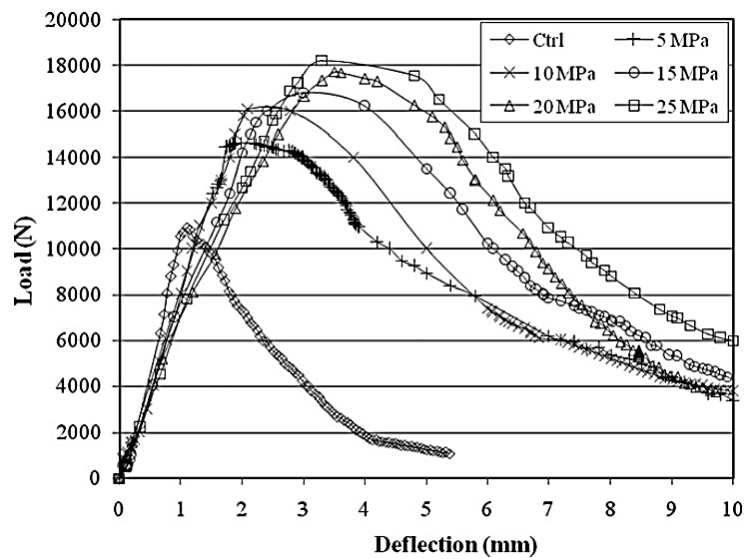
Source: Ipek, Yilmaz, and Uysal (2012)

The combination of pressure and heat treatment during curing may result in higher strengths. Whereas pre-setting pressure increases the material density and decreases the porosity, the heat treatment accelerates the pozzolanic reaction and modifies the microstructures of hydrates (Helmi *et al.*, 2016).

2.6.2   Thermal Curing or Heat Treatment

The hydration reactions of the cementitious materials increase with the heat-cure process. Hot water, steam, autoclave, dry heat air, and drying oven are examples of thermal curing. This process, which differs from the conventional water-cure procedure, uses equipment and elevated temperatures. The heat treatment temperature varies between 90°C and 200°C (Helmi *et al.*, 2016). In hot water curing, the specimens are kept in water with a temperature below

boiling point. Steam curing applies elevated temperatures and relative humidity, usually in a steam curing chamber. An autoclave uses steam at high pressure, applying pre-setting pressure in conjunction. In a dry heat air curing, hot air passes by the specimens. In addition, this procedure enables the heat treatment of large structural elements. Dry oven curing applies the heat uniformly, with a controlled heating rate. Despite this, specimens may be cured in water in the initial days to prevent water loss during the process. An ultra thermal cyclic chamber helps control temperature and humidity (Gu *et al.*, 2016; Prem, Murthy, and Bharatkumar, 2015).

Yang *et al.* (2009) increased the 28-day compressive strength by 20%, flexural strength by 10%, and fracture energy by 15% with thermal curing in water for seven days at 90°C. The increase in tensile strength may be caused by accelerated autogenous shrinkage, resulting in a higher radial confinement pressure (Yoo, Kim, and Kim, 2018). The procedure accelerated the strength rise rate and improved mechanical properties. In Prem, Murthy, and Bharatkumar's (2015), steam curing is reported to allow a notable 7-day compressive strength increase; however, at 28 days, the strength was like the result obtained with water curing. Similarly, Yoo, Kim, and Kim (2018) did not observe a noticeable increase in compressive strength from 6 to 28 days. It happens because steam curing only mobilizes the high early-age strength. Garas, Kurtis, and Kahn (2012) analyzed the usual steam-curing temperature in precast concrete plants, considering the total heat equal to the typical thermal treatment at 90°C for 48 h. The authors obtained a satisfactory microstructure with a thermal treatment at 60°C for 72 h. Even delaying the steam treatment up to 8 months after casting may increase the compressive strength by approximately 25% (Graybeal, 2007).

Considering the expansion of hydrated material (C-S-H) at elevated temperatures, pores reduce with these minerals, filling them (Figure 29). This result may be more evident in 28-day strength compression tests because, in 7-day tests, there is only a reduction in the diameter of macro defects. However, there are significant effects related to the acceleration of the pozzolanic reaction (Helmi *et al.*, 2016). Compared with ambient-cured UHPC, the steam-cured has much smaller porosity and micropores (Yoo, Kim, and Kim, 2018). Logical thinking suggests that heating would accelerate the propagation of microcracks

(formed during shrinkage) due to the thermal expansion of the solid phases and volumetric expansion of the air (and, hence, increased pressure) within entrapped voids, which may hinder the compressive strength earnings (Helmi *et al.*, 2016).

Figure 29: SEM images of different cure conditions: (a) 20°C water cure, (b) 3-day cure in 90°C hot water and steam, (c) 3-day cure in 90°C steam and cure later with 12 h 200°C dry air, and (d) 3-day cure with 90°C steam cure and cure later and 12 h 300°C dry air cure
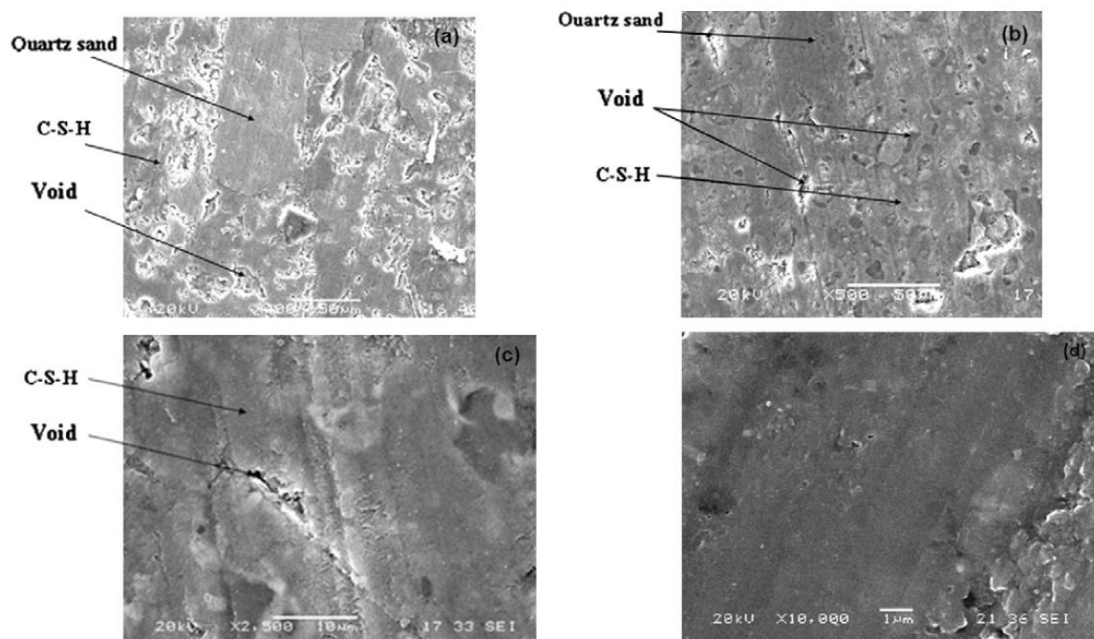
Source: Ipek *et al.* (2011)

With SEM micrograph analysis, it is possible to confirm that heat treatment may induce microcrack formation. This is initiated by thermal expansion during accelerated heat curing since UHPC contains a high proportion of fine-grained materials. These, with approximately 0.2 µm-width microcracks, occur at the borders of cement-coated grains within the mortar phase and emanate from entrapped air pores (Figure 30) (Helmi *et al.*, 2016). In Ipek *et al.*'s (2011) experiments, dry air curing, without steam curing, was directly applied. Despite the low heat rise rate, their samples were cracked or broken into pieces without reaching the temperature of 100°C. In dry oven curing, water loss may occur

during the process. Consequently, the hydration degree of cement, chloride resistance, and compressive and flexural strengths are lower than in other curing methods (Gu *et al.*, 2016).

Figure 30: SEM micrograph of typical microcracks after heat curing (a) originating at the ITZ and (b) at the periphery of connecting pores
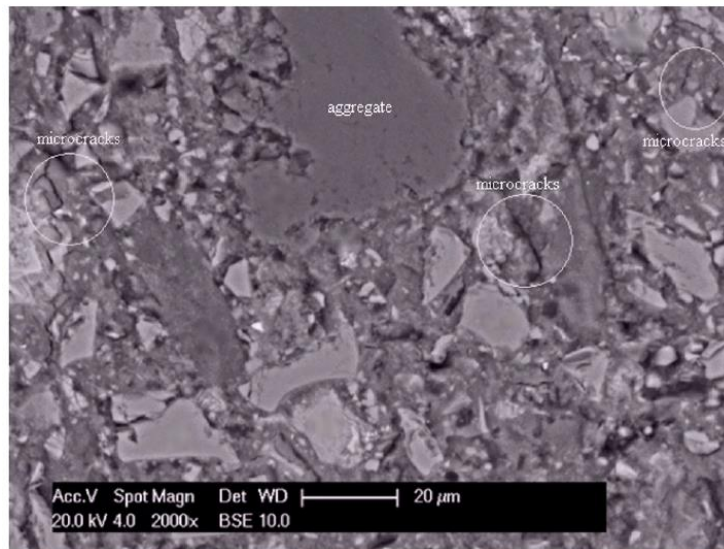
(a)
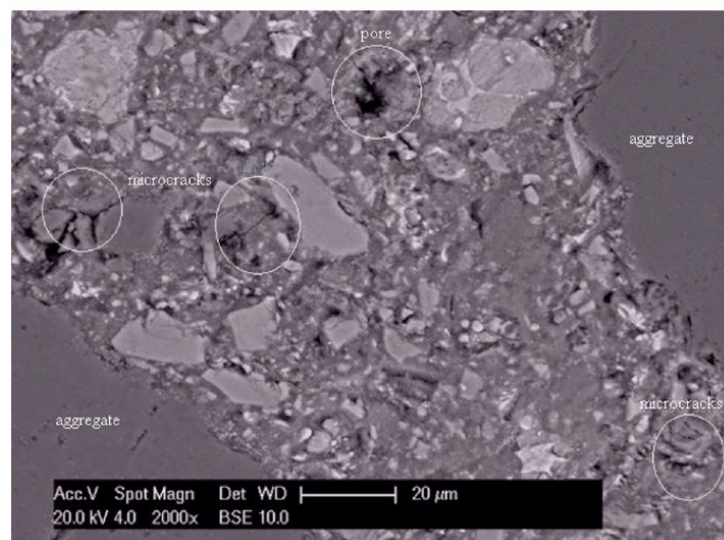
(b)

Source: Helmi *et al.* (2016)

2.6.3 Internal Curing

Internal curing (IC) is the method of internally providing additional water to a mixture after the setting. The process is possible by incorporating agents, similar to saturated materials that release the water to retain the internal relative humidity (RH) and ensure the cement paste capillary porosity is water-filled to the maximum degree of hydration (Justs *et al.*, 2015; Meng and Khayat, 2017). In addition, the benefits of IC include reducing shrinkage, reducing potential cracking, and increasing durability (Meng and Khayat, 2017). The most common agents used are superabsorbent polymers (SAP) and lightweight aggregates (LWA), such as lightweight expanded clay (LECA) (Liu *et al.*, 2017). Nevertheless, the method's disadvantage is the introduction of macropores, which may decrease the material's strength. The larger the agent particle size, the more water is absorbed.

UHPC design may use IC to reduce the self-desiccation shrinkage, causing lower self-induced stresses, which might avoid cracking (Justs *et al.*, 2015). For UHPC, SAP and porous superfine powder are recommended. However, despite SAP increasing the chemical shrinkage with the rise of cement hydration, the total shrinkage decreases (Liu *et al.*, 2017).

The low UHPC's water/cement ratio causes incomplete cement hydration due to the lack of free water and capillary pore space to precipitate hydration products (Justs *et al.*, 2015). Therefore, Justs *et al.* (2015) used small SAP in UHPC to minimize the size of the pores introduced and optimize the water distribution. Their analysis shows a higher hydration heat with IC. The hydration reaction started earlier and at a slower rate. As evident in Figure 31, the additional water maintains a higher relative humidity, consequently reducing autogenous shrinkage. As expected, there was a decrease in compressive (19%) and flexural (27%) strength and elastic modulus (14%), although the difference decreased over time.

Figure 31: Internal relative humidity of UHPC with different w/c and SAP additions in the first 5 to 7 days of hydration
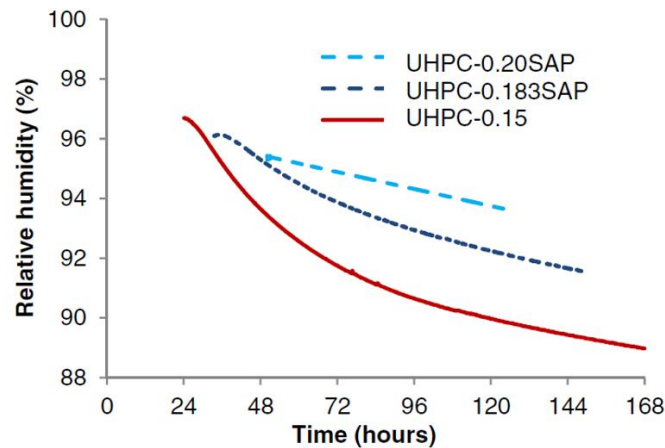
. Source: Justs *et al.* (2015)

Meng and Khayat (2017) employed lightweight sand (LWS) as an aggregate replacement and an IC agent to reduce autogenous shrinkage and increase mechanical properties. All mixtures were self-consolidated, and the flowability was enhanced with the LWS increase. The initial and final setting times were delayed gradually with the amount of material addition. Although LWS retards the early-age strength development, a 28-day compressive and flexural strength of 22% and 14% higher, respectively, was achieved with 25% of LWS. The Young's modulus was reduced slightly from 52 to 51 GPa. The ITZ SEM image may explain the improvement of mechanical properties (Figure 32), which presents an inter-penetrated microstructure between the LWS and the matrix, enhancing the interfacial bonding strength. In addition, mixtures with LWS presented an increased degree of hydration after 15 h, leading to more hydration products. Such an effect of LWS tends to offset its consequence of reducing strength due to the initial additional porosity introduced by LWS (Meng and Khayat, 2017). The autogenous shrinkage reduced up to 60% due to internal relative humidity (IRH) sustaining at a high level (97% at 72 h after a final setting with 75% of LWS), mitigating the self-desiccation.

Figure 32: SEM picture of the interface between sand and matrix of LWS at 25%. The cyan color indicates Si (LWS), and the yellow color indicates Ca (cement)
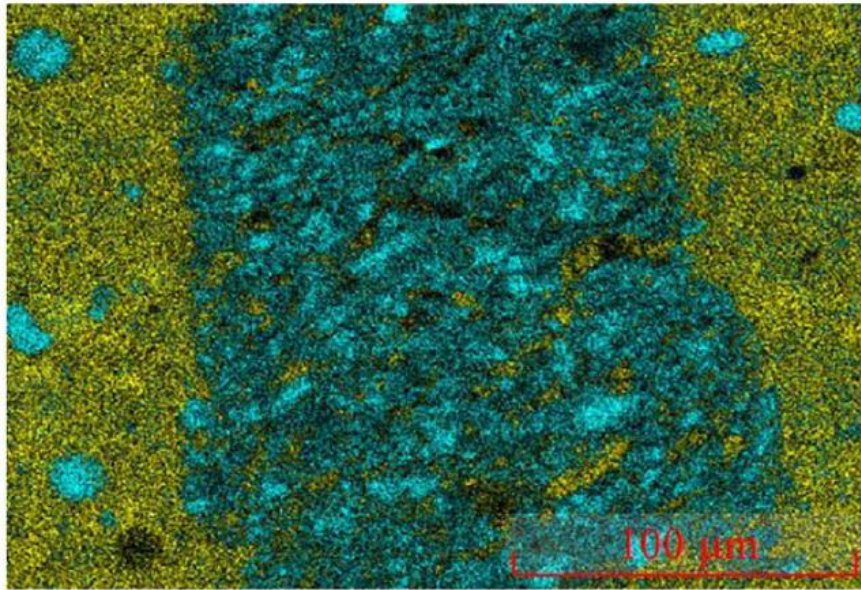
Source: Meng and Khayat (2017)

The SCM may reduce the autogenous shrinkage with a minor impact on strength (Liu *et al.*, 2017). In Van *et al.* (2014), the authors used amorphous rice husk ash (RHA) as an IC agent and studied the improvement of the UHPC microstructure. As seen in Figure 33, with different curing temperatures, SF, and RHA mixtures, the SCM significantly reduces autogenous shrinkage. Regarding the 28-day compressive strength, UHPC with RHA solely decreases by 3% approximately with the conventional curing method and 7% with thermal curing (48 h at 65°C). Unlike SAP, RHA becomes a "micro water reservoir" with good dispersion and high pozzolanic reactivity (Van *et al.*, 2014).

Figure 33: Autogenous shrinkage of UHPC containing RHA or SF at different curing treatment conditions
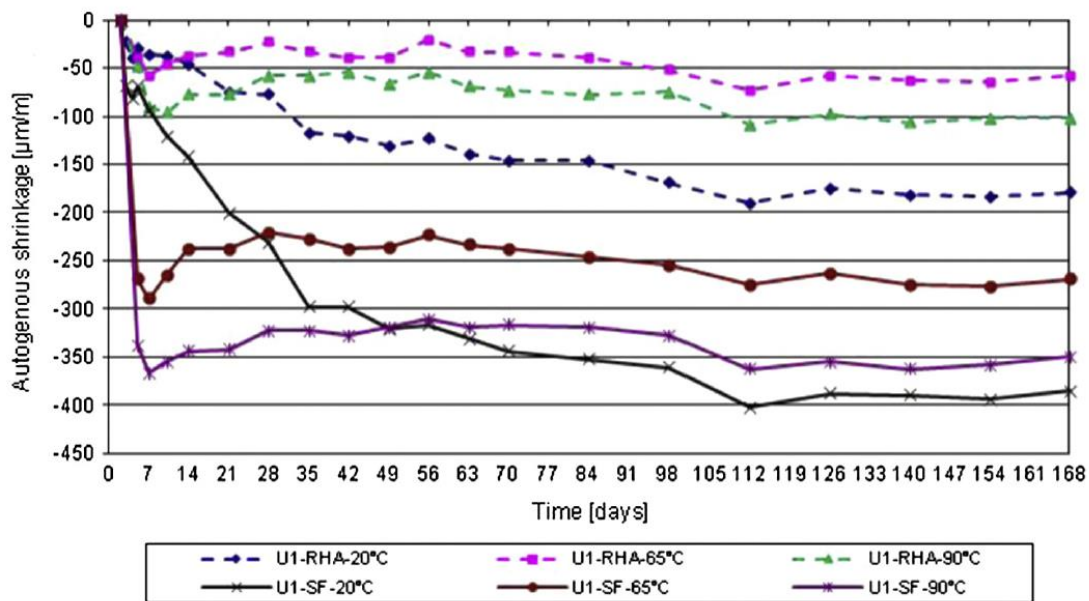
Source: Van *et al.* (2014)

2.7 DURABILITY

Because of the improvement of micro and macro UHPC properties, the material has exceptional durability that allows its use in several structural applications and environmental conditions. Its optimized microstructure provides very thin pore sizes and excellent resistance to fluid ingress (Wang *et al.*, 2014). Even after severe exposures to chloride ions, the mechanical properties of UHPC have no deterioration (Abbas, Soliman, and Nehdi, 2015). The superior material durability performance is presented in the un-cracked state because of the high compactness of the matrix and in the cracked state, due to the highly effective crack-width control that the material can develop under tensile stress (Al-Obaidi *et al.*, 2020). Therefore, UHPC structures will have a long lifetime, with less maintenance and reduced operating costs.

The typical durability indicators are porosity, electrical resistivity, diffusion coefficient, and permeability (Wang *et al.*, 2014). Figure 34 illustrates the significant gas permeability difference between UHPC, ordinary concrete, and a standard mortar. In this case, the confining pressure will induce a closure in the porous materials. In a rapid chloride ion penetrability test, the UHPC presents a Coulomb value of fewer than 100 Coulombs, whereas high-performance concrete

presents around 216 Coulombs and regular strength concrete has 1736 Coulombs (Abbas, Soliman, and Nehdi, 2015). During a chloride ion penetration test, the corrosion of UHPC fibers is limited to the surface, penetrating to a depth of merely 1 mm after 180 days in a 10% chloride ion concentration (Abbas, Soliman, and Nehdi, 2015).

Figure 34: Gas permeability vs. confining pressure in the initial dry state, i.e., after 105°C drying until mass stabilization, for UHPC (UHPFRC), ordinary concrete (OC), and standard mortar (M1)
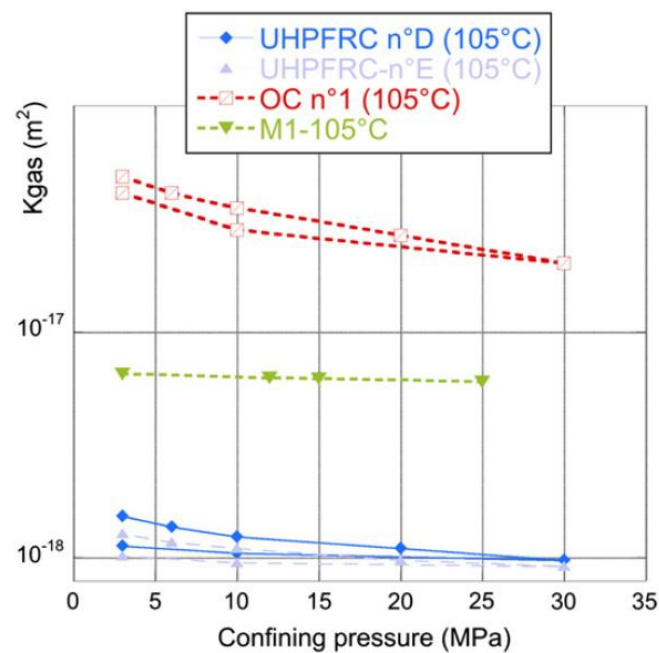
Source: Wang *et al.* (2014)

Ghafari *et al.* (2015) assessed the durability improvement in UHPC with nano-silica (nS) addition. The nano-silica mixture presents better results in all analyses than UHPC without nS and HPC. Due to the microstructure enhancement, the resistance to aggressive environments improves significantly as the value of the capillary pores decreases. Furthermore, most aspects relate to its porous structure since capillary pores are responsible for fluid migration in the concrete matrix (Ghafari *et al.*, 2015).

Abbas, Soliman, and Nehdi (2015) studied the influence of the length of steel fibers and dosage on UHPC durability. Although lengths do not affect the volume of permeable voids (VPV), the steel fiber volume increase leads to a lower

VPV. The steel fiber addition disturbs the continuity of capillary pores and reduces the VPV (Abbas, Soliman, and Nehdi, 2015). The authors observed the same effect in the rapid chloride ion penetrability test.

Wang *et al.* (2014) evaluated the effect of the thermal treatment in the gas permeability test as a durability indicator. According to the authors, at high curing temperatures, material permeability increases due to the gas passages created in the fiber/paste interface, as shown in Figure 35.

Figure 35: Effect of heat-treatment upon gas transport: (a) normalized gas permeability K(Pc)/10^{-17} at different heat-treatment temperatures and confinement and (b) fiber/paste interface of 400°C heat-treated UHPC
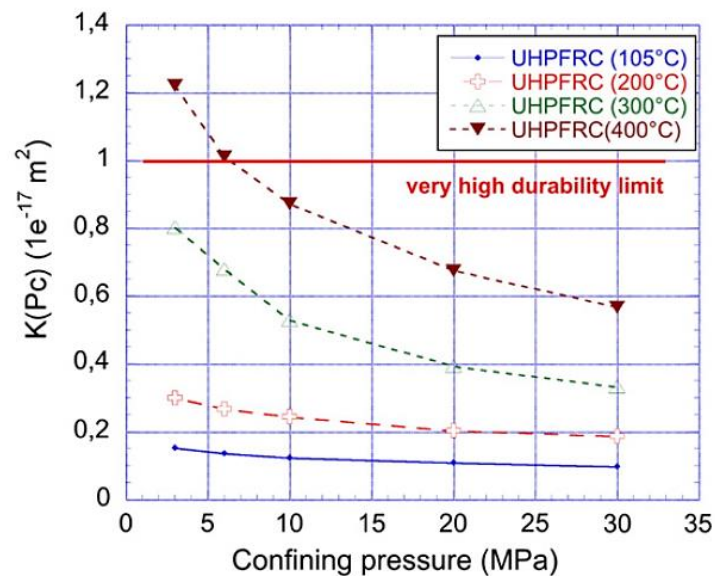
(a)
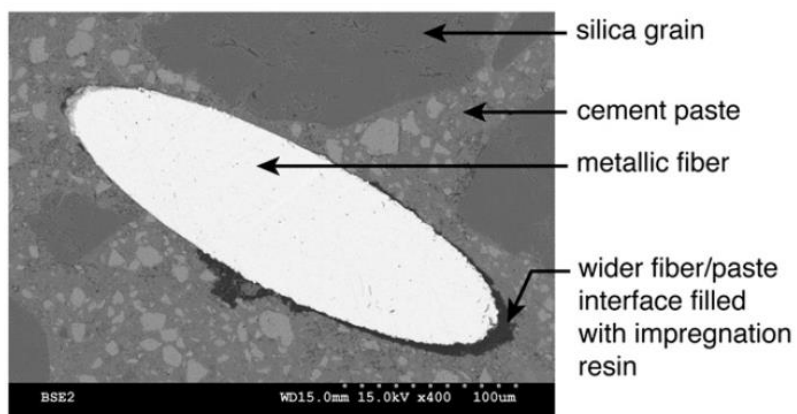
(b)

Source: Wang *et al.* (2014)

2.8 COMPRESSION BEHAVIOR

Compression is the most UHPC impactful mechanical property, usually used to compare it with other cementitious materials. Due to the high stiffness, the material exhibits a behavior with an approximately linear elastic first stage until the peak and then a descending branch with a final ductile stage, as shown in Figure 36. In addition, the compressive stress-strain relationship is usually modeled as a linear curve by using the maximum compressive strength and elastic modulus (Yang, Joh, and Bui, 2019). This simplification is possible due to 70% of the compressive strength diverging up to 5% from the linear elastic behavior, being able to reach 80 and 90% with steam treatment (Graybeal, 2007).

The compressive behavior of UHPC is closely related to the matrix strength, steel fiber shape, and steel fiber volume (Kim and Lim, 2023). According to Wu *et al.* (2017), 2.0% steel fiber addition increases compressive strength by approximately 37% due to the fiber bridging effect in the cracking development. In Kim and Lim (2023) studies, the maximum compressive strength and elastic modulus increased by approximately 27% for the UHPC with a 2.0% volume fraction. Adopting a hybrid blend of straight steel fibers with 13 mm and 6 mm lengths reduces the compressive strength slightly, compared with a mixture with 2.0% of 13 mm steel fiber because the short fiber has lower efficiency in restricting the development of cracks (Wu *et al.*, 2017).

Figure 36: Compressive stress-strain of UHPC
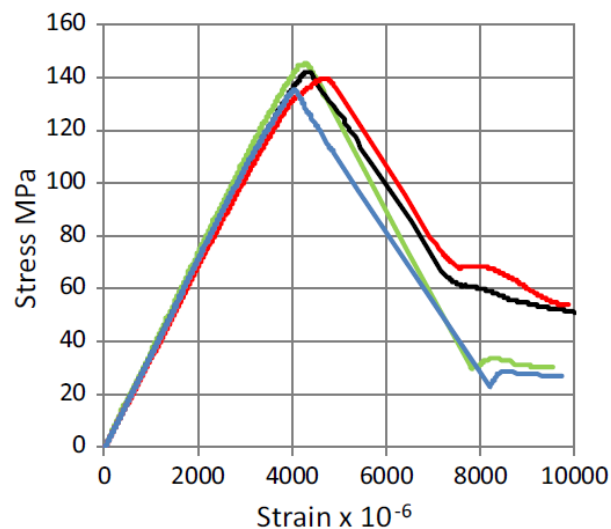
Source: Singh *et al.* (2017)

According to Graybeal (2007), the UHPC compression strength tends to stabilize after eight weeks after casting for untreated concrete and 48 h to material with steam treatment. The author presented an equation (Equation 22) to predict the strength ($f'_{c,t}$) at any time (t) based on the UHPC 28-day compressive strength (f'_c), taken from the Figure 37 diagram. The strength gain occurs rapidly with over 70 MPa within two days of setting without any supplemental curing treatment (Graybeal, 2007). Furthermore, it was developed a relationship (Equation 23) between the modulus of elasticity (E) and compressive strength (f'_c), which may cover a wide range of responses under different production types, such as untreated and steam cured. Lastly, an equation to describe the non-linear ascending branch compressive stress-strain behavior was presented (Equation 24) related by the modulus of elasticity and a reduction factor (α), which defines the decrease in the actual stress from the linear elastic stress. The two fitting parameters in Equation 25, *a* and *b*, were defined as 0.011 and 0.44, respectively, for untreated UHPC and 0.001 and 0.24, respectively, for steam-cured.

$$f'_{c,t} = f'_c \cdot \left[1 - exp\left(-\left(\frac{t - 0.9}{3}\right)^{0.6}\right)\right] \tag{22}$$

$$E = 3840 \cdot \sqrt{f'_c} \tag{23}$$

$$f_c = \varepsilon_c \cdot E \cdot (1 - \alpha) \tag{24}$$

$$\alpha = a \cdot e^{\frac{\varepsilon_c \cdot E}{b f'_c}} - a \tag{25}$$

Figure 37: Compressive strength gain as a function of time after casting
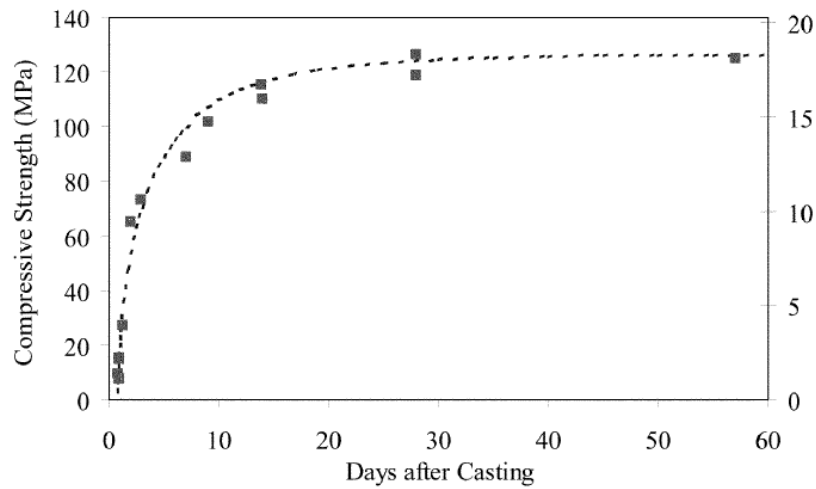
Source: Graybeal (2007)

Concerning the compression failure modes, Kim and Lim (2023) describe the crack pattern for the UHPC without fibers as several cracks simultaneously initiated parallel to the loading direction. On the other hand, the UHPC with fibers presents both transverse and longitudinal cracks, where the bridging effect is evident, as shown in Figure 38. In addition, due to this effect, the compressive strength increases along with the increase of the fiber volume fraction, although the strain corresponding to the peak compressive strength is not significantly altered (Kim and Lim, 2023).

Figure 38: Failure mode and crack patterns at the end of the compression test: (a) 0% fiber and (b) 2.0% fibers

(a)   (b)

Source: Kim and Lim (2023)

In the evaluation of the mechanical properties, strain rate sensitivity analysis is essential because some tests present different material behavior. As exhibited in Figure 39, the peak stress increased with the increase in strain rate. According to Wu *et al.* (2017), this effect occurred due to the lateral inertia of friction to the contact surface under rapid loading. Furthermore, rapid loading causes the occurrence of more microcracks until the propagation of the macrocracks, which increases the fracture energy and compressive strength (Wu *et al.*, 2017).

Figure 39: Effect of strain rates on compression stress-strain curves of UHPC at 28 days and 2% of steel fibers
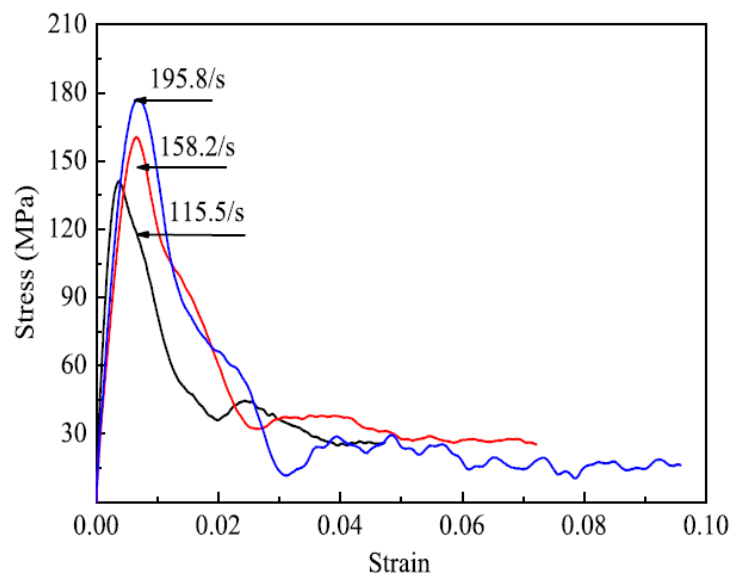
Source: Wu *et al.* (2017)

2.9 TENSILE BEHAVIOR

Despite being ignored in design with CC, the tensile strength is relevant in structures with UHPC. Moreover, this material advent HSC's performance under tension (Yang, Joh, and Bui, 2019). The global tensile behavior of UHPC is the resulting work of many fibers inclined in the matrix, particularly after crack initiation exhibiting a sustained post-cracking tensile strength (Zhou and Qiao, 2019; Graybeal and Baby, 2013). According to Hafiz and Denarié (2020), the tensile response is influenced by the material microstructure, fiber bond, crack

onset, growth and self-healing, instantaneous mechanical response, delayed mechanical response, and autogenous deformations. In addition, the UHPC tensile strength at 7 and 14 days is about 80% and 88% of the value at 28 days, respectively (Zhou and Qiao, 2020).

Wille, El-Tawil, and Naaman (2014) divided the tensile behavior of fiber-reinforced concrete into four categories: Level 1 is deflection softening or crack controlling with minnor enhancement in mechanical properties, Level 2 is deflection hardening, Level 3 is tensile strain hardening, and Level 4 is high energy absorbing, which is presented in Figure 40. This division is essential to understand the different types of behavior that may occur due to the matrix and fiber properties. Fiber bridging action plays a significant role in controlling the strain hardening and softening performance of UHPC in tension. It depends on fiber characteristics, fiber-matrix bond characteristics, and fiber dispersion and orientation, which are directly affected by the fiber volume (Zhou and Qiao, 2019). The primary energy dissipation mechanism of strain-hardening materials is multiple cracking, aggregating all the processes across many cracks, increasing the energy dissipation capacity and delaying crack localization (Xu and Wille, 2015). For instance, the energy dissipated before post-cracking is only about 15% of the total energy absorption, and the rest of the 85% is dissipated during the fiber pullout process (Zhou and Qiao, 2020). In addition, Wille, El-Tawil, and Naaman (2014) suggest 1% as the critical fiber volume fraction to obtain a strain-hardening behavior.

Figure 40: Illustration and definition of the performance levels of fiber-reinforced concrete
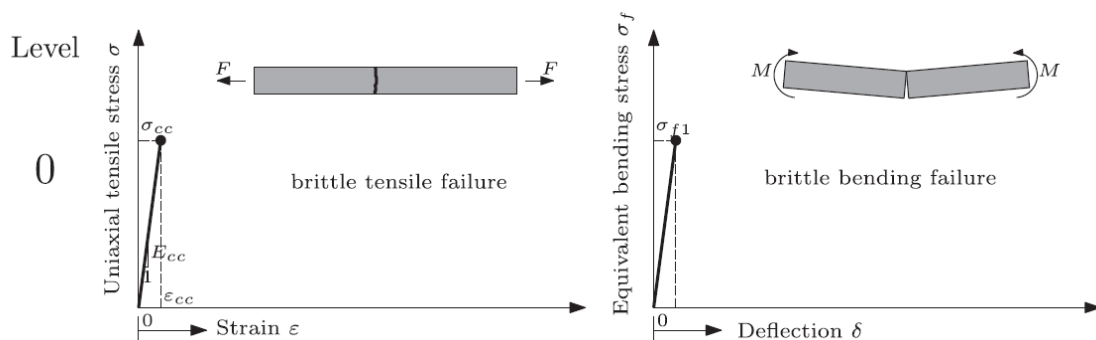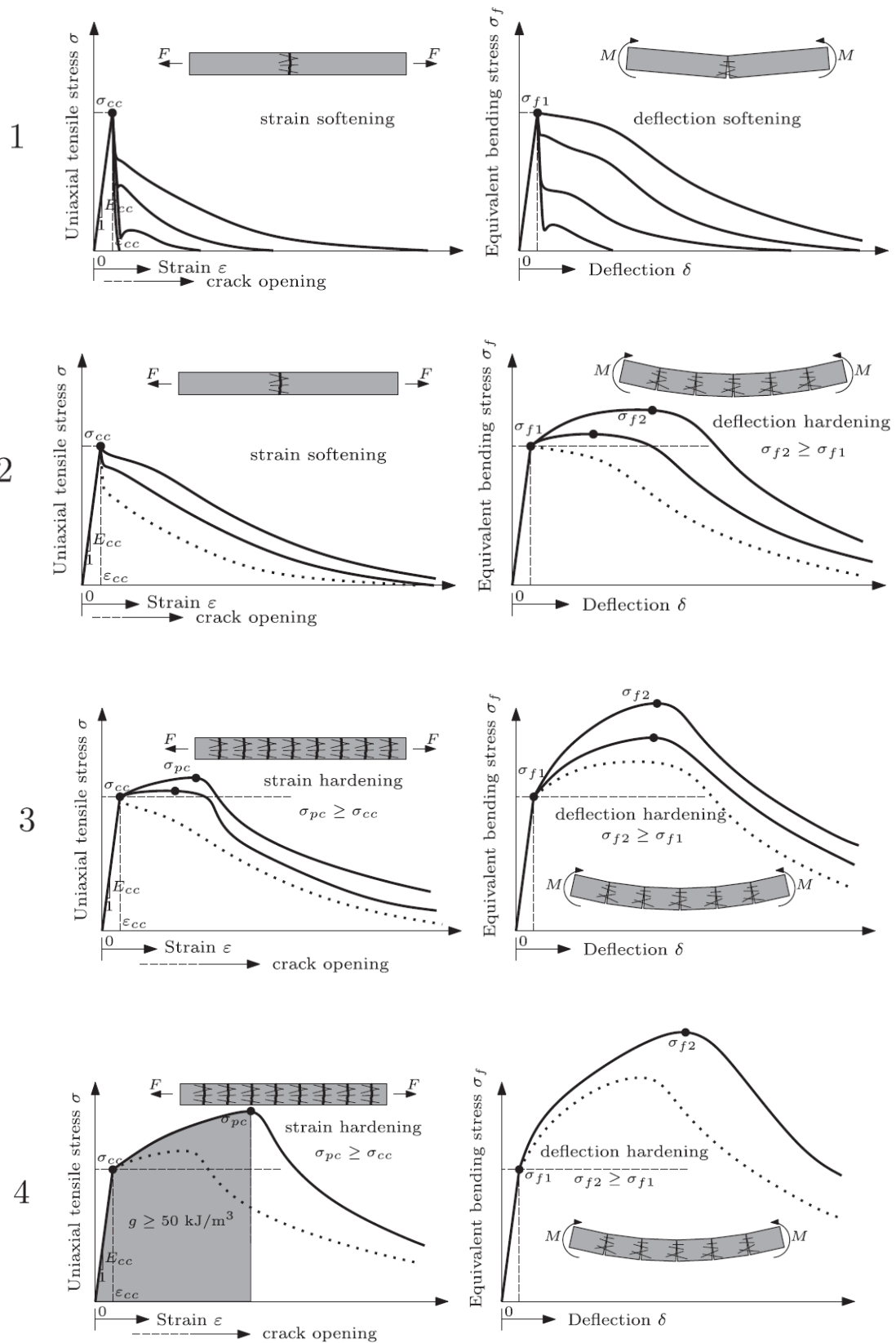
Source: Wille, El-Tawil, and Naaman (2014)

Zhou and Qiao (2019) explain the work mechanisms when UHPC is subjected to a tensile force. They consider the first interaction between the fiber and matrix elastic until the first crack occurs. Then, matrix and fiber bridging are mobilized with the load's rise. The cementitious material cohesion provides the former effect and the latter by bonding and debonding at the fiber-matrix interface. Furthermore, the peak tensile stress is reached when the fibers get their maximum contribution and start decreasing due to the debonding from the matrix. Figure 41 presents the tensile behavior with all mechanisms.

Figure 41: Idealized tensile stress-crack width (stress-strain) relationship
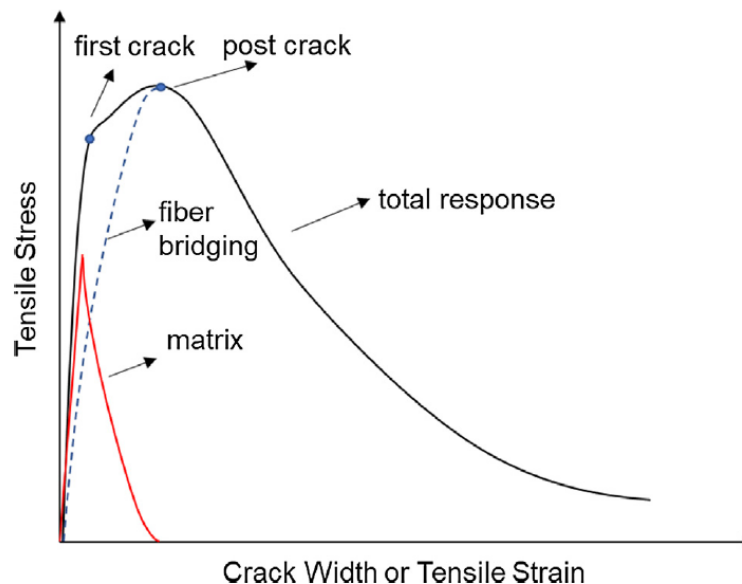
Source: Zhou and Qiao (2019)

Graybeal and Baby (2013) idealized a uniaxial tensile mechanical behavior based on their DTT responses. As presented in Figure 42, the diagram is divided into four stages. The first phase is the elastic phase, which continues through the section's first cracking. Then the multiple cracking phase is the post-cracking part resisted by uncracked matrix sections between discrete cracks and the fiber bridging. The third phase is characterized by increasing the crack opening and the start of fibers debonding. Lastly, the localized phase occurs when an individual crack causes the fibers to debond and pull out of the matrix (Graybeal and Baby, 2013).

Figure 42: Idealized UHPC uniaxial tensile mechanical response
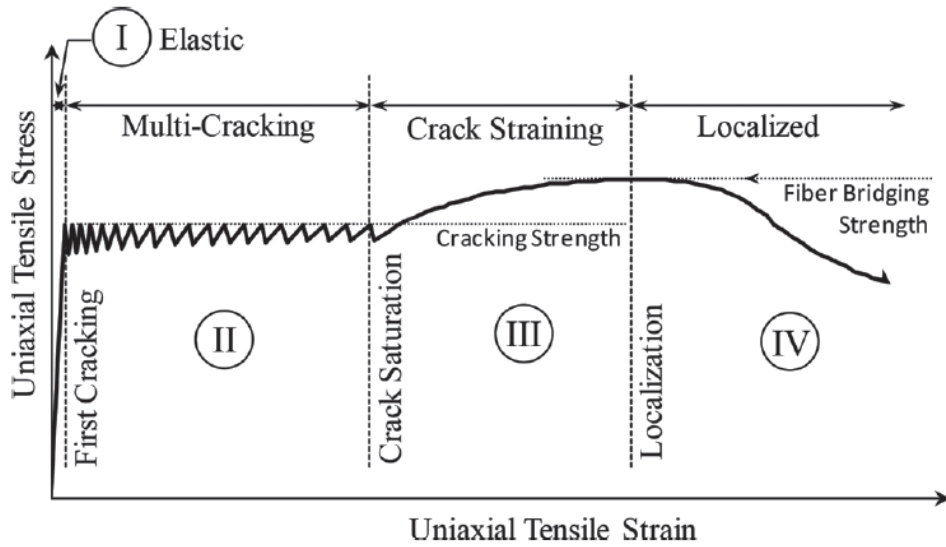
Source: Graybeal and Baby (2013)

Zhou and Qiao (2020) presented a simplified trilinear tensile stress-strain relationship. It is divided into three phases: linear elastic phase, strain-hardening phase (multiple cracking), and strain-softening phase (fiber pullout), as shown in Figure 43. Each model part may be defined as a linear function with variables according to the material parameters first cracking stress (σ_{cc}) and strain (ε_{cc}), post-cracking stress (σ_{pc}) and strain (ε_{pc}), and ultimate strain (ε_u), as presented in Equation 26. In addition, this model may be implemented in numerical finite element models to simulate the mechanical behavior of UHPC (Zhou and Qiao, 2020).

$$\sigma = \begin{cases} \dfrac{\varepsilon}{\varepsilon_{cc}} \cdot \sigma_{cc} & 0 \leq \varepsilon \leq \varepsilon_{cc} \\[3mm] \sigma_{cc} + \dfrac{\varepsilon - \varepsilon_{cc}}{\varepsilon_{pc} - \varepsilon_{cc}} \cdot \left(\sigma_{pc} - \sigma_{cc}\right) & \varepsilon_{cc} \leq \varepsilon \leq \varepsilon_{pc} \\[3mm] \left(1 - \dfrac{\varepsilon - \varepsilon_{pc}}{\varepsilon_u - \varepsilon_{pc}}\right) \cdot \sigma_{pc} & \varepsilon \geq \varepsilon_{pc} \end{cases} \qquad (26)$$

Figure 43: Idealized simplified tensile response of UHPC
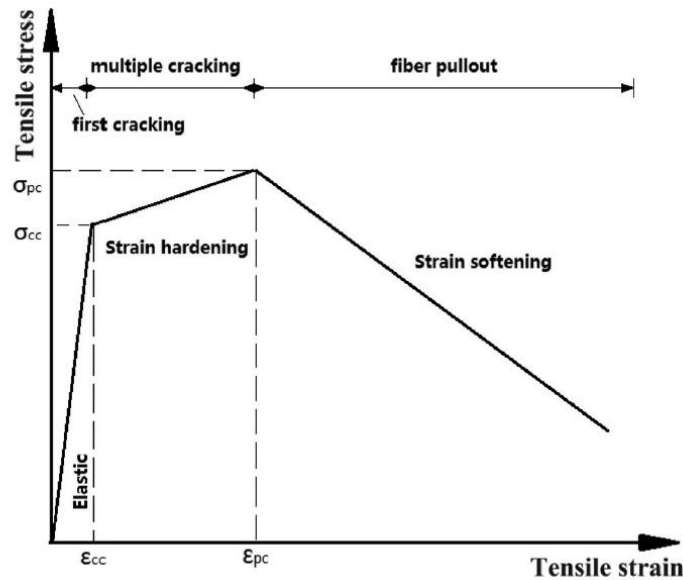
Source: Zhou and Qiao (2020)

Evaluating the UHPC tensile response experimentally is not easy and may be performed by direct and indirect methods. According to Savino *et al.* (2018), direct uniaxial tensile tests are preferred to indirect ones because their estimated strength could be affected by the size effect and test setup. Conversely, the direct method is challenging to ensure evenly distributed stresses throughout the cross-section and control a stable load versus displacement/crack opening response (Wille, El-Tawil, and Naaman, 2014). In addition, direct test response may present local stress effects, such as premature failure and relative rotation of the specimen ends, invalidating the post-cracking response (Graybeal and Baby, 2013). One of the indirect tests is the splitting tension test, which, in UHPC, may present the first crack opened approximately at a third of the specimen height and a wedge rupture that is different than is expected per the theory of elasticity (Savino *et al.*, 2018). Voit and Kirnbauer (2014) utilized a wedge-splitting method to evaluate the fracture energy and correlate it with the bending tensile strength to deduce tension strength parameters. The analytical models for UHPC tensile behavior may be divided into the micro and meso-scale models and the macro-scale models (Yang, Joh, and Kim, 2012). The first analyzes the fibers individually

in conjunction with the fiber-matrix interfaces, and the second considers the average actions of all the fibers.

The tensile response of UHPC may be analyzed and modeled from the stress transfer at the fiber-matrix interface (Zhou and Qiao, 2019). It may be divided into modeling the matrix's tensile behavior, the pullout behavior of a single fiber, and the fiber bridging behavior. According to Zhou and Qiao (2019), the matrix tensile response is quite brittle, with an initial stage of elasticity before the first crack and then softening until fracture. The matrix post-cracking tensile may be expressed by a linear, bilinear, exponential, or power curve (Zhou and Qiao, 2019). The pullout behavior may be divided into three regions depending on the stress level: perfectly bonded, partially bonded, and fully debonded and frictional slip region. Each region has equations to express the force-slip relationship. The fiber bridging behavior is determined by integrating the contribution of all fibers in the UHPC matrix. It is commonly expressed as the function of the slip, fiber orientation angle, and fiber embedment length (Zhou and Qiao, 2019). Figure 44 presents the validation of the model developed by Zhou and Qiao (2019).

Figure 44: Comparison of experimental and analytical tensile responses of UHPC with different fiber volume fractions
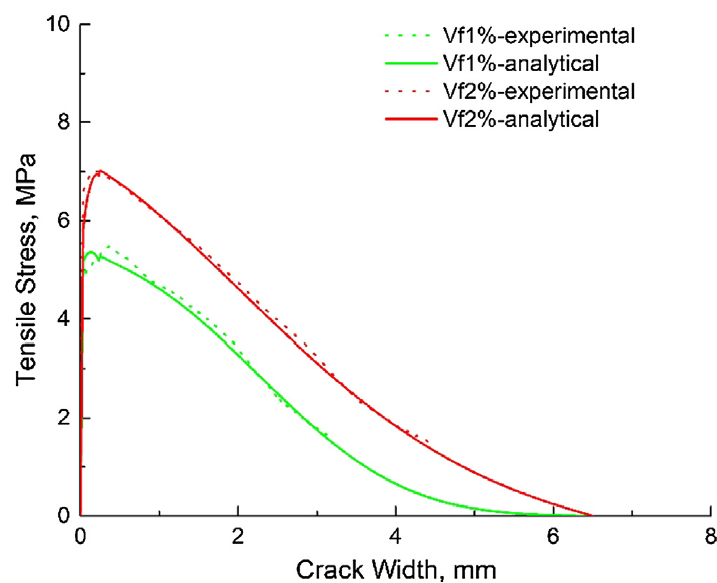
Source: Zhou and Qiao (2019)

Wille, El-Tawil, and Naaman (2014) presented a typical tensile stress-strain curve and divided it into three parts. Part I is the strain-based elastic part, determined by the initial tensile behavior (E_{cc}); part II is the strain-based strain hardening part, determined by the dissipated energy per unit volume ($g_{f,A}$); and part III is the crack opening-based softening part, characterized by the dissipated energy per crack surface area ($G_{F,B}$), as shown in Figure 45. A bi-linear tensile curve may characterize the model up to softening, and the authors present the equations to determine the parameters necessary to define it.

Figure 45: Strain hardening tensile behavior of UHPC and idealized modeling approach
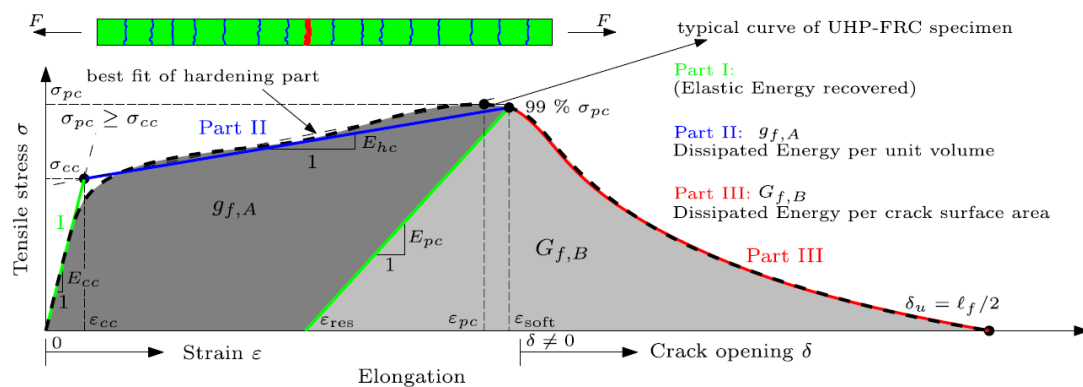
Source: Wille, El-Tawil, and Naaman (2014)

To analyze the UHPC tensile behavior at high strain rates Pyo, El-Tawil, and Naaman (2016) evaluated the cracking and post-cracking strength, energy absorption capacity, and strain capacity with different strain rates. As shown in Figure 46, specimens loaded at a high strain rate presented remarkable peak strength and strain capacity, which indicates UHPC utilization for impact and blast resistance. In addition, the material presented a strain rate insensitivity under quasi-static load. According to Zhou and Qiao (2020), tensile strength under quasi-static load may increase up to 10% due to the strain rate. Pyo, El-Tawil, and Naaman (2016) determined the average tensile stress in the fibers and suggested using high-strength fibers to ensure a good impact response because the fiber is heavily loaded during impact.

Figure 46: Rate effect on UHPC stress-strain tensile response
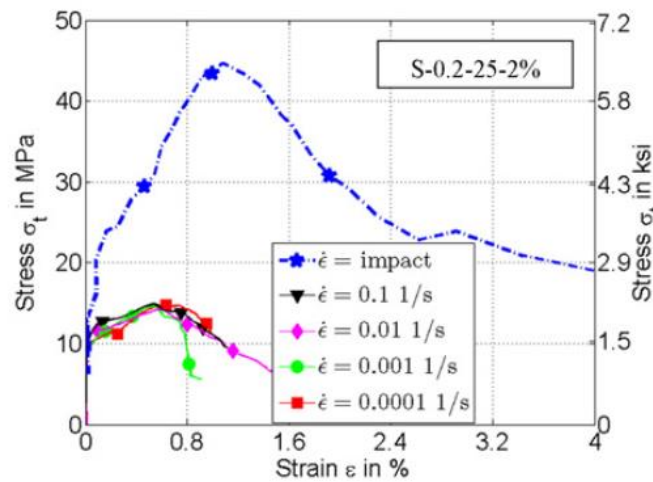
Source: Pyo, El-Tawil, and Naaman (2016)

2.10 FLEXURAL BEHAVIOR

Combining the improved UHPC compressive and tensile behavior, the flexural tends to associate both and enhance the structural performance. The flexural behavior is similar to the tension with the microcracks formation that increases the strain capacity and with the elastic, hardening, and softening stages (Singh et al, 2017; Qiu *et al.*, 2020). Figure 47 presents a UHPC average flexural load-deflection curve with a deflection-hardening behavior.

Figure 47: UHPC flexural load-deflection curve
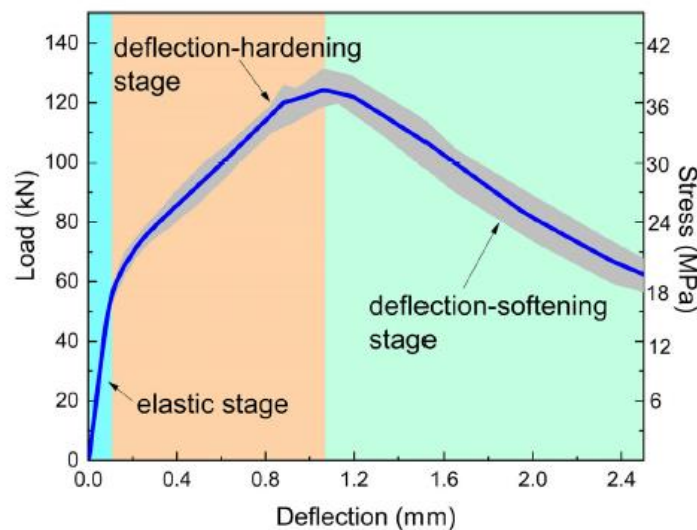
Source: Qui *et al.* (2020)

2.10.1 Bending tests

Prismatic specimens are utilized in evaluating the flexural behavior of UHPC. They are also employed as an indirect method to determine the tensile stress-strain diagram. According to Meng *et al.* (2017), the notched three-point bending test is easy to conduct and has more cracking stability since the notch helps localize the fracture plane. Despite the simplicity of the indirect methods, the test response presents some inconsistencies. Three-point bending test shows values for modulus of rupture 10% higher than the four-point test, and an unexpected crack may arise in the vicinity area of the notch (Savino *et al.*, 2018). Four-point tests have shown that the deflection is influenced by the formation of shear cracks outside the pure bending region (Savino *et al.*, 2018). As examples of difficulties using the flexure test as a tensile behavior indirect method, Graybeal and Baby (2013) present the concern of the complexity necessary to back-calculate the uniaxial behavior and the undesirable multiple cracking behaviors that occur in a notched specimen. It is important to note that in the bending and tension tests, the rate of actuator displacement does not lead to the same strain rates due to the different strain distributions in each sample (Meng *et al.*, 2017).

Wille and Parra-Montesinos (2012) evaluated the size of the prismatic specimen, casting method, and support conditions in flexural tests. They observed a nearly identical behavior for a medium (102 × 102 × 406 mm) and large (152 × 152 × 508 mm) specimen size, with a slightly higher bending strength at the former. A high speed in a casting with a back-and-forth movement led to a thin layer with a preferred fiber alignment along the beam axis, increasing flexural strength. As expected, the specimens with high-friction support presented higher bending strength than the low-friction supports due to the horizontal friction reaction force, which increases the section moment of resistance, overestimating it (Wille and Parra-Montesinos, 2012).

Meng *et al.* (2017) studied the effects of the notched beams' loading rate and notch-to-depth ratio (N/D) on flexural performance. As presented in Figure 48, the flexural strength increases with higher loading rates. It may be partially attributed to the increase in matrix-fiber interfacial bond strength, justified by the single fiber pullout response at different loading rates (Meng *et al.*, 2017). Conversely, the N/D increase causes a reduction in the peak load by up to 78%

at high loading rates. The authors observed a relation between the two parameters analyzed and mentioned that the effect of the N/D on the flexural strength may be amplified by applying higher loading rates. The same trend is noted in the fracture energy analysis.

Figure 48: Load-deflection curves of notched beams with different loading rates
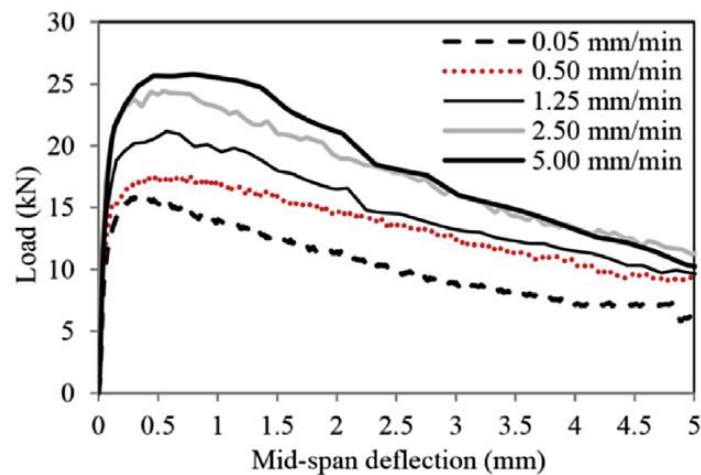
Source: Meng *et al.* (2017)

2.10.2 Reinforced beams

To evaluate the UHPC usability in structural elements is necessary to test reinforced specimens subjected to bending. The practical differences start with the shear reinforcement that restricts the material free flow and alters the placement method, which may disturb the orientation and dispersion of the fibers (Singh *et al.*, 2017). In addition, the rebar's presence affects the bending moment and the crack formation in the beams (Yang, Joh, and Kim, 2012). According to Qiu *et al.* (2020), the reinforced UHPC beams flexural behavior may be divided into elastic, crack development, and yield stages. The first exhibits a linear relationship between the load and mid-span displacement. Then, the second refers to a crack development stage until the yield load. At this point, a noticeable increase in the number of cracks is observed, and its width grows more rapidly (Singh *et al.*, 2017). Lastly, the third stage is characterized by the peak load and a significant displacement increase due to the steel fibers' pullout and the fiber bridging's failure. As expected, the fibers resist the crack opening, allowing the

beam to take a further load until it reaches the ultimate moment capacity, even after the reinforcement is yielded (Singh *et al.*, 2017).

Qiu *et al.* (2020) evaluated the crack development in the reinforced UHPC beams. It may be a maximum tensile strain indication because the crack spacing is inversely proportional to this parameter (Graybeal, 2008). Concerning the crack spacing and width, the authors observed a decrease when the reinforcement ratio increased, and conversely, an increase when the UHPC cover thickness was raised. They compared codes and guidelines for predicting the crack width in UHPC and fiber-reinforced concrete components. Mostly, they provided an acceptable agreement with the mean crack spacing and the measured crack widths.

Yang *et al.* (2020) studied the behavior differences between reinforced beams with UHPC and HSC. Concerning the failure mode, the authors observed an abrupt failure by concrete crushing in the compressive zone in HPC and a collapse due to a major crack in UHPC, which widened remarkably after the rebar yield until the rebar fracture. Due to the high stiffness of the UHPC beam, as a result of the denser microstructure of the matrix and the presence of the steel fibers, it exhibited a superior flexural strength, capacity, and rigidity compared with the HSC beam (Yang *et al.*, 2020).

Shafieifar, Farzad, and Azizinamini (2018) conducted a parametric study with different section sizes, reinforcement ratios, and effective depth ratios. In addition, the authors analyzed the efficiency of analytical equations to predict the ultimate moment capacity. Varying reinforcement ratio and effective height of the section, different failure modes were observed, including flexure, shear-flexure, and shear failure (Shafieifar, Farzad, and Azizinamini, 2018). Concerning the analytical equations, it is essential to consider the tension contribution to not underestimate the moment capacity of UHPC elements, leading to conservative design results.

2.10.3 Inverse analysis

The inverse analysis is a method to determine the tensile stress-strain relationship through indirect tests such as flexural. It requires a cross-section

analysis with an iterative routine based on the equilibrium conditions and compatibility. Sometimes it is accompanied by a predefined stress-strain relationship for UHPC compression, tension, and rebar (Yang *et al.*, 2020). Furthermore, it may be determined by a point-by-point analysis or simplified curves based on the experimental key points. In the former, the method progressively builds the constitutive law in each loading step (López *et al.*, 2015). According to Baby *et al.* (2012), simplified curves are convenient for design issues or finite elements model analyses. For the four-point bending test, it is necessary a transformation of the deflection into curvature, and then the moment-curvature curve will be converted into the stress-strain relationship (Baby *et al.*, 2012). The mechanical properties of UHPC influence the moment-curvature relationship, and the nonlinearity of the UHPC is significant (Yang, Joh, and Kim, 2012).

Baby *et al.* (2012) presented a four-point bending test inverse analysis proposal with two LVDTs on the bottom face to obtain the tensile strain. The main difference from other methods is that the midspan strain at the extreme tension fiber is not derived from the deflection, and a mechanical assumption is not applied. Compared to the proposed author's method, a simplified inverse method presented a slight strength overestimation and a strain underestimation that may have been induced by the assumption of uniform stress and by deflection into curvature conversion (Baby *et al.*, 2012). Compared with a DTT, the developed method slightly overestimates the strength and underestimates the post-cracking stress. The authors noted that these differences might occur due to the orientation of fibers in flexural tests and the specimen size effect.

López *et al.* (2015) developed an analytical moment-curvature closed-form formulation for a four-point bending test inverse analysis method. After transforming the mid-span deflection in curvature, the method applies an iterative process, minimizing the error between the experimental and analytical curves by varying the constitutive tensile parameters (López *et al.*, 2015). Compared with previous inverse analysis methods, the authors reproduced an experimental result with good precision analytically, including the descending loading branch. Furthermore, the shear deflection was a differentiator in calibrating the model well, especially the elastic modulus and first cracking tensile stress (López *et al.*,

2015). Although there is good agreement between the analytical and experimental curvatures, the tensile law obtained with the proposed method differs from a DTT. Therefore, other aspects must be evaluated because the inverse analysis methodology developed attempts to reproduce the test response. The difference in correspondence between the proposed method and the DTT may occur due to specimen size, way of casting, and fiber distribution (López *et al.*, 2015).

In Qian and Li (2007) and Qian and Li (2008), the authors presented a method to determine the tensile properties and strain capacity based on master curves developed from a parametric study of several four-point bending test responses. The first master curve was drawn from the direct relation between strain capacity and deflection capacity, as shown in Figure 49a. It depends on the specimen's geometry and is utilized to obtain the normalized modulus of rupture (MOR) according to the second master curve presented in Figure 49b. The second master curve is not recommended for using a tensile strain capacity of less than 0.5% due to the steep slope at the initial stage (Qian and Li, 2008). In addition, the hardening modulus in tension is considered zero to facilitate the inverse process and minimize the unknowns. The inverse method utilizes the data from the four-point bending force-deflection response to determine the equivalent strain capacity by the master curve and then the normalized MOR. Calculating the MOR as a function of the maximum moment, it is possible to determine the constant post-cracking tensile stress, due to the hardening modulus null, and then draw the simplified stress-strain relationship.

Figure 49: Master curves to determine the tensile strength by an inverse
method
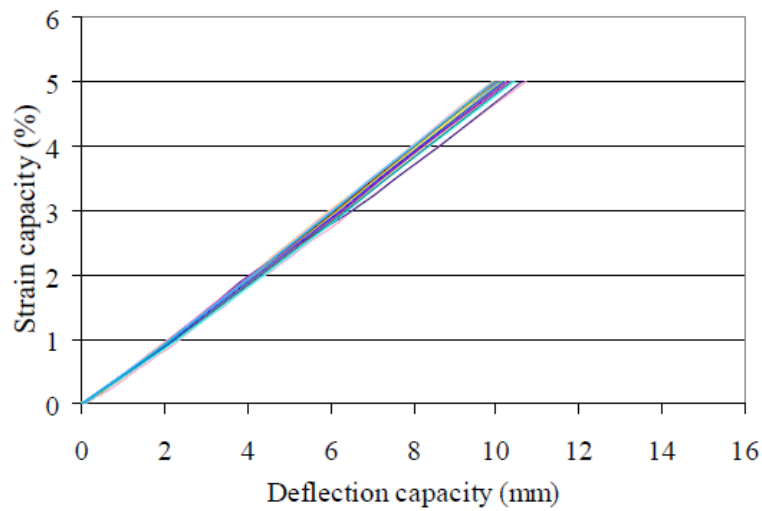
(a)
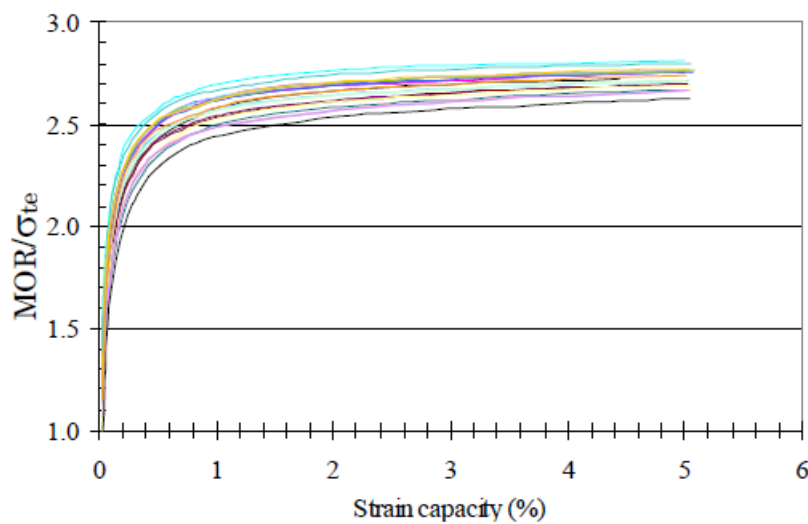
(b)

Source: Qian (2007); Qian and Li (2008)

Soranakom and Mobasher (2008) developed a closed-form solution for the
moment-curvature diagram to predict the load-deflection response of a fiber-
reinforced composite's four-point bending test. The localization of the major crack
was simulated as an average response over the crack spacing to correlate the
stress-crack width relationship to the stress-strain approach and then determine
the moment-curvature diagram (Soranakom and Mobasher, 2008). The method
is defined according to the material parameters as first cracking tensile strain
(ε_{cr}), tensile (E) and compressive (E_c) modulus, post-cracking modulus (E_{cr}),

tensile transition strain (ε_{trn}), ultimate tensile (ε_{tu}) and compressive (ε_{cu}) strain, compressive yield strain (ε_{cy}), and some normalized parameters, as presented in Figure 50. In addition, the deflection at mid-span is calculated by the numerical moment-area method of discrete curvature between the support and mid-span, presented in Soranakom and Mobasher (2007) (Soranakom and Mobasher, 2008). The back analysis is done interactively by altering the material parameters until the load-deflection predicted curve approximates the experimental curve. As a result, a simplified tensile stress-strain is defined with the selected material parameters. The authors pointed out that the flexural indirect and uniaxial tensile responses may diverge due to the difference in stress distribution between the uniaxial tension and bending tests.

Figure 50: Material models for homogenized fiber-reinforced concrete: (a) compression model and (b) tension model

(a) (b)
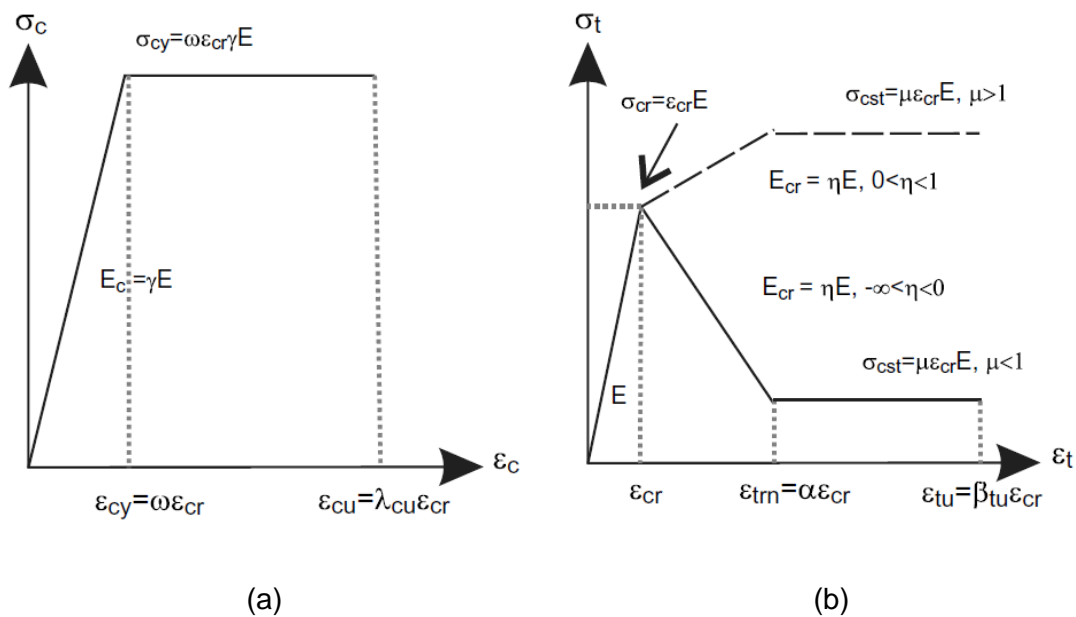
Source: Soranakom and Mobasher (2008)

As currently one of the primary references to UHPC design, the French standard NF P 18-470 (AFNOR, 2016) presents a step-by-step inverse method to four-point and three-point bending tests on notched prims. For the former type, the equations to convert the load-deflection response in stress-strain are

presented in Annex E. It considers the nonlinearity of the moment-curvature curve after yielding and the equilibrium conditions expressions to determine the relative depth of the neutral axis, stress, and strain under the corresponding moment-deflection. This process requires a high level of mathematical solution, and software must be utilized to solve the incremental analysis. The end of the annex presents a simplified representation of a bi-linear diagram with a plateau in the post-cracking region, as shown in Figure 51a. The step-by-step three-point bending test inverse analysis is presented in Annex D with the recommendations for bending tests on prisms. The tensile post-cracking law (stress-crack opening) is determined by the equilibrium conditions considering the cracked section, as shown in Figure 52. A simplified linear piecewise constitutive tensile curve may be defined according to the conventional law presented in NF P 18-710 and shown in Figure 51b. For converting the post-cracking law into a stress-strain diagram, the crack opening is divided by the minimum of 2/3 the section high and twice the length of the longest fiber contributing to non-brittleness (AFNOR, 2016).

Figure 51: Simplified stress-strain law for the inverse method of (a) four-point bending test (NF P18-470) and (b) three-point bending test (NF P18-710)
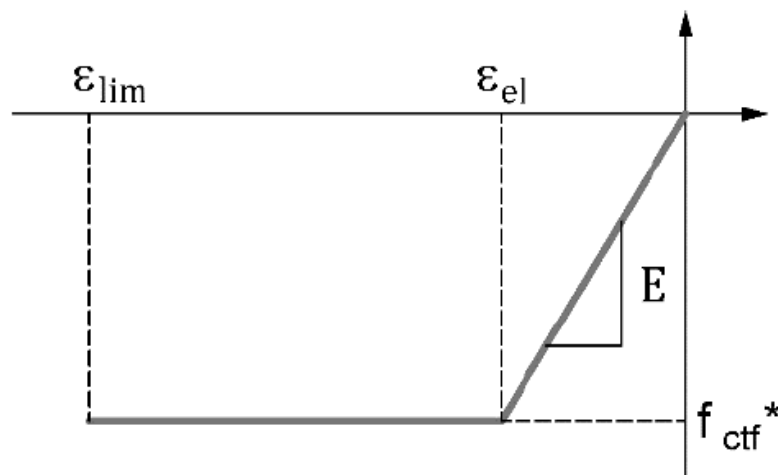
(a)
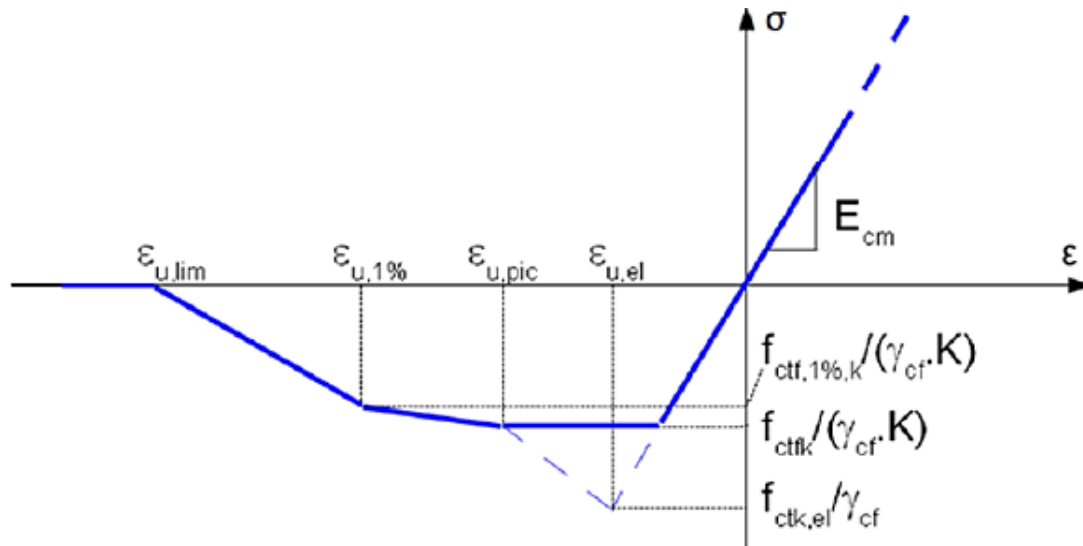
(b)

Source: AFNOR (2016)

Figure 52: Distribution of deformations and stresses over the cracked and non-cracked parts of the section depth
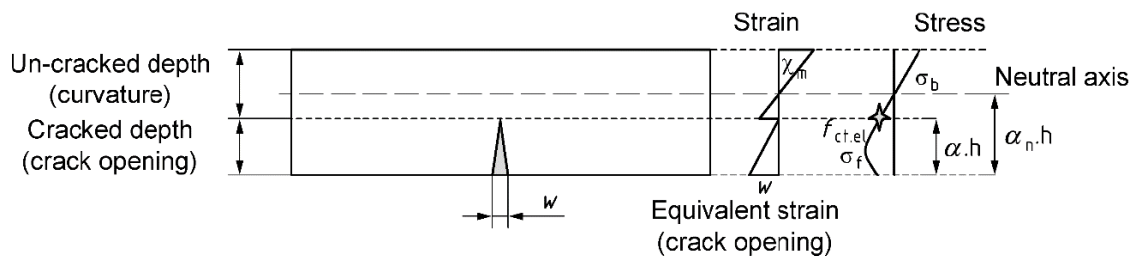
Source: AFNOR (2016)

According to Uchida *et al.* (2005), the Japan Society of Civil Engineers (JSCE) recommends an inverse analysis to obtain a simplified tensile stress-strain curve from the notched three-point bending test. The curve idealized utilizes the equivalent specific length (L_{eq}) to convert crack width to strain, as shown in Figure 53. It is determined from the flexural strength obtained by the numerical analysis using the stress-CMOD curve that is equivalent to the strength obtained by the section analysis using the stress-strain curve (Uchida *et al.*,

2005). The L_{eq} for a UHPC rectangular cross-section is calculated by Equation 27.

$$\frac{L_{eq}}{h} = 0.8 \cdot \left\{ 1 - \frac{1}{\left(1.05 + 6 \cdot \frac{h}{l_{ch}} \right)^4} \right\} \qquad (27)$$

where, l_{ch} is the characteristic length ($\approx 1.06 \times 10^4$ mm), and h is the height of the section. According to Yoo, Banthia, and Yoon (2016), the w_{1k} parameter is the crack width for which a certain stress level is retained after the first crack, and w_{2k} is the crack width at zero tensile stress. In addition, the JSCE recommends 0.5 mm and 4.3 mm for w_{1k} and w_{2k}, respectively (Yoo, Banthia, and Yoon, 2016). Therefore, the first cracking tensile strength (ft) is the tensile stress corresponding to a 0.5 mm crack width.

Figure 53: Idealized JSCE tensile stress-strain curve
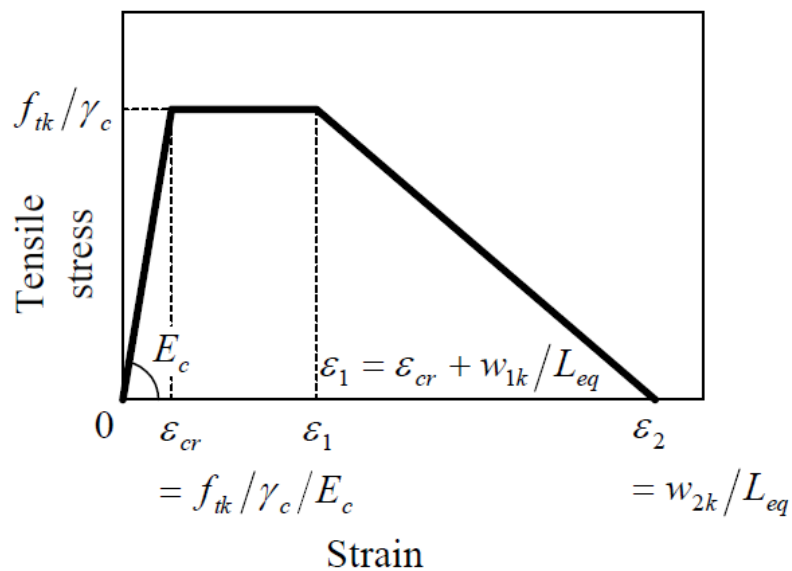
Source: Uchida *et al.* (2005)

2.11   SHEAR

As expected, the UHPC shear resistance is affected by the fiber volume and span-to-depth (a/d) ratio. Compared with CC, the UHPC shear capacity is, on average, 3.5 times higher, and the mid-span deflection is at least 2.5 times greater—that is, more ductile, as presented in Figure 54 with responses of beams without shear reinforcement and longitudinal reinforcement designed to avoid bending failure (Pourbaba, Joghataie, and Mirmiran, 2018). The ductile behavior occurs due to the presence of fiber, as with tension performance. According to Ngo *et al.* (2017), shear failure occurs when the a/d ratio varies between 0.4 and 0.7; after that, flexure failure predominates. In addition, Figure 55 presents a typical shear failure. Pourbaba, Joghataie, and Mirmiran (2018) compared the experimental shear strength results and the responses of ACI 318 and RILEM predictive models, and observed that the models are very conservative, with values of 3.79 and 3.72 times higher, respectively. They highlighted the need to develop more accurate UHPC shear prediction models.

Figure 54: Shear strength load-deflection response curves: UHPC-B21 to B24 and CC-B25 to B28
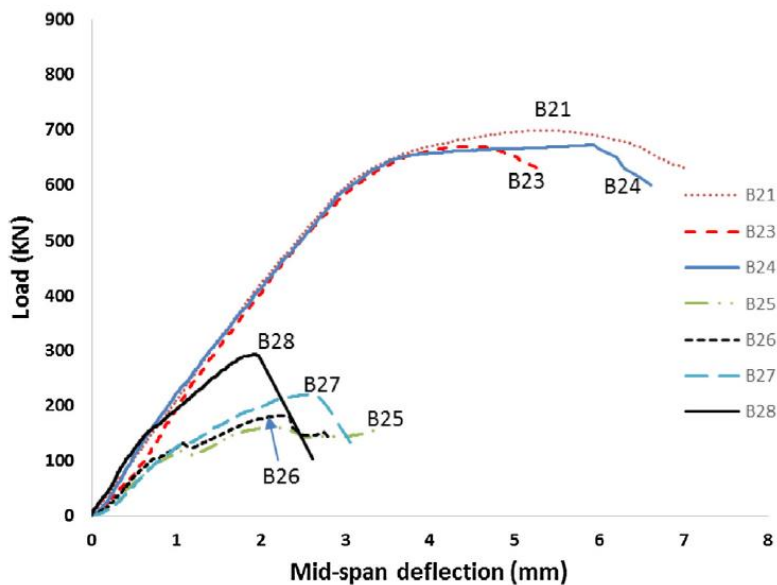
Source: Pourbaba, Joghataie, and Mirmiran (2018)

Figure 55: Cracking behavior of UHPC during the shear test

Source: Ngo *et al.* (2017)

Ngo *et al.* (2017) evaluated the shear resistance of UHPC, varying the a/d ratio. As presented in Figures 56a and 56b, the shape of the curves depend on the fiber volume and a/d ratio. An initial linear branch is observed due to the first cracking resistance, followed by a non-linear stage resembling strain-hardening behavior, similar to the tension curves presented in Figure 44. In addition, the authors idealized a typical shear stress-strain response, presented in Figure 56c. Interestingly, a few fiber contents, such as 0.5%, present the same hardening behavior of a larger amount, different from the tension behavior that is more sensitive to the fiber volume. This difference is attributed to the various fiber bridging mechanism modes. In tension, it is mostly the fiber pullout, while in shear, it's the dowel effect of short fibers that cross the cracked section (Ngo *et al.*, 2017).

Figure 56: Average shear stress-strain curves of UHPC: (a) a/d = 0.4, (b) a/d = 0.8, and (c) typical model
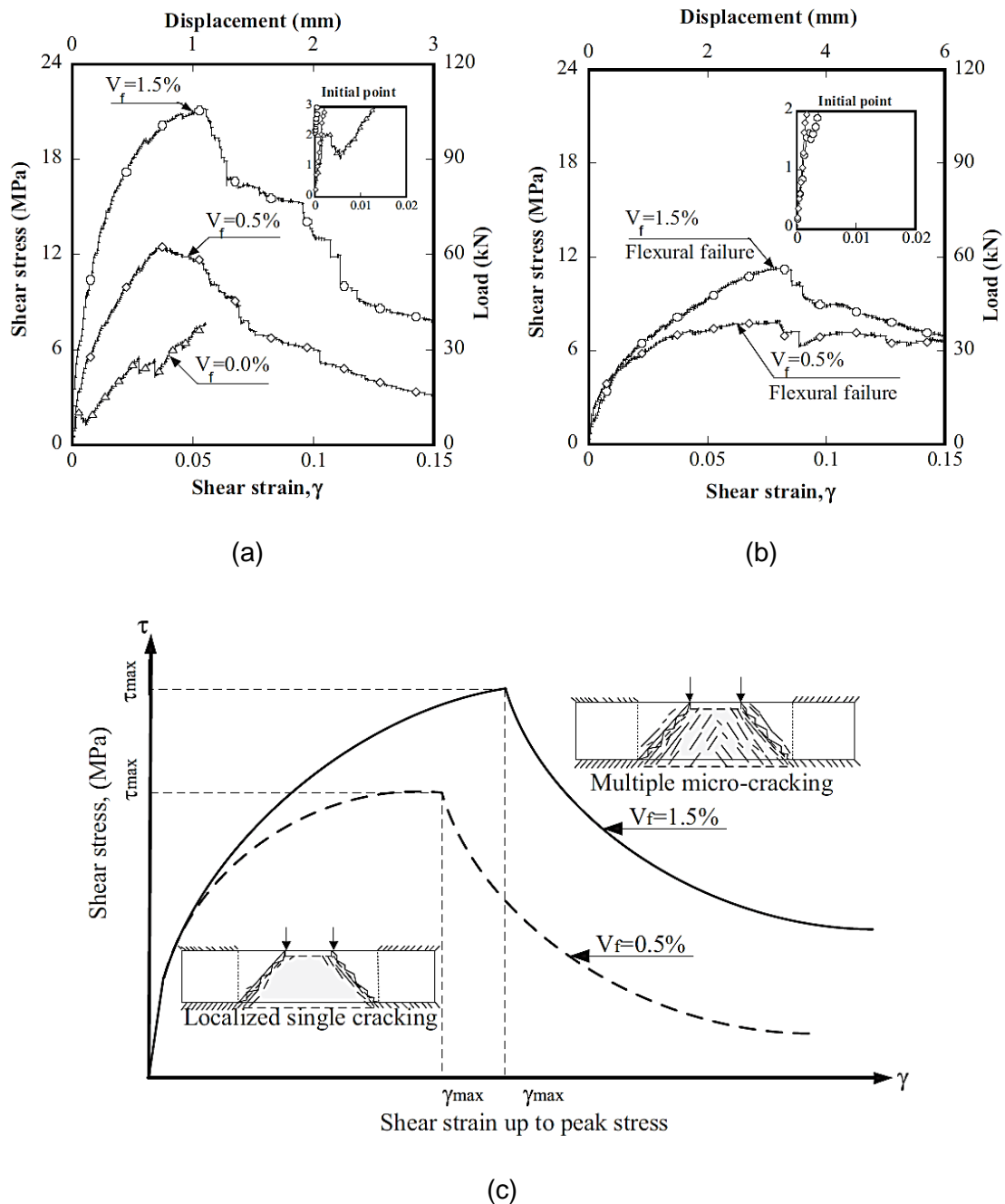
Source: Ngo *et al.* (2017)

2.12   PUNCHING SHEAR

The UHPC's improved mechanical characteristics allow the development of progressively slender structures, which may be subject to punching shear, e.g., flat slabs. The material may usually be applied in connections between CC

elements, as reinforcement in critical shear zones and NC-UHPC composite slabs. Replacing CC entirely in flat slabs, the UHPC presents the first crack strength and ultimate strength more than two times higher, but using it monotonically is costly (Qi *et al.*, 2021). A UHPC partial area with a full depth and perimeter located at a distance equal to the slab thickness from the loading plate face was deemed the optimal application of UHPC in flat slabs (Zhou, Qi, and Wang, 2023).

In the work by Zhou, Qi, and Wang (2023), a composite NC-UHPC slab with a UHPC area with full-depth and enclosed by a perimeter located at about one to two times of slab thickness from the loading plate face presents a combined punching shear-flexural failure mode and more ductility, indicating better safety and ability of energy dissipation. The punching shear failure plane's angle in UHPC ranges between 20° and 45° (Qi *et al.*, 2021). In addition, the increase of UHPC coverage area may increase the strength of the slabs on cracking, yield, and ultimate state, along with the post-cracking deformability, as shown in Figure 57.

Figure 57: Load versus center deflection curves to flat slabs with normal concrete (C), UHPC (U), and composite NC-UHPC increasing UHPCs areas (CU 0–3)
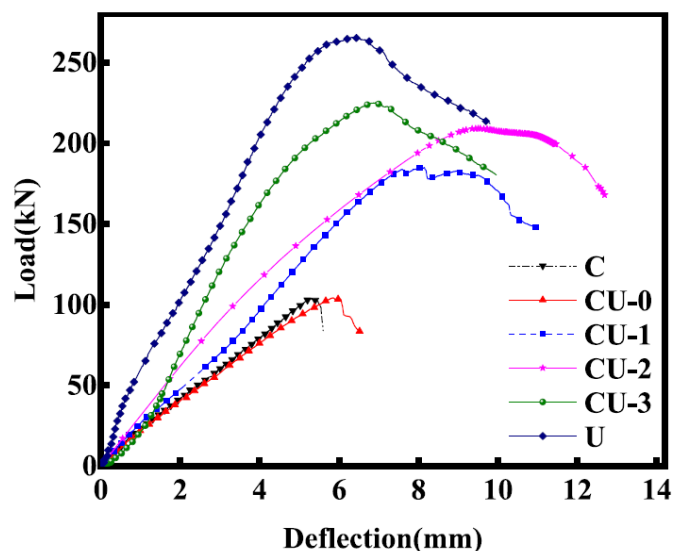
Source: Zhou, Qi, and Wang (2023)

Qi *et al.* (2021) studied the punching shear behavior of flat slabs composed of CC, UHPC, and CC-UHPC hybrid with partial-depth on compressive zone and full-depth. Concerning the failure mode, the CC and partial-depth hybrid types presented a punching shear failure, whereas the others combined punching shear-flexural failure. As expected, increasing the UHPC area may effectively enhance the slab's strengths and stiffness; therefore, the full-depth hybrid slabs have better responses, followed by UHPC ones. In addition, the application of full-depth hybrid CC-UHPC showed comparable energy dissipation ability in comparison with the entire UHPC slab (Qi *et al.*, 2021).

According to Bastien-Masse and Brühwiler (2016), a UHPC layer as an external tensile reinforcement for reinforced concrete (RC) can increase the punching shear resistance by at least 69% without modifying its rotation capacity. The authors developed a model to predict the force-rotation behavior and the punching shear resistance of a composite UHPC-RC slab. The contribution of a UHPC layer to the punching shear depends on the thickness of the layer and the tensile strength (Bastien-Masse and Brühwiler, 2016).

2.13 TORSION

UHPC presents a noticeable torsion resistance due to high compression and tension strength in all directions provided by its macroscopic homogeneity. As expected, the UHPC improves the post-cracking behavior, particularly after the peak torque—different from the CC without steel reinforcement, which fails abruptly by crushing (Yang *et al.*, 2013). Figure 58 presents the behavior of a UHPC beam subjected to a pure torsion load. The cracking behavior is similar to tension with multiple cracking, on all section perimeter almost simultaneously. In addition, the UHPC beams exhibit small crack widths for the ultimate torque level (Yang *et al.*, 2013).

Figure 58: Torque-twist curve of a UHPC beam with 2% fibers content
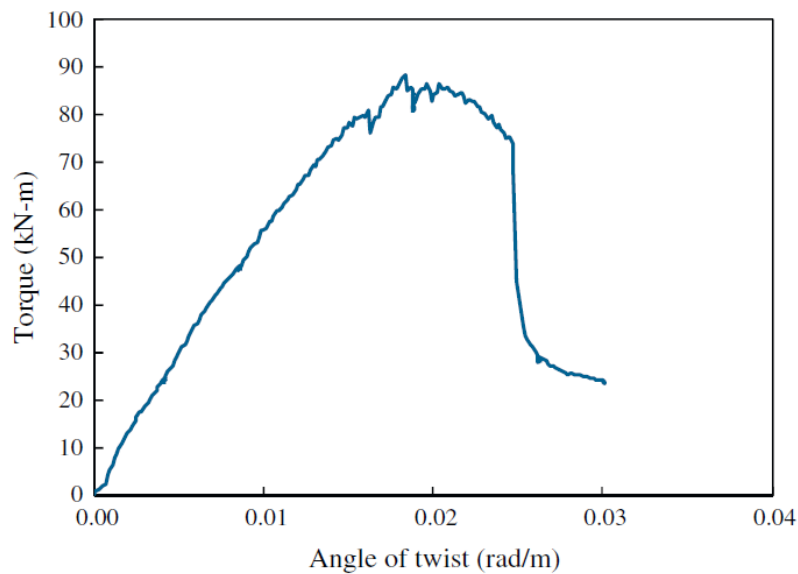
Source: Yang *et al.* (2013)

According to Yang *et al.* (2013), the cracking and ultimate torsional strength increased as the steel fiber content and the cracked torsional stiffness increased. The authors evaluated the response modifying transverse and longitudinal reinforcement ratio in the UHPC beams. The ultimate torsional strength increased as the stirrup and longitudinal steel ratios increased, but the influence of the stirrups ratio was more significant. In addition, transverse and longitudinal reinforcement affected the angle of the diagonal compressive stress (Yang *et al.*, 2013).

Mohammed, Bakar, and Bunnori (2016) evaluated the UHPC in the jacketing technique, varying the thickness and position of the material layer. Figure 59 demonstrates that beams strengthened with UHPC jackets improved the torsional moment up to 267% with a 25 mm layer, in addition to the twist angle in comparison to the control beam. The possibility of cracks can be remarkably reduced because the UHPC matrix initially prevents cracking (Mohammed, Bakar, and Bunnori, 2016).

Figure 59: Torque-twist curve of beams with UHPC full wrap varying the thickness in 10 mm to 25 mm (F10–F25)
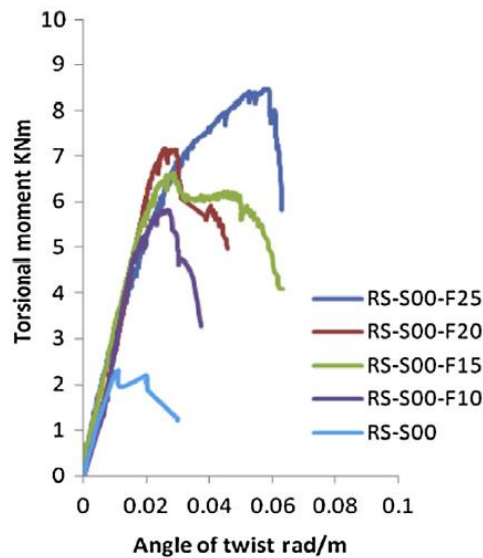
Source: Mohammed, Bakar, and Bunnori (2016)

2.14   CONCLUDING REMARKS

An appropriate selection of materials and procedures is essential to achieve the UHPC's mechanical and durability properties. The binder choice depends on the particle size, chemical composition, and dispersion medium. Aggregates and fillers are limited by particle size and shape. Fibers are primordial to UHPC performance; and their geometry, volume, and material type may affect the ductile response. The material fresh properties depend on the utilization of PCE with the appropriate dosage.

The quantity of each constituent material is influenced by particle packing, workability, and indirectly, density. The better possibility is to choose particle sizes in which the smaller grains fill the space between bigger grains. In addition, using materials with pozzolanic activity improves the material microstructure.

Besides the material selection, the correct material design and mixing procedures may influence the UHPC properties. The packing methods look for the proportions of each material based on the PSD and workability, seeking a minimum porosity and maximum density. With regard to the mixing procedures, depending on the equipment type, better material dispersion involves the mixing

duration, speed, and sequence. Unconventional production methods may enhance the UHPC properties, for instance, pre-setting pressure and thermal curing.

UHPC mechanical properties provide a range of structural-element possibilities characterized by a notable post-peak behavior. The high compressive strength enables elements with small sizes and high capacity. The ductile behavior of the tension allows large displacements with satisfactory stress levels. These enhanced properties directly improve the flexural, shear, and torsion behaviors.

3 CHARACTERIZATION AND DEVELOPMENT OF AN UHPC

This topic presents the methodology for assessing each component material and procedures to select the best for the UHPC mix dosage and production. The materials suppliers and the research laboratories are all located in the Sao Paulo state, as seen in Figure 60. The objective is to produce a UHPC mixture with local materials and available regular laboratory equipment, seeking better properties with them.

The individual component analysis starts with the collection procedure to choose the smallest particle material available without any impurities. Initially, a physical test was performed to determine the specific density, and then the chemical composition was examined. Due to the presence of small-sized particles, agglomeration problems were verified and worked to avoid them. In addition, all the characterization tests were performed according to the Brazilian standards and compared with the literature parameters.

The second step of the UHPC development is to define the mixture proportions and make a trial batch. The PSD and each material's specific density configure the Modified Andreasen and Andersen method for packing the particles. In addition, a high mixture energy must be provided, and the mixture procedure stages may affect the material properties. The placement, consolidation, demolding, and curing procedures followed the Brazilian concrete and NF P18-470 French standards. After the trial batch, some adjustments were necessary to achieve the desired properties.

In the end, the mechanical behavior was characterized by compression, splitting, and flexural tests. These tests were performed mainly according to NF

P18-470 (AFNOR, 2016) besides the Brazilian concrete standards and with available local laboratory equipment. In addition, workability and durability tests were developed to characterize the material's physical behavior.

Figure 60: UHPC raw materials suppliers (yellow arrow) and research laboratories (blue arrow) in Sao Paulo state
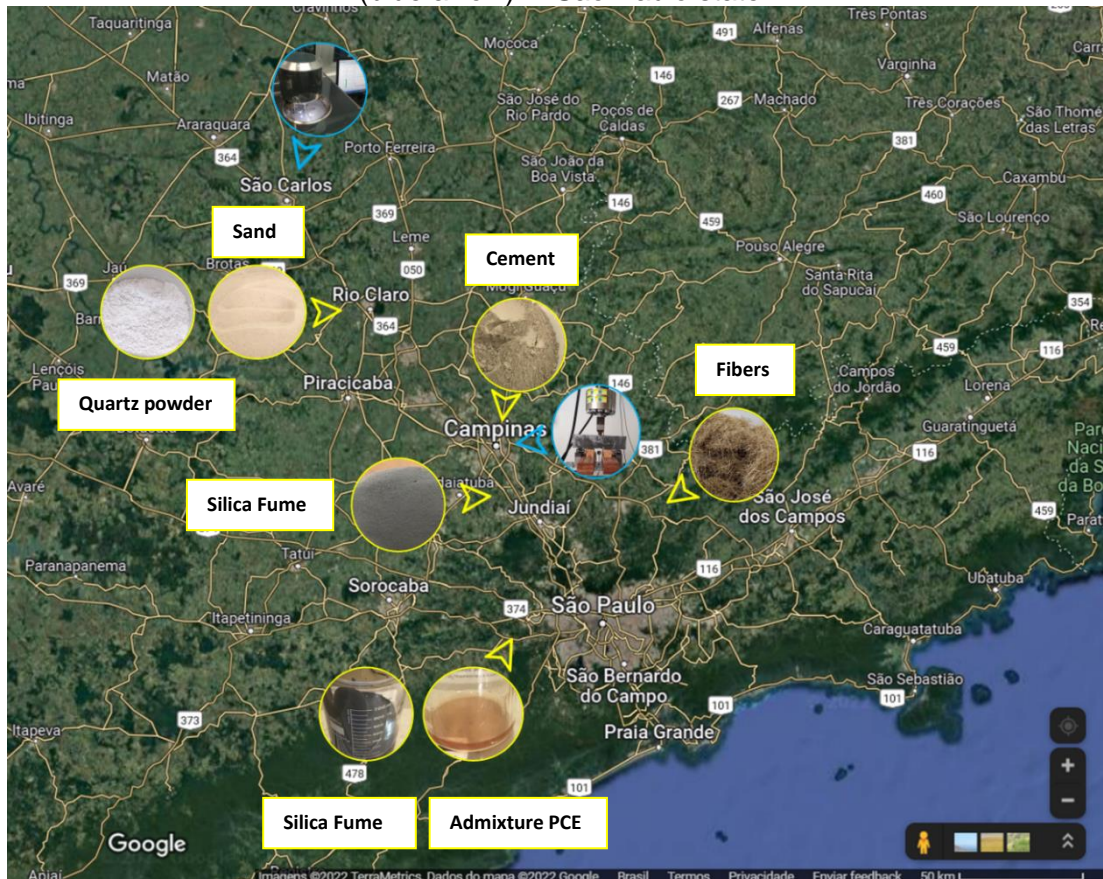
Source: Author

3.1 MATERIALS

The first task in producing a UHPC mixture is to select the available suppliers in the vicinity to facilitate the pickup of the materials. Sao Paulo is the Brazilian state with the most significant number of industries and biggest engineering research centers, easing this process. The studied references may present an initial idea of the necessary characteristics of the UHPC component; however, these must be physically and chemically analyzed, and advanced equipment is necessary due to the materials' specificity. In addition, the supplier must provide a quality test report for high-industrialized materials, such as the polycarboxylate superplasticizer. The mix design is based on these

characterization analyses, and the simple component selection may improve the UHPC properties. This triage is developed until the UHPC achieves the aimed strength. The selection criteria and local materials available are detailed in the following topics.

3.1.1 Cement

As an industrialized material, the characteristics of cement are predictable, and its selection consists of the type definition. In Table 1, the Brazilian cement types with smaller particles are CP II-F and CP V. This parameter is essential for a better material packing density. Due to the last presenting a higher compressive strength, it was selected to compose the UHPC mixture. The PSD curve is presented with other components in the mix design topic. The mean primary particle size (d50) was 9.714 μm. To analyze the alkalis and SO_3 content, the chemical composition of the utilized cement was obtained with an XRF spectrometry. A Rigaku Ultima IV diffractometer was utilized, and the response is presented in Table 4. The composition exhibits a moderate percentage of SO_3, close to Table 2 material, and low alkalis amount, where Na_2O is absent due to very low quantity. This response validates the parameters required for the cement to produce the UHPC mixture.

Table 4: Cement CP V chemical composition

Chemical Element	%	Oxides	%
Al	2.207	Al_2O_3	3.297
Si	10.317	SiO_2	17.111
S	3.340	SO_3	6.131
K	0.812	K_2O	0.673
Ca	77.090	CaO	67.844
Ti	0.326	TiO_2	0.306
Fe	3.904	Fe_2O_3	3.117
Sr	0.309	SrO	0.201
In	1.695	In_2O_3	1.319

Source: Author

The physical parameter determined was the specific density. The Brazilian standard NBR 16605 (ABNT, 2017) presents the methodology to perform the test, as shown in Figure 61. The specific density determined was 2.941g/cm³. A visual examination to seek cement lumps is done before every dosage. The material must be stocked correctly to avoid this problem, and its expiration date must be verified.

Figure 61: Cement-specific density test

Source: Author

3.1.2 Silica Fume

The better local SF was defined from the minimum physical and chemical standards requisites and the particles' agglomeration presence. To base the selection, all suppliers provided the material quality test report. In particular, the Brazilian standard NBR 13956-1 (ABNT, 2012) presents the requirements for SF used with Portland cement, as seen in Table 5.

Table 5: NBR 13956-1 SF chemical and physical requirements (%)

Requisite	Limit
SiO$_2$	≥ 85,0
Humidity	≤ 3,0
Ignition loss	≤ 6,0
Solid content in aqueous dispersion	± 2% producer reference
Performance index with Portland cement at 7days	≥ 105

Fineness #325	≤ 10,0

Source: ABNT (2012)

The material was analyzed in the dry state and in an aqueous medium, as presented in Figure 62. Due to the tiny particle size, the SF has an agglomeration tendency, and a visual analysis must be done before the dosage in the first state material. This agglomeration modifies the packing idealized by the PSD models, increasing the size and decreasing the surface area. SF in an aqueous medium eliminates this problem but is more expensive. It is important to advise that the material in suspension is comprised of 50% solids and 50% water, and this water content must be deducted from the mixing water (MC Bauchemie, 2020). Table 6 presents the dry-state supplier parameters within the limits of Brazilian standard. The PSD was determined with a d50 equal to 2.223 μm. As with cement, the specific density was defined 2.039g/cm³, according to the NBR 16605 (ABNT, 2017).

Figure 62: SF in (a) a dry state and (b) an aqueous medium

(a)

(b)

Source: Author

Table 6: SF in dry state chemical and physical parameters (%)

Test	Value
SiO2	96,00
Ignition loss	1,70
CaO	0,50
MgO	0,30

Source: TECNOSIL (2019)

The UHPC mixture with the dry state SF presented agglomeration problems identified in the trial batch's fractured samples and the compressive test cylinder flattened surfaces by the diamond-end grinding machine, as shown in Figure 63. Theoretically, if the SF is mixed with the sand in an initial mixture stage, the aggregate will assist in deagglomerating, but this method was ineffective. An attempt was made to manually break the particles' agglomeration, but it was not feasible because the material adhered to the recipient. Therefore, this study preferred the SF in the aqueous medium to minimize this issue, improving the UHPC properties. The next chapter presents the benefits of this choice in compressive strength as part of the design adjustments. As recommended by the supplier, the preservation of patterns of color and smell indicates whether the material is applicable for the mixture.

Figure 63: Dry SF agglomeration in the mixture
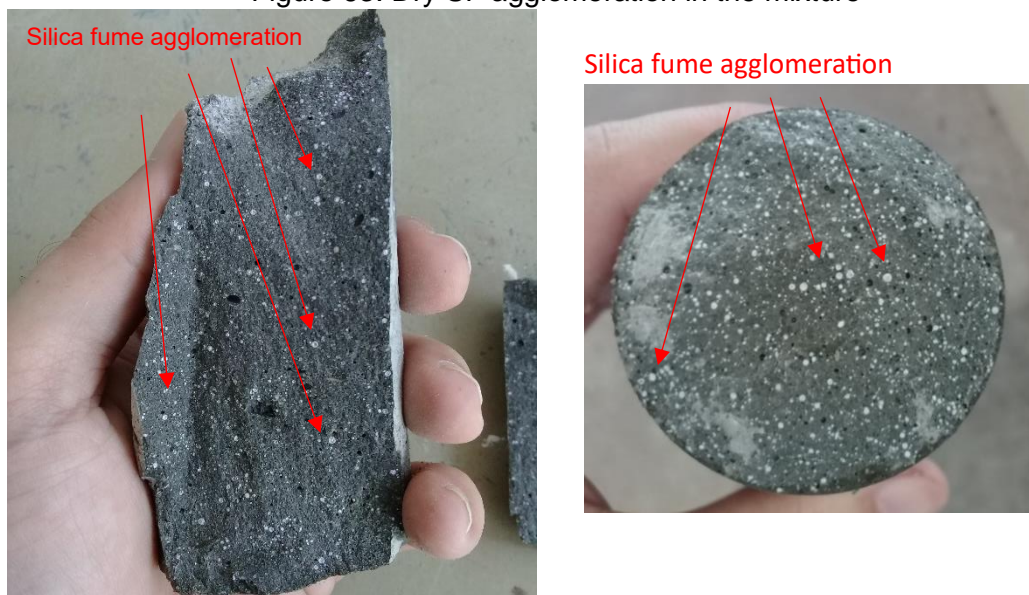
Source: Author

3.1.3 Aggregates

Although sand is a common raw material in concrete production, for UHPC mixture, it needs to be free of any contaminant and have its moisture known. The aggregate utilized in this work is composed of quartz, as Richard and Cheyrezy (1995) recommended. The material received beneficiation to diminish the impurities as with sieving to reduce the maximum particle size. The supplier's material mineralogical and chemical composition report is presented in Table 7.

The NBR 7211 (ABNT, 2009) exemplifies the harmful materials in the sand for concrete as the micaceous, ferruginous, and expanding clay minerals, everyone identified in low quantity in the selected material. Before each dosage, the sand was dried in a laboratory oven to avoid the modification of the mixing water content. The specific density was 2.656g/cm³ defined according to NBR 16916 (ABNT, 2021), as shown in Figure 64.

Table 7: Mineralogical and chemical composition of the quartz sand

SiO$_2$	99.77%	Li	3 ppm
Al	393 ppm	Mg	15 ppm
B	< 1 ppm	Mn	10 ppm
Ba	4 ppm	Na	56 ppm
Ca	42 ppm	Ni	< 1 ppm
Co	< 3 ppm	P	6 ppm
Cr	< 1 ppm	Sr	< 1 ppm
Cu	< 1 ppm	Ti	186 ppm
Fe	272 ppm	V	< 1 ppm
K	85 ppm	Zr	19 ppm

Source: BMRC (2023)

Figure 64: Sand-specific density test

Source: Author

The grading was analyzed, obtaining the maximum aggregate size of 500 µm, d50 of 93.489 µm, and 2.39 fineness modulus, calculated according to NBR 7211 (ABNT, 2009) with the material gradation curve. The Brazilian standard NBR NM 248 (ABNT, 2003) was consulted to realize the fine aggregate sieve analysis test. Furthermore, the supplier report classifies the material as a rounded shape with a sphericity index of around 0.8, as preferred by De Larrard and Sedran (1994) and shown in Figure 65.

Figure 65: Sand rounded shape
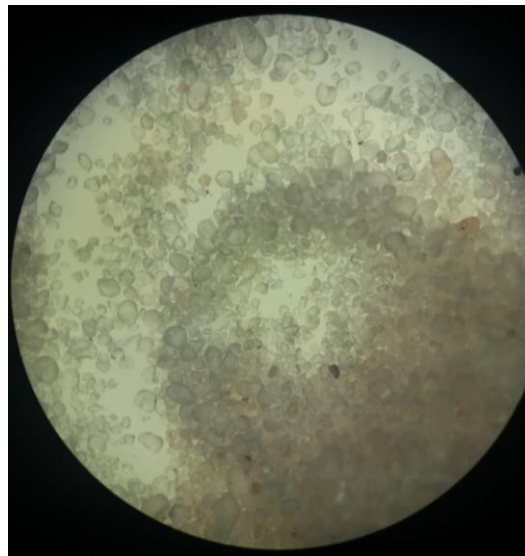
Source: Author

3.1.4 Filler

The filler has the function of improving the packing density. The material tested was a 325 mesh and d50 of 9.987 µm quartz powder, provided by the sand supplier with the same mineralogical and chemical composition. This material is produced by grinding sand particles, and the finest available was selected, considering that, according to the supplier, some smaller particle dimensions are manufactured by demand. The characterization developed was the specific density test, which resulted in 2.551 g/cm³, according to the NBR 16605 (ABNT, 2017), presented in Figure 66.

Figure 66: Quartz powder-specific density test

Source: Author

3.1.5 Fibers

Until today, there is only one supplier of high-strength steel microfibers in Brazil, commercially known as Dramix®. It is a high-carbon straight-steel fiber with 13 mm length and 0.20 mm diameter (65 aspect ratio), 2,160 MPa tensile strength, 210,000 Young's modulus, 7.85 specific gravity, and a bright surface (Bekaert, 2023). All the fiber characteristics comply with the material utilized in the studied references. The fiber ratio adopted was 2% by volume, as Richard and Cheyrezy (1995) suggested. No further characterization test was necessary to produce and analyze the UHPC mixture. Regarding storage, the supplier warns to keep the material dry and not stacked.

3.1.6 Admixtures

This work used an admixture to achieve the UHPC workability provided by the SF in an aqueous medium supplier. It is a methacrylic acid-based (MPEG) polycarboxylate superplasticizer (PCE) with a density of 1.12 kg/L and a recommended dosage between 0.2% and 5.0% by cement mass (MC-Bauchemie, 2020). The Brazilian standard NBR 11768-1 (ABNT, 2019) presents requirements for concrete admixtures, wherein, for high-performance superplasticizers such as PCE, the material needs to fulfill those shown in Table 8. The supplier's material report ensures that all standard requirements are satisfied. In the preliminary tests, the definition of the admixture dosage was the

least amount to make a self-compacting material. Initially, a small amount of additive was tested due to concerns about the formation of air bubble. The quantity was increased until the desired consistency was obtained, as shown in Figure 67. Hence, the value adopted was 3% of the PCE by cement mass. At another time, it was found that the mixture method may ease workability achievement.

Table 8: NBR 11768-1 Concrete superplasticizer admixture requirements

Minimal water reduction (%)		≥ 15.0
Air content increase (%)		≤ 2.0
Compressive strength multiplication index	7days	≥ 1.15
	28days	≥ 1.2
Setting time (min)	Start	≥ 30
	End	≤ 90

Source: ABNT (2019)

Figure 67: Progressive development of UHPC consistencies

Source: Author

Figure 68 presents a flowchart with a summary of the materials selection methodology.

Figure 68: Materials selection methodology flowchart
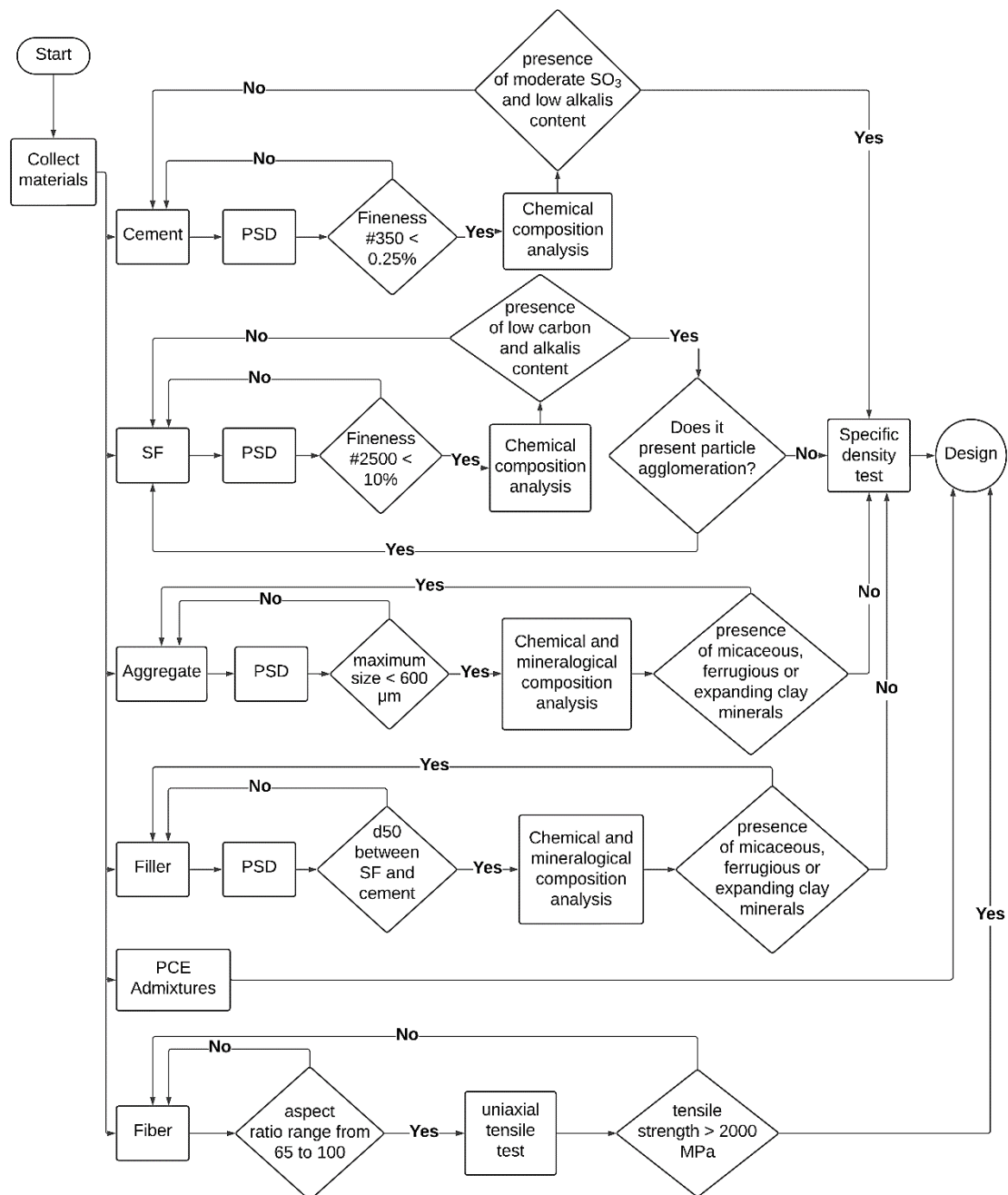
Source: Author

3.2 METHODS

Besides better material selection, the literature review presented that the production procedures may influence the UHPC properties. In addition, the physical and mechanical behavior must be tested to characterize the material as UHPC. These tests were performed with local laboratory equipment and followed the recommendations based on Brazilian and French standards. The production

procedures tested and the physical and mechanical tests performed are described in the following topics.

3.2.1 Mixture Procedure

The horizontal pan mixer utilized is a 0.55 kW three-speed with 10 liters of capacity, as shown in Figure 69. Its speed is divided into low (≈ 100 RPM), medium (≈ 180 RPM), and high (≈ 275 RPM), manually controlled.

Figure 69: Three-speed UHPC mixer

Source: Author

Initially, the three-stage mixture procedure was tested because it is the most commonly employed by the researchers. The mixture protocol followed the sequence:

- First, all dry materials (cement, SF, quartz powder, and sand) were mixed for 5 minutes at low speed, with material stepped placement. The sand and SF were initially mixed, hereupon the cement, and lastly, the quartz powder. Until then, the dry SF was tested.

- The water and superplasticizer were then added and mixed until the desired consistency was achieved. It started with medium speed and graduated to high when the material was no longer skipping off from the mixer.

At this moment, the fibers were not employed as the last mixture stage. The velocity of each stage was defined as the more highly feasible to give greater energy to the mixture. Although the material had good homogeneity and fluidity within the recommended superplasticizer dosage range in the first batches, seeking a higher compressive strength caused problems, such as poor workability, including a dry mixture shown in Figure 70. Another problem was the extended time in the last stage to achieve the desired workability, reaching 40 minutes.

Figure 70: Poor fluidity in three-stage mixture UHPC

(a)   (b)

Source: Author

Due to the workability issue in the mixing procedure trial to obtain a higher compressive strength, the four-stage mixture procedure was employed. The mixture protocol followed the sequence:

- First, half of the cement and the aqueous medium SF were mixed at low speed for 5 minutes. At this moment, the dry SF agglomeration was identified as a possible strength reducer; therefore, the aqueous medium one was changed.

- Then, the remaining cement with the water and superplasticizer were mixed at medium speed for 5 minutes.
- The sand was then added and mixed for 5 minutes at high speed. Lastly, the fibers were dispersed evenly and mixed for 5 minutes at high speed.

The four-stage UHPC mix sequence and mixture aspect are presented in Figure 71. It is possible to identify the mixture aspect and the time of each stage. Due to the better results achieved with this method with same three-stage mixture procedure materials, it was selected to be used to test with the fibers.

Figure 71: Four-stage UHPC mixture sequence

Source: Author

3.2.2 Placement and Consolidation

The UHPC specimen placement and consolidation may be similar to CC. According to NF P18-470 (AFNOR, 2016), the filling of the molds and compacting shall be adapted to the UHPC consistency. The compressive strength cylinders samples, 10 × 20 cm in dimensions, were placed by gravity with external vibration to eliminate the superficial bubbles. The flexural prisms samples, 10 × 10 × 40 cm in dimensions, were molded by the corner as recommended by the NF P18-470 (AFNOR, 2016) with external vibration, as shown in Figure 72. The molds size was chosen to respect the relation $a \geq 5 \cdot L_f$ (*a* being the smallest side of the mold and L_f the length of the longest fibers), to ignore the influence of the fiber orientation, in accordance to NF P18-470 (AFNOR, 2016). The primary trials to achieve the compressive strength were performed without fibers and a cylinder mold with dimensions 5 × 10 cm to save the material and cast a large number of samples.

Figure 72: UHPC prism placement sequence

Source: Author

3.2.3 Demolding and Curing

After being molded, the samples were covered with a plastic sheet (Figure 73a) to prevent rapid water loss and demolded after 24 h to cylinders and 48 h to prisms samples, as recommended for NBR 5738 (ABNT, 2015). The curing was developed for 28 days in a controlled temperature ($23 \pm 2°C$) and humidity (95%) chamber or immersed in a calcium hydroxide ($Ca(OH)_2$) solution (Figure 73b) with a controlled temperature ($23 \pm 2°C$), as recommended by the Brazilian standard.

Figure 73: UHPC conventional curing methods: (a) plastic sheet cover in a humid chamber and (b) samples immersed in a $Ca(OH)_2$ solution

(a)   (b)

Source: Author

3.2.4 Compression Test

The mechanical tests were performed mainly according to NF P18-470 (AFNOR, 2016), including the characteristics of the specimens, loading rate, and ending test criteria. Five-cylinder specimens with 5 × 10 cm dimensions were molded for compression tests without fibers at 7 days to evaluate the compressive strength evolution. In addition, three-cylinder specimens with dimensions of 10 × 20 cm were molded with fibers for compressive tests at 7 days and 28 days, with the number of specimens defined according to the horizontal

pan mixer capacity. The average values of the results of the samples were reported.

The main difficulty in obtaining the complete compression strain-stress response is the appropriate test velocity to not lose the post-peak descend branch. Sometimes, with a controlled-by-strain testing machine, the test duration is extended because of the small rate applied. This study utilized a hydraulic universal testing machine (HUTM) (MFL SYSTEME) with a 2000 kN capacity, controlled by force (Figure 74a), and the displacement was obtained externally by a Mitutoyo metric dial indicator with 0.01 mm graduation, as shown in Figure 74b. The entire test was recorded to pair up the testing machine's force-time response with the displacement measured by the dial indicator at every 0.5 sec, as shown in Figure 74c. The HUTM's oil flow control adjusts the test velocity and is sensitive to the load level and oil temperature, so correction must be done for every test and, sometimes, during it.

To evaluate the load rate sensitivity, two velocity ranges were tested: first with a loading rate between 0.4 MPa/s and 0.8 MPa/s, according to the NF P18-470 recommendations, and second ranging from 0.8 MPa/s and 1.15 MPa/s. In addition, the specimens were prepared according to NBR 5738 (ABNT, 2015), leveling the top and bottom surfaces (Figure 74d) checked with a steel set square. The elasticity modulus was determined according to NBR 8522-1 (ABNT, 2021), and the test setup is presented in Figure 75.

Figure 74: Compression test loading setup: (a) HUTM, (b) displacement indicator, (c) test recording, and (d) specimens with top leveled

(a)

(b)

(c)

(d)

Source: Author

Figure 75: The elasticity modulus test setup

Source: Author

3.2.5 Splitting Test

To evaluate the tensile behavior splitting test was performed. The test proceeded according to NBR 7222 (ABNT, 2011) in a servo-hydraulic compression machine (EMIC PC200 CS) with 2000 kN capacity, controlled by displacement and a loading rate of 0.05 ± 0.02 MPa/s (Figure 76). As with the compression test, three-cylinder specimens were molded for tests at 7 days and 28 days.

Figure 76: Tensile splitting test setup

Source: Author

3.2.6 Flexural Tests

In order to determine the tensile strength indirectly, a 4-point and notched 3-point bending test was performed in a servo-hydraulic bending machine (INTERMETRIC IM750SRV) with 500 kN capacity, controlled by displacement, and a loading rate of 0.1 mm/min and 0.06 mm/min, for 4-point and notched 3-point bending, respectively (Figures 77a and 77b). The bending test was performed at 28 days according to the NF P18-470 (AFNOR, 2016) recommendations for dimensions and preparation of specimens, loading rate, and test stop criteria. Four prisms were molded for each bending test type, with sizes 10 × 10 × 40 cm, considering a height between 7 cm and 20 cm and five and eight times the length of the longest fibers (13 mm). The loading rate definition considered the test duration, which implies the oil heat up and quantity of data per second.

Figure 77: Bending test setup: (a) 4-point bending and (b) 3-point bending

(a) (b)

Source: Author

3.2.7 Inverse Analysis

In the point-by-point inverse analysis, a mathematics-based software was utilized to solve the equilibrium and compatibility equations. Maplesoft and Microsoft Mathematics were tested. The former presented an effective method with the automatic routine to solve the equations simultaneously without splitting the terms. Due to the high quantity of data per second in each bending test, an average value was determined to limit the number of points for the inverse analysis. The load and deflection averages were calculated for each second in the four-point bending test. In the notched three-point bending test, the mean was determined by a moving average at each 0.02 mm crack width.

In a four-point bending test, the first stage to obtain the stress-strain relationship is to convert the load-displacement diagram into a moment-curvature diagram. At the midspan, the moment is easily calculated for each load value. According to the Euler-Bernoulli beam theory, the deflection is determined by the double integration of the curvature function. Knowing that the moment value is constant in the middle third of the span, the curvature is also constant. Therefore, the first integration transforms the constant curvature into a linear equation.

The second integration is difficult to determine without the boundary conditions, and then the trapezoidal rule was utilized as recommended in Baby *et al.* (2012). This curvature double integration process is summarized in Figure 78. The incremental procedure was used for the non-linear curvature determination, as presented in Figure 79. From the elastic relationship curvature equation (Equation 28), the theoretical midspan deflection is calculated and then compared with the experimental value, while the difference is not less than an acceptable error (10^{-6}), the curvature value is incremented in 0.00015. The midspan displacement is calculated by the area of the trapezoid, as presented in Figure 78. With the curvature value in each test point, the strain and stress are determined by the equilibrium and compatibility equations.

$$\chi = \frac{216 \cdot \delta}{23 \cdot p^2} \tag{28}$$

where χ is the curvature, δ is the midspan displacement, and p is the span.

Figure 78: Curvature double integration process

1st Integration

$f(x) = \chi \cdot x$

$f(x/2)$

$f(x/2-0.005)$

2nd Integration - Trapezoidal Rule = δ
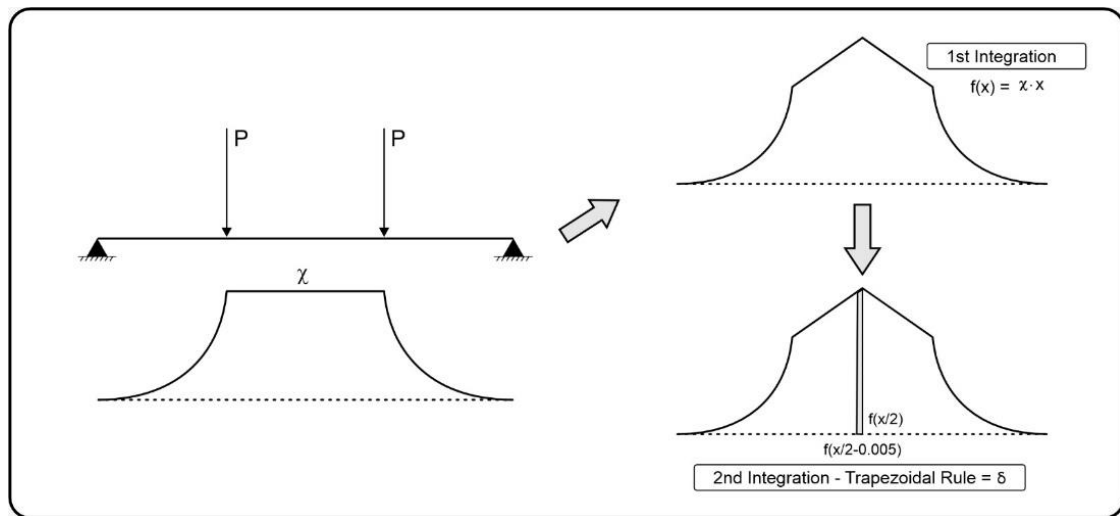
Source: Author

In a notched three-point bending test, the null value of CMOD is determined when the initial load stabilizes before it rises, subtracting the following clip-on gage measures by the value at this point. The inverse analysis equilibrium and compatibility equations utilize the pair load-CMOD to determine the stress in each point. After that, the crack width is converted to strain by dividing it by an equivalent specific length to obtain the stress-strain diagram.

Figure 79: Incremental inverse method from curvature
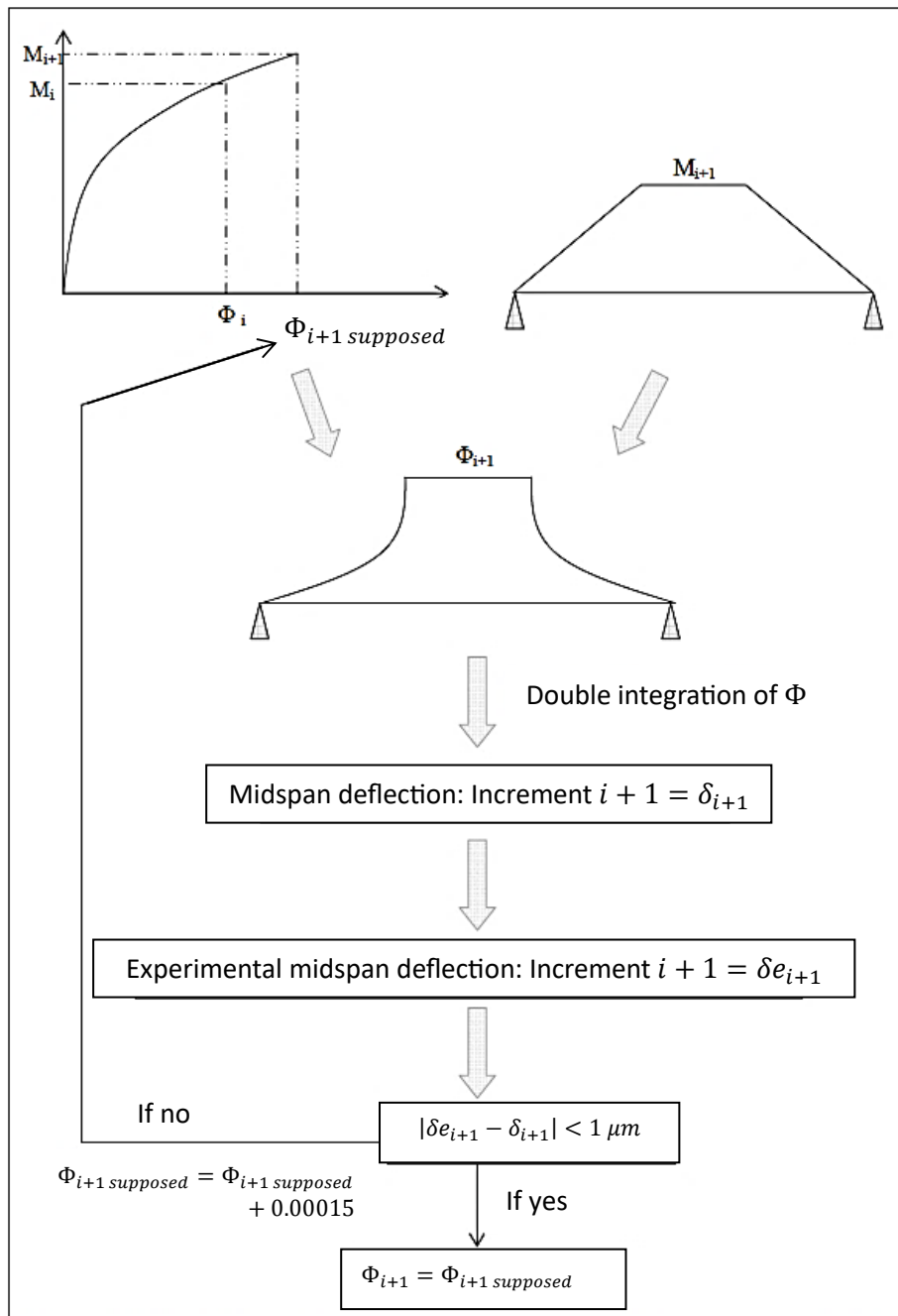
Source: Adapted from Baby (2012)

Due to the effortful point-by-point inverse analysis response, requiring sophisticated mathematical software and high labor time, which is proportional to the number of points, some simplified inverse analysis methods were tested. In the method employed by López *et al.* (2015), the curvatures were determined by the midspan deflection and utilized to calculate the moment by the closed-form moment-curvature formulation. Then, the constitutive tensile parameters were

adjusted to minimize the difference between the moment calculated and the experimental moment.

In the Qian and Li (2008) method, the master curves were utilized to determine the strain capacity and the effective tensile strength. The crack strain was calculated by Hooke law with the elasticity modulus and the ultimate strain by the maximum midspan deflection. It is important to note that the specimens were not tested until the complete rupture due to the test stop criteria. In the Soranakom and Mobasher's (2008) method, the initial material parameters were defined and utilized to determine the moments and curvature at incremental strain points, then the theoretical midspan deflection was calculated and compared with the experimental values. At the same time, the load obtained by the moment calculated in the method was compared with the test load. The material parameters were adjusted for which the method load-deflection curve fit the experimental curve.

In standards simplified methods proposed by AFNOR (2016), the four-point bending inverse analysis is simplified by a bi-linear curve and the notched three-point bending inverse analysis by a quadri-linear curve. The material parameters that compose the curves were defined as the equations presented in NF P18-470 and NF P18-710. According to NF P18-710 (AFNOR, 2016), the characteristic length to convert the CMOD into strain is equal to the minimum of two-thirds of the specimen height and twice the length of the longest fiber contributing to non-brittleness. The JSCE simplified method reduces the notched three-point bending inverse analysis in a tri-linear curve. The material parameters that constitute this curve were defined according to Uchida et al. (2005).

Due to the hardening behavior obtained in the bending test, the Wille, El-Tawil, and Naaman (2014) method was tested to determine a typical tensile stress-strain hardening curve. The empirical equations to define the material parameters utilize the fiber characteristics and suggested values for UHPC.

3.2.8 Compression and Flexural Damage Tests

Cyclic tests were performed in compression and 4-point bending to evaluate the UHPC damage behavior. The tests occurred at 28 days and were

molded with two cylinders with dimensions of 10 × 20 cm for the cyclic compression test and two prisms with dimensions 10 × 10 × 40 cm for the cyclic 4-point bending test. The cyclic test procedure developed in Krahl, Carrazedo, and El Debs (2018), presented in Figure 80, was adapted to perform the loading/unloading process by displacement but manually controlled. In addition, the tests were performed using a universal testing machine (EMIC DL 60.000) with a step of 0.05 mm for the loading and unloading stages. To not lose contact with the specimen, each unloading stage ended when the force dropped to 50 kN for compression and 10 kN for flexure. In addition, each loading stage ended when the force decreased after surpassing the maximum force in the previous unloading stage. The degradation was determined by the slope of the loading/unloading curve, and the damage variable (d) was calculated according to Equation 29.

$$d = 1 - \frac{S}{S_0} \qquad (29)$$

where S is the current loading/unloading slope of the damaged material, and S_0 is the initial loading/unloading slope or the maximum loading/unloading slope at a hardening behavior.

Figure 80: Cyclic loading procedure for tension tests
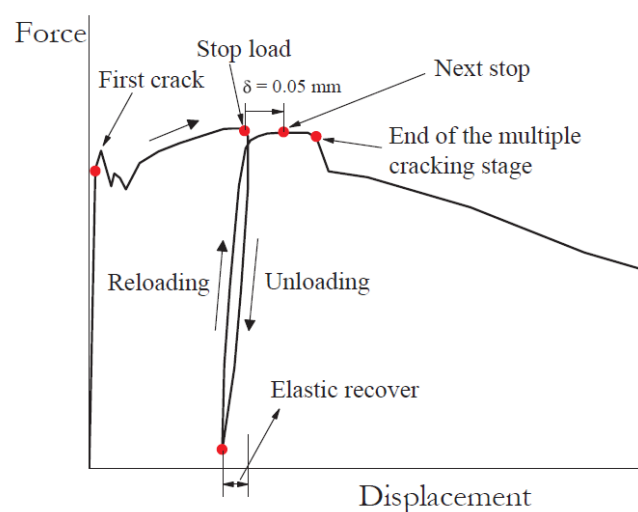
Source: Krahl, Carrazedo, and El Debs (2018)

3.2.9 Workability and Durability Evaluation Parameters Tests

According to NBR 15823-2 (ABNT, 2017), the slump-flow workability test was performed to verify the material spreading, flow duration, and visual stability index. The material was specified in the consistency classes based on Table 4 of NF P18-470 (AFNOR, 2016). It may be classified as C_a for self-compacting UHPC, C_v for viscous UHPC, and C_t for UHPC with flow threshold. In order to verify the self-compacting application requirements, the NBR 15823-1 (ABNT, 2017) employs the characteristics of the material flow to classify the spreading, the plastic viscosity, and the visual stability index classes. The test procedure sequence is presented in Figure 81.

Figure 81: UHPC workability test sequence

(a) (b) (c)
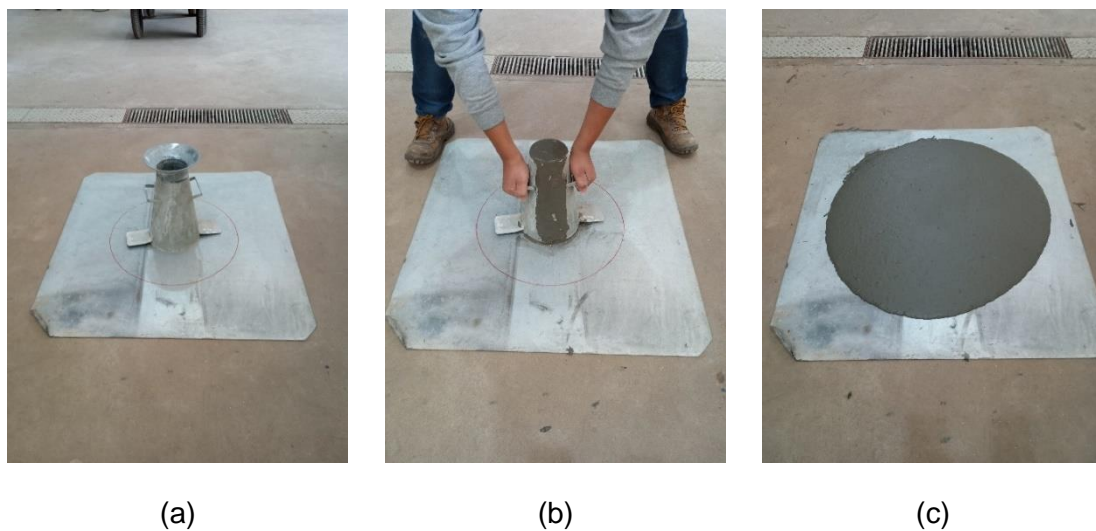
Source: Author

The durability of the UHPC mixture was analyzed in fresh and hardened states by determining the material porosity. The NBR 9833 (ABNT, 2008) presents the procedure for the gravimetric test method for fresh concrete to determine the unit weight, yield, and air content. Due to the UHPC fluidity, a mold for mortar test was utilized. The determination of water porosity in the hardened state utilized the NBR 9778 (ABNT, 2005). Both test samples are presented in Figure 82.

Figure 82: Air voids test determination: (a) in the fresh state and (b) in the hardened state

(a)   (b)

Source: Author

3.3 CONCLUDING REMARKS

In the material selection, simple criteria may assist in the better choice between local materials. The cement type must have the smallest particles, such as Brazilian CP V and preferentially moderate percentage of SO_3 and low alkalis amount. The SF, as an industrialized material, fulfills the requirements of the standards, but the agglomerations may be a problem solved with the material in the aqueous medium. As with cement, aggregates and fillers are chosen based on particle size to improve the material packing, and the presence of impurities must be observed not to compromise the quality of the mixture. The concern in selecting fibers and PCE is defining the amount to develop the UHPC ductile and self-compacting properties.

Concerning the methods to produce the UHPC, the available procedures and laboratory equipment were tested. To produce the UHPC, considering the utilized horizontal pan mixer, the four-stage mixture procedure was more efficient. The placement, consolidation, demolding, and curing methods followed the Brazilian and French standards recommendations. Finally, the physical and mechanical behaviors were analyzed according to standards recommendations for specimen size, loading rate, and ending test criteria. These parameters are

essential to obtain the complete mechanical behavior, including the post-peak descending branch. The workability and durability tests validate the self-compacting and low porosity material properties.

4   UHPC MIX DESIGN AND PHYSICAL AND MECHANICAL PROPERTIES

4.1 OVERVIEW

This topic presents the evolution of pursuing the best UHPC properties with local materials and the chosen composition's physical and mechanical study. It starts with the particle packing analysis of the mix design until the produced material's properties.

4.2 MIX DESIGN

The Modified Andreasen and Andersen method defined the mix design, calculating the proportion of each UHPC raw material. To determine the PSD of the powders (cement, SF, and quartz powder), the laser particle sizer FRITSCH Analysette 22 NanoTec was used, as shown in Figure 83. In addition, due to the bigger particle size of the sand, the sieving method was utilized in determining the PSD, according to the NBR NM 248 (ABNT, 2003).

Figure 83: Laser particle sizer
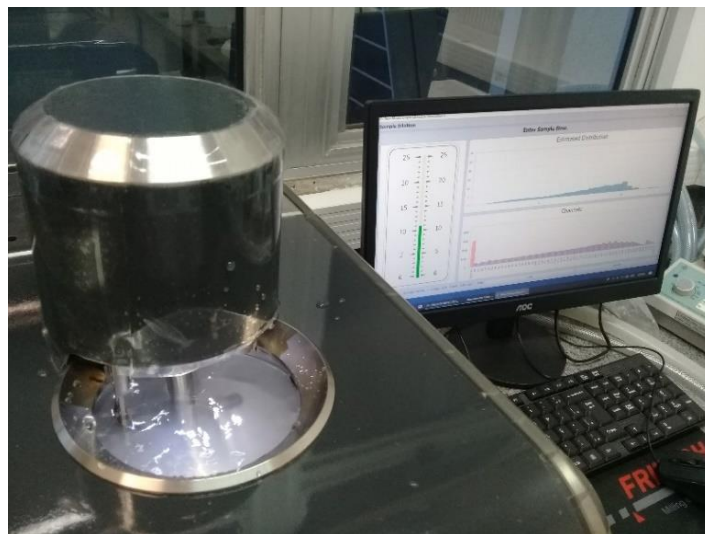
Source: Author

To calculate the amounts of the UHPC's component, each specific density (g) is necessary because they relate the PSD proportion with the material amount. In addition, the mean primary particle size (d50) is useful for a preliminary analysis of the particle sizes of the materials. In conjunction with the supplier material reports, the Brazilian standards NBR 16916 (ABNT, 2021) and NBR 16605 (ABNT, 2017) were used to calculate these parameters.

A spreadsheet with defined particle sizes to enter the cumulative percentage is sufficient to determine the proportion of each UHPC component that approaches the composed mix to the target curve. Adding the proportion of the percentages of each material in the defined particle size will totalize the 100% of solids. After defining the water-to-binder ratio, the percentage of water is added so that the mix proportions may be determined for all components, with the material consumption in kg/m³.

The primary composed mix curve determined with the Modified Andreasen and Andersen method is presented in Figure 84. The method parameters were D_{min}= 0.138 µm, D_{max} = 497.80 µm, and q = 0.23, achieving an RSS equal to 1770.21. The raw materials proportions were 875.24 kg/m³ of cement, 207.62 kg/m³ of SF, 913.48 kg/m³ of sand, 99.89 kg/m³ of quartz powder, and 216.57 kg/m³ of water. Table 10 gives the detailed mix proportions of UHPC concerning the weight of cement.

Figure 84: PSD of UHPC components
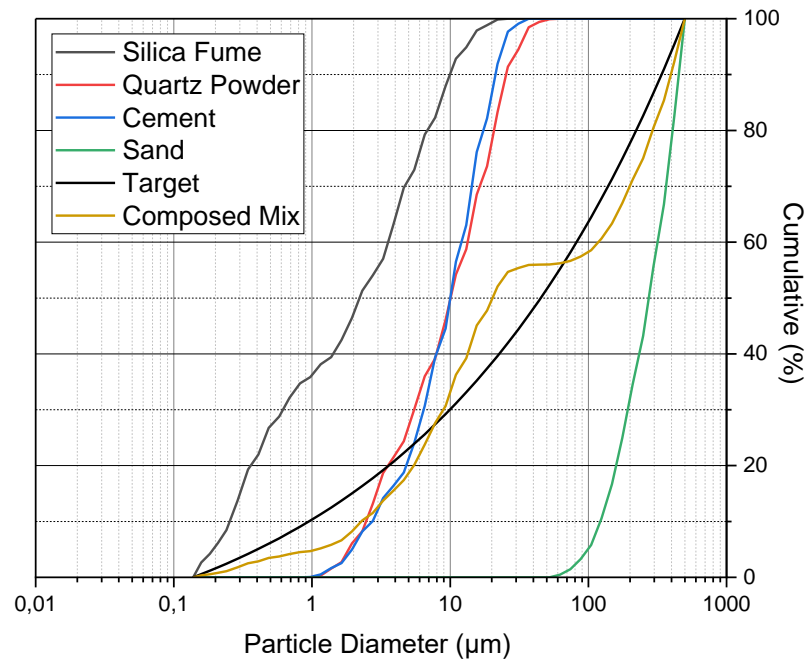
Source: Author

Table 10: Mix proportions of UHPC (mass/cement mass ratio)

Cement	Silica Fume	Sand	Quartz Powder	Water	Water binder ratio
1.0	0.237	1.044	0.114	0.247	0.20

Source: Author

Seeking the UHPC's mechanical response evolution, some adjustments in the mix proportions were made to improve the compressive strength. Every mix tried is described in the next topic, including the different procedures and materials tested. The main modification refers to reducing the water-to-binder ratio with increased cement, maintaining the other materials' amount. This strategy was effective until the occurrence of the workability problem, which was solved by changing the mixture procedure.

In addition, it was verified that the particle size of the quartz powder is similar to cement. Moreover, the thermal curing was discarded, considering the production of a UHPC with available laboratory equipment. Therefore, the quartz powder did not act as a filler or react to form hydration products. The solution was to remove it to consider the anhydrous cement benefit, including self-healing and

high compressive strength. The PSD of the UHPC without filler is presented in Figure 85. The composed mix has an RSS equal to 2166.16, and Table 11 gives the elaborated mix proportions with a 1076.90 kg/m³ cement consumption.

Figure 85: PSD of UHPC without filler (wf)
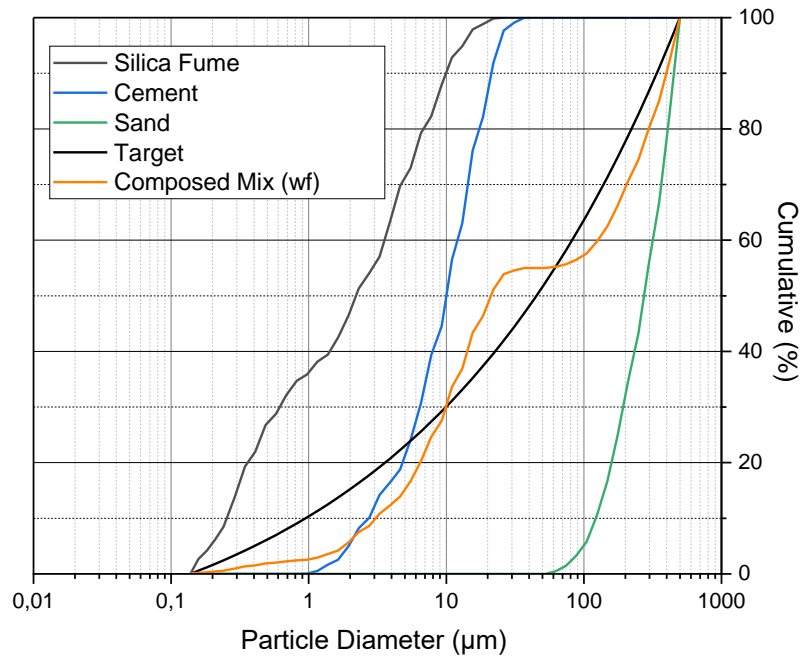
Source: Author

Table 11: Mix proportions of UHPC without filler (mass/cement mass ratio)

Cement	Silica Fume	Sand	Water	Water binder ratio
1.0	0.101	0.847	0.22	0.20

Source: Author

Finally, the last adjustment in the mix proportions was the increase in the cement consumption to reduce the water-to-binder ratio in the mixture without quartz powder. The final proportions are 1185.75 kg/m³ of cement, 108.86 kg/m³ of SF, 875.81 of sand, and 237.15 of water. The superplasticizer dosage was 3.0% by cement mass and 2.0% by fiber ratio by UHPC volume. Table 12 presents the mixture proportions of the definitive UHPC.

Table 12: Mix proportions of definitive UHPC (mass/cement mass ratio)

Cement	Silica Fume	Sand	Water	Water binder ratio
1.0	0.092	0.739	0.20	0.183

Source: Author

4.3 COMPRESSIVE STRENGTH

Compressive strength in each mix adjustment was tested at 7 d to evaluate the particle packing design model and some modifications in the material proportions and mixture procedures. The process was divided into four initial superplasticizer admixture adjustments and twelve material and procedures adjustments. The mixtures were named to indicate, in sequence, the specimen size (MS, 5 × 10 cm and CS, 10 × 20 cm); the superplasticizer admixture content; SF type (DSWT, dry silica without treatment; DSS, dry silica sieved; and SAM, silica in aqueous medium); the cement consumption in kg/m³; the water-cement ratio; and some test procedures (3S, three-stage mixture; 4S, four-stage mixture; WF, mixture without filler; ODS, oven-dried sand; and 2%F, 2% of fiber content). For example, MS4.0 [DSWT] - 870/0.247 (3S) indicates that the mixture has a specimen size of 5 × 10 cm, 4.0% of superplasticizer admixture, dry silica without treatment, 870 kg/m³ of cement consumption and a 0.247 water-cement ratio, and a three-stage mixture procedure. All the mixtures tested described are as follows:

- MS2.5 [DSWT] - 870/0.247 (3S): Initial particle packing design (Table 10) with 2.5% of superplasticizer.
- MS3.0 [DSWT] - 870/0.247 (3S): Initial particle packing design with 3% of superplasticizer.
- MS4.0 [DSWT] - 870/0.247 (3S): Initial particle packing design with 4% of superplasticizer.
- MS5.0 [DSWT] - 870/0.247 (3S): Initial particle packing design with 5% of superplasticizer.
- MS4.0 [DSS] - 875/0.247 (3S): Initial particle packing design with 4% of superplasticizer and the dry SF sieved to remove the agglomerated particles.

- MS4.0 [DSS] - 950/0.247 (3S): UHPC with the previous conditions, and the first cement consumption increased (950 kg/m³).

- MS4.0 [DSS] - 950/0.247 (4S): UHPC with the previous conditions and a four-stage mixture procedure.

- MS4.0 [DSS] - 950/0.2 (4S): UHPC with the previous conditions and a 0.2 water/cement ratio.

- MS4.0 [SAM] - 950/0.2 (4S): UHPC with the previous conditions and the aqueous medium SF.

- MS3.5 [SAM] - 1100/0.22 (4S-WF)[a]: Second particle packing design (Table 11) with the second cement consumption increase (1100 kg/m³) without the quartz powder and 3.5% of superplasticizer.

- MS3.5 [SAM] - 1185/0.2 (4S-WF)[a]: UHPC with the previous conditions and the third cement consumption increase (1185.75 kg/m³) to reduce the water/ cement ratio to 0.2.

- MS3.0 [SAM] - 1185/0.2 (4S-WF): UHPC with the previous conditions and 3% of superplasticizer.

- CS3.0 [SAM] - 1185/0.2 (4S-WF): UHPC with the previous conditions and specimen size 10 × 20 cm.

- CS3.0 [SAM] - 1185/0.2 (4S-WF-ODS): UHPC with the previous conditions with a 10 × 20 cm specimen size, and the sand dried in an oven to eliminate any humidity influence.

- CS3.0 [SAM] - 1185/0.2 (4S-WF-ODS-2%F): UHPC with the previous conditions and 2% of fibers added.

- CS2.5 [SAM] - 1185/0.2 (4S-WF-ODS-2%F): UHPC with the previous conditions and 2.5% of superplasticizer.

The initial evaluation in defining the optimum superplasticizer admixture content suggests that the gain in workability may improve the material density. In addition, a higher amount may reduce the compressive strength, as presented in Figure 86 and Table 13. The mixtures with 2.5% and 3% managed to produce the material. However, they were not self-compacting; therefore, it was necessary to test higher values. On the other hand, the superior limit of the supplier recommendation (5%) provides better workability but smaller compression

strength. Hence, a 4% superplasticizer content was initially defined as the optimum value with a higher 7 d mean compressive strength (70.40 MPa) and a self-compacting material. Another aspect noted was the increase in bubble formation with a higher amount of superplasticizer admixture, as presented in Figure 87. This problem may influence the material's mechanical response and was partially solved with a vibrating table. The following analysis studied the discrepancies in the values in the same batch and how to improve the material's compressive strength.

Figure 86: UHPC compressive strength at the superplasticizer adjustment
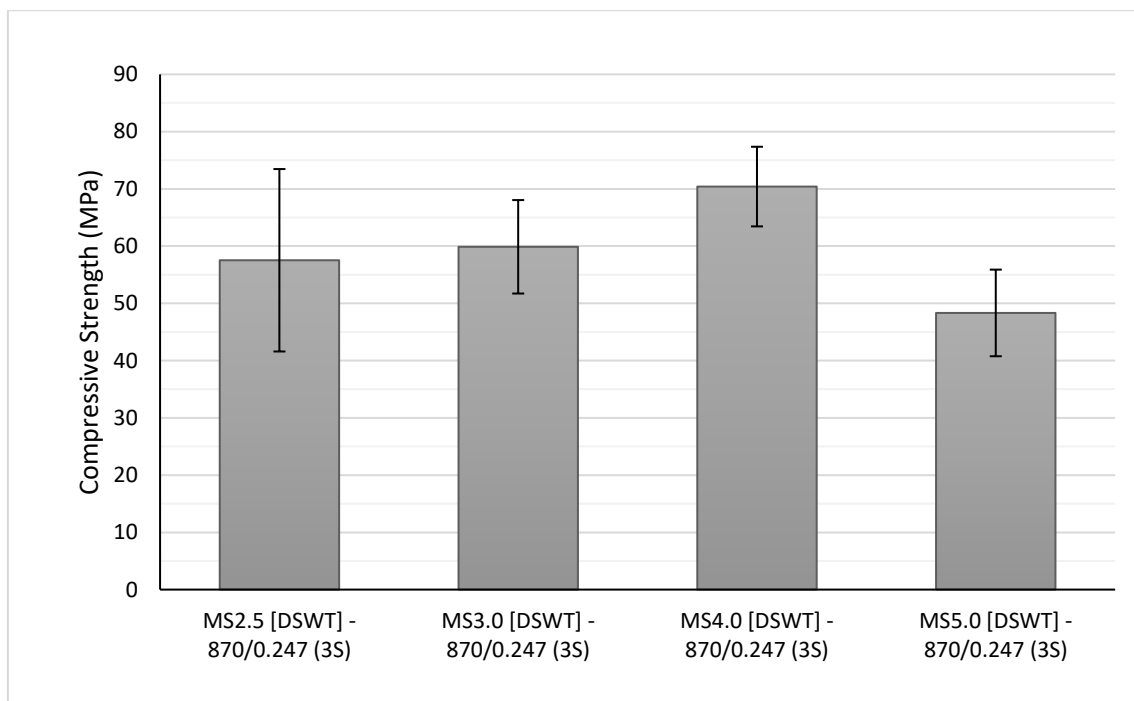
Source: Author

Table 13: UHPC superplasticizer admixture content adjustment (n =5)

Mix	Mean (MPa)	Standard Deviation (MPa)	Coefficient of variance (%)
MS2.5 [DSWT] – 870/0.247 (3S)	57.53	15.93	27.70
MS3.0 [DSWT] – 870/0.247 (3S)	59.88	8.16	13.63
MS4.0 [DSWT] – 870/0.247 (3S)	70.40	6.96	9.88
MS5.0 [DSWT] – 870/0.247 (3S)	48.33	7.57	15.66

Source: Author

Figure 87: UHPC inner bubbles in specimen with 4% superplasticizer

Source: Author

The compressive strength adjustment evolution was evaluated at each material and procedure adjustment. Initially, the tests were performed with specimens sized 5 × 10 cm; the results are presented in Figure 89 and Table 14. The target strength was 80 MPa at 7 d without fibers and 100 MPa at 7 d with fibers, and the values obtained confirm the efficiency of the mix proportions adjustments and materials selection.

The initial mixture procedure modification was the dry SF sieving to try to reduce the effects of the particle agglomerations. As shown in Figure 88, this

method diminished the quantity of the bigger agglomeration balls but did not reflect an increase in compressive strength (51.88 MPa).

Figure 88: UHPC particle agglomeration reduction: (a) dry SF without sieving and (b) dry SF with sieving

(a)   (b)
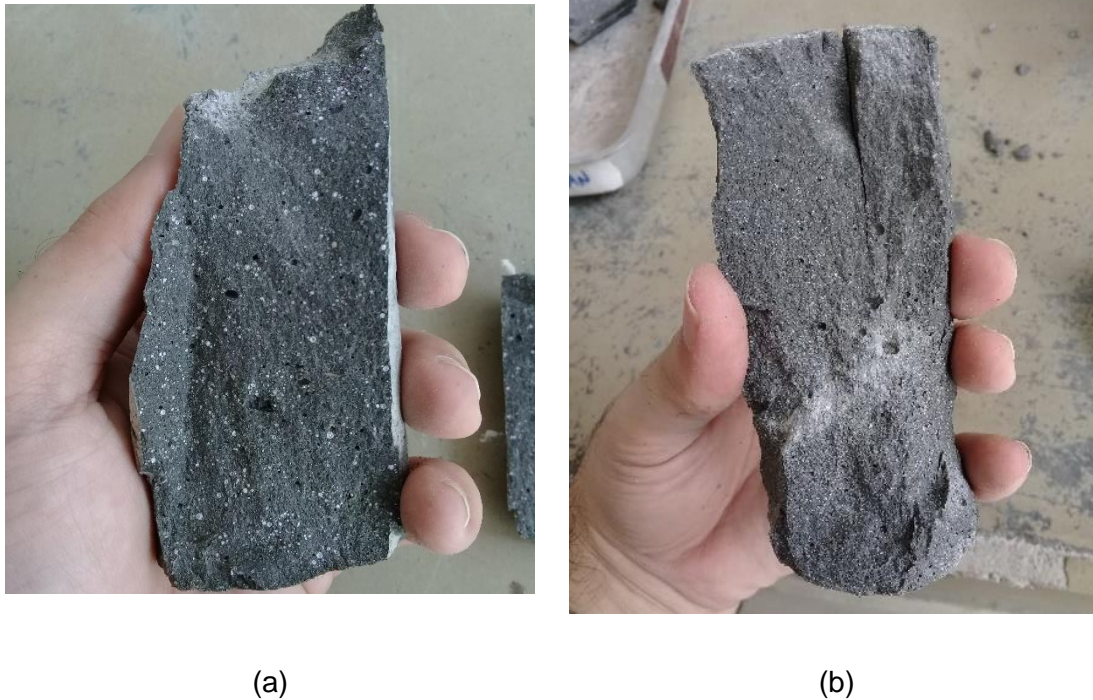
Source: Author

The cement consumption was increased to 950 kg/m³ to improve the material's compressive strength, maintaining the initial water-cement ratio of 0.247. This adjustment did not have a significant effect in the first moment because the workability worsened (62.10 MPa). Then, MS4.0 [DSS] - 950/0.247 (4S) was developed with the four-stage mixture procedure improving the material fluidity after the increase in cement consumption. Although the workability problem has been solved, the compressive strength did not increase as expected (58.76 MPa). Therefore, MS4.0 [DSS] - 950/0.20 (4S) was produced with a reduced water-cement ratio of 0.2. This simple adjustment increased compressive strength by 12.5% (69.57 MPa). At this moment of the study, the SF in an aqueous medium was presented as a solution for the dry SF particle

agglomeration. The material tested resulted in an increase of 16% in compressive strength (80.77 MPa).

In the next step, the packing particle design was adjusted to analyze the interference of another cement consumption increase, for 1100 kg/m³, in the method. It is essential to notice that the following two mixes were developed remotely with an undergraduate student's help, marked with a superscribed letter "a." A reduction in the superplasticizer admixture to 3.5% was tested, named MS3.5 [SAM] - 1100/0.22 (4S-WF)[a], but without a significant compressive strength increase (68.29 MPa). The following adjustments were another cement consumption increase to reduce the water-cement ratio to 0.2 and the previous materials' proportion with 3% superplasticizer, resulting in a medium compressive strength of 57.98 MPa and 56.23 MPa, respectively. The sequence of results in the last adjustments did not reflect the initial modifications logic that resulted in compressive strength increases. This irregularity was attributed to errors in the test procedures that were not possible to verify during this remote work period.

Figure 89: UHPC 7 d compressive strength adjustment 5 × 10 cm specimen evolution
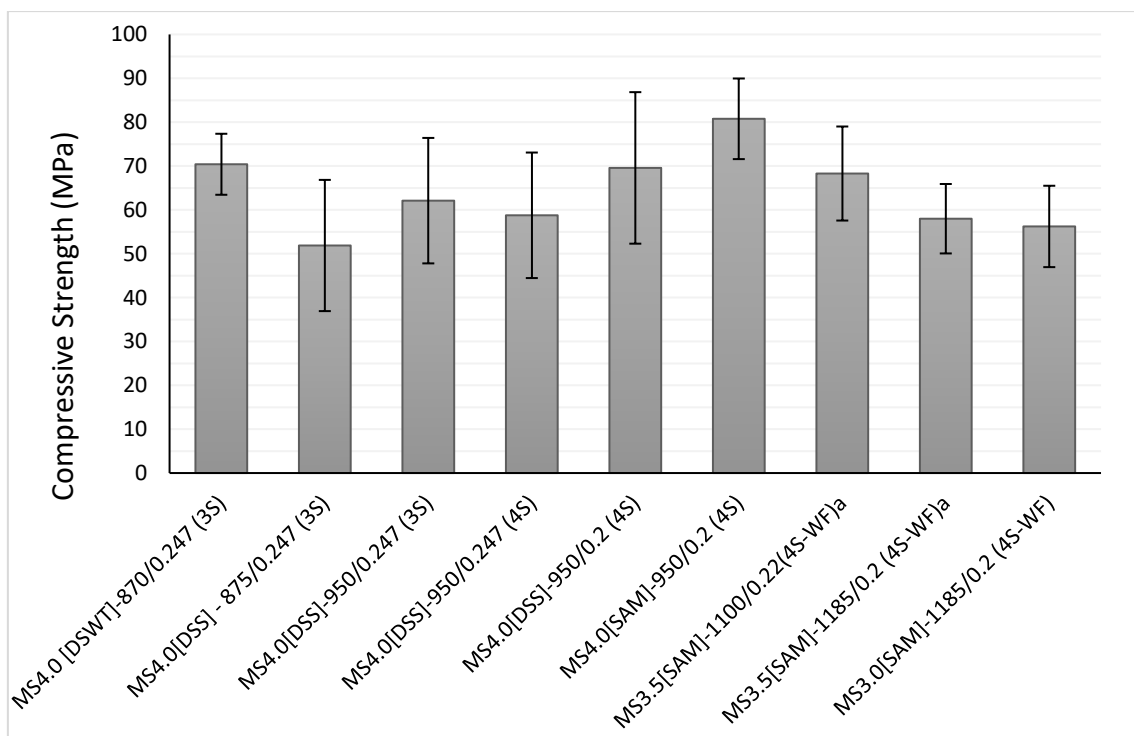
Source: Author

Table 14: UHPC compression test results at 7 d (MPa) 5 × 10 cm specimen (n = 5)

Mix	Mean (MPa)	Standard Deviation (MPa)	Coefficient of variance (%)
MS4.0 [DSWT] – 870/0.247 (3S)	70.40	6.96	9.88
MS4.0 [DSS] – 870/0.247 (3S)	51.88	14.96	28.84
MS4.0 [DSS] – 950/0.247 (3S)	62.10	14.30	23.03
MS4.0 [DSS] – 950/0.247 (4S)	58.76	14.31	24.35
MS4.0 [DSS] – 950/0.20 (4S)	69.57	17.27	24.83
MS4.0 [SAM] – 950/0.20 (4S)	80.77	9.19	11.38
MS3.5 [SAM] – 1100/0.22 (4S-WF)[a]	68.29	10.72	15.70
MS3.5 [SAM] – 1185/0.20 (4S-WF)[a]	57.98	7.91	13.65
MS3.0 [SAM] – 1185/0.20 (4S-WF)	56.23	9.28	16.50

Source: Author

Two major failure modes were identified and directly correlated with the compressive strength results. Mixtures with higher compressive strength as MS4.0 [DSWT] - 870/0.247 (3S), MS4.0 [DSS] - 950/0.2 (4S), and MS4.0 [SAM] - 950/0.2 (4S) presented a cone and split failure mode in some specimens, as shown in Figure 90b. The other batches presented a columnar failure mode in the majority of specimens, reducing the compressive strength, as shown in Figure 90a. The columnar failure may be occurred by an "unlevelling" of the top and bottom specimen faces, resulting in an eccentric load. This hypothesis may explain the reduced results in the tests done during the remote work period, as shown in Figure 90c.

Figure 90: UHPC 5 × 10 cm ruptured specimens: (a) with a columnar failure mode, (b) with a cone and split failure mode, (c) with a columnar failure mode during the remote work period

(a)   (b)   (c)
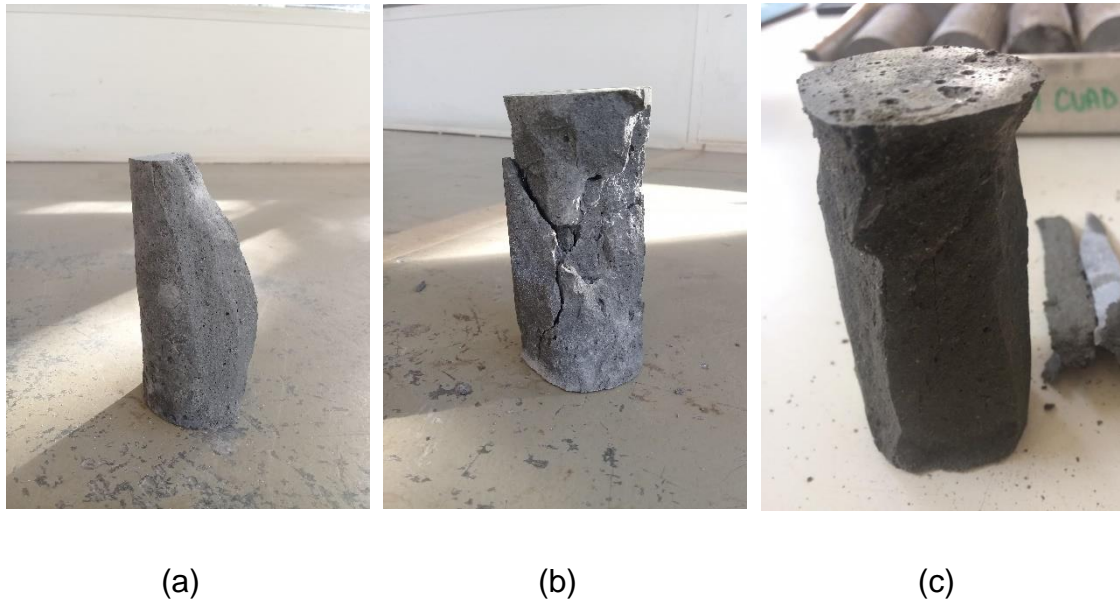
Source: Author

Returning to do the compression tests in person, the influence of the specimen size was evaluated, and then the fibers were incorporated; the results are presented in Figure 91 and Table 15. With the same material at MS3.0 [SAM] - 1185/0.2 (4S-WF), an increase of 39% in compressive strength was verified with the 10 × 20 cm specimen (CS3.0 [SAM] - 1185/0.2 (4S-WF)). This rise is attributed to a minor test procedures disturbance with a more significant load area. Then another simple method was tested with the sand being dried in an oven, and the mean compressive strength increased by 6% (82.86 MPa) with this easy adjustment. Previously, this method was not utilized because minimal water content in the sand were verified with a moisture analyzer.

Finally, the UHPC with fibers was tested. The mean compressive strength increased by 28% (106.19 MPa), with 2% of fibers by volume. To reduce the amount of bubbles produced by the reaction of the superplasticizer, CS2.5 [SAM] - 1185/0.2 (4S-WF-DOS-2%F) was tested with 2.5% of admixture. The reduction did not affect the mean compressive strength (106.14 MPa).

The failure mode of the 10 × 20 cm specimens presented a cone and split shape in most of it, as shown in Figure 92a. Once again, this result evidences the advantage in the tests with a 10 × 20 cm specimen size in addition to the smallest standard deviation samples. At this point of the work, the top and bottom surface leveling was verified with a bubble level, as shown the Figure 92b. When the fibers were added, the main failure mode verified was a shear type with the direction according to the fiber position, as shown in Figure 92c.

Figure 91: UHPC 7 d compressive strength adjustment 10 × 20 cm specimen evolution
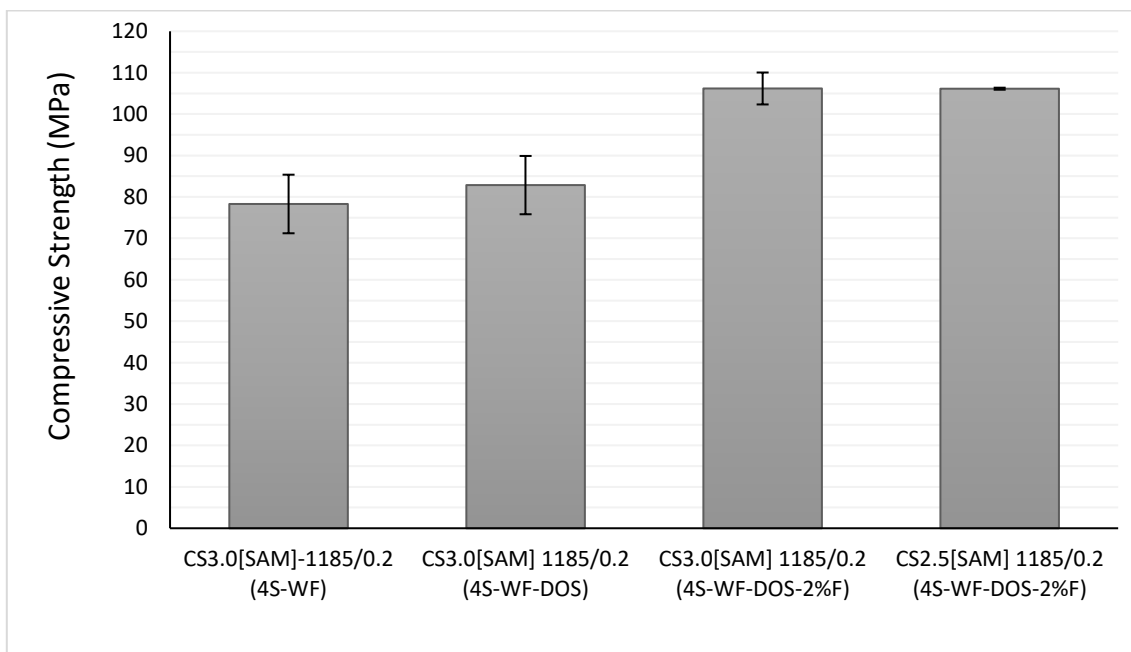
Source: Author

Table 15: UHPC compression test results at 7 d (MPa) 10 × 20 cm specimen (n = 3)

Mix	Mean (MPa)	Standard Deviation (MPa)	Coefficient of variance (%)
CS3.0 [SAM] – 1185/0.20 (4S-WF)	78.30	7.07	9.03
CS3.0 [SAM] – 1185/0.20 (4S-WF-ODS)	82.86	7.04	8.50
CS3.0 [SAM] – 1185/0.20 (4S-WF-ODS-2%F)	106.19	3.85	3.63
CS2.5 [SAM] – 1185/0.20 (4S-WF-ODS-2%F)	106.14	0.24	0.23

Source: Author

Figure 92: UHPC 10 × 20 cm ruptured specimens: (a) without fibers, (b) top surface level verification, and (c) with fibers

(a)   (b)   (c)

Source: Author

Although some adjustments in the mixtures studied did not directly influence the 7 d compressive strength, a progression may be achieved with simple materials and methods modifications. The results demonstrate that reducing the water-cement ratio by 20% may increase the compressive strength by 12.5%, along with utilizing the SF in an aqueous medium, and the sand dried in an oven may increase it by 16% and 6%, respectively. Finally, adding the fibers to the mixture may increase the 7 d compressive strength by 28%. All the progressions are presented in Figure 93. It is important to note that some adjustments were necessary to solve the agglomeration and workability problems. In addition, the results were obtained with the same materials collected at the beginning of the research, and it was decided not to use unconventional procedures, such as thermal curing. Figure 94 presents a flowchart with a summary of the compressive strength evolution methodology.

Figure 93: UHPC 7 d compressive strength progression
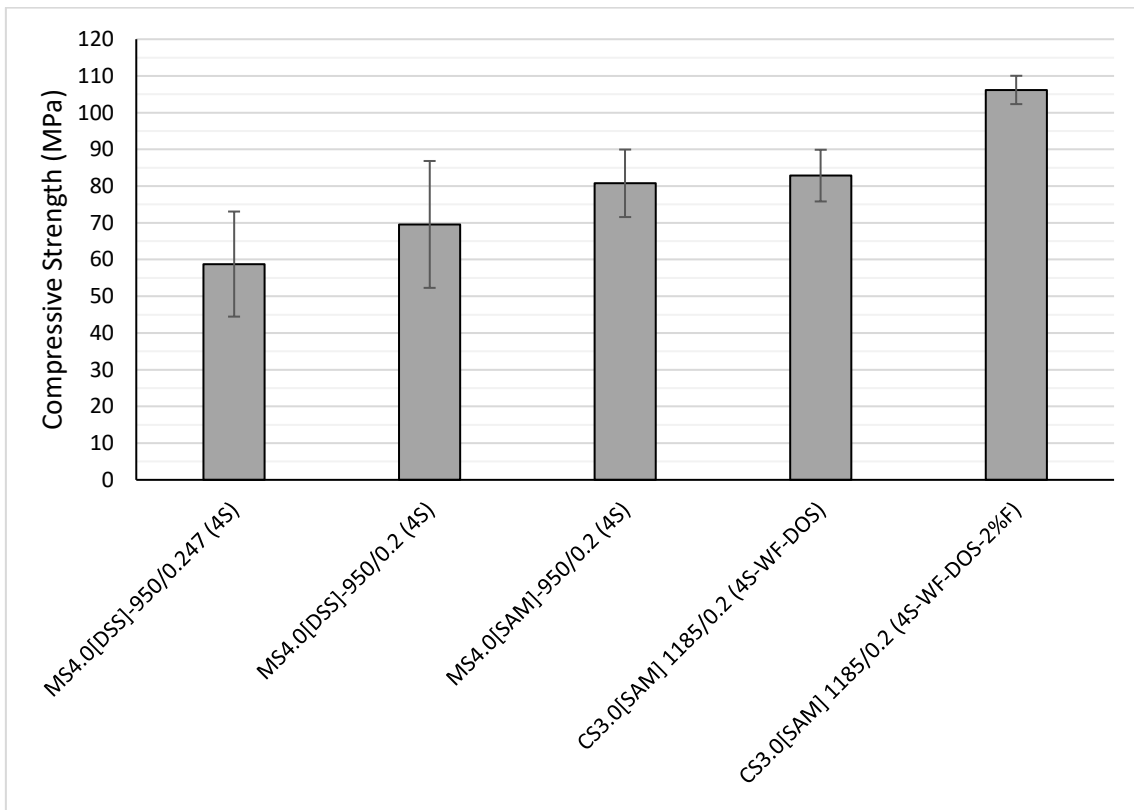
Source: Author

Figure 94: UHPC compressive strength evolution methodology
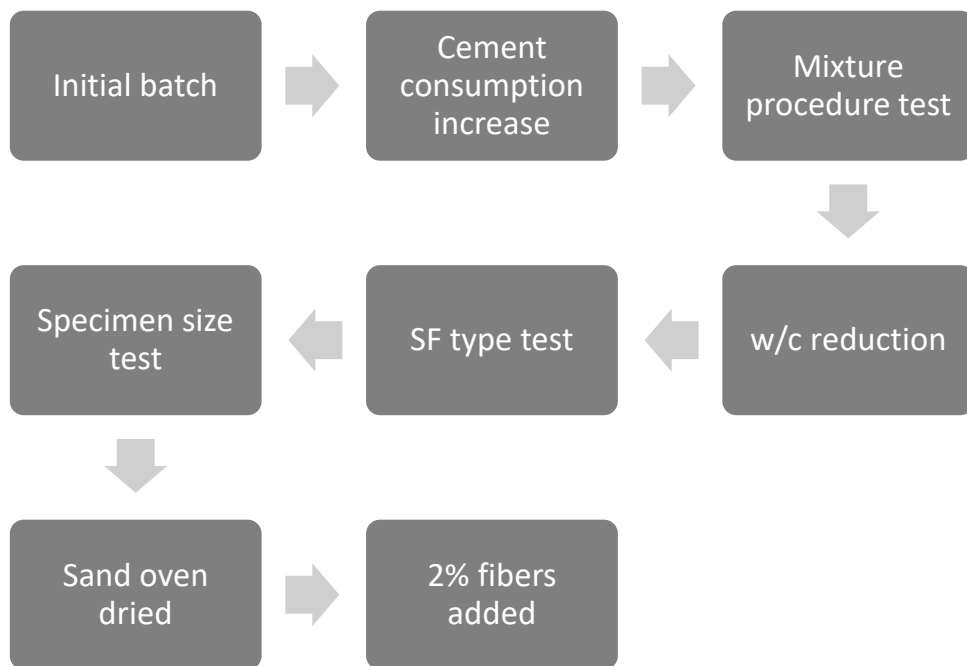
Source: Author

4.4 COMPRESSIVE BEHAVIOR

The UHPC's compressive response utilizing HUTM with an external displacement dial indicator was considered satisfactory with the acquisition of the complete behavior. It was determined with the final mix CS3.0 [SAM] - 1185/0.2 (4S-WF-DOS-2%F). As shown in Figure 95, the initial ascending stage remained linear until approximately 90% of the peak strength of 130 MPa. Through this linear strain-stress relationship, an elasticity modulus of 42 GPa was graphically obtained, near the 43.8 GPa obtained with Equation 23, and 41.45 GPa determined according to NBR 8522-1 (ABNT, 2021). The post-peak response presented two discontinuities: a horizontal slip near the peak strength and the material rupture vertical slip. It occurs due to the difficulty of obtaining the stress-strain response in the descending branch, mainly in high-level stress. A possible solution is to reduce the load rate in the post-crack stage and an accurate displacement control; however, in a HUTM, having this control is not easy. In addition, the material response exhibits a diagonal last stage due to the fiber bridging at the cracks interface, which sustains a low-stress decrease rate even at high strain levels. Therefore, to compose the complete compression response was resolved to trim the horizontal slip and join the curve before the vertical slip with the diagonal stage, as shown in Figure 96. Notably, the average curve was defined from the mean of stress values whose strain is common. In addition, it was necessary to describe because all the samples' responses do not have the same values of strain.

Figure 95: UHPC compression with discontinuity in post-cracking behavior at 28 d
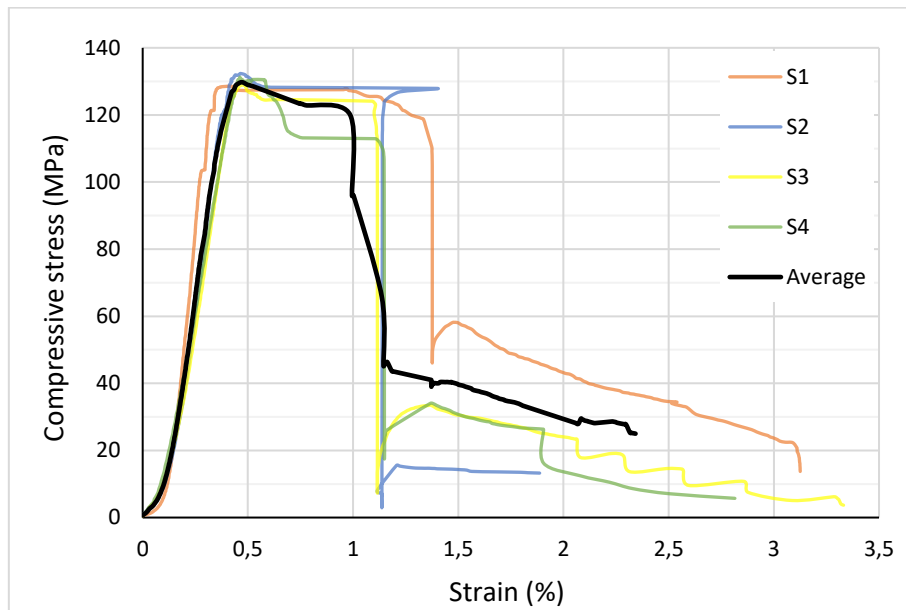
Source: Author

Figure 96: UHPC compression with smooth post-cracking behavior at 28 d
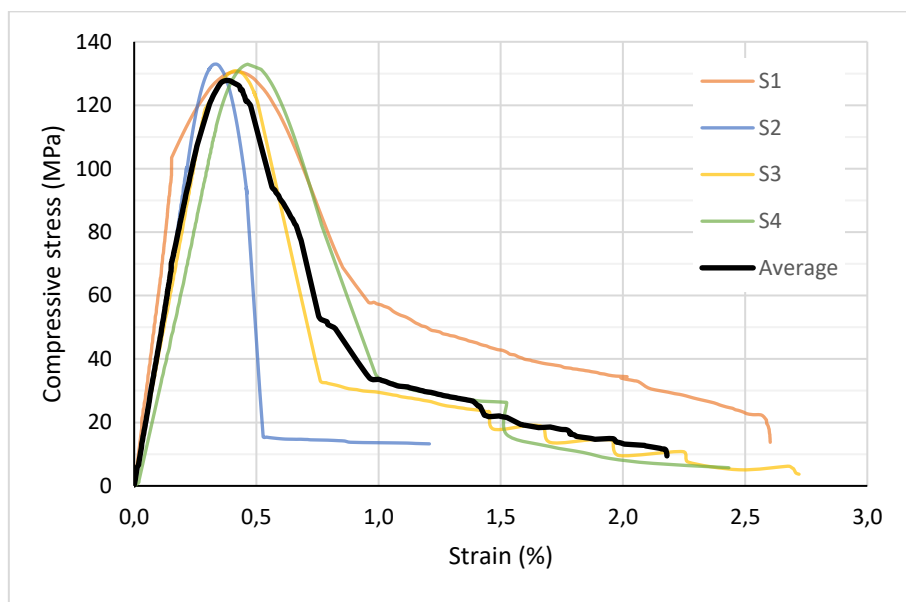
Source: Author

At seven days of age, the material achieved approximately 80% (105 MPa) of the peak strength at 28 d and presented minor stiffness (30 GPa elasticity modulus graphically determined) due to lesser maturity. As shown in Figure 97, the post-peak response is smooth compared to the 28 d compression behavior

with the same ductility gain by the fiber bridging effect. The same previous method was utilized and is presented in Figure 98 to smoothen the post-peak branch.

Figure 97: UHPC compression with discontinuity in post-cracking behavior at 7 d
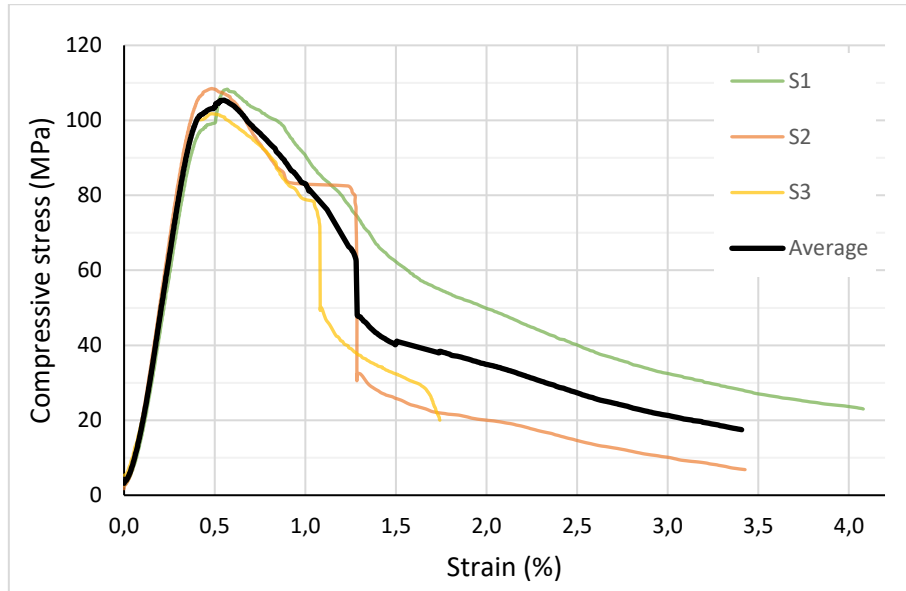
Source: Author

Figure 98: UHPC compression with smooth post-cracking behavior at 7 d
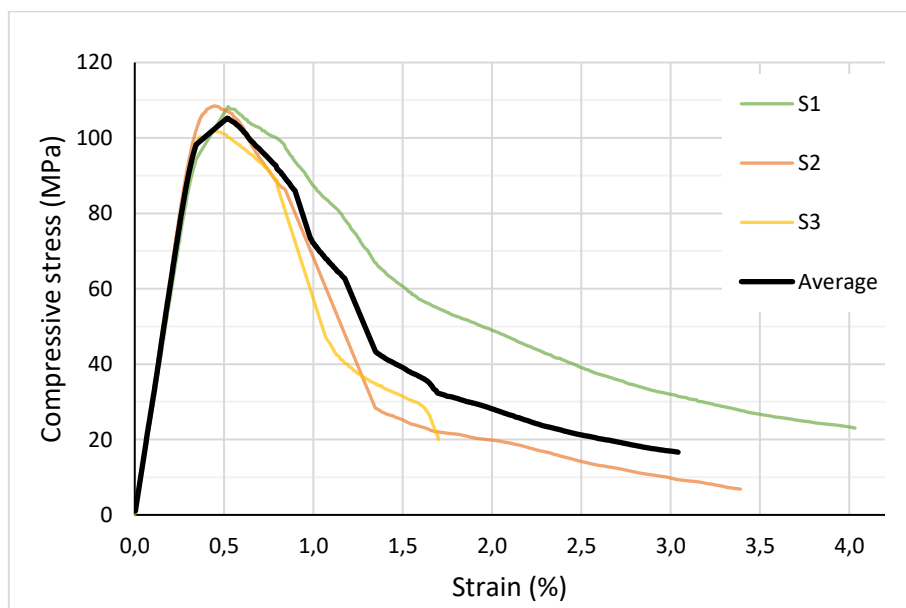
Source: Author

The stress-strain response of the UHPC subjected to a higher load rate compression test presented a greater peak strength (135 MPa), as expected, and abrupt rupture, as shown in Figure 99. The test duration was approximately half the time of the required loading rate by NF P18-470. Notably, the post-peak ductile response by the fibers' bridging behavior sustained a 3% strain, possibly due to the load rate. As with the 7 d compressive behavior, the post-peak branch smoothen method was applied and shown in Figure 100. Figure 101 presents the average response of the compression test at 28 days, 7 days, and 28 days with high velocity.

Figure 99: High-velocity test UHPC compression with discontinuity in post-cracking behavior
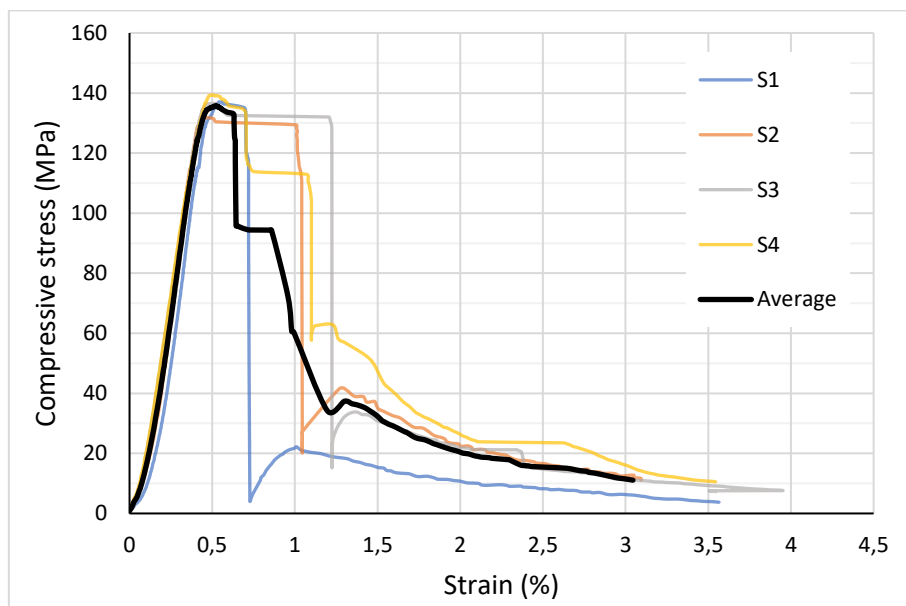
Source: Author

Figure 100: High-velocity test UHPC compression with smooth post-cracking behavior
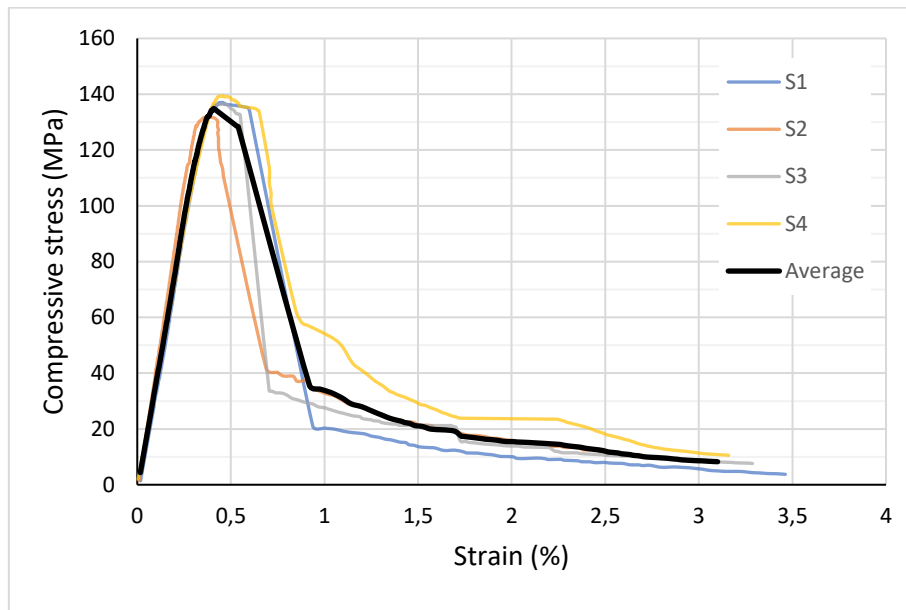
Source: Author

Figure 101: UHPC compression behavior at 7 days, 28 days, and 28 days with high velocity
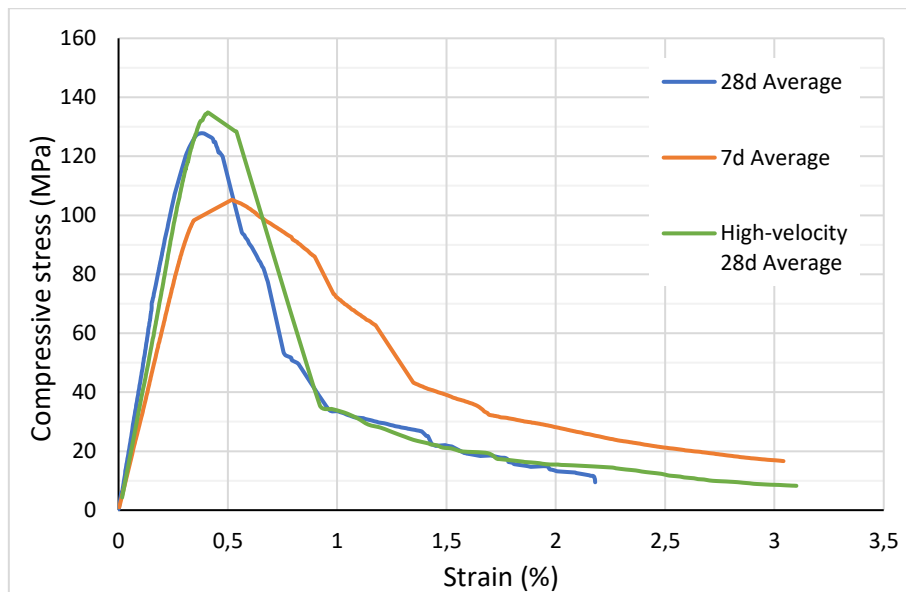
Source: Author

The failure mode and crack patterns follow the usual concrete compression test modes through the shear planes, as shown in Figures 102a and

102b. Figure 102c presents a pushout failure mode due to the bridging effect that holds the split matrix parts, as shown in Figure 102d.

Figure 102: Failure mode and crack pattern of UHPC compression test: (a) y-shaped failure, (b) shearing along a single plane, (c) pushout failure, and (d) detail of fibers through the crack

(a)

(b)

(c)

(d)

Source: Author

4.5 SPLITTING BEHAVIOR

The splitting test was developed to evaluate the UHPC tensile behavior. The response presents an initial linear branch and then a post-peak descend

curve, as shown in Figures 103a and 103b. At 7 days and 28 days, the average maximum splitting tensile strength ($f_{ct,sp}$) was 16.59 MPa and 18.35 MPa, respectively. The elastic limit was identified graphically and determined as 14 MPa and 18.35 MPa to 7 days and 28 days, respectively. In particular, this test presents some limitations. The average maximum splitting tensile strength at 7 days represents 90% of the 28 days. In addition, due to the pullout resistance being higher than the specimen deformability stress, preventing the split, the load area varies during the test. In Figure 102b, the post-peak curve presents oscillations in the response mainly due to specimen squeezing, including strength increases. Figures 104a–d present the failure mode of the specimens at 7 and 28 days, and it is evident the enlargement of the load area. It is important to note that the main crack is wider in the back of the specimen than in the front, possibly due to the placement method, which aligns the fibers in the cylinder bottom.

Figure 103: UHPC splitting test behavior: (a) at 7 days and (b) at 28 days
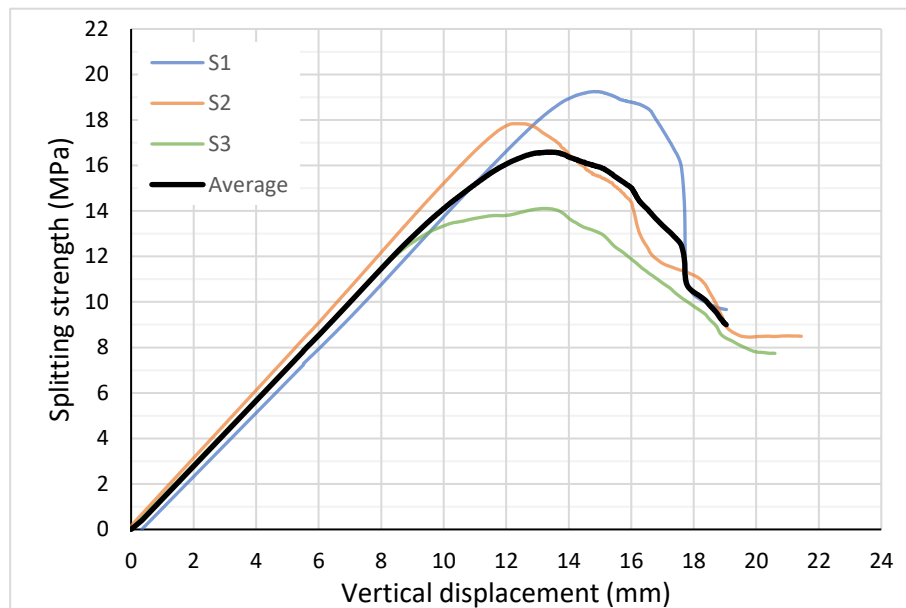
(a)
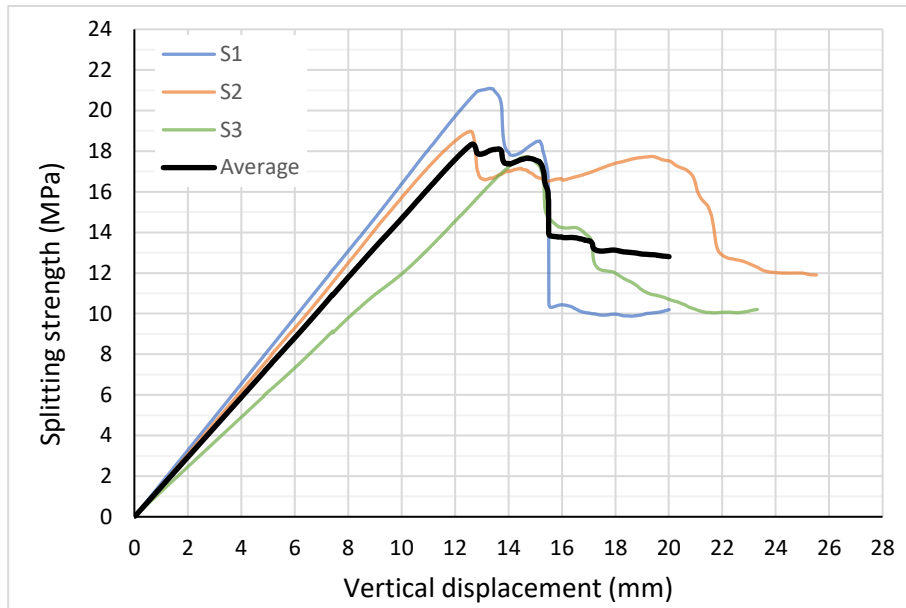
(b)

Source: Author

Figure 104: Failure mode of UHPC splitting test: (a) specimen front at 7 days, (b) specimen back at 7 days, (c) specimen front at 28 days, and (d) specimen back at 28 days

(a)

(b)

(c)   (d)

Source: Author

4.6 FLEXURAL BEHAVIOR AND INVERSE ANALYSIS

The UHPC flexural behavior was analyzed from the 4-point and 3-point bending tests. The average response per second was calculated to reduce the quantity of data examined. In addition, at the 3-point bending test analysis, the average value per every 0.2 micrometers of crack width was considered. The diagrams Load × Displacement and Load × Crack Width are presented in Figures 105a and 105b, respectively. These responses were utilized to obtain the stress-strain diagram from an inverse analysis according to the NF P18-470 (AFNOR, 2016).

Figure 105: UHPC bending test response: (a) 4-point and (b) 3-point

(a)

(b)
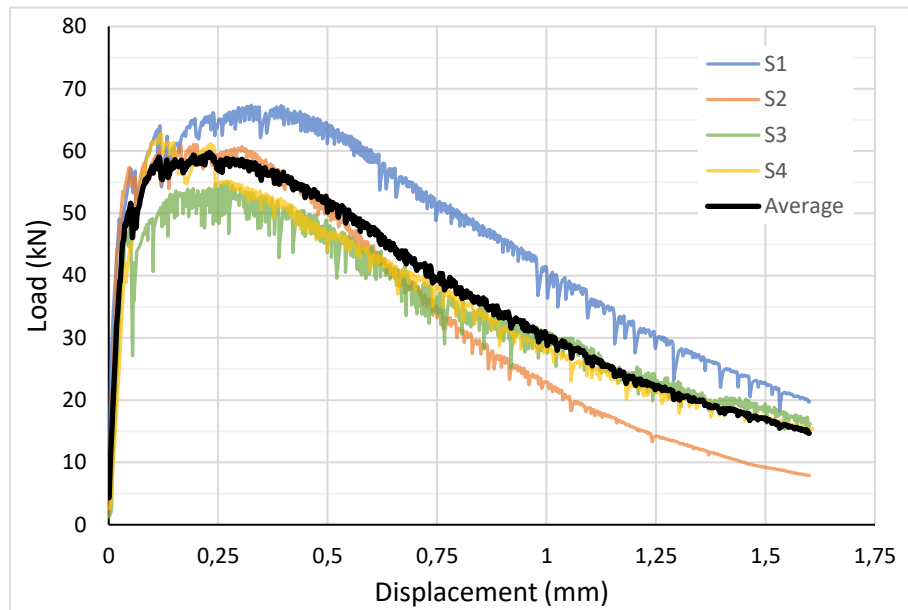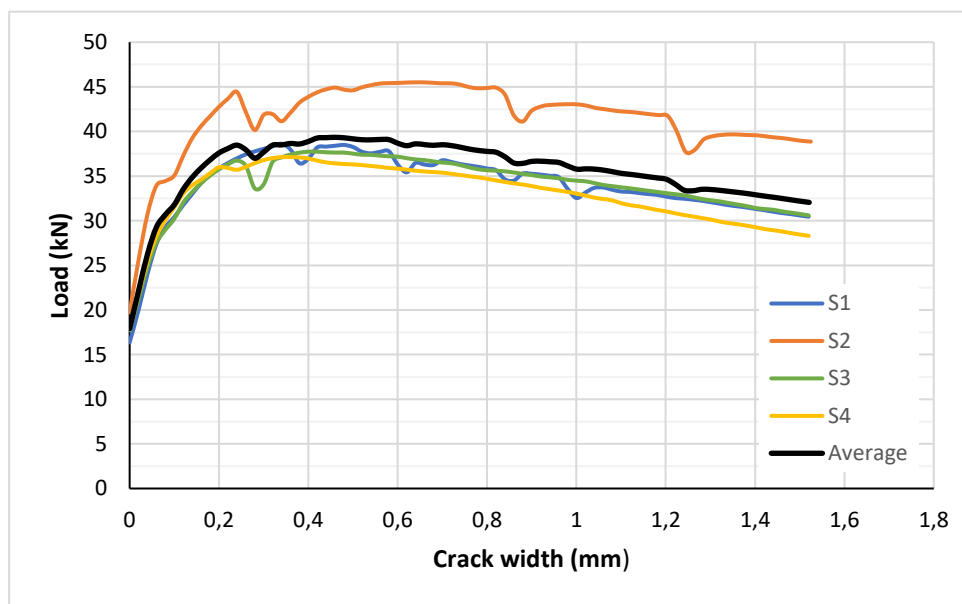
Source: Author

The inverse analysis of a 4-point bending test starts with the curvature determination to define the moment-curvature relationship. As the NF P18-470

(AFNOR, 2016) suggests, an iterative process was used to obtain the non-linear curvature. Figure 106 presents the moment-curvature diagram obtained with the non-linear response and an equivalent linear. In particular, the UHPC ductility improvement must be considered through the non-linear curvature. Then, with each pair moment-curvature, the relative depth of the neutral axis, stress, and strain are calculated from the equilibrium conditions expressions. The Maple math software assisted with the calculations due to the equations' high degree. The stress-strain curve obtained by the inverse method presents oscillations in the response, mainly after a 1% strain, as shown in Figure 101. Therefore, a moving average was defined to represent the UHPC tensile behavior, as shown in the orange line in Figure 107.

Figure 106: Moment-curvature diagram from 4-point bending test
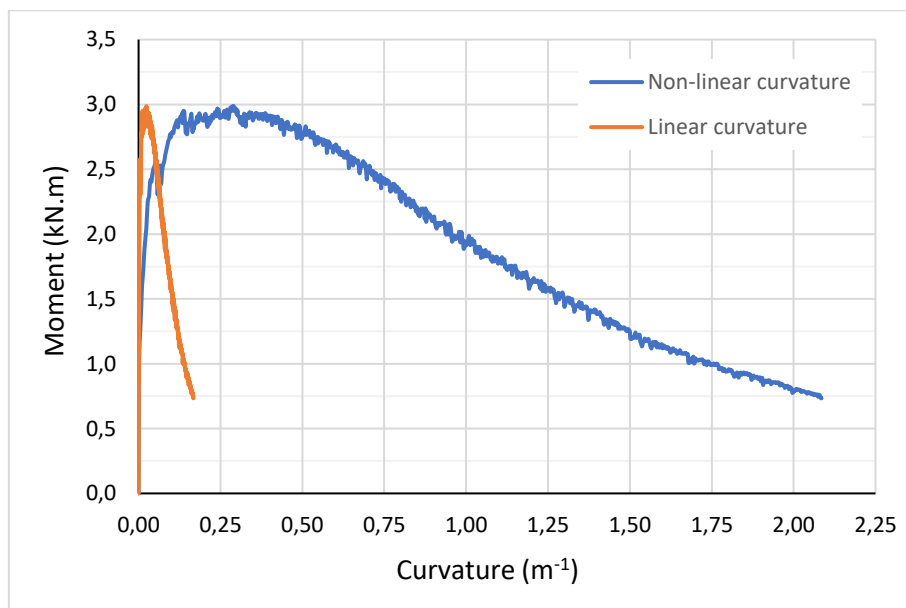
Source: Author

Figure 107: Stress-strain response by 4-point bending inverse method (blue) and its moving average (orange)
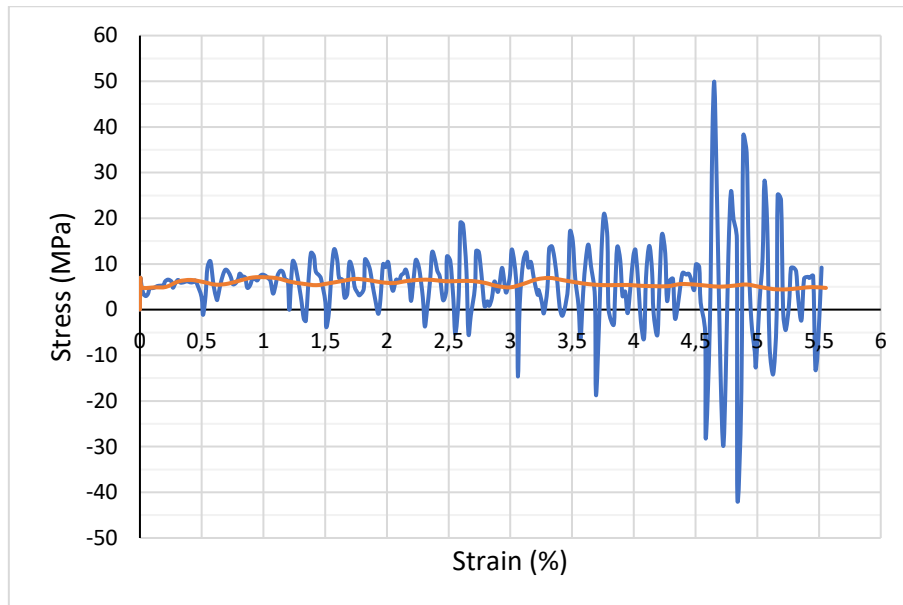
Source: Author

The first parameter defined in the 3-point bending inverse analysis is the limit of elasticity in bending. It is calculated according to Annex D in NF P18-470 (AFNOR, 2016) with the beam modulus of rupture. Then the equilibrium and compatibility equations utilize the pair Load-CMOD to determine the stress in each point. As with the 4-point bending inverse analysis, the Maple math software assisted with the calculations due to the high degree of the equations, and the curve obtained presented oscillations in the response. The moving average curve was defined to represent the UHPC tensile behavior, as shown in Figure 108. Finally, the crack width is converted into strain, and the stress-strain relationship is obtained. Figure 109 presents the responses determined by 3-point and 4-point inverse analysis. As expected, the 3-point bending test provides a higher stress value due to the notch influence on the crack direction. In the 4-point bending test, the crack will follow the weak direction according to the fiber alignment. In addition, after 3.5% strain, the responses meet.

Figure 108: Stress-crack width response by 3-point bending inverse method
(blue) and its moving average (orange)
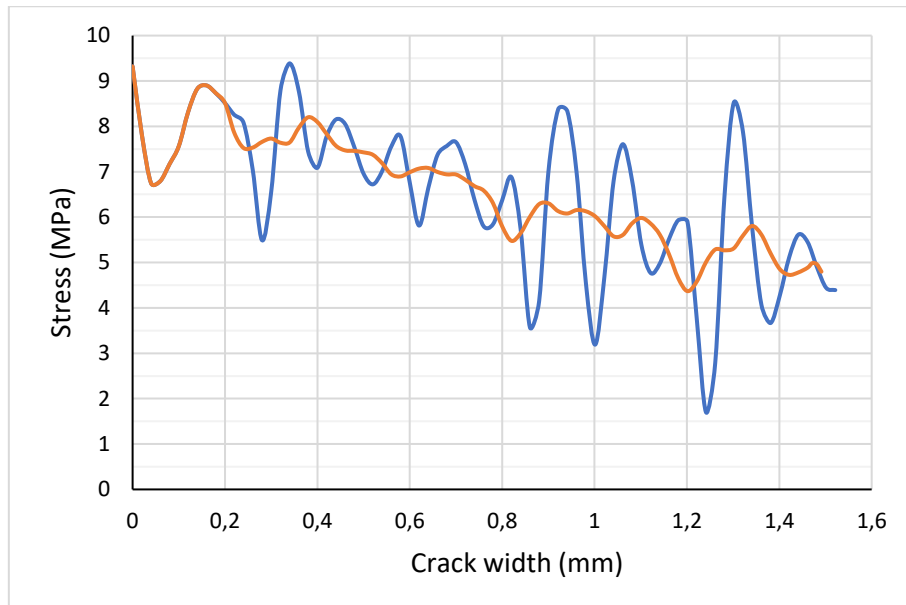
Source: Author

Figure 109: UHPC stress-strain relationship by an inverse method
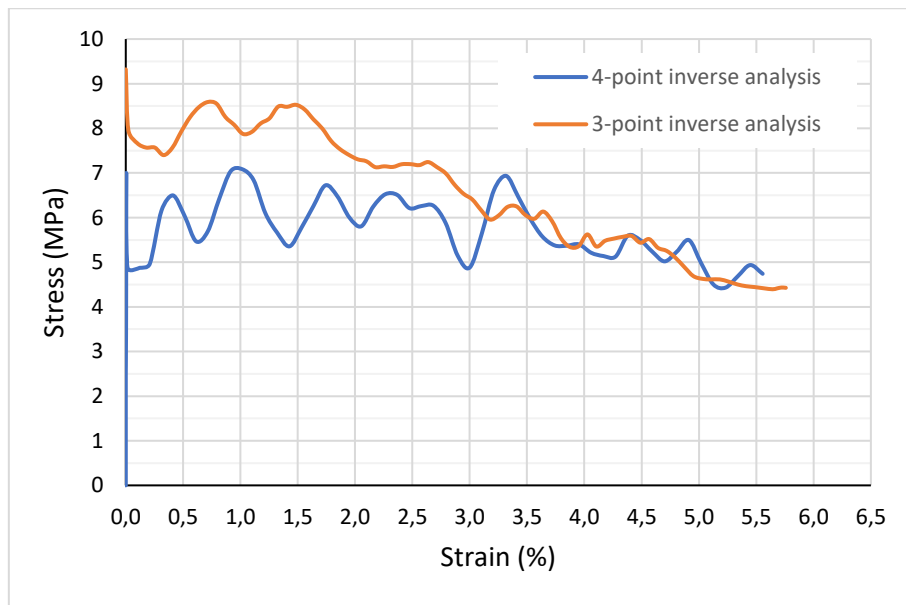
Source: Author

The simplified inverse methods tested are an option to represent the
tensile behavior narrowly, although apparently, each method better corresponds

to a UHPC post-crack performance level. The material parameters defined in the López *et al.* (2015) method were obtained to minimize the difference between the experimental moment, calculated, and presented in Table 16. Figure 110 presents the moment's correlation, and Figure 111 shows the determined curvature.

Table 16: López *et al.* (2015) method parameters

First cracking tensile strength (f_t)	7348.5 kN/m²
Ultimate tensile strength ($f_{t,u}$)	1202 kN/m²
Ultimate tensile strain ($\varepsilon_{t,u}$)	1.381%
Maximum tensile strain ($\varepsilon_{t,max}$)	2.447%
Elastic modulus (E)	160000000 kN/m²

Source: Author

Figure 110: The López *et al.* (2015) method of moment correlation
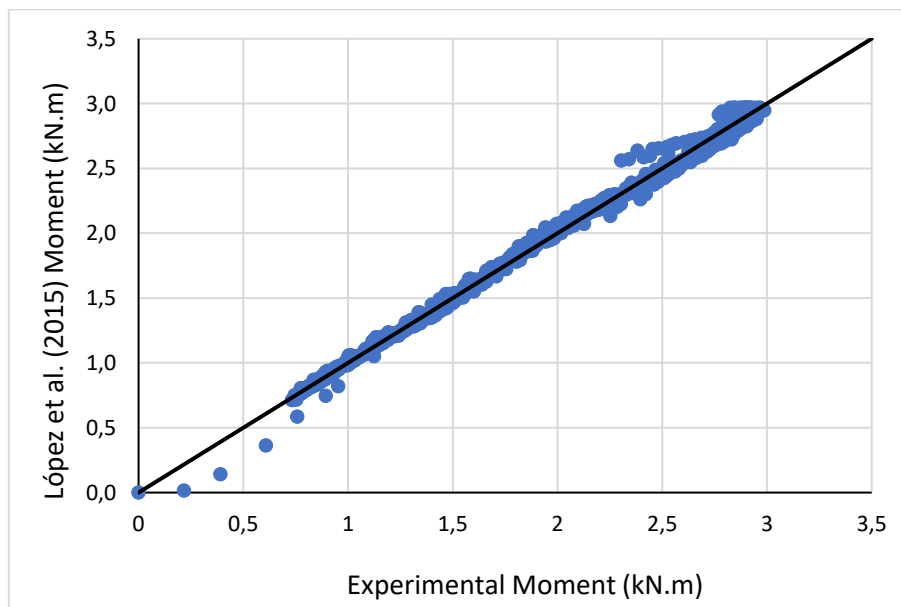
Source: Author

Figure 111: López *et al.* (2015) method curvature
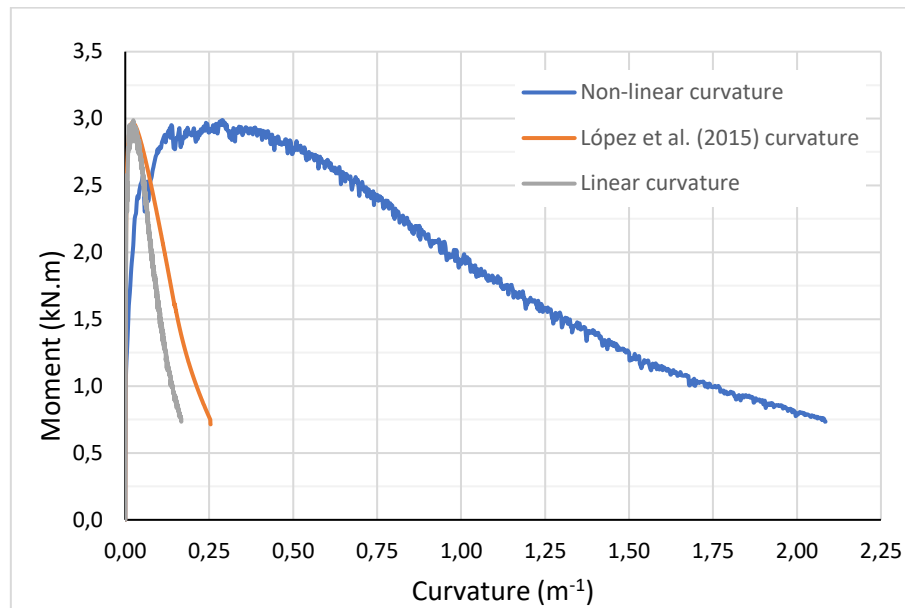
Source: Author

In the Qian and Li (2008) method, the strain capacity was defined according to the deflection capacity, considered 1.6 mm. It is important to note that the deflection capacity adopted does not consider the material rupture because the test was stopped before according to the test stop criteria. In the first master curve, the strain capacity of 1.4% was determined. The second master curve utilizes the beam modulus of rupture at the maximum moment to define the constant post-cracking tensile stress. The mater curve superior limit was considered to obtain the lower value, 6.58 MPa, for safety. The post-cracking tensile strain was defined by Hooke law and the Elastic Modulus was determined according to NBR 8522-1 (ABNT, 2021).

The parameters defined in Soranakom and Mobasher (2008) method were adjusted to approach the experimental load-deflection response. The homogenized strain softening was the closest model with the parameters presented in Table 17 and the bending response in Figure 112.

Table 17: Soranakom and Mobasher (2008) method parameters

Tensile modulus (E)	80 GPa
First cracking tensile strain (ε_{cr})	0.02 %
Constant stress level (μ)	0.3
Normalized compressive yield strain (ω)	80
Normalized ultimate tensile strain (β_{tu})	280
Normalized ultimate compressive strain (λ_{cu})	360
Normalized compressive strain (γ)	0.25
Strain at transition point (ε_{trn})	0.3 %
Normalized transition strain (α_{trn})	12
Normalized post-crack modulus (η)	-0.07

Source: Author

Figure 112: The Soranakom and Mobasher (2008) method bending response compared with the experimental one
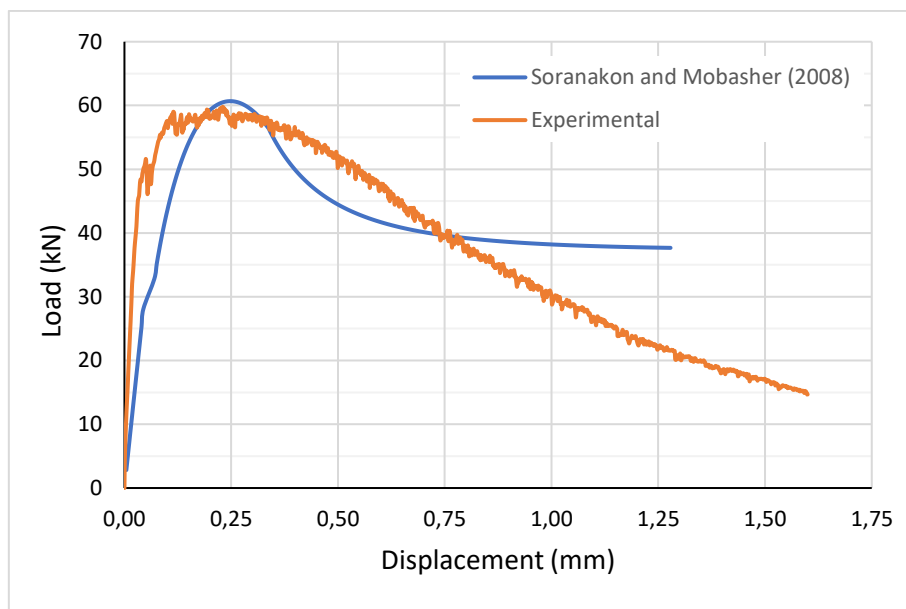
Source: Author

Finally, the simplified Wille, El-Tawil, and Naaman (2014) method for UHPC strain hardening was evaluated. The parameters determined to define the idealized modeling are presented in Table 18. They were calculated mainly according to the material properties and fiber content with empirical equations.

Table 18: The parameters of the Wille, El-Tawil, and Naaman (2014) method

Elastic modulus of the Concrete (E_c)	46352.04 MPa
Elastic modulus (E_{cc})	49425 MPa
Fictitious point of transition (σ_{cc})	7 MPa
Associated strain of fictitious point of transition (ε_{cc})	0.0142 %
Equivalent bond strength between fiber and matrix (τ)	12 MPa
Parameter of fiber pull-out (λ)	0.961538
Tensile strength of the composite (σ_{pc})	13 MPa
Maximum fiber tensile stress (σ_{fpc})	722.22 MPa
Strain-hardening modulus (E_{hc})	800 MPa
Associated strain of composite tensile at softening (ε_{soft})	0.7594 %
Energy absorption capacity (g)	68 kJ/m³
Crack spacing (S_{cr})	4.8 mm
Average residual crack openings (δ_{pc})	0.025979 mm
Fracture energy (G_f)	0.0204 kJ/m²
Ultimate crack opening (δ_u)	6.5 mm
Ultimate strain (ε_u)	8.1392 %

Source: Author

Figure 113 presents the simplified inverse methods responses in addition to the Wille, El-Tawil, and Naaman (2014) strain-hardening method. The López *et al.* (2015) and Soranakom and Mombasher (2008) methods exhibited a strain-softening behavior with low post-cracking capacity in a conservative approach compared with the 3-point and 4-point inverse analysis. The Wille, El-Tawil, and

Naaman (2014) method, as proposed by the authors, represents the strain-hardening behavior, in this case with high energy absorbing, overestimating UHPC tensile response. The method that better represents the experimental response is the Qian and Li (2008) method, with a constant post-cracking stress and smaller ultimate strain merely because the bending test stopped before the rupture. All methods presented a good first cracking tensile stress and strain compared to the 3-point and 4-point inverse analyses.

Figure 113: Bending test inverse analysis and simplified inverse methods
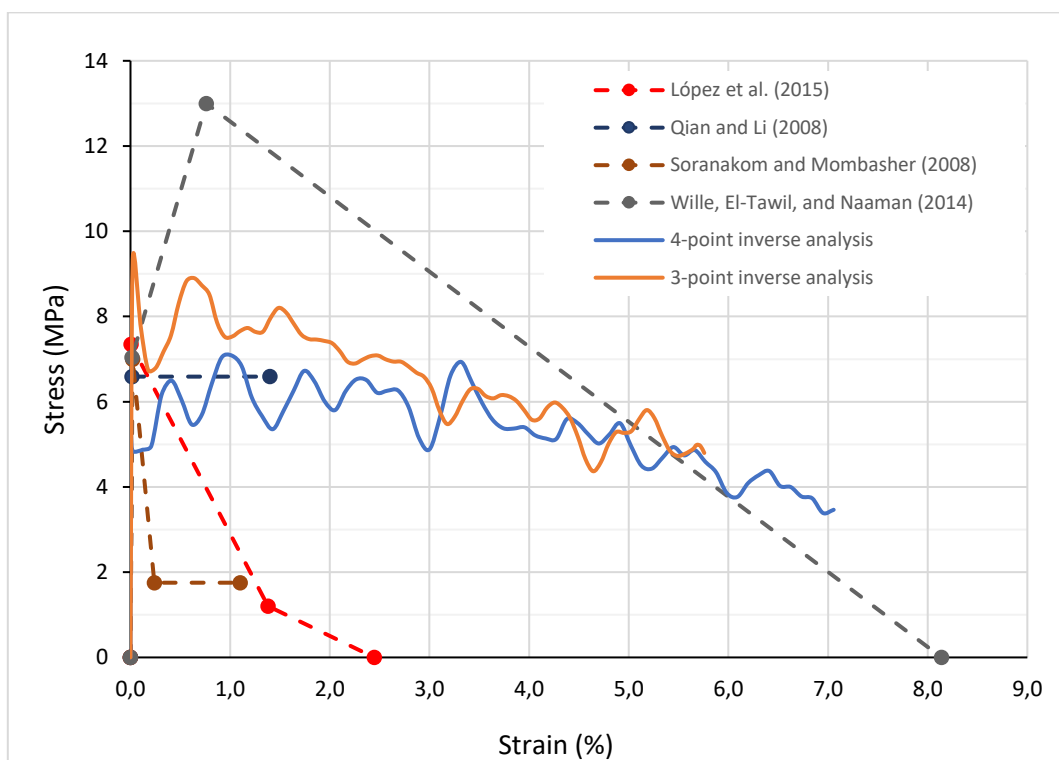
Source: Author

Besides the point-by-point inverse analysis, the NF P18-470 (AFNOR, 2016) presents a simplified method for 3-point and 4-point bending tests. A bilinear model with constant post-cracking stress represents the 4-point bending response and a quadrilinear the 3-point bending response. The parameters defined are presented in Table 19.

Table 19: Parameters of AFNOR (2016) simplified inverse analysis for 3-point and 4-point bending test

4-point bending	
Bending elastic modulus (E)	80664.62 MPa
Post-cracking stress limit ($f_{ctf}*$)	6.34 MPa
Associated strain of limit of elasticity (ε_{el})	0.00785 %
Limit strain (ε_{lim})	1.98 %
3-point bending	
Tensile limit of elasticity ($f_{ct,el}$)	9.32 MPa
Elastic limit strain ($\varepsilon_{u,el}$)	0.023 %
Post-cracking strength (f_{ctf})	6.34 MPa
Associated strain of 0.3mm crack width ($\varepsilon_{u,pic}$)	0.432 %
Post-cracking strength corresponding to a 0.01H crack width ($f_{ctf,1\%}$)	5.07 MPa
Associated strain of 0.01H crack width ($\varepsilon_{u,1\%}$)	1.502 %
Tensile strain limit ($\varepsilon_{u,lim}$)	4.875 %

Source: Author

JSCE presents an idealized tensile stress-strain curve in its design recommendations. The curve is a trilinear model, and Table 20 presents the parameters to define it. It is important to note that the JSCE determines the equivalent specific length (L_{eq}) differently from AFNOR (2016).

Table 20: Parameters of JSCE simplified inverse analysis for 3-point bending

Elastic modulus (E_c)	41450 MPa
Tensile strength (f_t)	7.43 MPa
First cracking tensile strain (ε_{cr})	0.018 %
Associated strain of 0.5mm crack width (ε_1)	0.084 %
Associated strain of 4.3mm crack width (ε_2)	16.134 %

Source: Author

Figure 114 compares the simplified responses of the AFNOR (2016) and JSCE's simplified 3-point inverse analysis with the point-by-point inverse analysis. As expected, the AFNOR (2016) simplified 3-point inverse analysis presents a higher tensile cracking strength and a trilinear softening stage. The multi-stage descending branch softens the post-cracking response, reproducing the UHPC ductility. AFNOR's (2016) simplified 4-point inverse analysis presents constant post-cracking stress, which goes through the point-by-point 4-point inverse analysis as a mean value. The simplified response that better fits the point-by-point curves is the JSCE simplified 3-point inverse analysis. Although the ultimate tensile strain probably should be less than 16.134% of the method. Still, the 6% strain is already a significant value, and this simplified analysis represents the tensile behavior until this strain. Generally, the standard simplified methods provide better responses than the proposed methods studied in the literature.

Figure 114: Bending test inverse analysis and standards simplified methods
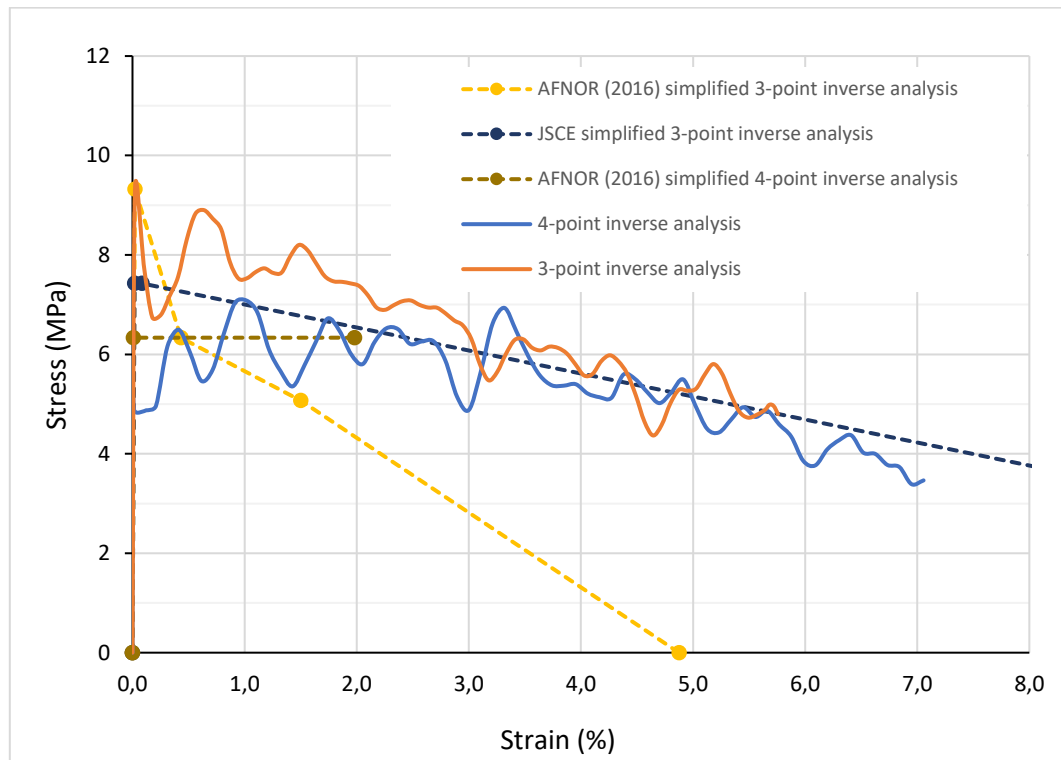
Source: Author

4.7 UHPC DAMAGE

The cyclic tests were developed to analyze the damage behavior on UHPC in compression and bending. Figure 115 presents the cyclic compression response in conjunction with the static test response. The cyclic result may be analyzed by a curve that envelopes the maximum stress of each loading/unloading stage. It is noticed that the cyclic tests did not obtain a post-peak response, which characterizes the UHPC compression behavior. In addition, the slope of the first loading/unloading curves does not change significantly, which results in a material without damage parameter.

Figure 115: UHPC cyclic compression response
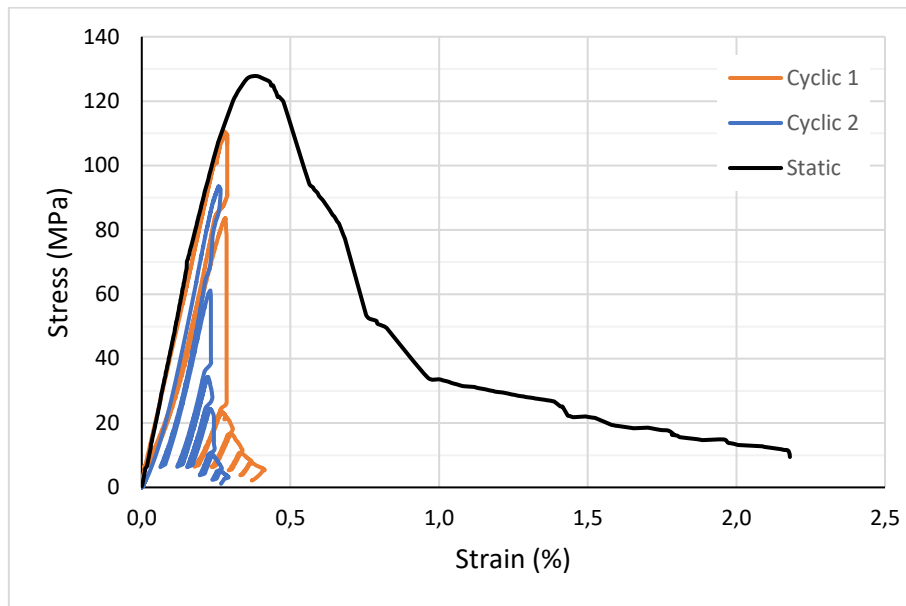
Source: Author

The cyclic bending curves were determined by 4-point bending tests, with a degradation obtained of the slopes in the load-displacement relation. It is important to note that the first slope in the cyclic test differs from the static test response, as shown in Figure 116. It may be justified as a specimen with initial damage before the test. According to Krahl, Carrazedo, and El Debs (2018), the rapid damage increase in the bending test is associated with the unstable tensile nature of the formation of cracks. In addition, even the specimen transportation for the test laboratory may induce this initial damage. The damage variable calculated for each loading/unloading stage slope was associated with the tensile strain determined in the inverse analysis of the static 4-point bending test. The curves' displacements were compared for the same load level to relate the cyclic and static bending responses. Then the tensile damage curve was obtained, as presented in Figure 117. The first damage variable obtained was high (0.92) due to the associated tensile strain (1%). In addition, obtaining values before the 1% tensile strain was impossible due to the previous initial damage.

Figure 116: UHPC cyclic bending response
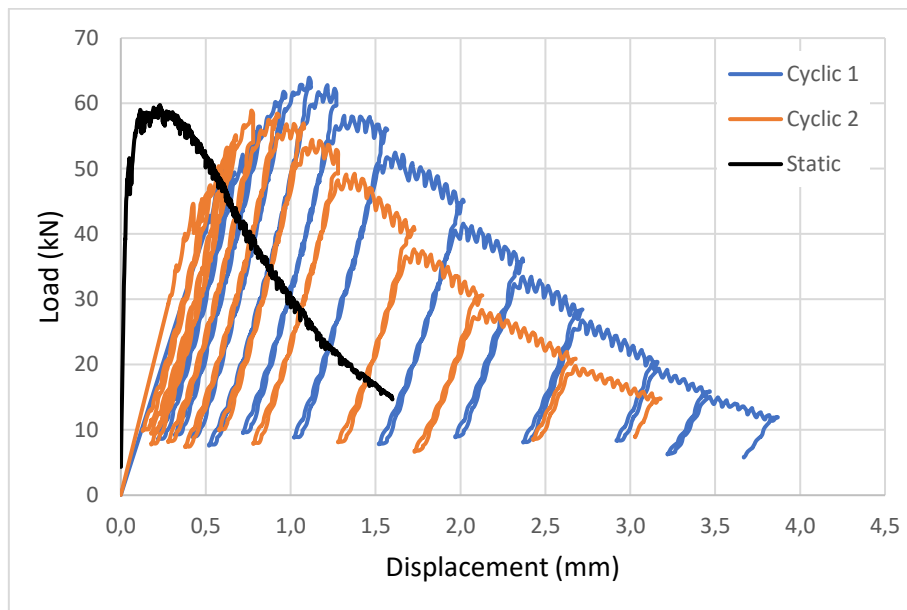
Source: Author

Figure 117: UHPC damage variable in tension by the cyclic bending
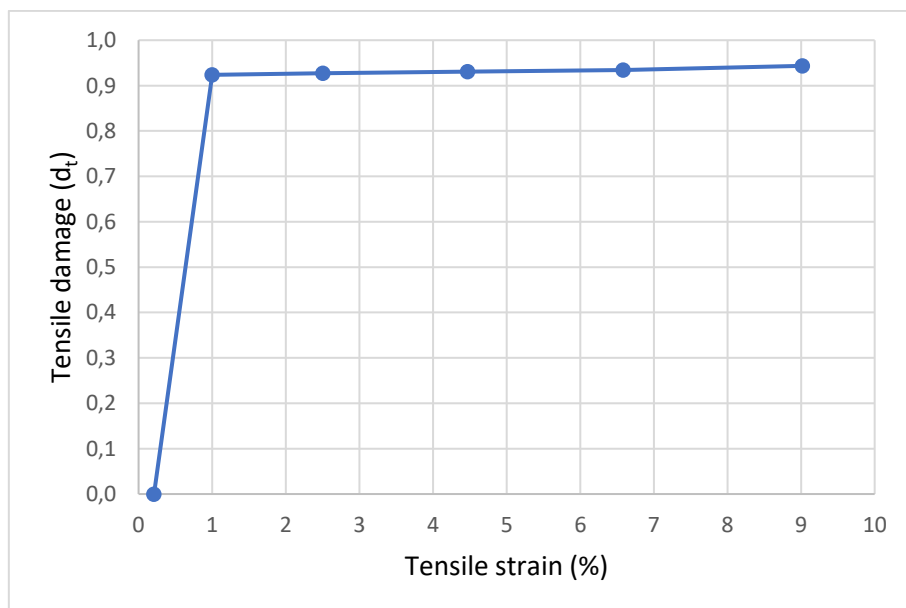
Source: Author

4.8 UHPC PROPERTIES

This topic summarizes the mechanical, workability, and durability properties after selecting materials and methods to produce UHPC. It is important

to note that every value obtained is higher than the minimum specified in the NF P18-470 (AFNOR, 2016). Table 21 presents the properties of the produced UHPC.

Table 21: UHPC mechanical, workability, and durability properties

Mechanical Properties	
7-days compressive strength ($f_{c,7}$)	106.14MPa
28-days compressive strength ($f_{c,28}$)	130.95MPa
28-days tensile strength (3-point bending) ($f_{ct,3b,28}$)	9.32 MPa
28-days tensile strength (4-point bending) ($f_{ct,4b,28}$)	7.08 MPa
28-days elastic tensile strength (3-point bending) ($f_{ct,el,3b,28}$)	6.99MPa
28-days elastic tensile strength (4-point bending) ($f_{ct,el,4b,28}$)	6.50MPa
7-days tensile strength (splitting test) ($f_{ct,sp,7}$)	16.59MPa
28-days tensile strength (splitting test) ($f_{ct,sp,28}$)	18.35MPa
7-days elastic tensile strength (splitting test) ($f_{ct,el,sp,7}$)	14 MPa
28-days elastic tensile strength (splitting test) ($f_{ct,el,sp,28}$)	18.35 MPa
Elastic Modulus (E)	41.45GPa
Workability Slump-flow Properties	
Spreading	735mm
Flow duration	5sec
Visual stability index	VSI (IEV) 0 – highly stable
Durability Properties	
Air content (fresh concrete)	1.02%
Water porosity (hardened concrete)	3.00%

Source: Author

The UHPC-produced mechanical properties are characterized by high compressive and tensile strength and a rigid material elastic modulus. According to the standard mentioned above, the 28-day compressive strength complies with the minimum characteristic cylinder strength of 130 MPa, classified as UHPFRC 130/145. The tensile strength obtained by the inverse method analysis of the bending test results is higher than the 28-day limit of elasticity of 6.0 MPa. There was no reference value for the tensile strength by the splitting test. In addition, a correlation factor of approximately 2.6 was observed between the tensile strength

by 4-point bending inverse analysis and the 28-day tensile strength by the splitting test. Due to the pullout resistance being higher than the specimen deformability stress, preventing the split, it was not a consistent test.

The 735 mm slump-flow spreading is classified as viscous UHPC (C_v) class, according to NF P18-470 (AFNOR, 2016), although near the upper limit of 760 mm to self-compacting UHPC (C_a). In addition, NBR 15823-1 (ABNT, 2017) considers the material produced as suitable for most structural applications, having to be careful with possible air entrapping and problems in corner filling.

The durability properties achieved are superior to the improved potential durability classes of NF P18-470 (AFNOR, 2016) and the references studied. In the mentioned standard, the limit for water porosity at 90 days is 6.0%. In the study by Wang and Gao (2016), the authors achieved satisfactory UHPC properties with fresh air content of up to 5.0% for a water-to-binder ratio of 0.20.

4.9 CONCLUDING REMARKS

Concerning the particle packing analysis and the compressive strength evolution, the material selected and the available procedures and laboratory equipment were satisfactory to produce UHPC. The particle packing method presented the initial material proportions as the starting point for the compressive strength evolution. The best adjustments in the mix proportions were the water-cement ratio reduction and utilized the SF in an aqueous medium, with a 12.5% and 16% compressive strength increase, respectively. The addition of the fibers resulted in a 28% increase in the 7 d compressive strength. Furthermore, the influence of the specimen size was analyzed. High values discrepancies and columnar failure mode for the 5 × 10 cm size may indicate an eccentricity in the test applied load. This work suggests that, including the initial tests, be developed with the 10 × 20 cm specimen size and rigorous control of the specimens' top and bottom surfaces leveling.

The complete compression behavior was obtained with the linear initial ascending stage and the post-peak response. The curve presented discontinuities because the hydraulic universal test machine does not have an accurate test displacement control. It was resolved with the horizontal slip

trimmed and joined with the last curve part. In addition, the UHPC at 7 days presented approximately 80% of the 28 days' strength, and the influence of the test strain rate was confirmed with an increase of 4% in the peak strength.

The splitting test was developed to obtain the tensile behavior, but the post-peak branch presents oscillations in the response. It occurred mainly due to the specimen squeezing during the test. In addition, 4-point and 3-point bending tests were analyzed to determine the tensile stress-strain curve by an inverse method. Due to the equations' high degree, the Maple math software was utilized to determine the tensile stress and strain at each point of the bending test curve. Furthermore, simplified inverse methods were analyzed, and it was observed that some represented better the strain-softening behavior and others the strain-hardening. The simplified tensile responses presented in standards presented the curves better fitting with the point-by-point inverse analysis.

To evaluate the UHPC damage behavior, cyclic tests were performed in compression and bending. The curves did not present the ductile post-peak behavior at the cyclic compression response, and the damage variable was not determined. A 4-point bending cyclic test determined the tension damage curve with a high initial value due to previous initial damage in the specimens. Finally, the mechanical, workability, and durability properties were verified and noted that every value obtained was higher than the minimum specified in NF P18-470 (AFNOR, 2016).

5 UHPC NUMERICAL MODELLING

The finite element (FE) material modeling provides a method to perform the structural behavior in several scenarios. These simulations allow a parametric analysis to study the influence of each element modification in the global response or a specific detail. According to Shafieifar, Farzad, and Azizinamini (2018), the FE model may predict the behavior of specimens with different geometries, loading conditions, and reinforcing details with reasonable accuracy.

The FE software utilized was the Abaqus version 2017 with the concrete damage plasticity (CDP) model. According to the software manual, the CDP uses concepts of isotropic damage elasticity in combination with isotropic tensile and

compressive plasticity to represent the inelastic behavior of concrete. The model contains multiple inputs such as elasticity parameters (elastic modulus and Poison ratio); plasticity parameters (dilation angle, ψ); stress ratio (f_{b0}/f_{c0}); eccentricity (e); failure surface adjustment, K, and viscosity); stress-strain curves; and damage parameters (d_t, d_c) (Fakeh, Jawdhari, and Fam, 2023). Veronese *et al.* (2022) define the plasticity parameters as presented below:

- Dilation angle (ψ) is related to the inclination that the plastic potential can reach under high confinement stress or the friction angle of concrete in a Coulomb or Mohr-Coulomb shear strength.

- Stress ratio (f_{b0}/f_{c0}) is the ratio between the yield stress in the biaxial and uniaxial states.

- Eccentricity (e) depends on the shape of the yield surface in the meridian plane, being 0 for a straight line and 0.1 for the hyperbolic shape (Drucker Prager theory).

- Failure surface adjustment (K) is the relationship between the distances from the hydrostatic axis and the tension and compression meridians.

- The viscosity parameter refers to the use of viscosity in the equations to facilitate the convergence process of numerical models.

This work replicates the compression and flexural tests to obtain the CDP parameters, and the models were calibrated with the experimental results. The step was defined as 1% of the experimental ultimate displacement. In addition, the solution technique was Full Newton with automatic stabilization by energy.

5.1 COMPRESSIVE MODEL

The compressive test was modeled with three-dimensional elements and verified the CDP parameters adjustments. Elements with 8-node linear (C3D8R) and 20-node quadratic (C3D20R) were tested with reduced integration. Both responses were similar, however, the C3D20R computational cost was 3.5× higher than C3D8R; consequently, the 8-node element was utilized. In addition, the mesh refinement was verified, varying the element size and shape. Initially, the regular hexahedral and axisymmetric element shape was analyzed with a 1

cm mesh, as shown in Figures 118a and 118c. The results were more accurate for the axisymmetric element with consistent failure modes. Furthermore, a 0.5 cm mesh size was tested and did not present a response improvement. Despite the computational cost increase of 1.5×, the 0.5 cm mesh was chosen due to the refined failure mode representation, as shown in Figures 118b and 118d.

The load was applied in the top area of the cylindrical model to simulate the compression test, as shown in Figure 118e. In addition, the base was restrained in the axial direction (Figure 118f), with one node impeded in other directions to avoid slippage. The numerical response was the pair displacement and force in the model top until a 5 mm displacement was applied.

Figure 118: FE compression model: (a) 1 cm mesh axisymmetric element, (b) 0.5 cm mesh axisymmetric element, (c) 1 cm mesh regular hexahedral element, (d) 0.5 cm mesh regular hexahedral element, (e) area of load application, and (f) base restraints

(a)

(b)

(c)

(d)

(e) (f)
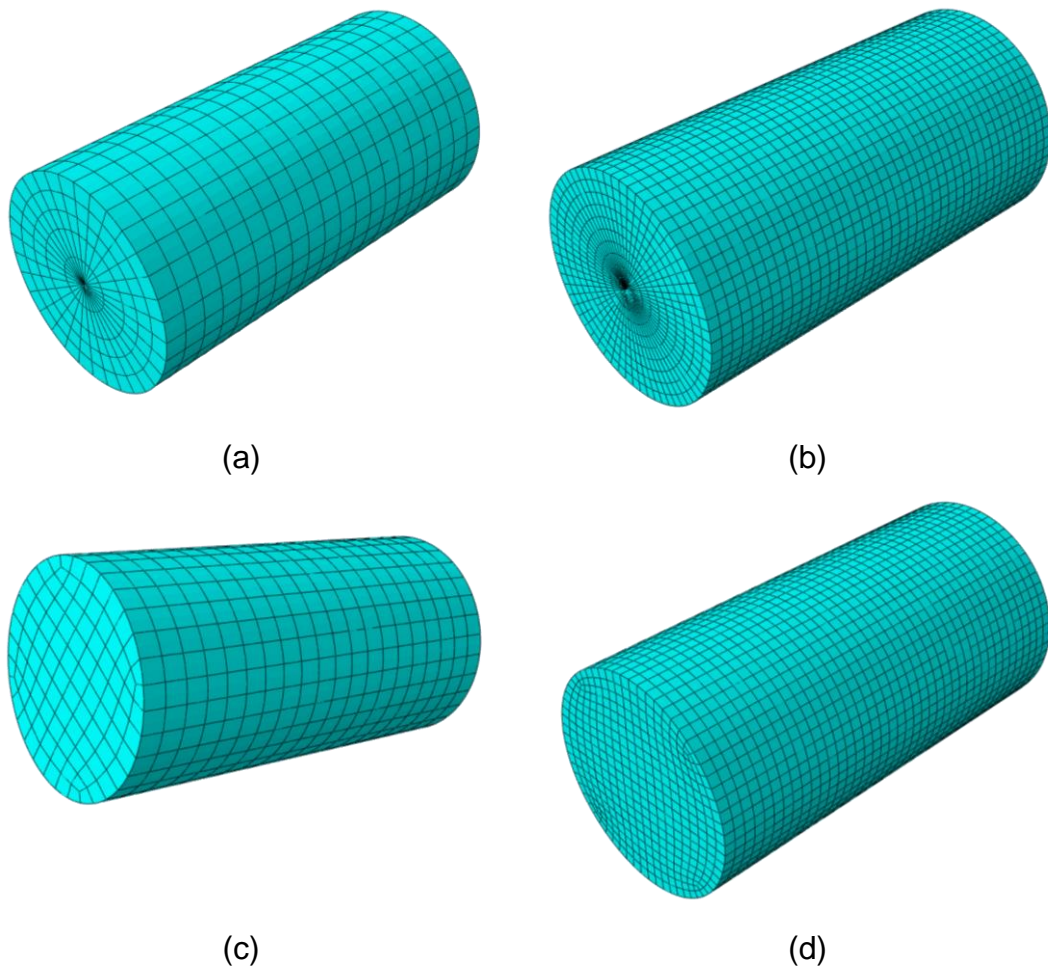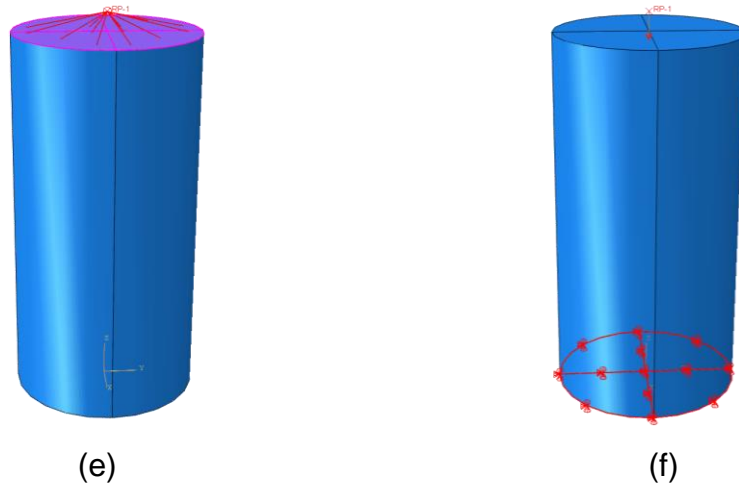
Source: Author

From the test data, a theoretical curve based on the experimental results was proposed for the behavior of the UHPC. As presented in Figure 119, the constitutive model was determined by points that cover the experimental response.

Figure 119: FE compression constitutive model
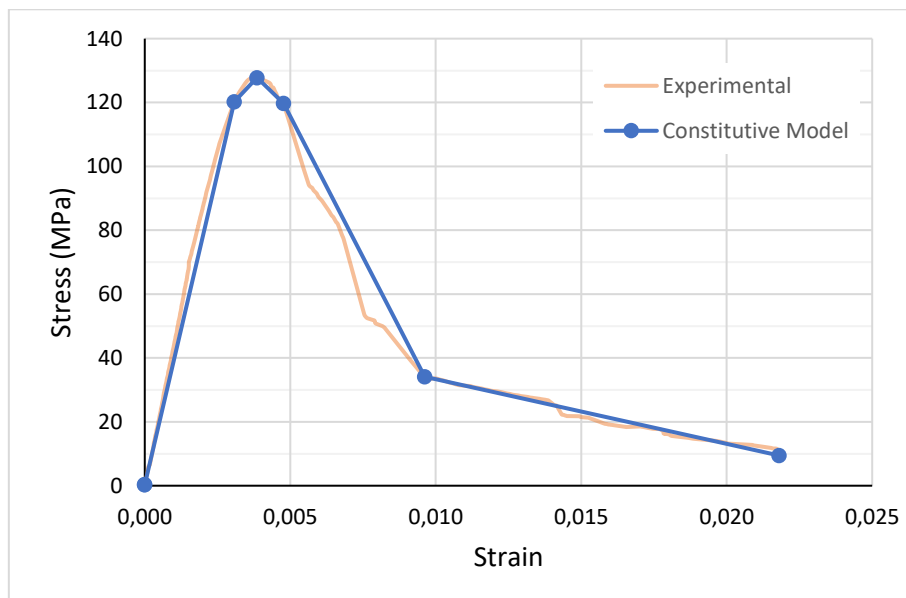
Source: Author

Initially, the model was tested in accordance with the CDP parameters presented by Shafieifar, Farzad, and Azizinamini (2018), as shown in Table 22, Elastic Modulus 42 GPa, and Poisson ratio 0.18. In addition, Figure 120 depicts the element type definition with the type and shape described above. The response was calibrated to approximate the numerical response to the experimental data by varying the dilation angle and the f_{b0}/f_{c0} ratio, considering a viscosity parameter of 0.000001 and the C3D8R axisymmetric element, as shown in Figure 121. The f_{b0}/f_{c0} ratio of 1.1 presented a curve after the experimental response, and the increase of the dilation angle shifted the curve to the right moving away from the target. Therefore, the f_{b0}/f_{c0} ratio was increased to 1.16, and the dilation curve was altered to 56, calibrating the compression model CDP parameters.

Table 22: Initial UHPC CDP parameters

Dilation Angle	Eccentricity	f_{b0}/f_{c0}	K	Viscosity Parameter
56	0.1	1.1	0.6667	0

Source: Shafieifar, Farzad, and Azizinamini (2018)

Figure 120: FE element type definition
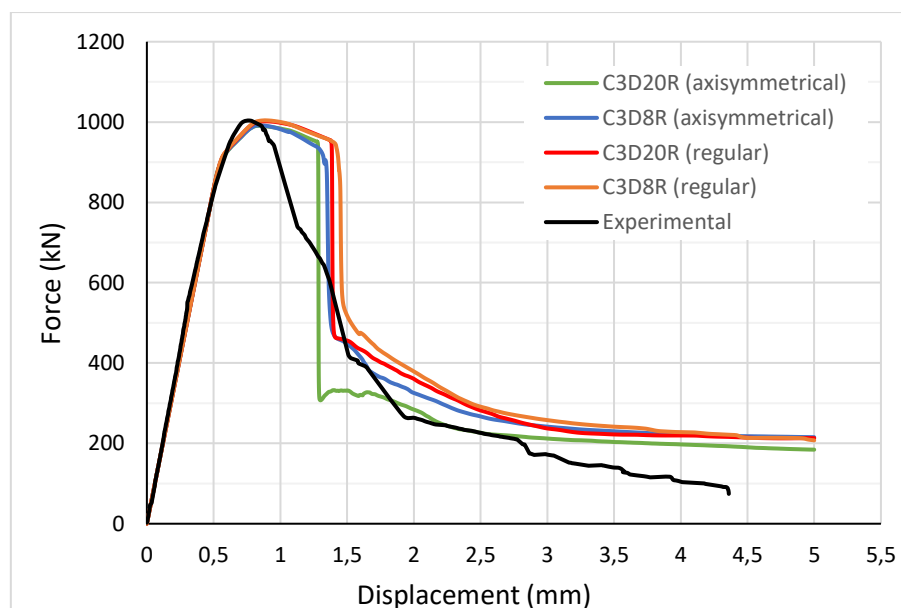
Source: Author

Figure 121: FE compression model calibration
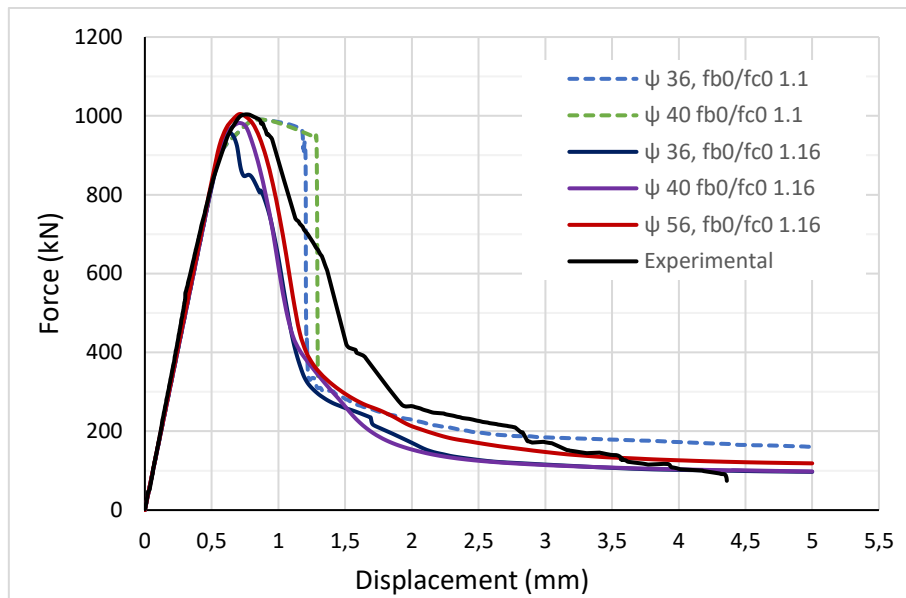
Source: Author

The FE material modeling with Abaqus enables verification of the failure mode and crack pattern. This is possible due to the damage parameter, which indicates the material degradation at each stress-strain level. In the UHPC compression modeling, initially, a shear crack arises, as presented in Figure 122a. Then the displacement increased, and the fiber bridging effect led to a pushout failure mode with the enlargement in the specimen half height and top inclined cracks like a cone and split failure mode, as shown in Figure 122b. Figure 122c presents a specimen ruptured with crack patterns similar to the FE model.

Figure 122: FE compression failure mode: (a) initial shear crack, (b) ultimate cone and split failure mode, and (c) specimen ruptured

(a)   (b)   (c)
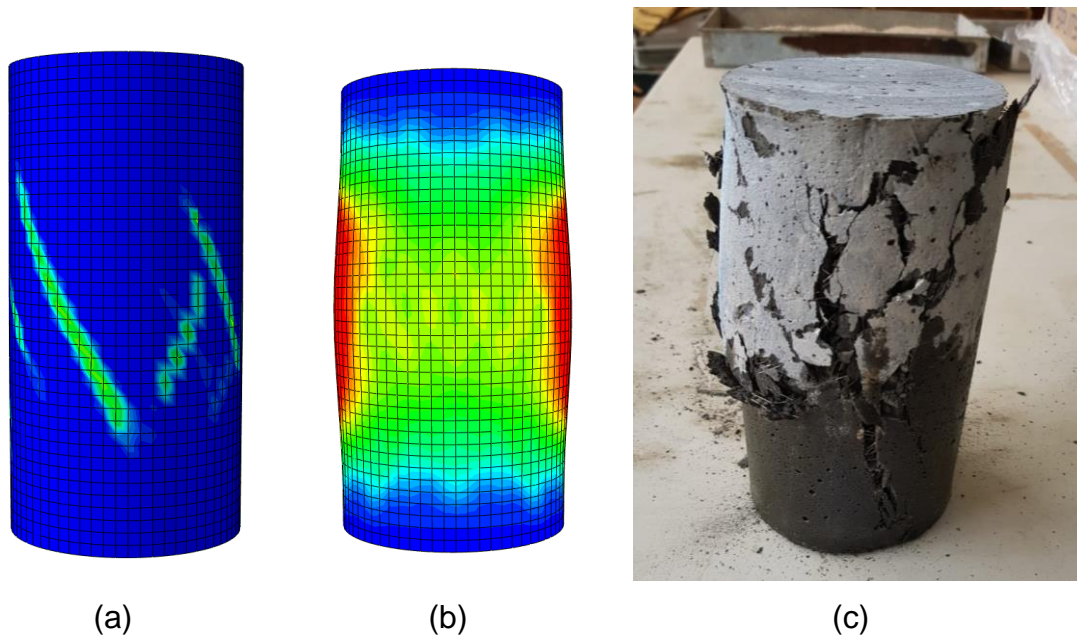
Source: Author

5.2 FLEXURAL MODEL

The bending test was simulated to evaluate the behavior of the material modeled at compression subjected to flexure. The same CDP parameters calibrated were utilized, and the 3-point and 4-point bending tests were evaluated. The element utilized was a three-dimensional 8-node linear (C3D8R) with reduced integration and mesh size of 0.5 cm due to the refined failure mode representation, as presented in Figures 123a and 123b.

Figure 123: FE flexural model mesh: (a) 3-point bending and (b) 4-point bending
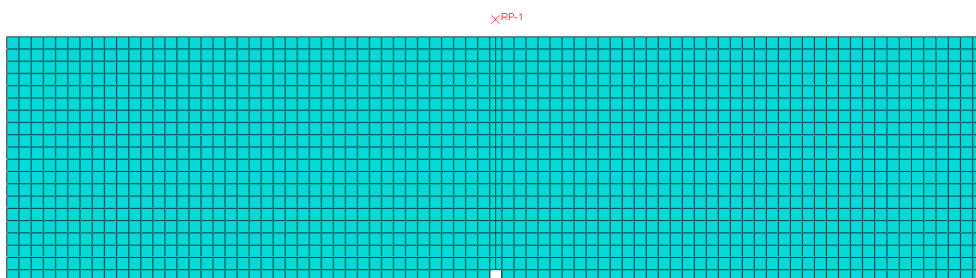
(a)
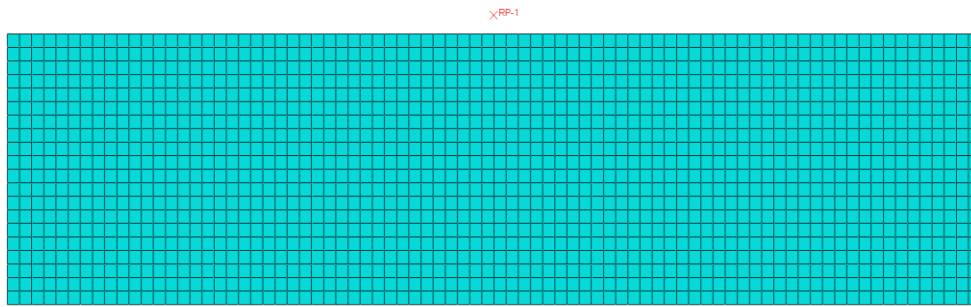
(b)

Source: Author

In the 3-point bending test model, the CMOD was obtained by the distance between two points at the notch in the middle of the prism width, as presented in Figure 124a. In addition, Figures 124b and 124c present the application area of the load displacement with a thickness of an element size and the prism support restraints, respectively. As with the compression model, one node impeded in other directions to avoid slippage. The curve force-CMOD experimental curve verified the numerical response until a 1.5 mm crack mouth opening displacement.

Figure 124: 3-point bending model details: (a) CMOD in the notch (red points), (b) area of load application, and (c) base restraints

(a)

(b)   (c)
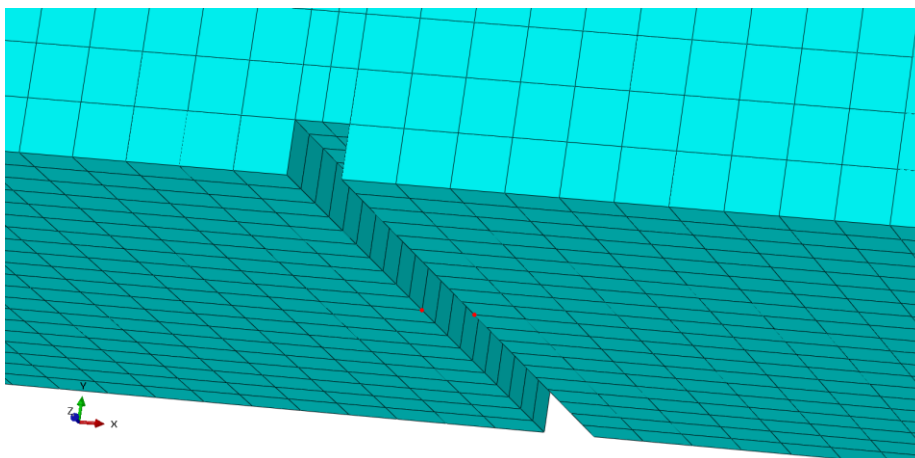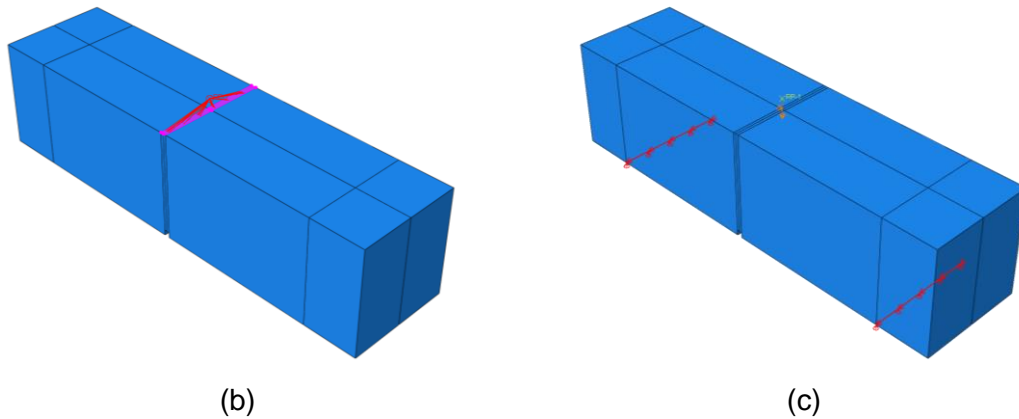
Source: Author

The 4-point bending model presents the same assembly as the 3-point bending model with the load application area and support restraints presented in Figures 125a and 125b, respectively. The experimental displacement response was measured with linear variation displacement transducers (LVDT) at the top of the prism to avoid the development of cracking. In the numerical response, the displacement is the relative distance obtained in a node localized at the top of the prism subtracted by the displacement in the supports. Figure 125c presents the nodes localized at the center of the prism, where the displacement at the top and in the supports was obtained. The numerical response was the pair displacement and force until an approximately 1.5 mm displacement was applied.

Figure 125: 4-point bending model details: (a) area of load application, (b) base restraints, and (c) displacement measure nodes (red points)

(a)   (b)

(c)
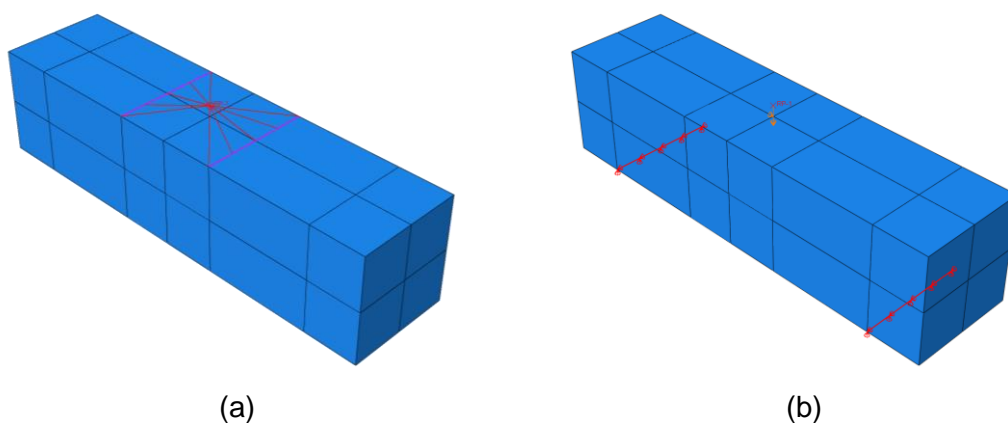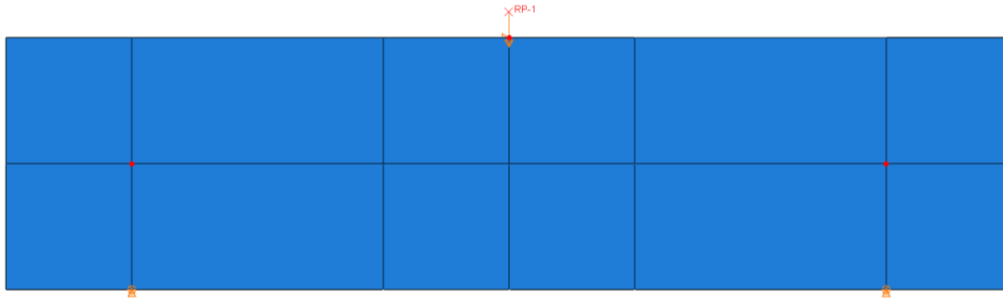
Source: Author

The tensile constitutive models were determined according to the inverse analysis response for 3-point and 4-point bending. Figure 126 presents the curves developed to cover the experimental response considering an initial linear branch, a drop or not in the multiple cracking stage, and the softening branch that varies the ultimate strain. The post-cracking branch varied to approximate the numerical to the experimental response.

Figure 126: FE tensile constitutive models: (a) 3PCM1, (b) 3PCM2, (c) 4PCM1, and (d) 4PCM2

(a)

(b)

(c)　　　　　　　　　　　　　(d)
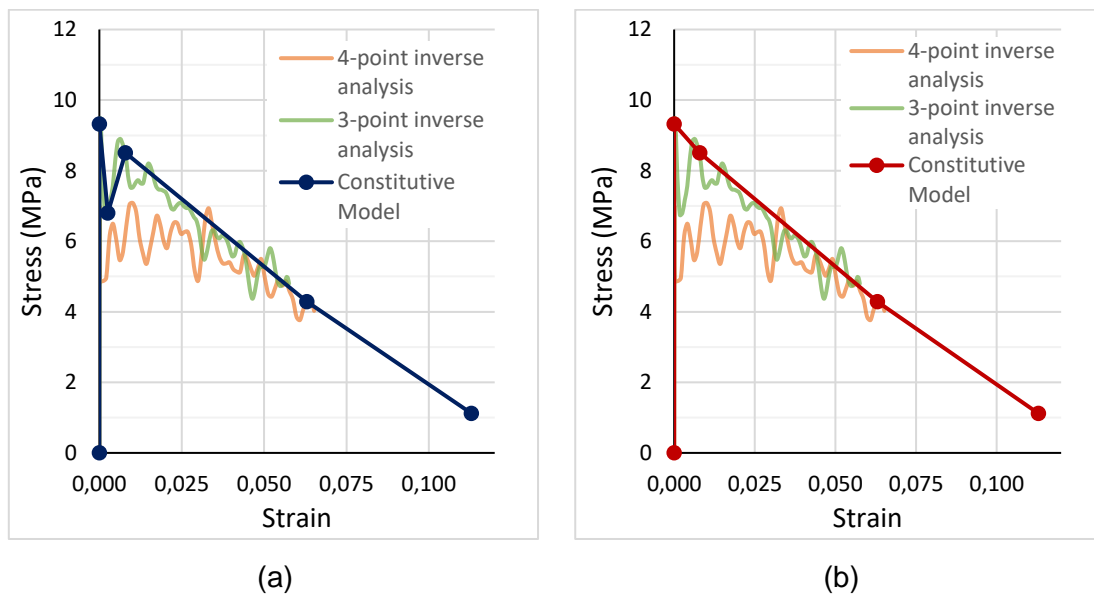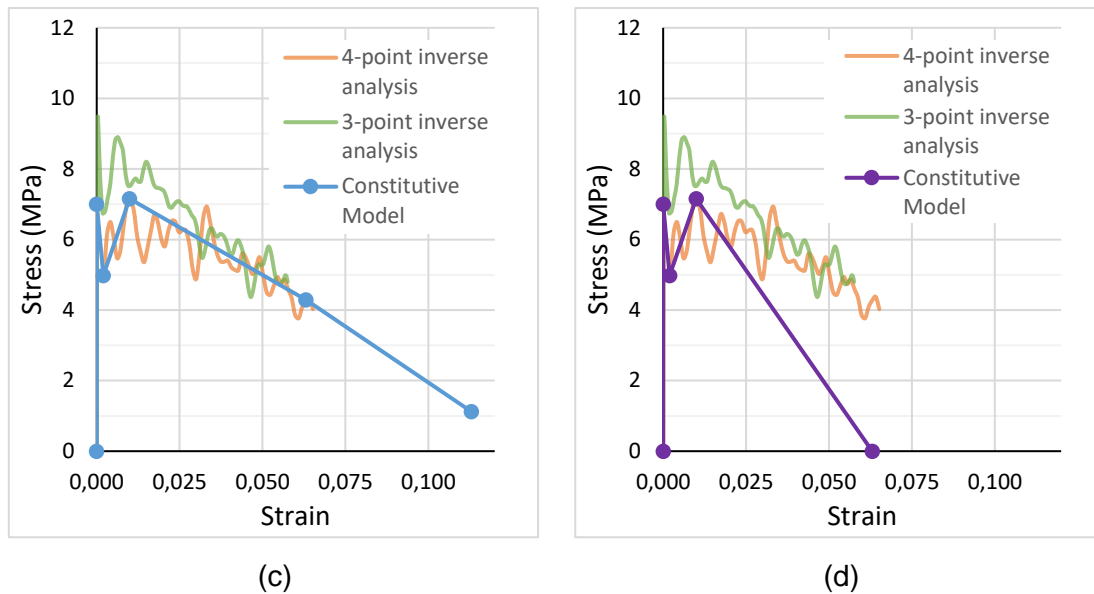
Source: Author

Considering the CDP parameters calibrated in the compressive model, the flexural models evaluated the constitutive model that approaches the numerical response to the experimental response. In the 3-point bending model, the constitutive curve referred to as 3-point inverse analysis with a drop in the multiple cracking stage (3PCM1) covers the experimental response well until approximately 0.9 mm CMOD. After that point, the curve did not decline, moving away from the target. In addition, taking into account the good responses convergence, the constitutive models of 4-point bending were tested (4PCM1 and 4PCM2) to utilize this model for both bending tests, but the result was not satisfactory, confirming the difference between each bending response, as shown in Figure 127a.

Conversely, the 4-point bending model did not converge the responses. The 4PCM1 constitutive model was tested, but the post-peak response did not decrease, presenting a high tensile strain hardening. Furthermore, the curve with a reduced ultimate strain (4PCM2) and the 3-point bending constitutive models (3PCM1 and 3PCM2) were analyzed to identify the curve parameters that managed the post-peak response but without success. Finally, it was identified that the numerical response presents two macrocracks below the load application points. This configuration did not correspond to the actual crack patterns. Therefore, a model with a 0.5 cm notch (mesh element size) was developed to

induce a single macrocrack in the failure mode (4PCM1-N). Nevertheless, the numerical response did not present a descending branch in the post-peak, as presented in Figure 127b.

Figure 127: FE flexural model definition: (a) 3-point bending and (b) 4-point bending

(a)

(b)
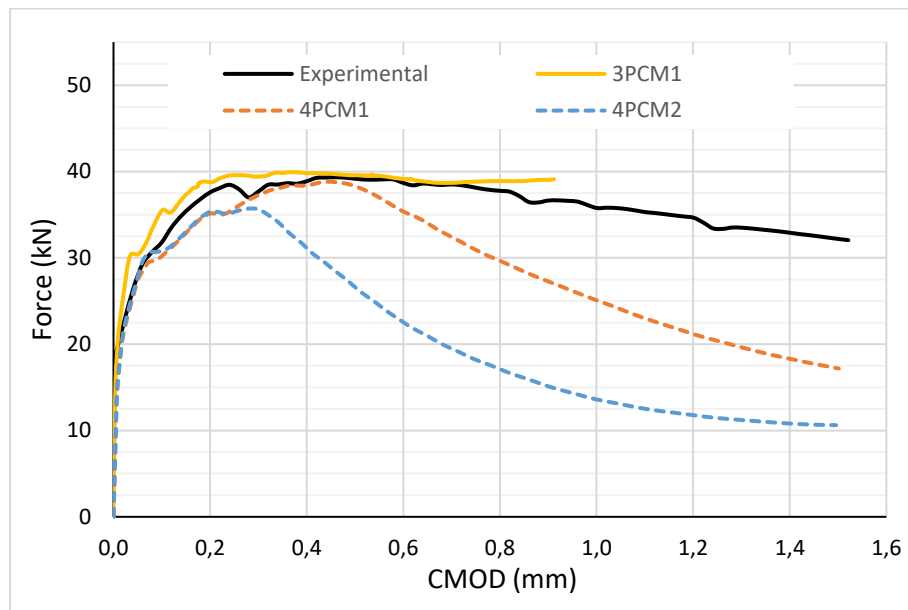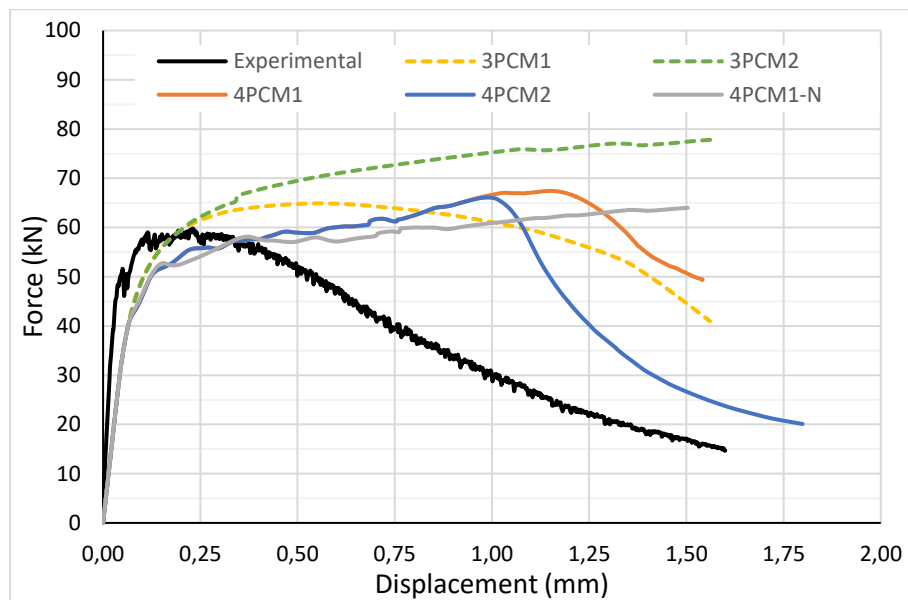
Source: Author

The failure mode and crack patterns were evaluated for 3-point and 4-point bending models to analyze the numerical response consistency. Figures 128a–c present the numerical and experimental failure modes for 3-point bending. The notch induces a single macrocrack (Figure 128b); however, the fiber bridging effect led to damage around the crack region. In addition, due to the fiber orientations, the macrocrack may incline in an unpredictable direction (Figure 128c). The 4-point bending failure mode must develop in the middle third of the span and start with multiple microcracks before the formation of the macrocrack. As aforementioned, the numerical model exhibited two macrocracks below the load points, as shown in Figure 129a. A model with a 0.5 cm notch was developed, and the failure mode resembled the actual crack patterns, as shown in Figure 129b. Figure 129c presents an experimental specimen ruptured with crack patterns similar to the FE model.

Figure 128: FE 3-point bending failure mode: (a) numerical response, (b) experimental straight crack development, and (c) experimental inclined crack development
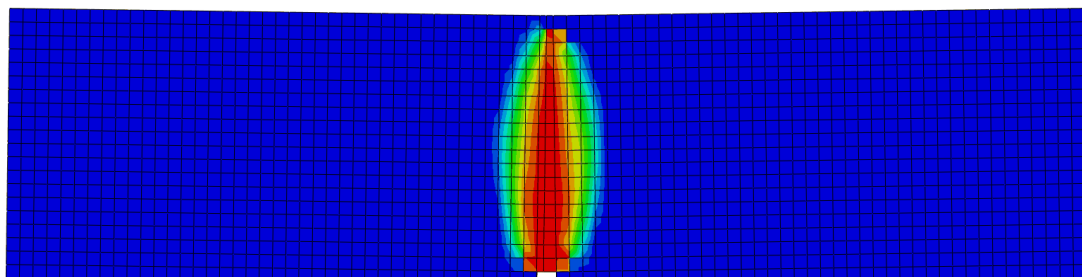
(a)

(b)

(c)

Source: Author

Figure 129: FE 4-point bending failure mode: (a) numerical response two macrocracks, (b) numerical response single macrocrack, and (c) experimental ruptured specimen

(a)

(b)

(c)
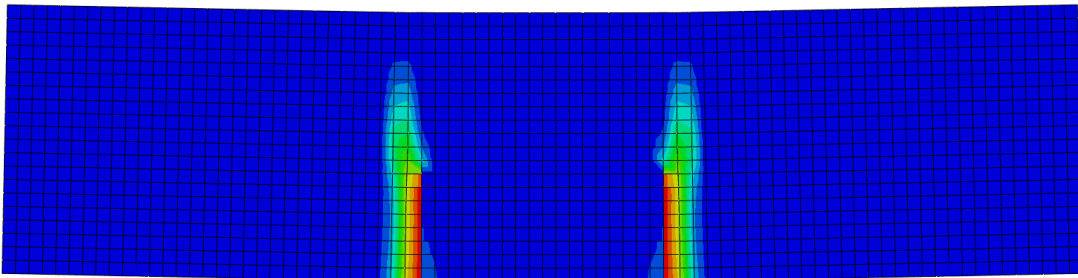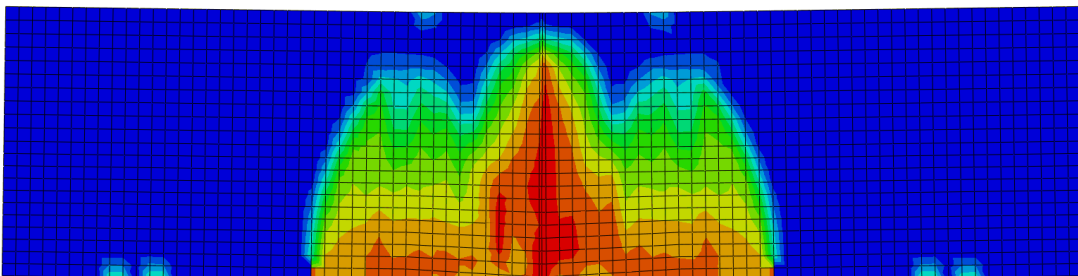
Source: Author

The 4-point cyclic bending test was modeled with the CDP-calibrated parameters and 4PCM1 constitutive model to evaluate the modeling parameters in other load conditions. The loading scheme was determined to increase 0.25 mm at each cycle with a rate of 0.125 mm per second, as presented in Figure 130a. As expected, the numerical response did not converge to the experimental

response as with the static 4-point bending analysis. As presented in Figure 130b, the model develops the cycles; however, the tensile damage variable response must be refined to change the loading/unloading slope of the damaged material. In addition, the cyclic loading scheme was performed in the 3-point bending model, but as shown in Figure 130b, the response did not converge.

Figure 130: FE cyclic flexural model definition: (a) cyclic load definition and (b) cyclic bending response
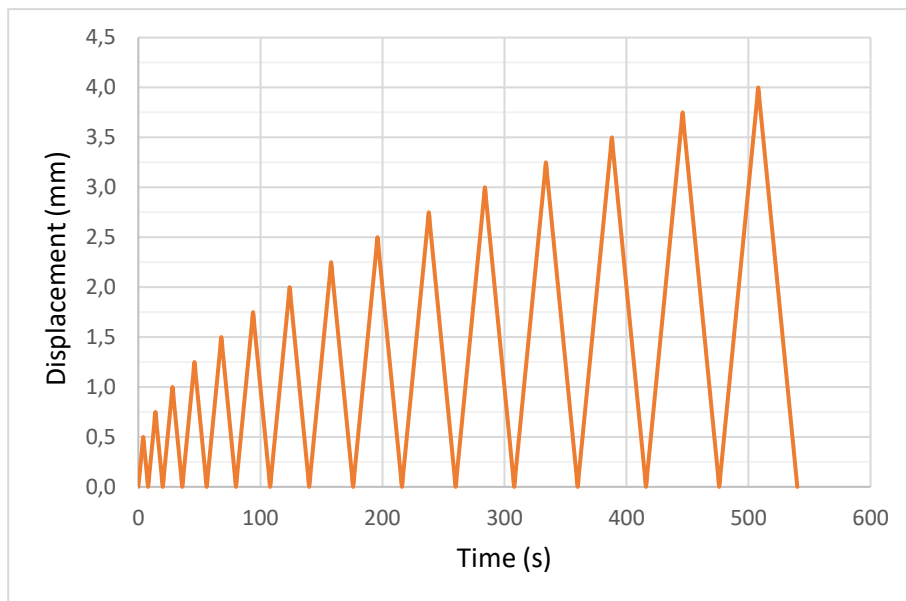
(a)
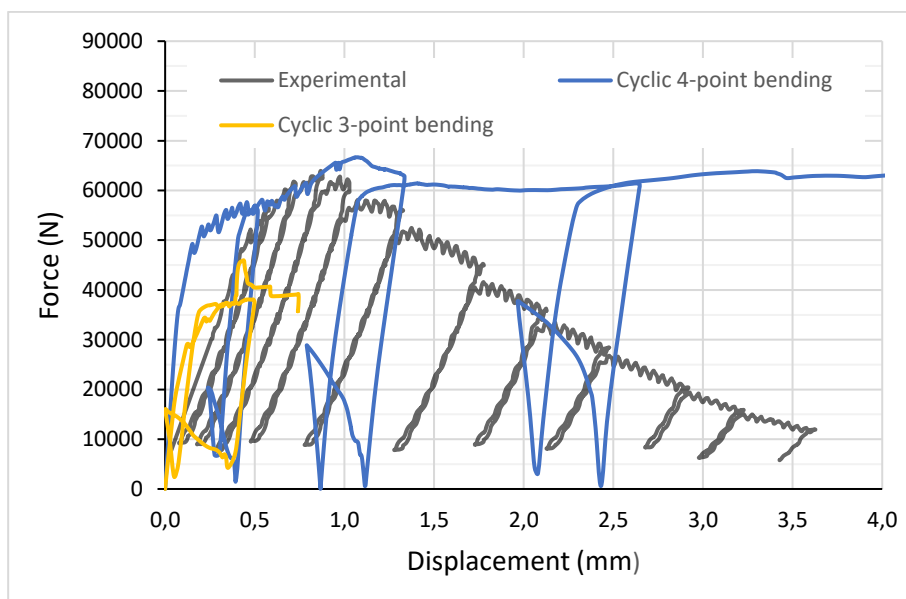
(b)

Source: Author

5.3 CONCLUDING REMARKS

The UHPC modeling was developed to replicate the mechanical test responses with the numerical CDP model and material constitutive curves. An 8-node linear element (C3D8R) with reduced integration and axisymmetric shape presented results more accurate with consistent failure modes and lower computational cost. The compression test was utilized to calibrate the CDP parameters, and the values of the better response are presented in Table 23. With the model calibrated, the 3-point and 4-point bending responses were analyzed with constitutive models determined according to the inverse analysis stress-strain curves. In the 3-point bending, the constitutive model 3PCM1 presents a curve that covers well the experimental response until approximately 0.9 mm CMOD.

Conversely, the 4-point bending response did not converge, even with different constitutive models and a 0.5 cm notch to induce a single macrocrack in the failure mode. As with the static test, the 4-point cyclic response did not replicate the experimental result; possibly, the tensile damage variable response must be refined to change the loading/unloading slope of the damaged material in the numerical response. The compression and flexural failure mode and crack patterns were evaluated, and both conditions managed a numerical response similar to the specimen ruptured.

Table 23: Calibrated UHPC CDP parameters

Dilation Angle	Eccentricity	f_{b0}/f_{c0}	K	Viscosity Parameter
56	0.1	1.16	0.6667	0.000001

Source: Author

6 CONCLUSIONS

The main objective of this work is to develop a methodology to design, produce and evaluate UHPC mixture utilizing local materials and available regular laboratory equipment, seeking the best properties with them. A study of each UHPC component, mixture design, and production method was necessary to understand which parameters are fundamental for better material selection and carefulness in the mix procedures.

The methodology is based on evaluating the available materials according to the defined selection criteria and utilizing the production methods tested to achieve the desired UHPC properties. In selecting materials, mineralogical and chemical compositions and particle size are necessary for an adequate decision. The quantity of each constituent material is influenced by particle packing, workability, and indirectly, density. The better possibility is to choose particle sizes in which the smaller grains fill the space between bigger grains. In addition, using materials with pozzolanic activity improves the material microstructure. The production methods tested suggest that the four-stage mix procedure presents better results for workability and durability with high cement content, allowing greater mechanical strengths. Furthermore, the standard placement, consolidation, demolding, and curing processes ensure the material quality.

After determining the primary composed mix curve with the design method, the compressive strength evolution methodology suggest some adjustments to refine the mix design to obtain the required properties. The best adjustments in the mix proportions were the water-cement ratio reduction and the SF in an aqueous medium, with a 12.5% and 16% compressive strength increase, respectively. The addition of the fibers resulted in a 28% increase in the 7 d compressive strength. The specimen size influenced the compression response in this part of the work. High value discrepancies and a columnar failure mode for the 5 × 10 cm size may indicate an eccentricity in the test applied load. Therefore, the 10 × 20 cm specimen size and rigorous control of the specimens' top and bottom surfaces leveling are recommended to obtain a consistent response.

The physical and mechanical characterization of UHPC using the available local laboratory equipment, confirms the outstanding material behavior. The complete compression behavior was obtained with the linear initial ascending

stage, the post-peak response, and a 130.95 MPa 28-day compressive strength. In addition, the UHPC at 7 days presented approximately 80% of the 28 days' strength, and the influence of the test strain rate was confirmed with an increase of 4% in the peak strength.

The tensile behavior was evaluated by splitting and flexural tests. The former presented an initial linear branch, and then a post-peak descending curve with a maximum splitting tensile strength ($f_{ct,sp}$) of 18.35 MPa at 28 days. In addition, due to the pullout resistance being higher than the specimen deformability stress, preventing the split, the load area varies during the test. It presents oscillations in the response mainly due to specimen squeezing, including strength increases in the descending branch.

In the flexural tests, the stress-strain tensile curves were obtained by an inverse analysis method for 3-point and 4-point bending, described in NF P18-470 (AFNOR, 2016). The 28-day tensile elastic and maximum strengths were 6.99 and 9.32 for 3-point bending, respectively, and 6.50 and 7.08 for 4-point bending, respectively. Furthermore, simplified inverse methods were analyzed and observed that some represents better the strain-softening behavior and others the strain-hardening. The AFNOR (2016) simplified responses and JSCE simplified 3-point inverse analysis presented responses that better fit with the point-by-point inverse analysis compared with the proposed methods studied in the literature.

To evaluate the UHPC damage behavior, cyclic tests were performed in compression and bending. In the cyclic compression response, the curves did not present the ductile post-peak behavior, and the damage variable was not determined. The tension damage curve was determined by a 4-point bending cyclic test with a high initial value (0.92) due to previous initial damage in the specimens.

Regarding the mechanical, workability, and durability properties were verified; and it was noted that every value obtained was higher than the minimum specified in NF P18-470 (AFNOR, 2016). The material was classified as viscous UHPC class and considered suitable for most structural applications, with care needed for possible air entrapment and problems in the corner filling. Furthermore, the determined air content in the fresh state was 1.02%, and water

porosity in the hardening state was 3.0%. These parameters were considered notable according to the references studied.

Lastly, a numerical model was developed to obtain parameters to make possible the structural simulations in several scenarios. The UHPC modeling was developed to replicate the mechanical test responses with the numerical CDP model and material constitutive curves. The compression test was utilized to calibrate the CDP parameters, and then they were utilized in the 3-point and 4-point bending models. In the 3-point bending, the numerical response covers well the experimental curve until approximately 0.9 mm CMOD. Conversely, the 4-point bending response did not converge, even with different constitutive models and setups. In addition, the cyclic 4-point bending test was not possible to replicate; possibly, the tensile damage variable response must be refined to change the loading/unloading slope of the damaged material. The compression and flexural failure mode and crack patterns were evaluated, and both conditions managed a numerical response similar to the specimen that ruptured.

As a suggestion for future works, an optimization method in the mix design to reduce cement consumption may assist the development of UHPC as a sustainable material. Performing the cyclic test with different setups to try to obtain the compression damage parameter and the tensile damage parameter at lower strains may improve the numerical response, including the cyclic.

7 REFERENCES

ABBAS, S.; SOLIMAN, A.; NEHDI, M. Exploring mechanical and durability properties of ultra-high performance concrete incorporating various steel fiber lengths and dosages. **Construction and Building Materials**, v. 75, p. 429-441, 2015.

ALKAYSI, M.; EL-TAWIL, S.; LIU, Z.; HANSEN, W. Effects of silica powder and cement type on durability of ultra high performance concrete (UHPC). **Cement and Concrete Composites**, v. 66, p. 47-56, 2016.

AL-OBAIDI, S.; BAMONTE, P.; LUCHINI, M.; MAZZANTINI, I.; FERRARA, L. Durability-based design of structures made with ultra-high-performance/ultra-high-durability concrete in extremely aggressive scenarios: Application to a geothermal water basin case study. **Infrastructures**, v. 5, n. 11, p. 102, 2020.

AMERICAN SOCIETY FOR TESTING AND MATERIALS (ASTM). **ASTM C150 – Standard Specification for Portland Cement.** West Conshohocken, p. 9. 2020.

ASSOCIAÇÃO BRASILEIRA DE NORMAS TÉCNICAS (ABNT). **NBR NM 248 – Aggregates – Sieve analysis of fine and coarse aggregates.** Rio de Janeiro, p. 6. 2003.

ASSOCIAÇÃO BRASILEIRA DE NORMAS TÉCNICAS (ABNT). **NBR 9778 – Hardened mortar and concrete – Determination of absorption, voids and specific gravity.** Rio de Janeiro, p. 4. 2005.

ASSOCIAÇÃO BRASILEIRA DE NORMAS TÉCNICAS (ABNT). **NBR 9833 – Fresh concrete – Determination of the unit weight, yield and air content by gravimetric test method.** Rio de Janeiro, p. 7. 2008.

ASSOCIAÇÃO BRASILEIRA DE NORMAS TÉCNICAS (ABNT). **NBR 7211 – Aggregates for concrete – Specification.** Rio de Janeiro, p. 9. 2009.

ASSOCIAÇÃO BRASILEIRA DE NORMAS TÉCNICAS (ABNT). **NBR 7222 – Concrete and mortar – Determination of the tension strength by diametrical compression of cylindrical test specimens.** Rio de Janeiro, p. 5. 2011.

ASSOCIAÇÃO BRASILEIRA DE NORMAS TÉCNICAS (ABNT). **NBR 13956-1 – Silica fume for use with Portland cement in concrete, mortar and paste – Part 1: Requirements.** Rio de Janeiro, p. 6. 2012.

ASSOCIAÇÃO BRASILEIRA DE NORMAS TÉCNICAS (ABNT). **NBR 5738 – Concrete – Procedure for molding and curing concrete test specimens.** Rio de Janeiro, p. 9. 2015.

ASSOCIAÇÃO BRASILEIRA DE NORMAS TÉCNICAS (ABNT). **NBR 15823-1 – Self-consolidating concrete Part 1: Classification, control and receipt in the fresh state.** Rio de Janeiro, p. 14. 2017.

ASSOCIAÇÃO BRASILEIRA DE NORMAS TÉCNICAS (ABNT). **NBR 15823-2 – Self-consolidating concrete Part 2: Slump-flow test, flow time and visual stability index – Abrams cone method.** Rio de Janeiro, p. 5. 2017.

ASSOCIAÇÃO BRASILEIRA DE NORMAS TÉCNICAS (ABNT). **NBR 16605 – Portland cement and Other powdered material – Determination of the specific gravity.** Rio de Janeiro, p. 4. 2017.

ASSOCIAÇÃO BRASILEIRA DE NORMAS TÉCNICAS (ABNT). **NBR 16697 – Portland cement – Requirements.** Rio de Janeiro, p. 16. 2018.

ASSOCIAÇÃO BRASILEIRA DE NORMAS TÉCNICAS (ABNT). **NBR 11768-1 – Chemical admixtures for Portland cement concrete – Part 1: Requirements.** Rio de Janeiro, p. 27. 2019.

ASSOCIAÇÃO BRASILEIRA DE NORMAS TÉCNICAS (ABNT). **NBR 16916 – Fine aggregate – Determination of density and water adsorption.** Rio de Janeiro, p. 7. 2021.

ASSOCIAÇÃO BRASILEIRA DE NORMAS TÉCNICAS (ABNT). **NBR 8522-1 – Hardened concrete – Determination of elasticity and deformation modulus Part 1: Static modulus by compression.** Rio de Janeiro, p. 24. 2021.

ASSOCIATION FRANÇAISE DE NORMALISATION (AFNOR). **NF P18-470 – Concrete – Ultra-high performance fibre-reinforced concrete – Specifications, performance, production and conformity**. Paris, 2016.

ASSOCIATION FRANÇAISE DE NORMALISATION (AFNOR). **NF P18-710 – National addition to Eurocode 2 – Design of concrete structures: specific**

rules for Ultra-High Performance Fibre-Reinforced Concrete (UHPFRC).
Paris, 2016.

BABY, Florent. **Contribution à l'identification et la prise en compte du comportement en traction des BFUP à l'échelle de la structure**. 2012. PhD Thesis. Université Paris-Est.

BABY, F.; GRAYBEAL, B.; MARCHAND, P.; TOUTLEMONDE, F. Proposed flexural test method and associated inverse analysis for ultra-high-performance fiber-reinforced concrete. **ACI Materials Journal**, v. 109, n. 5, p. 545, 2012.

BARIL, M. A.; SORELLI, L.; RÉTHORÉ, J.; BABY, F.; TOUTLEMONDE, F.; FERRARA, L.; BERNARDI, S.; FAFARD, M. Effect of casting flow defects on the crack propagation in UHPFRC thin slabs by means of stereovision Digital Image Correlation. **Construction and building materials**, v. 129, p. 182-192, 2016.

BASTIEN-MASSE, M.; BRÜHWILER, E. Composite model for predicting the punching resistance of R-UHPFRC–RC composite slabs. **Engineering Structures**, v. 117, p. 603-616, 2016.

BEKAERT. EC Declaration of Performance of the product Dramix® OL 13/.20. Available in: < https://www.bekaert.com/doc/Dramix_OL > Accessed on: May 27, 2023

BENEFICIAMENTO DE MINÉRIOS RIO CLARO (BMRC). **Chemical analysis report**. Available in: https://bmrc.com.br/produtos/analises/. Accessed on: May 27, 2023

CHEN, J. J.; KWAN, A. K. H. Superfine cement for improving packing density, rheology and strength of cement paste. **Cement and Concrete Composites**, v. 34, n. 1, p. 1-10, 2012.

COURTIAL, M.; NOIRFONTAINE, M.; DUNSTETTER, F.; SIGNES-FREHEL, M.; MOUNANGA, P.; CHERKAOUI, K.; KHELIDJ, A. Effect of polycarboxylate and crushed quartz in UHPC: Microstructural investigation. **Construction and Building Materials**, v. 44, p. 699-705, 2013.

DE LARRARD, F.; SEDRAN, T. Optimization of ultra-high-performance concrete by the use of a packing model. **Cement and concrete research**, v. 24, n. 6, p. 997-1009, 1994.

DE LARRARD, F.; SEDRAN, T. Mixture-proportioning of high-performance concrete. **Cement and concrete research**, v. 32, n. 11, p. 1699-1704, 2002.

DILS, J.; BOEL, V.; DE SCHUTTER, G. Influence of cement type and mixing pressure on air content, rheology and mechanical properties of UHPC. **Construction and Building Materials**, v. 41, p. 455-463, 2013.

FAKEH, M.; JAWDHARI, A.; FAM, A. Calibration of ABAQUS Concrete Damage Plasticity (CDP) Model for UHPC Material. In: **International Interactive Symposium on Ultra-High Performance Concrete**. Iowa State University Digital Press, 2023.

FÉDÉRATION INTERNATIONALE DU BÉTON (FIB). **Model Code 2010. No. vol. 65 in fib Bulletin**, International Federation for Structural Concrete (fib). 2012.

GARAS, V.; KURTIS, K.; KAHN, L. Creep of UHPC in tension and compression: effect of thermal treatment. **Cement and Concrete Composites**, v. 34, n. 4, p. 493-502, 2012.

GHAFARI, E.; AREZOUMANDI, M.; COSTA, H.; JÚLIO, E. Influence of nano-silica addition on durability of UHPC. **Construction and Building Materials**, v. 94, p. 181-188, 2015.

GHAFARI, E.; COSTA, H.; JÚLIO, E.; PORTUGAL, A.; DURÃES, L. The effect of nanosilica addition on flowability, strength and transport properties of ultra high performance concrete. **Materials & Design**, v. 59, p. 1-9, 2014.

GRAYBEAL, B. Compressive behavior of ultra-high-performance fiber-reinforced concrete. **ACI materials journal**, v. 104, n. 2, p. 146, 2007.

GRAYBEAL, B. Flexural behavior of an ultrahigh-performance concrete I-girder. **Journal of Bridge Engineering**, v. 13, n. 6, p. 602-610, 2008.

GRAYBEAL, B.; BABY, F. Development of direct tension test method for ultra-high-performance fiber-reinforced concrete. **ACI Materials Journal**, v. 110, n. 2, p. 177, 2013.

GU, C.; SUN, W.; GUO, L.; WANG, Q. Effect of curing conditions on the durability of ultra-high performance concrete under flexural load. **Journal of Wuhan University of Technology-Mater. Sci. Ed.**, v. 31, n. 2, p. 278-285, 2016.

HAFIZ, M.; DENARIE, E. Modelling of the tensile behavior of SH-UHPFRC at low and high stress levels, under very low loading rates. **Construction and Building Materials**, v. 255, p. 119338, 2020.

HANNAWI, K.; BIAN, H.; PRINCE-AGBODJAN, W.; RAGHAVAN, B. Effect of different types of fibers on the microstructure and the mechanical behavior of ultra-high performance fiber-reinforced concretes. **Composites Part B: Engineering**, v. 86, p. 214-220, 2016.

HELMI, M.; HALL, M.; STEVENS, L.; RIGBY, S. Effects of high-pressure/temperature curing on reactive powder concrete microstructure formation. **Construction and building materials**, v. 105, p. 554-562, 2016.

HIREMATH, P.; YARAGAL, S. Influence of mixing method, speed and duration on the fresh and hardened properties of Reactive Powder Concrete. **Construction and Building Materials**, v. 141, p. 271-288, 2017.

HUANG, H.; GAO, X.; KHAYAT, K. Contribution of fiber alignment on flexural properties of UHPC and prediction using the Composite Theory. **Cement and Concrete Composites**, v. 118, p. 103971, 2021.

IPEK, M; YILMAZ, K; SÜMER, M; SARIBIYIK, M. Effect of pre-setting pressure applied to mechanical behaviours of reactive powder concrete during setting phase. **Construction and Building Materials**, v. 25, n. 1, p. 61-68, 2011.

IPEK, M.; YILMAZ, K.; UYSAL, M. The effect of pre-setting pressure applied flexural strength and fracture toughness of reactive powder concrete during the setting phase. **Construction and Building Materials**, v. 26, n. 1, p. 459-465, 2012.

ITAMBÉ®. Available in: < https://www.cimentoitambe.com.br/>. Accessed in: June 18, 2021.

JUSTS, J.; WYRZYKOWSKI, M.; BAJARE, D.; LURA, P. Internal curing by superabsorbent polymers in ultra-high performance concrete. **Cement and Concrete Research**, v. 76, p. 82-90, 2015.

KANG, S.; KIM, J. The relation between fiber orientation and tensile behavior in an Ultra High Performance Fiber Reinforced Cementitious Composites (UHPFRCC). **Cement and Concrete Research**, v. 41, n. 10, p. 1001-1014, 2011.

KANG, S.; KIM, J. Numerical simulation of the variation of fiber orientation distribution during flow molding of ultra high performance cementitious composites (UHPCC). **Cement and Concrete Composites**, v. 34, n. 2, p. 208-217, 2012.

KANG, S.; CHOI, J.; KOH, K.; LEE, K.; LEE, B. Hybrid effects of steel fiber and microfiber on the tensile behavior of ultra-high performance concrete. **Composite Structures**, v. 145, p. 37-42, 2016.

KIM, J.; LIM, W. Prediction of compressive strength and elastic modulus for ultra-high-performance concrete. **Construction and Building Materials**, v. 363, p. 129883, 2023.

KRAHL, P.; CARRAZEDO, R.; EL DEBS, M. Mechanical damage evolution in UHPFRC: Experimental and numerical investigation. **Engineering Structures**, v. 170, p. 63-77, 2018.

KWON, S.; KANG, S.; LEE, B. Y.; KIM, J. The variation of flow-dependent tensile behavior in radial flow dominant placing of Ultra High Performance Fiber Reinforced Cementitious Composites (UHPFRCC). **Construction and Building Materials**, v. 33, p. 109-121, 2012.

LEE, N.; KOH, K.; KIM, M.; RYU, G. Uncovering the role of micro silica in hydration of ultra-high performance concrete (UHPC). **Cement and Concrete Research**, v. 104, p. 68-79, 2018.

LI, W.; HUANG, Z.; HU, G.; DUAN, W.; SHAH, S. Early-age shrinkage development of ultra-high-performance concrete under heat curing treatment. **Construction and Building Materials**, v. 131, p. 767-774, 2017.

LI, L.; KWAN, A. Effects of superplasticizer type on packing density, water film thickness and flowability of cementitious paste. **Construction and Building Materials**, v. 86, p. 113-119, 2015.

LI, P.; YU, Q.; BROUWERS, H. Effect of PCE-type superplasticizer on early-age behaviour of ultra-high performance concrete (UHPC). **Construction and Building Materials**, v. 153, p. 740-750, 2017.

LIN, Y.; YAN, J.; WANG, Z.; FAN, F.; ZOU, C. Effect of silica fumes on fluidity of UHPC: Experiments, influence mechanism and evaluation methods. **Construction and Building Materials**, v. 210, p. 451-460, 2019.

LIU, J.; SHI, C.; MA, X.; KHAYAT, K.; ZHANG, J.; WANG, D. An overview on the effect of internal curing on shrinkage of high performance cement-based materials. **Construction and Building Materials**, v. 146, p. 702-712, 2017.

LÓPEZ, J.; SERNA, P.; NAVARRO-GREGORI, J.; CAMACHO, E. An inverse analysis method based on deflection to curvature transformation to determine the tensile properties of UHPFRC. **Materials and Structures**, v. 48, p. 3703-3718, 2015.

MC BAUCHEMIE BRASIL INDUSTRIA E COM. LDTA. **Quality Certificate of the product CENTRILIT FUME S – AMT – 01**. Vargem Grande Paulista, 2020.

MC BAUCHEMIE BRASIL INDUSTRIA E COM. LDTA. **Quality Certificate of the product MC-POWERFLOW 4001 – AMT – 01**. Vargem Grande Paulista, 2020.

MENG, W.; KHAYAT, K. Effects of saturated lightweight sand content on key characteristics of ultra-high-performance concrete. **Cement and Concrete Research**, v. 101, p. 46-54, 2017.

MENG, W.; YAO, Y.; MOBASHER, B.; KHAYAT, K. Effects of loading rate and notch-to-depth ratio of notched beams on flexural performance of ultra-high-performance concrete. **Cement and Concrete Composites**, v. 83, p. 349-359, 2017.

MOHAMMED, T.; BAKAR, B.; BUNNORI, N. Torsional improvement of reinforced concrete beams using ultra high-performance fiber reinforced concrete (UHPFC) jackets–experimental study. **Construction and Building Materials**, v. 106, p. 533-542, 2016.

NGO, T.; PARK, J.; PYO, S.; KIM, D. Shear resistance of ultra-high-performance fiber-reinforced concrete. **Construction and Building Materials**, v. 151, p. 246-257, 2017.

NOWAK-MICHTA, Aneta. Additional Porosity as a Side Effect of Polycarboxylate Addition and Its Influence on Concrete's Scaling Resistance. **Materials**, v. 13, n. 2, p. 316, 2020.

OERTEL, T.; HUTTER, F.; TÄNZER, R.; HELBIG, U.; SEXTL, G. Primary particle size and agglomerate size effects of amorphous silica in ultra-high

performance concrete. **Cement and Concrete Composites**, v. 37, p. 61-67, 2013.

OERTEL, T.; HUTTER, F.; HELBIG, U.; SEXTL, G. Amorphous silica in ultra-high performance concrete: First hour of hydration. **Cement and concrete research**, v. 58, p. 131-142, 2014.

PARK, J.; YOO, D.; PARK, G.; KIM, S. Feasibility of reducing the fiber content in ultra-high-performance fiber-reinforced concrete under flexure. **Materials**, v. 10, n. 2, p. 118, 2017.

POURBABA, M.; JOGHATAIE, A.; MIRMIRAN, A. Shear behavior of ultra-high performance concrete. **Construction and Building Materials**, v. 183, p. 554-564, 2018.

PREM, P.; MURTHY, A.; BHARATKUMAR, B. Influence of curing regime and steel fibres on the mechanical properties of UHPC. **Magazine of Concrete Research**, v. 67, n. 18, p. 988-1002, 2015.

PYO, S.; EL-TAWIL, S.; NAAMAN, A. Direct tensile behavior of ultra high performance fiber reinforced concrete (UHP-FRC) at high strain rates. **Cement and Concrete Research**, v. 88, p. 144-156, 2016.

QI, J.; CHENG, Z.; ZHOU, K.; ZHU, Y.; WANG, J.; BAO, Y. Experimental and theoretical investigations of UHPC-NC composite slabs subjected to punching shear-flexural failure. **Journal of Building Engineering**, v. 44, p. 102662, 2021.

QIAN, S.; LI, V. Simplified inverse method for determining the tensile strain capacity of strain hardening cementitious composites. **Journal of Advanced Concrete Technology**, v. 5, n. 2, p. 235-246, 2007.

QIAN, S.; LI, V. Simplified inverse method for determining the tensile properties of strain hardening cementitious composites (SHCC). **Journal of Advanced Concrete Technology**, v. 6, n. 2, p. 353-363, 2008.

QIU, M.; SHAO, X.; ZHU, Y.; ZHAN, J.; YAN, B.; WANG, Y. Experimental investigation on flexural cracking behavior of ultrahigh performance concrete beams. **Structural Concrete**, v. 21, n. 5, p. 2134-2153, 2020.

RICHARD, P.; CHEYREZY, M. Composition of reactive powder concretes. **Cement and concrete research**, v. 25, n. 7, p. 1501-1511, 1995.

ROSSI, P. Influence of fibre geometry and matrix maturity on the mechanical performance of ultra high-performance cement-based composites. **Cement and Concrete Composites**, v. 37, p. 246-248, 2013.

ROSSI, P.; DAVIAU-DESNOYERS, D.; TAILHAN, J. Probabilistic numerical model of cracking in ultra-high performance fibre reinforced concrete (UHPFRC) beams subjected to shear loading. In: **International Interactive Symposium on Ultra-High Performance Concrete**. Iowa State University Digital Press, 2016.

SAVINO, V.; LANZONI, L.; TARANTINO, A.; VIVIANI, M. Tensile constitutive behavior of high and ultra-high performance fibre-reinforced-concretes. **Construction and Building Materials**, v. 186, p. 525-536, 2018.

SCHACHINGER, I.; SCHUBERT, J.; MAZANEC, O. Effect of mixing and placement methods on fresh and hardened ultra high performance concrete (UHPC). In: **International Symposium on Ultra High Performance Concrete**. 2004. p. 575-586.

SCHRÖFL, Ch.; GRUBER, M.; PLANK, J. Preferential adsorption of polycarboxylate superplasticizers on cement and silica fume in ultra-high performance concrete (UHPC). **Cement and Concrete Research**, v. 42, n. 11, p. 1401-1408, 2012.

SHAFIEIFAR, M.; FARZAD, M.; AZIZINAMINI, A. A comparison of existing analytical methods to predict the flexural capacity of Ultra High Performance Concrete (UHPC) beams. **Construction and Building Materials**, v. 172, p. 10-18, 2018.

SINGH, M.; SHEIKH, A.; MOHAMED ALI, M.; VISINTIN, P.; GRIFFITH, M. Experimental and numerical study of the flexural behaviour of ultra-high performance fibre reinforced concrete beams. **Construction and Building Materials**, v. 138, p. 12-25, 2017.

SOBUZ, H.; VISINTIN, P.; MOHAMED ALI, M.; SINGH, M.; GRIFFITH, M.; SHEIKH, A. Manufacturing ultra-high performance concrete utilising conventional materials and production methods. **Construction and Building materials**, v. 111, p. 251-261, 2016.

SORANAKOM, C.; MOBASHER, B. Closed-form solutions for flexural response of fiber-reinforced concrete beams. **Journal of engineering mechanics**, v. 133, n. 8, p. 933-941, 2007.

SORANAKOM, C.; MOBASHER, B. Correlation of tensile and flexural responses of strain softening and strain hardening cement composites. **Cement and concrete Composites**, v. 30, n. 6, p. 465-477, 2008.

ŠVEC, O.; ŽIRGULIS, G.; BOLANDER, J.; STANG, H. Influence of formwork surface on the orientation of steel fibres within self-compacting concrete and on the mechanical properties of cast structural elements. **Cement and Concrete Composites**, v. 50, p. 60-72, 2014.

SWITEK-REY, A.; DENARIÉ, E.; BRÜHWILER, E. Early age creep and relaxation of UHPFRC under low to high tensile stresses. **Cement and Concrete Research**, v. 83, p. 57-69, 2016.

TAM, C.; TAM, V.; NG, K. Assessing drying shrinkage and water permeability of reactive powder concrete produced in Hong Kong. **Construction and Building Materials**, v. 26, n. 1, p. 79-89, 2012.

TECNOSIL INDUSTRIA E COMÉRCIO MAT CONTRUÇÃO LTDA. **Certificate of Analysis of the product DOWSIL^{TM} SM Silica Fume G94**. Santos Dumont, 2019.

VAN, V.; RÖßLER, C.; BUI, D.; LUDWING, H. Rice husk ash as both pozzolanic admixture and internal curing agent in ultra-high performance concrete. **Cement and Concrete Composites**, v. 53, p. 270-278, 2014.

VERONESE, R.; MEDEIROS, W.; PARSEKIAN, G.; SHRIVE, N. Numerical analysis of eco-friendly ductile cementitious composite influence on structural masonry reinforcement. **Engineering Structures**, v. 252, p. 113686, 2022.

VOIT, K.; KIRNBAUER, J. Tensile characteristics and fracture energy of fiber reinforced and non-reinforced ultra high performance concrete (UHPC). **International Journal of Fracture**, v. 188, p. 147-157, 2014.

UCHIDA, Y.; NIWA, J.; TANAKA, Y.; KATAGIRI, M. Outlines of 'Recommendations for design and construction of ultra high strength fiber reinforced concrete structures' by JSCE. In: **Proc., Int. Workshop on High Performance Fiber Reinforced Cementitious Composites in Structural Applications**. 2005.

WANG, J.; CHEN, Z.; WU, K. Properties of calcium sulfoaluminate cement made ultra-high performance concrete: Tensile performance, acoustic emission

monitoring of damage evolution and microstructure. **Construction and Building Materials**, v. 208, p. 767-779, 2019.

WANG, R.; GAO, X. Relationship between flowability, entrapped air content and strength of UHPC mixtures containing different dosage of steel fiber. **Applied Sciences**, v. 6, n. 8, p. 216, 2016.

WANG, W.; LIU, J.; AGOSTINI, F.; DAVY, C.; SKOCZYLAS, F.; CORVEZ, D. Durability of an ultra high performance fiber reinforced concrete (UHPFRC) under progressive aging. **Cement and Concrete Research**, v. 55, p. 1-13, 2014.

WANG, C.; YANG, C.; LIU, F.; WAN, C.; PU, X. Preparation of ultra-high performance concrete with common technology and materials. **Cement and concrete composites**, v. 34, n. 4, p. 538-544, 2012.

WILLE, K.; NAAMAN, A.; EL-TAWIL, S.; PARRA-MONTESINOS, G. Ultra-high performance concrete and fiber reinforced concrete: achieving strength and ductility without heat curing. **Materials and structures**, v. 45, n. 3, p. 309-324, 2012.

WILLE, K.; EL-TAWIL, S.; NAAMAN, A. Properties of strain hardening ultra high performance fiber reinforced concrete (UHP-FRC) under direct tensile loading. **Cement and Concrete Composites**, v. 48, p. 53-66, 2014.

WILLE, K.; PARRA-MONTESINOS, G. Effect of Beam Size, Casting Method, and Support Conditions on Flexural Behavior of Ultra-High-Performance Fiber-Reinforced Concrete. **ACI Materials Journal**, v. 109, n. 3, 2012.

WU, Z.; SHI, C.; HE, W.; WANG, D. Static and dynamic compressive properties of ultra-high performance concrete (UHPC) with hybrid steel fiber reinforcements. **Cement and Concrete Composites**, v. 79, p. 148-157, 2017.

WU, Z.; SHI, C.; KHAYAT, K. Influence of silica fume content on microstructure development and bond to steel fiber in ultra-high strength cement-based materials (UHSC). **Cement and Concrete Composites**, v. 71, p. 97-109, 2016.

WU, Z.; SHI, C.; KHAYAT, K. Investigation of mechanical properties and shrinkage of ultra-high performance concrete: Influence of steel fiber content and shape. **Composites Part B: Engineering**, v. 174, p. 107021, 2019.

XIE, T.; FANG, C.; MOHAMAD ALI, M.; VISINTIN, P. Characterizations of autogenous and drying shrinkage of ultra-high performance concrete (UHPC): An experimental study. **Cement and Concrete Composites**, v. 91, p. 156-173, 2018.

XU, Y.; LIU, J.; LIU, J.; ZHANG, P.; ZHANG, Q.; JIANG, L. Experimental studies and modeling of creep of UHPC. **Construction and Building Materials**, v. 175, p. 643-652, 2018.

XU, M.; WILLE, K. Fracture energy of UHP-FRC under direct tensile loading applied at low strain rates. **Composites Part B: Engineering**, v. 80, p. 116-125, 2015.

YANG, I.; JOH, C.; BUI, T. Estimating the tensile strength of ultrahigh-performance fiber-reinforced concrete beams. **Advances in Materials Science and Engineering**, v. 2019, 2019.

YANG, I.; JOH, C.; KIM, B. Flexural response predictions for ultra-high-performance fibre-reinforced concrete beams. **Magazine of Concrete Research**, v. 64, n. 2, p. 113-127, 2012.

YANG, I.; JOH, C.; LEE, J.; KIM, B. Torsional behavior of ultra-high performance concrete squared beams. **Engineering Structures**, v. 56, p. 372-383, 2013.

YANG, I.; PARK, J.; BUI, T.; KIM, K.; JOH, C.; LEE, H. An experimental study on the ductility and flexural toughness of ultrahigh-performance concrete beams subjected to bending. **Materials**, v. 13, n. 10, p. 2225, 2020.

YANG, S.; MILLARD, S.; SOUTSOS, M.; BARNETT, S.; LE, T. Influence of aggregate and curing regime on the mechanical properties of ultra-high performance fibre reinforced concrete (UHPFRC). **Construction and Building Materials**, v. 23, n. 6, p. 2291-2298, 2009.

YANG, R.; YU, R.; SHUI, Z.; GUO, C.; WU, S.; GAO, X.; PENG, S. The physical and chemical impact of manufactured sand as a partial replacement material in Ultra-High Performance Concrete (UHPC). **Cement and Concrete Composites**, v. 99, p. 203-213, 2019.

YOO, D.; BANTHIA, N.; YOON, Y. Flexural behavior of ultra-high-performance fiber-reinforced concrete beams reinforced with GFRP and steel rebars. **Engineering Structures**, v. 111, p. 246-262, 2016.

YOO, D.; KANG, S.; LEE, J.; YOON, Y. Effect of shrinkage reducing admixture on tensile and flexural behaviors of UHPFRC considering fiber distribution characteristics. **Cement and concrete research**, v. 54, p. 180-190, 2013.

YOO, D.; KANG, S.; YOON, Y. Effect of fiber length and placement method on flexural behavior, tension-softening curve, and fiber distribution characteristics of UHPFRC. **Construction and Building materials**, v. 64, p. 67-81, 2014.

YOO, D.; KIM, S.; KIM, M. Comparative shrinkage behavior of ultra-high-performance fiber-reinforced concrete under ambient and heat curing conditions. **Construction and Building Materials**, v. 162, p. 406-419, 2018.

YOO, D.; KIM, S.; LEE, J.; YOU, I.; LEE, S. Implication of calcium sulfoaluminate-based expansive agent on tensile behavior of ultra-high-performance fiber-reinforced concrete. **Construction and Building Materials**, v. 217, p. 679-693, 2019.

YOO, D.; KIM, J.; PARK, J. Effect of fiber spacing on dynamic pull-out behavior of multiple straight steel fibers in ultra-high-performance concrete. **Construction and Building Materials**, v. 210, p. 461-472, 2019.

YOO, D.; YOON, Y. Structural performance of ultra-high-performance concrete beams with different steel fibers. **Engineering Structures**, v. 102, p. 409-423, 2015.

YALÇINKAYA, Ç.; YAZICI, H. Effects of ambient temperature and relative humidity on early-age shrinkage of UHPC with high-volume mineral admixtures. **Construction and Building Materials**, v. 144, p. 252-259, 2017.

YU, R.; SPIESZ, P.; BROUWERS, H. Mix design and properties assessment of ultra-high performance fibre reinforced concrete (UHPFRC). **Cement and concrete research**, v. 56, p. 29-39, 2014.

YU, R.; SPIESZ, P.; BROUWERS, H. Development of Ultra-High Performance Fibre Reinforced Concrete (UHPFRC): Towards an efficient utilization of binders and fibres. **Construction and building materials**, v. 79, p. 273-282, 2015.

ZHOU, Z.; QIAO, P. Direct tension test for characterization of tensile behavior of ultra-high performance concrete. **Journal of Testing and Evaluation**, v. 48, n. 4, p. 2730-2749, 2018.

ZHOU, K.; QI, J.; WANG, J. Post-cracking punching shear behavior of concrete flat slabs partially reinforced with full-depth UHPC: Experiment and mechanical model. **Engineering Structures**, v. 275, p. 115313, 2023.

ZHOU, Z.; QIAO, P. Tensile behavior of ultra-high performance concrete: analytical model and experimental validation. **Construction and Building Materials**, v. 201, p. 842-851, 2019.

APPENDIX A – Database from the 7 days compression tests

Name	S1 (MPa)	S2 (MPa)	S3 (MPa)	S4 (MPa)	S5 (MPa)	Mean (MPa)	Standard Deviation (MPa)	Coefficient of Variance (%)
MS2.5 [DSWT] - 870/0.247 (3S)	63.38	32.40	63.56	74.77	53.52	57.53	15.93	27.70
MS3.0 [DSWT] - 870/0.247 (3S)	59.08	46.76	64.99	60.48	68.08	59.88	8.16	13.63
MS4.0 [DSWT] - 870/0.247 (3S)	77.08	70.38	60.68	71.07	72.77	70.40	6.96	9.88
MS5.0 [DSWT] - 870/0.247 (3S)	58.73	40.53	42.29	47.07	53.01	48.33	7.57	15.66
MS4.0[DSS] - 870/0.247 (3S)	46.33	64.88	69.35	33.11	45.72	51.88	14.96	28.84
MS4.0[DSS]- 950/0.247 (3S)	82.59	68.37	62.08	49.67	47.80	62.10	14.30	23.03
MS4.0 [DSS] – 950/0.247 (4S)	79.45	54.46	62.68	39.92	57.31	58.76	14.31	24.35
MS4.0 [DSS] – 950/0.20 (4S)	52.59	50.89	87.76	84.34	72.25	69.57	17.27	24.83
MS4.0 [SAM] – 950/0.20 (4S)	74.17	92.13	72.43	75.86	89.24	80.77	9.19	11.38
MS3.5 [SAM] – 1100/0.22 (4S-WF)[a]	56.08	72.16	74.94	57.95	80.31	68.29	10.72	15.70
MS3.5 [SAM] – 1185/0.20 (4S-WF)[a]	62.63	66.98	60.89	48.55	50.87	57.98	7.91	13.65
MS3.0 [SAM] – 1185/0.20 (4S-WF)	46.96	69.53	60.54	55.78	48.32	56.23	9.28	16.50
CS3.0 [SAM] – 1185/0.20 (4S-WF)	82.48	82.29	70.14	-	-	78.30	7.07	9.03
CS3.0 [SAM] – 1185/0.20 (4S-WF-ODS)	75.82	89.90	82.86	-	-	82.86	7.04	8.50
CS3.0 [SAM] – 1185/0.20 (4S-WF-ODS-2%F)	108.32	108.51	101.74	-	-	106.19	3.85	3.63
CS2.5 [SAM] – 1185/0.20 (4S-WF-ODS-2%F)	106.24	106.31	105.86	-	-	106.14	0.24	0.23